UNIVERSITÀ
DEGLI STUDI
DI PADOVA

Head Office: University of Padova
Dipartimento di Fisica e Astronomia "Galileo Galilei"

Ph.D. COURSE IN: PHYSICS
SERIES: 32

A new way to determine the neutrino mass hierarchy at reactors

Thesis written with the financial contribution from Fondazione Cariparo

Coordinator: Prof. Franco Simonetto
Supervisor: Prof. Luca Stanco

Ph.D.Student: Fatma Helal SAWY

Academic Year 2019

ABSTRACT

The neutrino mass ordering is one of the fundamental characteristics of the reference $3-$neutrino mixing scheme that still remains undetermined experimentally at present. Some of basic neutrino physics observables, which are planned to be measured in currently running and/or upcoming neutrino experiments, depend critically on the neutrino mass ordering. The Neutrino Mass Hierarchy Determination (ν MHD) is one of the main goals of the major current and future neutrino experiments. ν MHD corresponds to the sign of the so called atmospheric neutrino mass, $|\Delta m^2_{atm}|$. The medium baselines reactor anti-neutrino experiments are designed to determine the neutrino mass hierarchy without exploring the matter effect that is used in long baseline accelerator and atmospheric neutrino experiments. The strategy of mass hierarchy study, in medium baselines reactor experiments, can be based on the study of the neutrino vacuum oscillations. A technique was developed, referring to the interference of the two different oscillation frequencies driven by Δm^2_{31} and Δm^2_{23}, which at first order correspond to Δm^2_{atm} separated by the much smaller solar neutrino mass, Δm^2_{sol}.

Advances in statistical analysis techniques may play a decisive role in the discovery reach at neutrino physics experiments. The statistical analysis for neutrino mass ordering usually proceeds from the standard method based on $\Delta\chi^2$. This method shows some draw-backs and concerns, together with a debatable strategy. The issues of the standard method on ν MHD for the neutrino reactor experiments are explained. As a result, a new alternative statistical method was invented. The new method of determining the neutrino mass ordering in medium baseline experiments with reactor anti-neutrino is based on a bi-dimensional statistical estimator. Referring to the JUNO experimental conditions we developed a completely new technique that would provide a robust $5\,\sigma$ measurement in less than six years of running. The two orderings could be discriminated at the price of allowing for two different degenerated values of Δm^2_{atm}. This degeneracy on Δm^2_{atm} (around $12\times10^{-5}\ eV^2$) can however be tackled at an unprecedented accuracy of much less than 1%, i.e. 10^{-5} eV^2, within the same analysis. The sensitivity using the new estimator, $|F_{MO}$, was obtained assuming that the $|\Delta m^2_{atm}|$, identified as the mass difference between the lightest neutrino mass and the heaviest one, be unique for both hypotheses NH and IH. We will discuss the subtleties of such assumption. On the other hand, also the standard JUNO test statistic depends on some strong assumptions.

There are two kinds of sensitivity studies performed in the dissertation. One is that coming from the standard method, a single dimensional ($1D$) estimator $\Delta\chi^2$; the other one is obtained using the new alternative method via the bi-dimensional estimator F_{MO}. The sensitivity is obtained by taking into account the reactor cores' distribution uncertainty, Daya Bay and Huizhou nuclear power plants contributions, the spectrum shape uncertainty and the detector-related uncertainties, including the energy non-linear response of the detector. The background systematics, especially ^9Li, have minor impact on the sensitivity. Possible results after two, four and six years of running and the foreseen initially-reduced available reactor power have been studied, as well. F_{MO} estimator gives confidence to reject the false mass hierarchy at more than $5\,\sigma$. These results confirm the very positive perspectives for JUNO to determine the mass ordering in a vacuum-oscillation dominated regime if the proper statistical analysis is used.

ACKNOWLEDGMENT

First and foremost, I would like to thank the God, ALLAH, for his never-ending grace, mercy, and provision during what ended up being one of the toughest times of my life. Allah is the source of my power and my support. I am his daughter by definition.

I wish to thank my parents for their support and encouragement throughout my study. Special thanks to my big sister Nadia for her moral and emotional support in my life.

A very special gratitude goes out to all down at CARIPARO for helping and providing the funding for the work. I am also grateful to Padova University for this grate opportunity to study among its students and Italy in general. It was fantastic to have the opportunity to work my Ph.D research in its facilities. What a cracking place to work! I am also grateful to the university staff for their unfailing support and assistance for funding the PhD research. With a special mention to prof. Antonio Trovato for his help.

I would like to express my very great appreciation to prof. Luca Stanco. His willingness to give his time so generously has been very much appreciated. I would also like to express my deep gratitude to him, for his patient guidance, enthusiastic encouragement and useful critiques of this research work.

Besides my supervisor, I would like to thank prof. Giuseppe Salamanna for his valuable and constructive suggestions during the planning and development of this research work. Without his precious co-work it would not be possible to conduct this research.

I would like to offer my special thanks to Xuefeng Ding and Lin Tao for his wonderful collaboration, great support and were always willing to help me. I wish to acknowledge the help provided by our Italian and Chinese collaborators.

And finally, last but by no means least, also to colleagues in office. It was great sharing office with them during last three years.

INTRODUCTION

Every year there are many international conferences about neutrino physics, and some of the largest experiments in the world are for neutrino studies as well. What is the reason for this big interest of the whole world in the physics of this very tiny particle? The neutrino is a fundamental subatomic particle. Neutrinos are extremely weakly interacting particles that can travel in straight lines through normal matter for thousands of kilometers without interactions. Neutrinos are elusive particles that are difficult to study, and may help explaining some of the mysteries of our universe. They are the second abundant particles in the universe and the question why there is more matter than antimatter in the universe could find an answer through studying them. The discoveries over the past half-century have put neutrinos in the spotlight for further research into several fundamental questions about the nature of matter and the evolution of the universe.

Currently, the determination of the neutrino mass ordering using reactor neutrino spectrum is pursued by several experiments and proposals. There are some challenges facing anyone that tries to solve this problem. First, its evaluation from reactor experiments is based on the tiny interference effect between the Δm^2_{31} and Δm^2_{23} oscillations. Second, current analyses require several years of data taking and an extreme energy resolution to achieve anyhow less than $5\,\sigma$. Third, the sensitivity may depend on the input values of the oscillation parameters used by the global fits on the oscillation analysis. In particular, the neutrino atmospheric mass may have different values for normal ordering (NH) or inverted one (IH). The answer to the third point depends on the used analysis method. It is mandatory to establish the robustness of all these analyses.

The Jiangmen Underground Neutrino Observatory (JUNO) experiment will allow to single out one of the missing fundamental information, the neutrino mass hierarchy, in an almost independent way of the other neutrino parameters. In particular, they will be no dependence on the phase of the leptonic CP violation, δ_{CP}, no strong dependence on three vs four neutrino pattern, no dependence on θ_{13}, no dependence on matter effects. The mass hierarchy study can be performed by looking at the vacuum oscillation pattern in medium baselines reactor anti-neutrino experiments. The JUNO strategy is based on the observation that the contribution to the oscillation probability is represented by fast oscillating terms superimposed to a general oscillation pattern. Their relative size changes according to the two different possibilities, NH or IH, leading to a contribution

of opposite sign in the two cases. Therefore, it is possible to discriminate between the two possible mass hierarchies by studying the interference between the two oscillation frequencies driven by Δm^2_{31} and Δm^2_{23} in the reactor antineutrino spectrum. The discrimination power of the experiment is maximized when the Δm^2_{21} oscillation is maximal, and the baseline at JUNO has been chosen in such a way to realize this condition. Two important requirements, essential to reach the desired discrimination, are a large sensitive mass of the detector and a very good energy resolution, of the order of $3\%/\sqrt{E}$. Since the difference of neutrino oscillation in vacuum for different mass hierarchies is very small, energy resolution is the crucial factor for the success of JUNO. The goal is that the energy resolution can reach $3\%/\sqrt{E}$ at $1\,\mathrm{MeV}$ to detect electron neutrino coming from reactor plants. Furthermore, the PMT photo-cathode quantum efficiency need to be greater than 35% and the attenuation length of the liquid scintillator at $430\,\mathrm{nm}$ be greater than $20\,\mathrm{m}$. PMT's will have unprecedented size, PMT coverage and light yield would provide a good sensitivity to the mass hierarchy determination. These two characteristics, the large sensitive mass of the detector and a very good energy resolution, together with the position that is deep underground, will open the way to other possible relevant studies at JUNO.

The thesis is organized as follows, Ch. 1 provides an overview of the theoretical aspects about the neutrino oscillations. Ch. 2 is about the different experimental techniques focusing in reactor experiments. Then, in Ch. 3 we explain in details the under-construction experiment, JUNO. JUNO will start data taking in 2020 and it will run until 2026 to get the confirmation of MH at high significance. JUNO is one of the biggest multipurpose neutrino experiments. It will join the teams of T2K and NoνA. JUNO is the second China-based neutrino project, following the Daya Bay Reactor experiment, and is designed to determine the neutrino mass hierarchy via precision measurements of the reactor neutrino energy spectrum. After the determination of θ_{13} by Daya Bay and other experiments, the next challenge of the international neutrino community is to determine the neutrino mass hierarchy. Sensitivity analysis shows that the preferred range for the experiment stations must be $50 - 55\,\mathrm{km}$ away from a nuclear reactor. Jiangmen City, Guangdong Province, was chosen to be the experiment site for JUNO experiment. The detector site is $53\,\mathrm{km}$ from both Yangjiang and Taishan Nuclear Power Plants, with six $2.9\,\mathrm{GW}$ reactors (2^{nd} generation pressurized water reactor) at Yangjiang NPP and four $4.6\,\mathrm{GW}$ reactors (3^{rd} generation PWR) at Taishan NPP, giving a total thermal power of $35.8\,\mathrm{GW}$ for the 10 reactor cores. By 2020, the effective power will be the highest in the world. The experiment hall will be located about $700\,\mathrm{m}$ underground.

Ch. 4 presents an introduction for the statistical analysis techniques used for solving the neutrino mass ordering problem. A further step concerns the estimation of the sensitivity in determining the mass hierarchy. The dissertation is mainly about full comparison between two different statistical methods looking at construction, implementation and results outcome from medium base-line experiments. JUNO sensitivity to the neutrino mass hierarchy arises from the small phase shift in the oscillation terms depending on the two large mass squared differences Δm^2_{31} and Δm^2_{23}. The corresponding interference in the electron anti-neutrino survival probability becomes largest at a baseline of $\sim 55\,\mathrm{km}$ that coincides with the first solar oscillation maximum (governed by Δm^2_{21}). Depending on the mass hierarchy, the position of maxima and minima of the sub-dominant oscillations undergoes a shift of 180°. Resolving the position of the wiggles in the L/E spectrum requires an energy resolution of 3% at $1\,\mathrm{MeV}$, and an excellent understanding of the linearity of the energy response.

Evaluating the standard statistical methods and updating them is a necessary step in building a robust statistical analysis for the new physics problems. Indeed, Ch. 5 focus on the standard technique. As you will find the standard method shows some draw-backs and concerns. Firstly, the experimental sensitivity strongly depend on the value of the injected neutrino atmospheric mass difference as shown in the oscillation of $|\overline{\Delta\chi^2}|$ with $|\Delta m^2|_{inj}$. Secondly, the $\Delta\chi^2$ estimator provides us with different results due to different simulation procedures. When the simulation is performed on a single event basis and not on a semi-analytical basis [1], it does not take into account the correlation between the bins due to systematic uncertainties, and the significance drastically drops. The systematic uncertainties due to the $3\%/\sqrt{E}$ relatively energy resolution causes unbalanced migration effect between bins that consequently create side-bin correlations leading to significant reduction in the experiment sensitivity . That invalids the use of the standard approximation. Thirdly, when $\chi^2_{min(NH)}$ and $\chi^2_{min(IH)}$ are drawn in two dimensional map, their strong positive correlation manifests χ^2 as a bi-dimensional estimator. This strong positive correlation, leading to an overlap between the χ^2 distributions of the two hypotheses, results in a reduction of the experimental sensitivity. The fitting procedures and the minimization of χ^2 are done by the ROOT minimization libraries (the TMinuit algorithm), all the details being provided in Appendix C.

After the evaluation made for the standard algorithm, an alternative method was invented as discussed in Ch. 6. F-estimator is a technique of the generalized moments. We analytically construct the F-estimator using the quasi-optimal weights method that provides a recipe to derive statistical criteria for testing various hypotheses (in our case the two MH hypotheses). The same method was successfully used in data analysis of Troitsk neutrino mass experiment[1] that resulted in the best neutrino mass limit. In addition, it has been asked to construct specific statistical tests for searches of anomalies in tritium $\beta-$spectrum. Best ν mass bound from Troitsk ν mass [3] had been plagued by "Troitsk anomaly" for $\sim 10\,\text{years}$ ago.

The F_{MO} can achieve a great success for solving MHD in medium base-line reactor experiments. The two orderings could be discriminated at the price of allowing for two different values of Δm^2_{31}. This degeneracy on Δm^2_{31} (around $12\times10^{-5}\text{eV}^2$) can however be measured at an unprecedented accuracy of much less than 1%, i.e. 10^{-5}eV^2, within the same analysis. Evaluation and inclusion of systematic errors and backgrounds have been performed, the most relevant among them being the addition of the two remote reactor plants $250\,\text{km}$ away. Baselines of each contributing reactor core and its spatial resolution have been taken into account.

The results after two, four and six years of running are provided in Ch. 7 in addition to the results of the standard method. And finally, the conclusions are reported in Ch. 8.

[1]The Troitsk nu-mass program is conducted by the Institute for Nuclear Research of the Russian Academy of Sciences. It was initiated by Vladimir Lobashev with the goal to limit the mass of electron anti-neutrino by analyzing the shape of tritium β decay spectrum near the end point [2].

CONTENTS

LIST OF TABLES

LIST OF FIGURES

CHAPTER 1

NEUTRINO OSCILLATIONS

1.1 A Brief History of Neutrino Oscillations

The ultimate goal of the neutrino physics is to explore the fundamental properties of the neutrino, and to discover the basic natural laws giving the neutrino these properties. An historical overview about the ν origin discovery, the ν oscillations and the fundamental events that determined the understanding of the neutrino paradigm is given. The story starts in

1. 1930 when Pauli postulated a new particle to explain the apparent energy non conservation in Beta radioactive decays in a physics conference in Tubingen, Germany [4].

2. In 1933, Enrico Fermi proposed "neutrino" as the name for Pauli's postulated particle. He formulated a quantitative theory of weak particle interactions in which the neutrino plays a fundamental part [5, 6].

3. In 1956 (25 years later), two American scientists, Frederick Reines and Clyde Cowan, reported the first evidence for neutrinos' existence [7]. They used a fission reactor as a source of neutrinos and a well-shielded scintillator detector nearby for detection. The experiment is now known as Cowan-Reines neutrino experiment. A detector consisting of two tanks of water was employed, offering a huge number of potential targets in the protons of the water.

4. In 1957 (the real birth of neutrino physics), the Italian physicist, Bruno Pontecorvo formulated a theory about neutrino oscillations. He showed, that if different species of neutrinos exist, they might be able to oscillate back and forth between different species [6, 5]. Neutrino oscillation is a quantum mechanical phenomenon proposed by Pontecorvo in analogy with $(K^0 \Leftrightarrow \bar{K}^0)$ meson[1] oscillations. The oscillations are

[1]The neutral particle oscillation is the transmutation of a particle with zero electric charge into another neutral particle due to a change of a non-zero internal quantum number via an interaction that does not conserve that quantum number. The particle - antiparticle oscillation like in kaons, like $(K^0 \Leftrightarrow \bar{K}^0)$ and $(B^0 \Leftrightarrow \bar{B}^0)$ oscillation, was known but the flavor oscillation was not known at that time.

generated by the interference of different massive neutrinos, which are produced and detected coherently because of their very small mass differences. Since in that data only one active neutrino was known, the electron neutrino ν_e, in order to discuss neutrino oscillations, Pontecorvo invented the concept of a sterile neutrino, a neutral fermion that does not take part in weak interactions and interacts only gravitationally [5]. The importance of neutrino oscillations appears in many topics. They probe the low mass scales and they have not been integrated into the standard model[2].

5. In 1958, Maurice Goldhaber, Lee Grodzins, and Andrew Sunyar at Brookhaven National Laboratory demonstrate that the new neutrino has left handed helicity, meaning that it spins along the direction of its motion in the sense of a left handed screw[5].

6. In 1962, the muon neutrino, ν_μ, was discovered in the Brookhaven experiment of Lederman, Schwartz, Steinberger[3], who followed up a proposal made by Pontecorvo in 1959. A group of scientists from Columbia University and Brookhaven National Laboratory perform the first accelerator neutrino experiment and demonstrate the existence of two species of neutrinos, the electron neutrino, ν_e, and the muon neutrino, ν_μ. In the same year (1962) Maki, Nakagawa, and Sakata considered for the first time a model with the mixing of different neutrino flavors. Since then, it became clear that oscillations between different active neutrino flavors are possible if neutrinos are massive and mixed.

7. In 1967 Pontecorvo predicted the Solar Neutrino Problem [8] as a consequence of $\nu_e \to \nu_\mu$ (or $\nu_e \to \nu_{sterile}$) transitions even before the first measurement of the solar electron neutrino flux in the Homestake experiment [9], and in 1969 Gribov and Pontecorvo discussed solar neutrino oscillations due to neutrino mixing. However, the probability of neutrino oscillations was not calculated in a rigorous way in the scientific papers [10], but simply estimated on the basis of the analogy with kaon oscillations.

8. But just one year later (1968) solar neutrinos were observed by Raymond Davis in Homestake experiment[4] and a deficit of their flux as compared with the prediction from the Standard Solar Model was also established by Bahcall and his team [5]. Such an anomaly turned out to be solid evidence for new physics beyond the current Standard Model, because it was found to be attributed to neutrino oscillations, a

[2]The Standard Model of particle physics is a successful theory, which not only unifies the electromagnetic and weak interactions but also explains almost all the phenomena of this nature observed at or below the electroweak scale. When this theory was first formulated by Weinberg in 1967, its particle content was so economical that the neutrinos were assumed to be massless and hence there was no lepton flavor mixing.

[3]In 1987, Jack Steinberger, Leon Lederman, and Mel Schwartz won the Nobel Prize for this discovery.

[4]The Homestake Solar Neutrino Observatory was located 1478 m below the surface, in the Homestake Gold Mine at Lead, in South Dakota, USA [9]. Its purpose was to collect and count neutrinos emitted from the sun. It is considered as the first solar neutrino detection experiment. In 1(968), Raymond Davis and his team reported the results of the Homestake experiment. The pioneering Homestake experiment is a radiochemical experiment, which detects solar neutrinos through $Cl - Ar$ reaction. It used cl^{37} to detect neutrinos with neutrino energy threshold $E_\nu^{th} = 814$ KeV. Therefore, this experiment can detect only intermediate and high-energy neutrinos. Bahcall did the theoretical calculations and Davis designed the experiment. Bahcall calculated the rate at which the detector should capture neutrinos, Davis's experiment turned up only about one third of this figure. The experiment was the first to successfully detect and count solar neutrinos, and the discrepancy in results created the solar neutrino problem. The experiment operated continuously from 1970 until 1994.

spontaneous and periodic change from one neutrino flavor to another, which does not take place unless neutrinos have finite masses. By investigating these oscillations only the absolute value of the differences between the mass-square eigenstates can be measured, and thus we do not know which one is heavier. Actually, nowadays we know that $m_2^2 > m_1^2$. One of the main aims of neutrino physics today is to determinate the correct mass hierarchy of the other neutrino mass eigenstates.

9. In 1998, the oscillations were first discovered by Super-Kamiokande [5], not forgetting the missing-observation of Chooz experiment in the same year. The properties of neutrinos began to be determined, one after another, and it has become necessary to update the Standard Model [11].

10. In 2010, OPERA researchers observed the first tau neutrino ν_τ direct oscillation candidate event in a muon neutrino beam, the first time this transformation in neutrinos had been observed, providing further evidence that they have mass [12].

11. In 2012, the third mixing angle θ_{13}, was finally measured by Daya-Bay, Reno and Double-Chooz reactor experiments and T2K, an accelerator beam experiment [5]. The detection of solar neutrinos is considered today mainly an activity of high-energy physicists interested in the properties of neutrinos.

1.2 The Vacuum Neutrino Oscillations Phenomenon

Neutrino oscillations is a quantum mechanical phenomenon in which neutrino flavor changed spontaneously to another flavor. According to the standard 3 neutrino paradigm, neutrinos come with three flavors, ν_e, ν_μ and ν_τ, and with three ν_1, ν_2 and ν_3 mass eigenstates [13]. To better understand the ν mixing phenomena, we have to recall the neutrino unitary mixing-matrix U_{PMNS};

$$\begin{pmatrix} \nu_e \\ \nu_\mu \\ \nu_\tau \end{pmatrix} = \begin{pmatrix} U_{e1} & U_{e2} & U_{e3} \\ U_{\mu 1} & U_{\mu 2} & U_{\mu 3} \\ U_{\tau 1} & U_{\tau 2} & U_{\tau 3} \end{pmatrix} \begin{pmatrix} \nu_1 \\ \nu_2 \\ \nu_3 \end{pmatrix} \tag{1.1}$$

Using the unitarity of the mixing matrix, U_{PMNS}, the vacuum transition amplitudes from state α to β, $A_{\alpha\beta}$, are obtained via the probabilities $P_{\alpha\beta}$:

$$P_{\alpha\beta} = A^*_{\alpha\beta} A_{\alpha\beta} = \sum_{i,j=1}^{3} U^*_{\alpha i} U_{\alpha j} U_{\beta i} U^*_{\beta i} e^{-i(E_i - E_j)t} \tag{1.2}$$

As U_{ei} is the neutrino mixing-matrix element relating ν_e to mass eigenstate ν_i, the survival probability $P_{\bar{\nu}_e \to \bar{\nu}_e}$ is expressed as

$$P_{\bar{\nu}_e \longrightarrow \bar{\nu}_e} = |\sum_{i=1}^{3} U_{ei} exp\left(\frac{-im_i^2}{2E_i}\right) U^*_{ei}|^2, \tag{1.3}$$

where m_i is the mass of corresponding mass eigenstate and E_i is the corresponding energy eigenstate.

$$\begin{aligned} P_{\bar{\nu}_e \longrightarrow \bar{\nu}_e} = 1- & \cos^4\theta_{13}\sin^2 2\theta_{12}\sin^2(\Delta_{21}) \\ - & \cos^2\theta_{12}\sin^2 2\theta_{13}\sin^2(\Delta_{31}) \\ - & \sin^2\theta_{12}\sin^2 2\theta_{13}\sin^2(\Delta_{32}) \end{aligned} \tag{1.4}$$

θ_{ij} are the ν mixing-angles, the oscillation phases $\Delta_{ij} \equiv \frac{L\Delta m^2_{ij}}{4E_\nu}$, and $\Delta m^2_{ij} = m^2_i - m^2_j$. Following e.g. the development in [14] the survival probability can be re-written as

$$\begin{aligned} p_\lambda(\bar{\nu}_e \to \bar{\nu}_e) = 1 & - \frac{1}{2}\sin^2 2\theta_{13}(1 - cos\frac{\Delta m^2_{atm} L}{2E}) \\ & - \frac{1}{2}\cos^4\theta_{13}\sin^2 2\theta_{12}(1 - cos\frac{\delta m^2_{sol} L}{2E}) \\ & + \frac{1}{2}\sin^2 2\theta_{13}\left[\cos^2\left(\theta_{12} + \frac{\lambda\pi}{2}\right)\right](cos\frac{L}{2E}(\Delta m^2_{atm} - \delta m^2_{sol}) - cos\frac{L\Delta m^2_{atm}}{2E}) \end{aligned} \tag{1.5}$$

For $\lambda = 0$ one obtain $p_\lambda(\bar{\nu}_e \to \bar{\nu}_e) = p_{IH}(\bar{\nu}_e \to \bar{\nu}_e)$ and for $\lambda = 1$ one get $p_\lambda(\bar{\nu}_e \to \bar{\nu}_e) = p_{NH}(\bar{\nu}_e \to \bar{\nu}_e)$. The existing neutrino oscillation data allows us to know the values of Δm^2_{21}, and $|\Delta m^2_{31(32)}|$, with uncertainty, as well as the values of the three neutrino mixing angles θ_{12}, θ_{23}, and θ_{13} of the PMNS neutrino mixing matrix with high precision. However, the sign of $\Delta m^2_{31(32)}$ is not determined, yet. That creates what is known by name ν Mass Hierarchy Determination (MHD) problem (SubSec. 1.3.4).

There are many ways to parameterize the survival probability of reactor neutrinos. One is introduced through an effective atmospheric mass Δm^2_{ee} and phase ϕ.

$$p(\bar{\nu}_e \to \bar{\nu}_e) \approx 1 - \sin^2 2\theta_{13}\sin^2\Delta_{ee} - \cos^4\theta_{13}\sin^2 2\theta_{12}\sin^2\Delta_{21} \tag{1.6}$$

The $\overline{\nu}_e$ spectrum at JUNO experiment is shown in Fig. 1.1 in addition to a graphical representation to Δm^2_{ee}. This parameterisation is quit useful when a fitting procedure is applied as it will discuss in Ch. 5.

$$\Delta_{ee} \equiv \frac{L\Delta m^2_{ee}}{4E_\nu}, \qquad \Delta m^2_{ee} = \sin^2_{\theta_{12}}\Delta m^2_{13} + \cos^2_{\theta_{12}}\Delta m^2_{23} \tag{1.7}$$

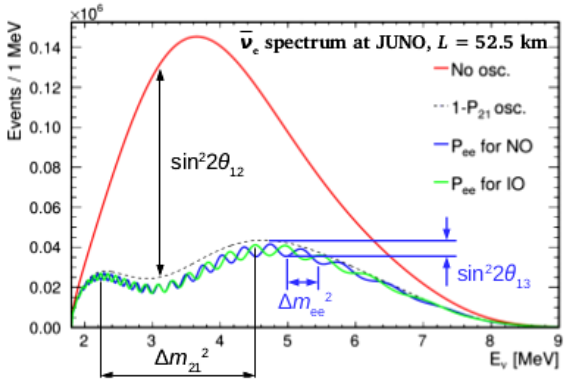

Figure 1.1: *$\overline{\nu}_e$ spectrum at JUNO.*

$$sin\phi = \frac{c_{12}^2 sin(2s_{12}^2 \triangle_{21}) - s_{12}^2 sin(2c_{12}^2 \triangle_{21})}{\sqrt{1 - sin^2 2\theta_{12} sin^2 \triangle_{21}}}, \qquad cos\phi = \frac{c_{12}^2 cos(2s_{12}^2 \triangle_{21}) + s_{12}^2 cos(2c_{12}^2 \triangle_{21})}{\sqrt{1 - sin^2 2\theta_{12} sin^2 \triangle_{21}}} \tag{1.8}$$

1.3 Open Issues on Neutrinos Physics

Although neutrinos were introduced over 80 years ago, their properties remain to a large extent unknown [15]. Some of the 3ν paradigm fundamental parameters are still missing until now like: the absolute masses of neutrinos, the amount of the possible leptonic charge parity violation (CPV), Dirac or Majorana neutrino nature and the neutrino mass ordering. We are going to discuss them one by one in the following subsections.

1.3.1 The nature of neutrinos and their mass spectrum

The nature of the neutrino and its mass spectrum is still an open question searching for an answer. The tiny masses of three known neutrinos means it is extremely difficult to identify their masses.

Do neutrinos follow Dirac or Majorana statistics?

If the mass of the neutrino is generated by the Dirac mechanism, it would have the Yukawa interactions with the Higgs. If the neutrino get its mass through Majorana mechanism, the neutrino and anti-neutrino are the same particle. By definition, a massive Majorana neutrino is its own antiparticle, leading to lepton number violation as a direct consequence. At present, the only experimentally workable way to probe the Majorana nature of massive neutrinos is to observe the neutrinoless double-beta ($0\nu\beta\beta$) decays[5] of some even-even nuclei, $N(Z, A) \rightarrow N(Z + 2, A) + 2e$, which occur via an exchange of the

[5] Double beta ($\beta\beta$) decay is a second-order weak process that transforms a nuclide of atomic number Z into its isobar with atomic number $Z + 2$. Their are two types of double beta decay: ordinary double

virtual Majorana neutrinos between two associated beta decays, as indicated in Fig. 1.2. In the context of light Majorana neutrino exchange, $m_{\beta\beta}$ is given by

$$m_{\beta\beta} = \sum_{i=1}^{3} m_i U_{ei}^2, \tag{1.9}$$

where m_i are the neutrino masses and the U_{ei} are elements of the neutrino unitary mixing-matrix (U_{PMNS}). Currently, numerous experiments search for neutrinoless double beta decay; GERDA, KemLAND-Zen, MAJORANA and other experiments.

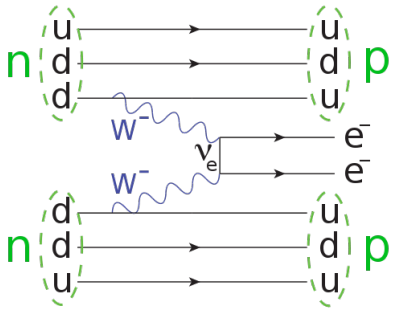

Figure 1.2: *Feynman diagram of neutrinoless double beta decay, with two neutrons decaying to two protons.*

The discovery of this process would demonstrate that neutrinos are Majorana particles and that total lepton number is not conserved in nature, two findings with far reaching implications in particle physics and cosmology.

1. The existence of Majorana neutrinos implies a new energy scale at a level inversely proportional to the observed neutrino masses. Such a scale, besides providing a simple explanation for the striking lightness of neutrino masses, is probably connected to several open questions in particle physics, like the origin of mass or the flavor problem.

2. Majorana neutrinos violate the conservation of lepton number, and this, together with CPV, could be responsible, through the mechanism known as leptogenesis, for the observed cosmological asymmetry between matter and antimatter [16].

What is the absolute mass scale of neutrinos?

There are three workable ways to probe the absolute mass scale of three known neutrinos. Since the flavor oscillations of massive neutrinos are only sensitive to the neutrino mass-squared differences, a determination of the absolute neutrino mass scale has to rely on some non-oscillation experiments. Searching for the $0\nu\beta\beta$ decay is one of the feasible ways for this purpose if massive neutrinos are the Majorana particles, since the magnitude of its effective mass $\langle m \rangle_{ee}$ is governed by m_i as

$$\langle m \rangle_{ee} \equiv \sum_{i}^{3} m_i U_{ei}^2 \tag{1.10}$$

beta decay and neutrinoless double beta decay. The ordinary decay mode consists in two simultaneous beta decays ($2\nu\beta\beta$), $N(Z, A) \rightarrow N(Z + 2, A) + 2e + 2\overline{\nu}_e$.

virtual Majorana neutrinos between two associated beta decays, as indicated in Fig. 1.2. In the context of light Majorana neutrino exchange, $m_{\beta\beta}$ is given by

$$m_{\beta\beta} = \sum_{i=1}^{3} m_i U_{ei}^2, \tag{1.9}$$

where m_i are the neutrino masses and the U_{ei} are elements of the neutrino unitary mixing-matrix (U_{PMNS}). Currently, numerous experiments search for neutrinoless double beta decay; GERDA, KemLAND-Zen, MAJORANA and other experiments.

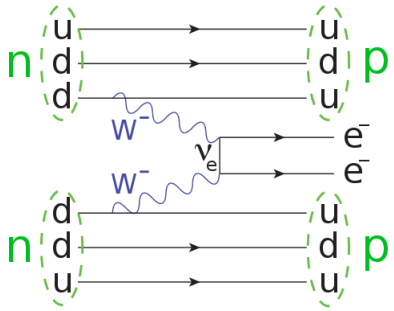

Figure 1.2: *Feynman diagram of neutrinoless double beta decay, with two neutrons decaying to two protons.*

The discovery of this process would demonstrate that neutrinos are Majorana particles and that total lepton number is not conserved in nature, two findings with far reaching implications in particle physics and cosmology.

1. The existence of Majorana neutrinos implies a new energy scale at a level inversely proportional to the observed neutrino masses. Such a scale, besides providing a simple explanation for the striking lightness of neutrino masses, is probably connected to several open questions in particle physics, like the origin of mass or the flavor problem.

2. Majorana neutrinos violate the conservation of lepton number, and this, together with CPV, could be responsible, through the mechanism known as leptogenesis, for the observed cosmological asymmetry between matter and antimatter [16].

What is the absolute mass scale of neutrinos?

There are three workable ways to probe the absolute mass scale of three known neutrinos. Since the flavor oscillations of massive neutrinos are only sensitive to the neutrino mass-squared differences, a determination of the absolute neutrino mass scale has to rely on some non-oscillation experiments. Searching for the $0\nu\beta\beta$ decay is one of the feasible ways for this purpose if massive neutrinos are the Majorana particles, since the magnitude of its effective mass $\langle m \rangle_{ee}$ is governed by m_i as

$$\langle m \rangle_{ee} \equiv \sum_{i}^{3} m_i U_{ei}^2 \tag{1.10}$$

beta decay and neutrinoless double beta decay. The ordinary decay mode consists in two simultaneous beta decays ($2\nu\beta\beta$), $N(Z, A) \rightarrow N(Z + 2, A) + 2e + 2\overline{\nu}_e$.

The upper bound of $|\langle m\rangle_{ee}|$ has been set to be about $0.2\,\mathrm{eV}$ by the present $0\nu\beta\beta$ -decay experiments [1]. Another way is to detect the effective neutrino mass in the beta decays, such as

$$^{3}_{1}H \rightarrow {}^{3}_{2}He + e + \overline{\nu}_e. \tag{1.11}$$

The KATRIN experiment is the most promising next-generation direct mass search experiment, which may hopefully probe m_{ν_e} with a sensitivity of about $0.2\,\mathrm{eV}$.

$$\langle m\rangle_e \equiv \sqrt{m_1^2|U_{e1}|^2 + m_2^2|U_{e2}|^2 + m_3^2|U_{e3}|^2} \tag{1.12}$$

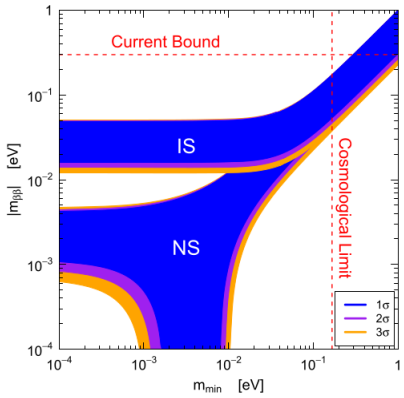

Figure 1.3: *Values of the effective Majorana mass $|m_{\beta\beta}|$ as a function of the lightest neutrino mass in the normal (NS, with $m_{min} = m_1$) and inverted (IS, with $m_{min} = m_3$) neutrino mass spectra after the measurement of non-zero θ_{13}. Republished with permission of World Scientific, from [17], copyright 1986; permission conveyed through Copyright Clearance Center Inc.*

Furthermore, one may get useful information on the mass scale of light neutrinos from cosmology and astrophysics. A global analysis of current cosmological data (especially those on the cosmic microwave background (CMB) and large-scale structures) has actually provided us with the most powerful sensitivity to the sum of light neutrino masses,

$$\sum_{\nu} \equiv \sum_{i} m_i. \tag{1.13}$$

For example, $\sum_\nu < 0.23\,\mathrm{eV}$ has recently been reported by the Planck Collaboration at the 95% confidence level [18]. Given the values of Δm^2_{21} and $|\Delta m^2_{31}|$ extracted from current neutrino oscillation data, the results of $|\langle m\rangle_{ee}|$, $\langle m\rangle_e$ and $\sum_\nu$ are all sensitive to the sign Δm^2_{31}.

1.3.2 Extra neutrino species and unitarity tests

From the definition of neutrino, it is an elementary particle and has a spin $\frac{1}{2}$, thus being a fermion. Neutrinos belong to the family of the leptons. It has a non vanishing mass. One of the fundamental questions in the neutrino physics and cosmology is whether there exist extra species of neutrinos that do not directly participate in the standard weak interactions. Such sterile (light or heavy) neutrinos are certainly hypothetical, but their possible existence is either theoretically motivated or experimentally implied. For

example, the canonical (type-I) seesaw mechanism provides an elegant interpretation of the small masses of ν_i (for i = 1, 2, 3) with the help of two or three heavy sterile neutrinos, and the latter can even help to account for the observed matter - antimatter asymmetry of the universe via the leptogenesis mechanism [19].

On the experimental side, the LSND [20], MiniBooNE [21] and reactor antineutrino [22] anomalies can all be explained as the active sterile anti-neutrino oscillations in the assumption of one or two species of sterile anti-neutrinos whose masses are around $1\,\mathrm{eV}$ [23, 24]. The LSND experiment [20] observed a 3.8 σ excess of $\overline{\nu}_e$ events, a ν_e 3.4 σ and 2.8 σ $\overline{\nu}_e$ excesses were observed by MiniBooNE [25] in short baseline experiments using ν_μ and anti-neutrinos.

As for the $\overline{\nu}_e \to \overline{\nu}_e$ oscillation in a reactor antineutrino experiment, the heavy sterile antineutrinos do not participate in any flavor oscillations, but they may violate the unitarity of the 3×3 MNSP matrix. In comparison, the light sterile anti-neutrinos can provide extra oscillation terms to $p_{\overline{\nu}_e \to \overline{\nu}_e}$.

In the presence of small mixing between 3 active and n sterile neutrinos, the 3×3 U_{PMNS} becomes a submatrix of the (3 + n)×(3 + n) unitary matrix which describes the overall flavor mixing effects,

$$\begin{pmatrix} \nu_e \\ \nu_\mu \\ \nu_\tau \\ \cdots \\ \cdots \\ \cdots \end{pmatrix} = \begin{pmatrix} U_{e1} & U_{e2} & U_{e3} & \cdots \\ U_{\mu 1} & U_{\mu 2} & U_{\mu 3} & \cdots \\ U_{\tau 1} & U_{\tau 2} & U_{\tau 3} & \cdots \\ \cdots & \cdots & \cdots & \cdots \\ \cdots & \cdots & \cdots & \cdots \\ \cdots & \cdots & \cdots & \cdots \end{pmatrix} \begin{pmatrix} \nu_1 \\ \nu_2 \\ \nu_3 \\ \cdots \\ \cdots \\ \cdots \end{pmatrix} . \tag{1.14}$$

Hence, the 3×3 U_{PMNS} matrix itself must be non-unitary. An experimental test of the unitarity of the 3×3 PMNS matrix is therefore important to probe or constrain the flavor mixing parameters of possible new physics associated with sterile neutrinos, and it can theoretically shed light on the underlying dynamics responsible for neutrino mass generation and lepton flavor mixing.

1.3.3 Lepton flavor mixing pattern and CPV

There are still many unsolved problems in neutrino physics considered as open questions in massive neutrinos and seeking for answers. The unanswered questions in neutrino physics are:

What is the Dirac CPV phase δ_{cp}?

In the standard three-flavor scheme the phase parameter δ_{cp} of the neutrino unitary mixing-matrix (U_{PMNS}) is fundamentally important because it uniquely controls the strength of leptonic CP and T violation in neutrino oscillations. Under CPT invariance, the CP- and T-violating asymmetries $A_{\alpha\beta}$

$$A_{\alpha\beta} \equiv P(\nu_\alpha \to \nu_\beta) - P(\overline{\nu}_\alpha \to \overline{\nu}_\beta) = P(\nu_\alpha \to \nu_\beta) - P(\nu_\alpha \to \nu_\beta) \tag{1.15}$$

in vacuum are explicitly given by

$$A_{\alpha\beta} = 2\sin(2\theta_{12})\cos(\theta_{13})\sin(2\theta_{13})\sin 2\theta_{23} \times sin\delta$$
$$\sum_{\gamma} \epsilon_{\alpha}\beta_{\gamma} \sin\frac{\Delta m^2_{21}L}{4E} \sin\frac{\Delta m^2_{31}L}{4E} \sin\frac{\Delta m^2_{32}L}{4E},$$

in which the Greek subscripts run over e, μ and τ. It becomes obvious that CP or T violation is a three-flavor 'appearance' effect, and a measurement of this effect will allow us to determine the value of δ_{cp} [1].

In a realistic medium baseline or long baseline neutrino oscillation experiment, however, the terrestrial matter effects may modify the oscillation behaviors and thus affect the determination of δ_{cp}. This kind of contamination is negligible for a variety of experiments provided the neutrino beam energy E and the baseline length L satisfy the condition $10^{-7}(L/km)^2(GeV/E) \ll 1$. If the unitarity of the 3×3 U_{PMNS} is slightly violated due to the existence of extra species of massive neutrinos, it is also possible for new CP- violating effects to show up in neutrino oscillations [6].

What are the Majorana CPV phases ρ and σ?

If the Majorana nature of massive neutrinos is finally established through a convincing measurement of the $0\nu\beta\beta$ decay, one will be left with a question that is probably most challenging in neutrino physics: how to determine the CPV phases ρ and σ in the standard three-flavor scheme? Because the $0\nu\beta\beta$ decay is a CP-conserving process, its effective mass term $\langle m\rangle_{ee}$ can only provide some indirect information on the combinations of δ_{cp}, ρ and σ. Hence a direct determination of ρ and σ depends on the observation of those processes that are both lepton number violating and CPV. Although the measurement of neutrino-antineutrino oscillations can in principle allow us to probe all the three CPV phases and even the absolute neutrino mass scale, it is in practice impossible to do such an experiment since the corresponding oscillation probabilities are suppressed by the factors $m_i^2/E^2 \lesssim 10^{-12}$.

The 3×3 Majorana neutrino mass matrix M_ν can be reconstructed in terms of three neutrino masses, three flavor mixing angles and three CPV phases in the basis where the flavor eigenstates of three charged leptons are identified with their mass eigenstates. Its six independent elements are

$$\langle m\rangle_{\alpha\beta} \equiv \sum_i (m_i U_{\alpha i} U_{\beta i}), \tag{1.16}$$

where α and β run over e, μ and τ. Current experimental constraints on the magnitudes of $\langle m\rangle_{\alpha\beta}$ can be found in [26]. While a theoretical model is always possible to predict the modules and phases of $\langle m\rangle_{\alpha\beta}$, its correctness or wrongness will not be testable until sufficient information about the CPV phases of U_{PMNS} be experimentally obtained.

What is the octant θ_{23}?

Although the neutrino mixing angle θ_{13} has already been determined in the Daya Bay experiment, the geometric structure of the 3×3 U_{PMNS} can not be fully fixed until the

octant of the mixing angle θ_{23}(i.e., $\theta_{23} < \pi/4$ or $\theta_{23} > \pi/4$) and the value of δ_{cp} are both known. Large mixing and especially a large value of θ_{13} gives us an opportunity to search for CPV in neutrino oscillations i.e. CP violation in the lepton sector. In comparison, the CKM quark flavor mixing matrix $\bigvee$ is found to possess a clearly hierarchical structure, $\bigvee_{tb} > \bigvee_{ud} > \bigvee_{cs} \gg \bigvee_{us} > \bigvee_{cd} \gg \bigvee_{cb} > \bigvee_{ts} \gg \bigvee_{td} > \bigvee_{ub}$, since its three mixing angles satisfy $\theta_{12} \gg \theta_{23} \gg \theta_{13}$, which should have something to do with the strong quark mass hierarchies. Fig. 1.4 represents the schematic illustration of the "flavor hierarchy" and "flavor desert" in the fermion mass spectrum at the electroweak scale.

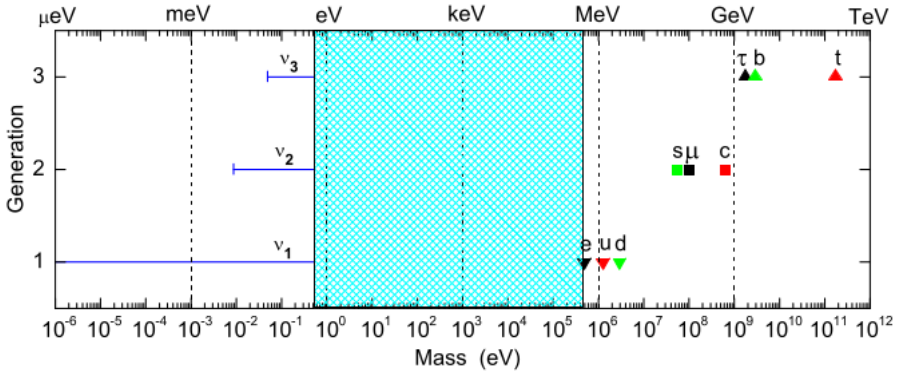

Figure 1.4: *A schematic illustration of the "flavor hierarchy" and "flavor desert" in the fermion mass spectrum at the electroweak scale. Here the neutrino masses are assumed to have a normal ordering. Reprinted from [1], Copyright 2011, with permission from Elsevier.*

1.3.4 The neutrino mass hierarchy problem

Determining the type of neutrino mass spectrum is one of the principal goals of the program on future research in neutrino physics because;

1. The neutrino mass hierarchy is one of the remaining undetermined fundamental features of the neutrino Standard Model.

2. Without the knowledge of what is the neutrino mass ordering, or the spectrum of neutrino masses, it is impossible to make progress in understanding the mechanism giving rise to non-zero neutrino masses and neutrino mixing [27]. Actually, determining this hierarchy is important for the neutrino Standard Model building.

3. Many basic neutrino physics observables that are planned to be measured in currently running and/or upcoming neutrino experiments, depend critically on the neutrino mass ordering. These include the CP violation asymmetry in long baseline neutrino oscillation experiments, the effective Majorana mass in neutrinoless double beta decay experiments, the sum of neutrino masses in the case of hierarchical neutrino mass spectrum etc. [27].

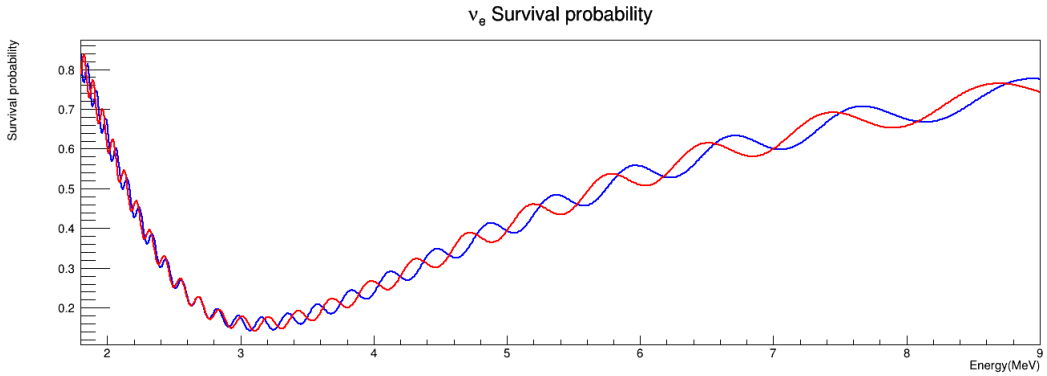

Figure 1.5: *Survival probability, $P_{\bar{\nu}_e}$, at $L = 52.5\,\mathrm{km}$, $sin^2_{12} = 0.2970$, and $\delta m^2_{sol} = 7.37 \times 10^{-5}$ ev^2, for NH hypothesis (blue line) $\Delta m^2 = 2.500 \times 10^{-3}$ ev^2 and $sin^2_{13}(NH) = 0.02140$ and for IH hypothesis (red line) $\Delta m^2 = -2.460 \times 10^{-3}$ ev^2 and $sin^2_{13}(IH) = 0.02180$, as reported in [1].*

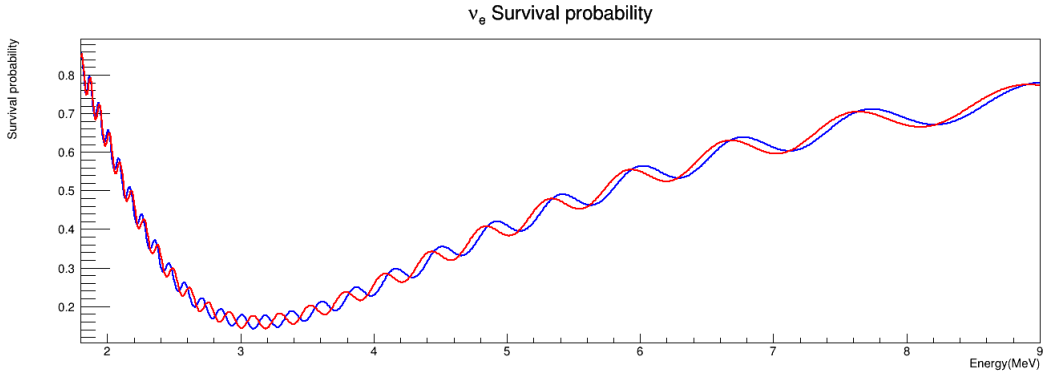

Figure 1.6: *Survival probability, $P_{\bar{\nu}_e}$, at $L = 52.5\,\mathrm{km}$, $sin^2_{12} = 0.2970$, $sin^2_{13} = 0.02150$, and $\delta m^2_{sol} = 7.37 \times 10^{-5} \mathrm{ev}^2$, for NH hypothesis (blue line) $\Delta m^2 = 2.5230 \times 10^{-3}$ ev^2 and for IH hypothesis (red line) $\Delta m^2 = -2.5230 \times 10^{-3}$ ev^2.*

	best-fit	3σ region
Sin^2_{12}	0.2970	0.2500 - 0.3540
$Sin^2_{13}(NH)$	0.02140	0.0185 - 0.0246
$Sin^2_{13}(IH)$	0.02180	0.0186 - 0.0248
δm^2_{sol}	7.37×10^{-5}	$6.93 \times 10^{-5} - 7.97 \times 10^{-5}$
$\Delta m^2(NH)$	2.500×10^{-3}	2.37×10^{-3} - 2.63×10^{-3}
$\Delta m^2(IH)$	2.460×10^{-3}	-2.60×10^{-3} to -2.33×10^{-3}

Table 1.1: *The recent best-fit values for the oscillation parameters, as indicated in [28].*

In reactor neutrino studies, the mass hierarchy can be determined by the position of maxima and minima of the sub-dominant oscillation wiggles where they undergo a shift of π as one can see in Fig. 1.5 and Fig. 1.6. That corresponds to opposite sign in the two cases of Normal Hierarchy (NH) and Inverted Hierarchy (IH). It is possible to discriminate between the two mass hierarchies, by studying the interference between the two oscillation frequencies driven by Δm^2_{32} and Δm^2_{31} [1]. Resolving the position of these wiggles in the ν energy spectrum requires an high energy resolution, and an excellent understanding of the linearity of the energy response [1]. The two mass parameters are usually defined

in terms of Δm^2, the neutrino atmospheric mass, and δm^2_{sol} the neutrino solar mass (Fig. 1.7).

$$\Delta m^2_{31} = \Delta m^2 + \frac{\delta m^2_{sol}}{2} \tag{1.17}$$

$$\Delta m^2_{32} = \Delta m^2 - \frac{\delta m^2_{sol}}{2} \tag{1.18}$$

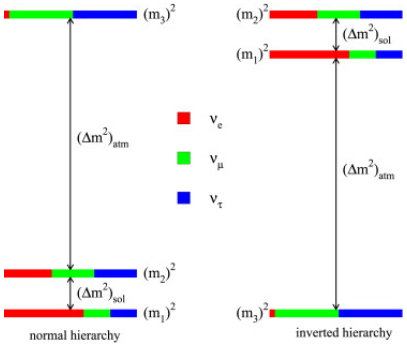

Figure 1.7: *Neutrino mass eigenstates for normal and inverted mass ordering.*

Determining the exact values of neutrino mass and mixing parameters is crucial to test neutrino models and flavor symmetries designed to predict these neutrino parameters. According to [29] and references within, the precise determination of mass hierarchy relies on the knowledge of Δm^2_{32}. They have shown that an incorrect Δm^2_{32} may bias the mass hierarchy determination to some extent. According to the global fit, the two values of neutrino atmospheric mass (the separation between the lightest and the heavier neutrino mass) in case of NH model and IH model are obviously not equal.

$$|\Delta m^2_{atm}|_{(NH)} \neq |\Delta m^2_{atm}|_{(IH)} \tag{1.19}$$

CHAPTER 2

NEUTRINO DETECTION

2.1 Introduction

The neutrinos are weakly interacting particles. At low energies, neutrinos interact with atomic electrons and nuclei as a whole. At higher energies, they interact with nucleons (neutrons or protons) inside a nucleus. At the highest energies, the neutrino will transfer enough energy to the nucleus to break it apart. The weak interactions as the main method for neutrino detection occur through:

1. The neutral current interaction Z^0, where the neutrino remains a neutrino, but it transfers energy and momentum to the target particle. We detect this energy transfer, either because the target recoils (e.g. neutrino-electron scattering, $\nu + e \rightarrow \nu + e$) or because it breaks up (e.g. $2H + \nu \rightarrow p + n + \nu$). If the target particle is charged and sufficiently light (e.g. an electron), it may be accelerated to a relativistic speed and consequently emits Cherenkov radiation, that can be observed directly. All three neutrino flavors can participate regardless of the neutrino energy.

2. The charged current interaction $W^{\pm}$, where the neutrino converts into the equivalent charged lepton (e.g. inverse beta decay). The experiment detects the charged lepton (electron, muon, or tau). At high-energy neutrino transforms into its partner lepton i.e. neutrino needs to have enough energy to produce the outgoing lepton. For example to produce a μ, the threshold energy is $E_{\nu_\mu} > 110\,\mathrm{MeV}$; the threshold energy for τ production is $E_{\nu_\tau} > 3.5\,\mathrm{Gev}$. Neutrinos from the sun and from nuclear reactors have enough energy to create electrons. Most accelerator-based neutrino beams can also generate muons, with electrons and taus as minor contributions. Instead, if the neutrino does not have sufficient energy to create its heavier partner's mass, the charged current interaction is unavailable to it.

The number of the observing neutrino interactions is expressed as

$$N_{obs} \propto M \times T \int \phi(E_\nu) \times \sigma(E_\nu) \times \epsilon(E_\nu) dE_\nu, \tag{2.1}$$

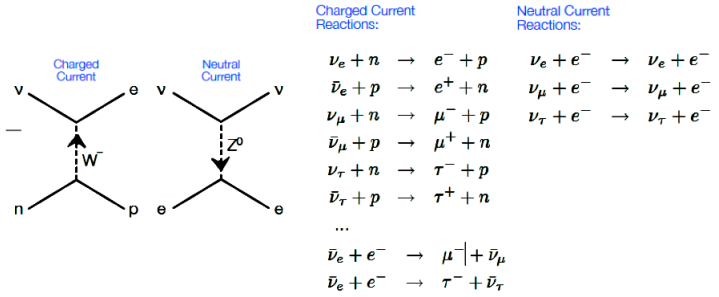

Figure 2.1: *Neutrino interactions via weak interaction.*

where N_{obs} is the observed number of neutrinos, M is the target mass, T is the exposure time, ϕ is the flux of neutrino in $\mathrm{events/cm^2/s}$, and σ is the reaction cross-section. Since the probability for interaction is very small ($\sim 10^{-38}\,\mathrm{cm^2}$), the chances of seeing a neutrino event are increased by using a detector of large mass (with high event efficiency) and high flux, i.e. sending a lot of neutrinos through it. There are various detection methods that have been used to detect neutrino. We will report about some of them.

This chapter is dedicated for the experimental neutrino physics and an overview of the status of the present knowledge of experimental neutrino physics.

Liquid Scintillators

Electron anti-neutrino $\overline{\nu}_e$ is usually detected in liquid scintillator experiments via inverse beta decay reaction (IBD), as shown in the following equation:

$$\overline{\nu}_e + p \rightarrow e^+ + n. \tag{2.2}$$

The $\overline{\nu}_e$ with an energy above the threshold of $1.8\,\mathrm{MeV}$ produces charged current interactions with the protons in the water, yielding positrons (e^+) and neutrons (n_0^1). This is very much like β^+ decay, where energy is used to convert a proton (p_1^1) into a neutron (n_0^1), a positron (e^+) and an electron neutrino ν_e, emitted through Eq. 2.2. The resulting positron annihilation with electrons in the detector material creates gamma rays $(\gamma - rays)$ with an energy of about $511\,\mathrm{KeV}$ that gives a prompt signal. The prompt signal corresponds to a pair of photons in coincidence that could be detected by the two scintillation detection around the target. The neutrons were captured by nuclei resulting in $\gamma - rays$ of about $2.2\,\mathrm{MeV}$ detected a $\sim 200\,\mu\mathrm{s}$ after the prompt signal from a (e^+) annihilation. It corresponds to a delayed signal, as indicated in Eq. 2.3.

$$n + p \rightarrow d + \gamma\,(2.2\,\mathrm{MeV}) \tag{2.3}$$

The coincidence of the prompt signal (positron signal) and delayed signal (neutron signal) in short time significantly reduced the background [1]. That is called "delayed coincidence". e^+ carries almost all energy of the $\overline{\nu}_e$ in this reaction. Therefore, generally the neutrino spectrum can be obtained just from the prompt signal with a $\sim 0.8\,\mathrm{MeV}$ shift. Since protons are at rest and neutrons are so heavy compared to electrons, the

neutron recoiled energy is neglected and the $\overline{\nu}_e$ energy E_ν is related to the e^+ energy E_e via the following approximation.

$$E_\nu = E_e + T_n - m_e + (m_n - m_p), \tag{2.4}$$

where m_e, m_n and m_p are the masses of the positron, neutron and proton, respectively. The neutrino energy threshold E_ν^{th} can be calculated as shown here;

$$E_\nu^{th} = m_e + (m_n - m_p) \cong 1.8\,\mathrm{MeV} \tag{2.5}$$

Where $m_n - m_p = 1.293$ MeV and $m_e = 0.511$MeV. E_ν can be expressed in terms of visible energy, E_{vis}. The visible energy is the energy of the photons emitted when the positron produced in the IBD reaction annihilates with an electron in the detector [27] i.e. the energy of e^+ event.

$$E_{vis} = E_e + m_e \tag{2.6}$$

$$E_\nu = E_{vis} - 0.5 + 1.293 = E_{vis} - 0.8 \tag{2.7}$$

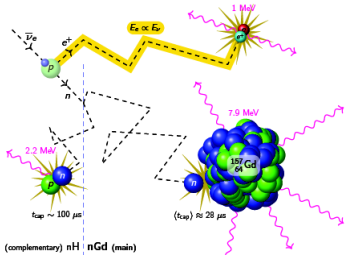

Figure 2.2: *Inverse Beta Decay reaction of the anti-electron neutrino. The detectable $\overline{\nu}_e$ spectrum (red line) is the $\overline{\nu}_e$ flux from reactor and the cross-section of IBD (blue line). The contributions of the four fission isotopes to the flux are shown for a typical pressurized water reactor. The detection process is indicated on the top [1].*

Examples of liquid scintillator experiments are: Borexino (solar neutrino experiment); KamLAND (reactor neutrino oscillation experiment); MiniBooNE (accelerator neutrino oscillation experiment); SNO+ (liquid-scintillator experiment using the SNO apparatus, under construction).

Cherenkov Detectors

Cherenkov radiation is produced whenever charged particles (e.g. electrons or muons) are moving through a given detector medium faster than the speed of light in that medium. In a Cherenkov detector, a large volume of clear material such as water or ice is surrounded by light-sensitive photomultiplier tubes. A charged lepton produced with sufficient energy and moving through such a detector does travel faster than the speed of light in the detector medium. The charged lepton generates a visible "optical shockwave" of Cherenkov radiation. This radiation is detected by the photomultiplier tubes and shows up as a

characteristic ring-like pattern of activity in the array of photomultiplier tubes. As neutrinos can interact with atomic nuclei to produce charged leptons that emit Cherenkov radiation, this pattern can be used to infer direction, energy, and (sometimes) flavor information about incident neutrinos. SNO and Kamiokande detectors are examples of Cherenkov detectors as we will discuss later.

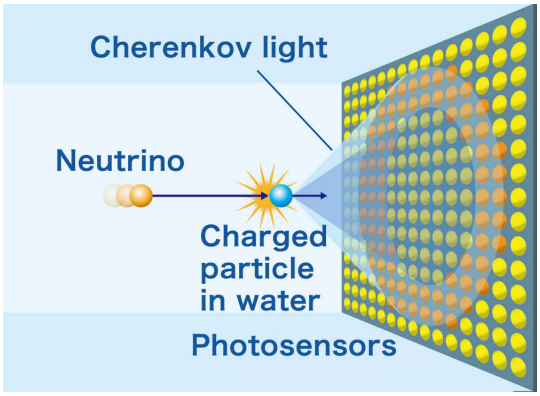

Figure 2.3: *Neutrino detection via Cherenkov radiation; the diagram is taken from [11].*

Neutrino reactions in the heavy water (H_2O_2) occur through charged current: as the neutrino approaches the deuterium nucleus a W boson is exchanged between the electron neutrino and a d quark in the neutron of the heavy water. This changes the neutron in the deuterium to a proton, and the neutrino to an electron. The electron will emit Cherenkov radiation and this cone of light will be detected by the photomultiplier tube array surrounded the detector. They can occur also through the Neutral Current reaction. The interaction breaks the deuterium nucleus and liberates the proton and the neutron. The neutron will then be thermalized in the heavy water as it scatters around. It will be eventually observed due to gamma rays which are emitted when it is captured on deuterium or on Chlorine.

Radiochemical Detectors

A neutrino converts a chlorine-37 atom into an argon-37 atom via the charged current interaction as described in Eq. 2.8. The threshold neutrino energy for this reaction is $0.814\ \mathrm{MeV}$. The fluid is periodically purged with helium gas that would remove the argon. The helium is then cooled to separate out the argon, and the argon atoms are counted based on their electron capture radioactive decays.

$$\nu_e + Cl^{37} \rightarrow Ar^{37} + e^- \tag{2.8}$$

$$\nu_e + Ga^{71} \rightarrow Ge^{71} + e^- \tag{2.9}$$

A similar detector design, with a much lower detection threshold of $0.233\ \mathrm{MeV}$, uses a gallium-germanium transformation as described in Eq. 2.9. A neutrino is able to react

with an atom of gallium-71, converting it into an atom of the unstable isotope germanium-71. The germanium was then chemically extracted and concentrated. Neutrinos were thus detected by measuring the radioactive decay of germanium. These radiochemical detection methods are useful only for counting neutrinos; no neutrino direction or energy information is available.

Examples of radiochemical experiments are: Homestake (chlorine) and SAGE (gallium). A chlorine detector in the former Homestake mine near Lead, South Dakota, containing 520 short tons (470 metric tons) of liquid, was the first to detect the solar neutrinos, and made the first measurement of the deficit of electron neutrinos from the sun. The SAGE experiment in Russia used about 50 tons, and the GALLEX/GNO experiments in Italy about 30 tons, of gallium as reaction mass. This experiment is difficult to scale up due to the prohibitive cost of gallium. Larger experiments have therefore turned to a cheaper reaction mass.

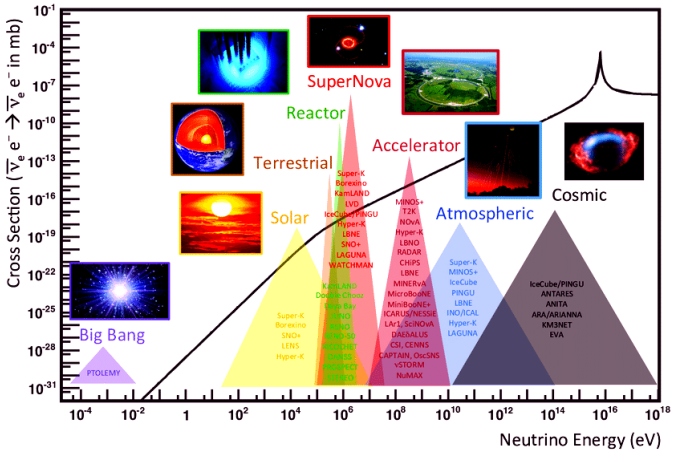

Figure 2.4: *Neutrino interaction cross section as a function of energy, showing typical energy regimes accessible by different neutrino sources and experiments. Figure is modified from [30].*

Since neutrinos interact only weakly with other particles, neutrino detectors must be very large to collect a significant number of neutrinos. Neutrino detectors are often built underground to isolate the detector from cosmic rays and other background radiation. The experiments are categorized as atmospheric, accelerator, solar or reactor neutrino experiments. Various different detector technologies have been used in neutrino experiments over the years, depending on the requirements of the particular study. Desirable features of a neutrino experiment will include several of the following [31]:

1. low energy threshold, so that low-energy neutrinos can be detected and studied (especially for solar neutrinos);
2. good angular resolution, so that the direction of the detected particle can be accurately reconstructed (especially for astrophysical neutrinos);
3. good particle identification, so that electrons and muons can be well separated (essential for oscillation experiments);
4. good energy measurement, so that the energy of the neutrino can be reconstructed (useful for oscillation measurements and astrophysics);

5. good time resolution, so that the time evolution of transient signals can be studied (essential for supernova neutrinos, and important for other astrophysical sources);

6. charge identification, so that leptons and anti-leptons can be separated (will be essential for neutrino factory experiments).

2.2 The Reactor Neutrino Experiments

Nuclear reactors have played a major role in the study of neutrino oscillations. They provide a pure, controllable and well-understood sources of neutrinos. In each nuclear reactor, $\overline{\nu}_e$ are mainly produced via beta decay ($\beta - decay$) of the fission products of the main four radioactive isotopes ^{235}U,^{238}U,^{239}Pu and ^{241}Pu in the nuclear fuel. The neutron decays by $\beta - decay$ into a proton (p) as following:

$$n \rightarrow p + e + \nu_e. \tag{2.10}$$

Beta decay is a consequence of the weak force, which is characterized by relatively long decay times. Nucleons are composed of up or down quarks, and the weak force allows a quark to change type by exchanging W boson that annihilate to create e^- and ν_e or e^+ and $\overline{\nu}_e$ pair. Decay times for many nuclides that are subject to beta decay can be thousands of years. As indicated in Eq. 2.11 and Eq. 2.12, $\overline{\nu}_e$ emission is caused by the conversion of a down quark to an up quark by emitting a W^- boson that subsequently decays into an electron and an electron anti-neutrino:

$$d \longrightarrow u + W^- \tag{2.11}$$

Then

$$W \longrightarrow e + \overline{\nu}_e \tag{2.12}$$

The reactor neutrino flux i.e. how many $\overline{\nu}_e$ are produced per fission depends on anti-neutrinos energy $E_\nu(MeV)$. Each fission produces other neutrons that sustain the chain reaction, a few nuclear fragments that decay producing about 6 $\overline{\nu}_e$, and of course kinetic energy. A typical reactor produces a thermal power of a few GigaWatt (GW = 6.24×10^{21} MeV/s) and neutrinos with a typical energy of about MeV. The flux (ϕ) of $\overline{\nu}_e$ produced per fission depends on their energy $E_{\overline{\nu}_e}(\mathrm{MeV})$.

$$\begin{aligned}\phi(E_{\overline{\nu}_e}) =& f_{^{235}U} \exp^{(0.870-0.160E_{\overline{\nu}_e}-0.0910E^2_{\overline{\nu}_e})} \\ &+ f_{^{238}U} \exp^{(0.976-0.162E_{\overline{\nu}_e}-0.0790E^2_{\overline{\nu}_e})} \\ &+ f_{^{239}Pu} \exp^{(0.896-0.239E_{\overline{\nu}_e}-0.0981E^2_{\overline{\nu}_e})} \\ &+ f_{^{241}Pu} \exp^{(0.793-0.080E_{\overline{\nu}_e}-0.1085E^2_{\overline{\nu}_e})},\end{aligned} \tag{2.13}$$

where f_k denotes the relative fission contribution of k isotope in the nuclear fuel and could be calculated using

$$f_k := \frac{N_k^{fiss}}{\sum_i N_i^{fiss}}. \tag{2.14}$$

Electron anti-neutrino $\overline{\nu}_e$ is detected in reactor neutrino experiments via inverse beta decay reaction (IBD). Unlike the focused accelerator neutrino beams produced, the reactor anti-neutrinos travel in all directions.

The Neutrino Mass Ordering Determination, the main goal of this thesis, can be evaluated in medium baseline reactor experiments with reactor energy anti-neutrinos spectrum. In such experiments a spectral distortion of the oscillation pattern driven by the atmospheric mass can be observed. For reactor anti-neutrinos there is no dependence on θ_{23} or the CP violating phase. Dependences on θ_{13}, θ_{12} and solar mass uncertainties are not large but they can be tricky. Contrary to the accelerator-based experiments a side benefit of the neutrino-reactor experiments is the independence of the oscillation probabilities from the CP violating phase as well as from strong matter effects in the contemplated energy region. However, as it will be shown later, the current uncertainty on the value of atmospheric mass introduces important degeneracies in the neutrino oscillations at reactor experiments. Depending on the mass hierarchy (MH), the position of maxima and minima of the sub-dominant oscillation wiggles undergo a shift of π as indicated in Fig. 1.5 and Fig. 1.6. Resolving the position of the wiggles in the energy spectrum requires an high energy resolution, and an excellent understanding of the linearity of the energy response [1]. That means that detector sensitivity to the neutrino mass hierarchy arises from this small phase shift in the oscillation terms depending on the two large mass-squared differences, Δm^2_{32} and Δm^2_{31}. What we should notice is that the precise determination of MH relies on the precise determination of Δm^2_{32} and on incorrect Δm^2_{32} may bias MHD. The contribution to the oscillation probabilities sensitive to MH is due to the fast oscillating terms superimposed to the general oscillation pattern. The relative size of this contribution changes according to the two different possibilities leading to a contribution of opposite sign in the two cases of normal hierarchy (NH) and inverted hierarchy (IH). It is possible to discriminate between the two mass hierarchies, by studying the interference between the two oscillation frequencies driven by Δm^2_{32} and Δm^2_{31} [1].

Currently, four reactor experiments are in operation; KamLAND, Double Chooz, Daya Bay and RENO experiments. They are new generation reactor experiments that measure the reactor $\overline{\nu}_e$ spectrum at baselines of $1 \sim 2\,\mathrm{Km}$. We review the status and the results of reactor neutrino experiments.

Kamioka Liquid scintillator Anti-Neutrino Detector (KamLAND)

The KamLAND has been constructed in order to check the Large Mixing Angle (LMA) solution of the solar neutrino problem. It has discovered a large deficit of the reactor neutrino flux in the year 2002. The primary goal of the KamLAND experiment is a search for the oscillation of ν_e emitted from distant power reactors [33, 32].

The KamLAND is a long-baseline reactor experiment with on average $180\,\mathrm{km}$ baseline. It is placed in the underground neutrino detection facility near Toyama, Japan. The experiment is located at the site of the earlier Kamiokande, with an average rock overburden of 2,700 m.w.e.[1] resulting in $0.34\,\mathrm{Hz}$ of cosmic-ray muons in the detector volume [33, 34]. As shown in Fig. 2.5, KamLAND detector is a massive liquid scintillator studying low energy neutrino oscillation [35]. KamLAND LS consists of 80% of the volume with normal-

[1] Mwe or m.w.e. refers to: Meter Water Equivalent.

Dodecane, 20% with Pseudocumene, and $1.52\,\mathrm{g/liter}$ of PPO ($2,5$-Diphenyloxazole)[2][35].

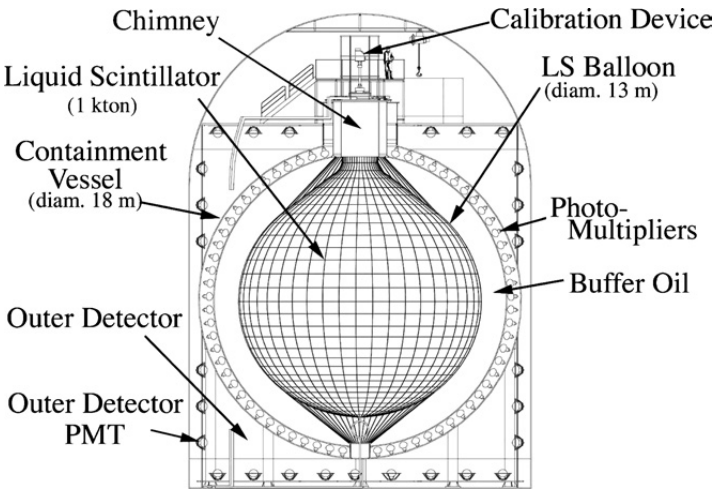

Figure 2.5: *The KamLAND detector [35].*

Fig. 2.6 reports the allowed region in the ($\sin^2\theta_{12}$, Δm^2_{21}) plane from the analysis of all solar neutrino data (black lines), from the analysis of the KamLAND reactor experiment (blue lines) and from the combined analysis of solar + KamLAND data (colored regions). Here the value of the θ_{13} has been marginalized following the most recent short-baseline reactor experiments [36]. From the figure, one can see that the determination of θ_{12} is mostly due to solar neutrino experiments, while the very accurate measurement of Δm^2_{21} is obtained thanks to the spectral information from KamLAND. There is also a mild but noticeable tension between the preferred values of Δm^2_{21} by KamLAND and by solar experiments. While the first one shows a preference for $\Delta m^2_{21} = 4.96 \times 10^{-5}\mathrm{eV}^2$, the combination of all solar experiments prefer a lower value: $\Delta m^2_{21} = 7.6 \times 10^{-5}\mathrm{eV}^2$. This discrepancy appears at the $2\,\sigma$ level.

[2]It is a flour which has been widely used in large scale liquid scintillators for high energy physics and neutrino experiments [35].

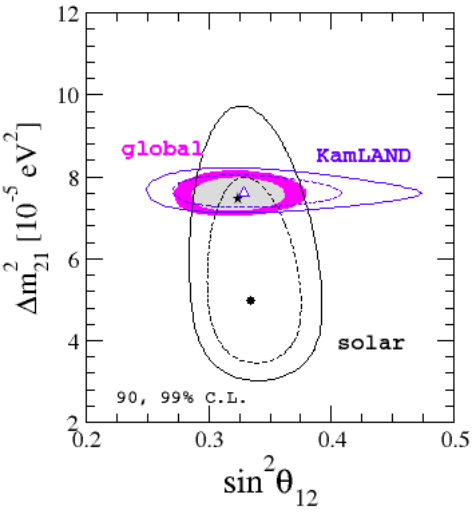

Figure 2.6: *The neutrino global fit result. Allowed regions at* 90 *and* 99% *C.L. from the analysis of solar data (black lines), KamLAND (blue lines) and the global fit (colored regions).* θ_{13} *has been marginalized according to the latest reactor measurements [39]. Triangle and circle respectively denote KamLAND and solar best fit. The global best fit is denoted by a star.*

Daya Bay

The Daya Bay is a Chinese Reactor Neutrino Experiment located roughly 50 km northeast of Hong Kong, in China. Daya Bay makes use of anti-neutrinos produced by the Daya Bay nuclear power plant to measure the neutrino mixing angle θ_{13}. The Daya Bay is designed to determine precisely θ_{13} with a sensitivity better than 0.01 for the parameter $sin^2 2\theta_{13}$, at the 90% confidence level [37].

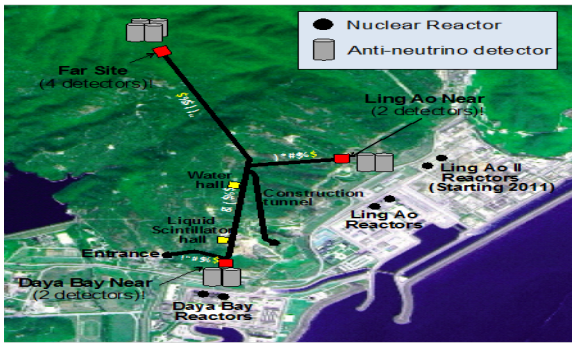

Figure 2.7: *Satellite photograph of the Daya Bay nuclear power plant complex showing the location of the reactors, a possible tunnel layout and possible locations for the near and far detectors [38].*

The experiment consists of eight anti-neutrino detectors, clustered in three locations within $1.9\,\mathrm{km}$ of six nuclear reactors. Each detector consists of $20\,\mathrm{tons}$ of liquid scintillator (linear alkylbenzene doped with gadolinium) surrounded by photomultiplier tubes and shielding [39]. The detectors are immersed in very large pools of water in order to shield them from ambient radioactivity and to be able to detect incoming cosmic-rays. Electron antineutrinos produced at six reactor cores with $2.9\,\mathrm{GW}$ thermal power are observed

at eight antineutrino $20\,\mathrm{ton}$ Gadolinium-doped liquid scintillator detectors, located at distances between 350 and $2000\,\mathrm{m}$ from the cores. The latest data release from Daya Bay has reported the detection of more than $2.5\,\mathrm{millions}$ of reactor antineutrino events, after $1.230\,\mathrm{days}$ of data taking [40]. A detailed description of the Daya Bay experiment can be found in [37, 39].

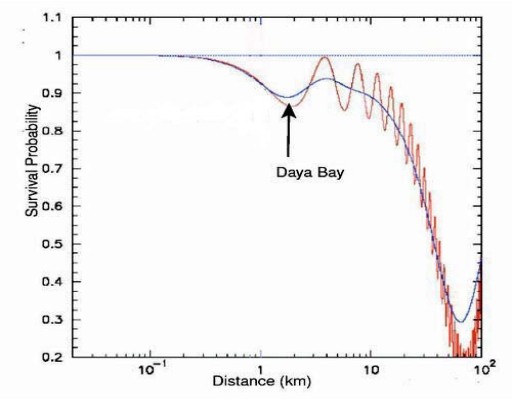

Figure 2.8: *Survival probability of reactor electron anti-neutrinos measured as a function of distance from their creation. The rapidly oscillating (red) curve is for* $4\,\mathrm{MeV}$ *anti-neutrinos, and the smoother (blue) curve accounts for the reactor anti-neutrino energy spectrum. The amplitude of the small oscillations comes from the CHOOZ limit and it is due to the atmospheric neutrino mass. The large oscillation amplitude comes from KamLAND's measurement and it is due to the solar neutrino mass. The arrows refer to the locations of the far detector in the Daya Bay site. The value of* Δm^2_{31} *is taken as* $2.5 \times 10^{-3}\ \mathrm{eV}^2$ *[38].*

The goal of the Daya Bay experiment is a measurement of $\sin^2 2\theta_{13}$ to 0.01 or better. Fig. 2.8 shows the survival probability for electron anti-neutrinos emitted from a nuclear reactor as a function of distance from the power plant.

Double Chooz

Chooz was a short-baseline reactor experiment in Chooz town, France. The main goal of the experiment is the measurement of θ_{13} mixing angle and in 2011 for the first time the experiment observed an indication for a non zero value of such an oscillation parameter [41]. The mixing angle was successively measured using only the far detector finding the best fit value of $sin^2(2\theta_{13}) = 0.090 - 0.029 + 0.032$ [41]. The Chooz experiment used neutrinos from two pressurized water reactors.

Double Chooz is a long-baseline reactor experiment with source-detector distances of the order of $1\,\mathrm{km}$ [42]. The Double Chooz experiment continues to take data using the same lab space as Chooz experiment [41].

Reactor Experiment for Neutrino Oscillation (RENO)

RENO is a short baseline reactor neutrino oscillation experiment in South Korea. The proposal of RENO was approved by the Ministry of Science and Technology in Korea in May 2005 [43] [44]. The experiment was designed to measure the neutrino mixing

angle θ_{13}, one of the main neutrino oscillation parameters responsible for ν_e oscillations into other neutrino flavors (ν_μ or ν_τ) [44]. RENO has two identical detectors, placed at distances of $294\,\mathrm{m}$ and $1383\,\mathrm{m}$ [44], that observe electron anti-neutrinos produced by six reactors at the Hanbit Nuclear Power Plant (the old name: the Yeonggwang Nuclear Power Plant) in Korea [43]. Each detector consists of $16.5\,\mathrm{tons}$ of gadolinium-doped liquid scintillator (LAB), surrounded by an additional $450\,\mathrm{tons}$ of buffer, veto, and shielding liquids. The detection methods and setup of the RENO experiment are discussed in detail elsewhere [43].

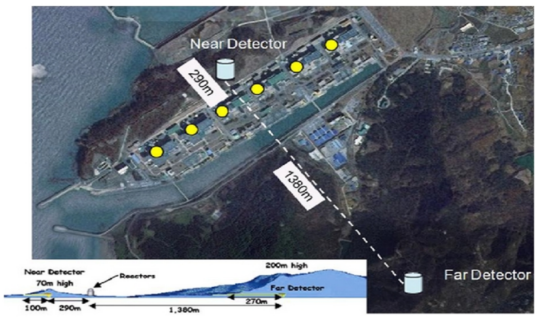

Figure 2.9: *A schematic setup of the RENO experiment.*

In 2012, RENO collaboration announced a $4.9\,\sigma$ observation of $\theta_{13} \neq 0$ [44], with

$$\sin^2 2\theta_{13} = 0.113 \pm 0.013(\mathrm{stat.}) \pm 0.019(\mathrm{syst.}) \tag{2.15}$$

In 2013, the RENO confirmed $\theta_{13} \neq 0$ with a significance of $6.3\,\sigma$ [45]:

$$\sin^2 2\theta_{13} = 0.100 \pm 0.010(\mathrm{stat.}) \pm 0.015(\mathrm{syst.}) \tag{2.16}$$

As indicated in Fig. 2.10, 90 and 99% C.L. (2 d.o.f.) allowed regions in the ($sin^2\theta_{13}$, Δm^2_{31}) plane from individual reactor neutrino experiments (dashed and solid lines) and from the combination of the three experiments (colored regions) [46].

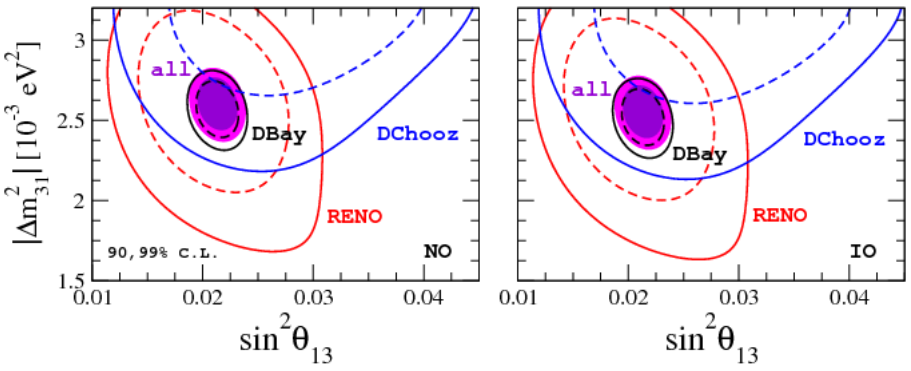

Figure 2.10: *The neutrino global fit result [47] of reactor neutrino experiments' simulations, Daya Bay [48], RENO [49] and Double Chooz [50]. The left (right) panels correspond to normal (inverted) mass ordering.*

After RENO, an underground detector of RENO-50 was planed to be constructed. RENO-50 would consist of $5000\,\mathrm{tons}$ of ultra low-radioactivity liquid scintillator and 3000

10-inch PMTs, located at roughly $50\,\mathrm{km}$ away from the Yonggwang nuclear power plant in Korea where the neutrino oscillation due to θ_{12} takes place at maximum. The detector was expected to detect neutrinos from nuclear reactors, the Sun, Supernova, the Earth, any possible stellar object and a J-PARC neutrino beam. It could be served as a multi-purpose and long term operational detector including a neutrino telescope. The main goal was to measure the most accurate (1%) value of θ_{12} and to attempt determination of the neutrino mass hierarchy. Unfortunately, the project is no more under consideration. Thus, only the similar project of JUNO will be accomplished (as will described in the next chapter).

CHAPTER 3

THE JUNO EXPERIMENT

3.1 Introduction

The Institute of High Energy Physics proposed the second phase of the reactor neutrino experiment (JUNO) in 2008. In February 2013 JUNO was approved by the Chinese Academy of Sciences and supported through the Strategic Priority Research Programe [51]. The sensitivity analysis showed that the preferred range for the experimental stations must be $50 - 55\,\mathrm{km}$ from a nuclear reactor [1]. Jiangmen City was chosen for the JUNO detector site that is $\sim 53\,\mathrm{km}$ from both Yangjiang and Taishan Nuclear Power Plants (NPPs).

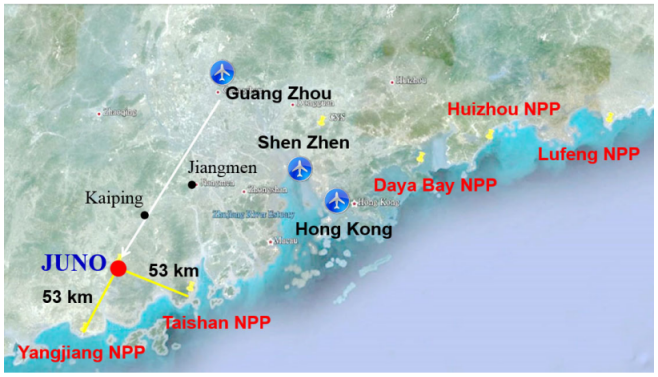

Figure 3.1: *Location of the JUNO site. The distances to the nearby Yangjiang NPP and Taishan NPP are both around* $53\,\mathrm{km}$. *Daya Bay NPP is* $215\,\mathrm{km}$ *away. Huizhou and Lufeng NPPs have not been approved yet [52].*

The JUNO detector will trap $\overline{\nu}_e$ generated from two NPPs located in Yangjiang and Taishan cities. The NNPs include six $2.9\,\mathrm{GW}$ reactors (second generation pressurized water reactor PWR) at Yangjiang NPP and four $4.6\,\mathrm{GW}$ reactors (third generation PWR) at Taishan NPP, giving a total thermal power of $35.8\,\mathrm{GW}$ [1]. A summary of the thermal power and baseline of each reactor to be used for JUNO is listed in Tab. 3.1.

Cores	YJ-C1	YJ-C2	YJ-C3	YJ-C4	YJ-C5	YJ-C6
Power (GW)	2.9	2.9	2.9	2.9	2.9	2.9
BaseLine (km)	52.75	52.84	52.42	52.51	52.12	52.21
Cores	TS-C1	TS-C2	TS-C3	TS-C4	DYB	HZ
Power (GW)	4.6	4.6	4.6	4.6	17.4	17.4
BaseLine (km)	52.76	52.63	52.32	52.20	215	265

Table 3.1: *The thermal power and baseline for JUNO detector of Yangjiang (YJ) and Taishan (TS) rector cores, in addition to the remote reactors Daya-Bay (DYB) and Huizhou (HZ) [1].*

The JUNO is designed to be a multipurpose experiment as reported in [1]. It can probe the neutrino oscillations to determine neutrino MH via measurement of reactor neutrino energy spectrum and to do precision measurements of neutrino oscillation mixing parameters. Moreover, the JUNO detector will provide an excellent opportunity for studying astro-neutrino physics being able to detect $\nu's$ from the astrophysical sources: supernova burst neutrinos, diffuse supernova neutrinos, Solar neutrinos and atmospheric neutrinos. In addition, JUNO will address the questions about other important current research topics like sterile neutrino and exotic searches. The data taking will possibly start in 2020.

3.2 The JUNO Detector

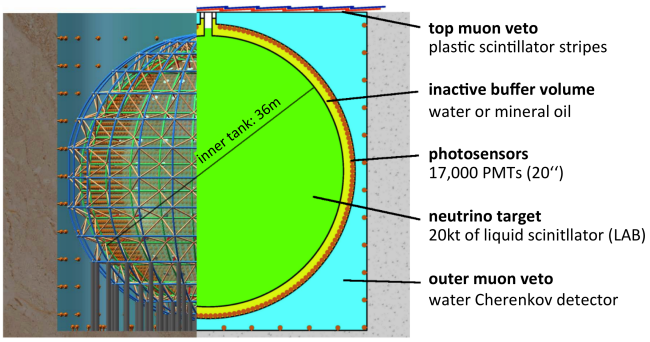

Figure 3.2: *Layout of the JUNO detector [1].*

The JUNO detector consists of:

1. The central detector (CD): it is a liquid scintillator detector of 20 kton target mass of Linear Alkyl-Benzene (LAB). The central detector is submerged in a water pool to be shielded from natural radioactivities from the surrounding rock and air. The central detector, which is the experiment's core component, will be the world's largest and highest precision liquid scintillator detector [1].

2. The veto system:

   (a) a water Cherenkov pool detector (WC). A pool filled with purified water and instrumented with PMTs. When energetic muons pass through the water, they can produce Cherenkov light. The Cherenkov photons can be detected by

PMTs. The arrangements of the PMTs as well as the number of PMTs needed in the water pool is currently under study to facilitate the highest efficiency detection of muons as well as good muon track reconstruction. One of the options is to have the water pool surface and central detector outer surface covered with reflective Tyvek to increase the light detection by PMTs without using a large number of PMTs.

Mineral oil ($6\,\mathrm{tons}$) is a natural scintillator. Thus, charged particles without sufficient energy to produce Cherenkov light still produce scintillation light. Low energy muons and protons, invisible in water, can be detected.

(b) A muon tracker: on the top of the water pool some decommissioned detectors are used as muon trackers from the OPERA experiment. They can provide independent muon information to help muon tagging for and track reconstruction.

(c) Water circulation system. There will be $20.000-30.000\ \mathrm{tons}$ of water in the pool depending on the different central detector designs. This system will include a water production system on the ground and a purification/circulation system underground in the experimental hall.

(d) Geomagnetic field shielding system. Though small, the Earth's magnetic field can affect the performance of PMTs. Either compensation coils or magnetic shields will be used to reduce the effect on PMTs.

(e) Mechanical system. The system includes top tracker support structure, water pool PMT support structure as well as a light and air tight cover for the water pool.

Furthermore, the PMT photo-cathode quantum efficiency will be greater than 35% and the attenuation length of the liquid scintillator at $430\,\mathrm{nm}$ will be greater than $20\,\mathrm{m}$ [1]. The reactor electron anti-neutrino survival probability as a function of L/E is described in Fig. 3.3. The mass hierarchy can be determined by the position of maxima and minima of the sub-dominant oscillation wiggles.

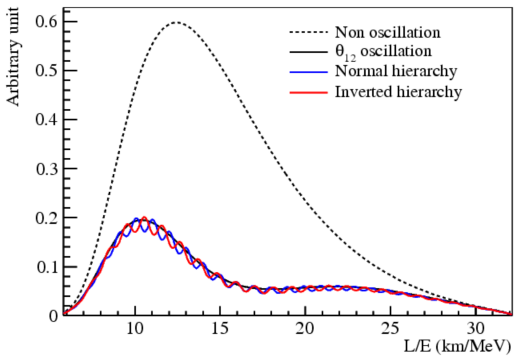

Figure 3.3: *Reactor electron anti-neutrino survival probability as a function of L/E. The mass hierarchy can be determined by the position of maxima and minima of the sub-dominant oscillation wiggles [1].*

3.3 Neutrino detection

JUNO uses protons as targets to detect electron anti-neutrino signals via Inverse Beta Decay (IBD) process. The threshold neutrino energy, the minimum neutrino energy to be detected, of this process is $E_{th} = 1.8\,\mathrm{MeV}$, and the cross section is $\sim O(10^{-44})\ \mathrm{cm}^2$. The neutrinos are detected via the inverse beta decay by measuring the correlated positron and neutron signals. With a careful design of the detector, the neutrino spectrum can be measured precisely, and we are looking for the distortion of the spectrum for the determination of the neutrino mass ordering. Compared to the small number of signal events $(60/\mathrm{day})$, the number of background events is in principle very high due to the large volume of detector.

The JUNO electronics system consists of two readout systems; the first for the central detector and the second for veto detector. The electronics system main task is to read out signals from the PMTs of the two sub-detectors, to process the data and then to transfer the data to the Data Acquisition (DAQ) system. The readout electronics consists of amplification, analog to digital conversion, data processing, collection and transmission, triggering, high voltage control etc. All channels in the system will be recorded by high-speed sampling, and then the data containing possible physics events will be selected by the trigger. Since the whole detector will be in water, to avoid signal loss due to long distance transmission, most parts of electronics system will also be put in the water, close to the detector body. Then the electronics system needs to be a reliable underwater high-speed sampling system. The data acquisition system will record all the events passing trigger criteria including signal and background events. The DAQ must record data from the electronics systems of central detector and veto detector with precise timing and charge information. The DAQ builds a full event with data fragments from different sub-detectors, analyzes and processes the data, and saves all the relevant data to disk. The design baseline requires reading out event data at the rate of $2\ \mathrm{GB/s}$, which will be increased to $10\ \mathrm{GB/s}$ when a $10\,\mathrm{kpc}$ distance supernova explosion happens. A distributed architecture is needed to fulfill these requirements and a modular and extendible data flow schema is also required. The experimental data collected by the JUNO detector are transferred to the data center through a dedicated network for further data processing and analysis. A rough estimation suggests a level of 10,000 CPU cores and $10\ \mathrm{PB}$ disk storage connected by a $40\,\mathrm{Gbps}$ backbone high-speed network. For possible peak demands, the platform is required to be able to integrate the computing resources from all JUNO members via a distributed computing environment. The offline system will calibrate raw data from the detector, produce reconstructed data, generate Monte Carlo data, and provide software tools for physics analysis. The offline software includes framework and experiment related software. The framework is the underlying software supporting the whole system. Based on the framework the experiment related software will be developed, such as software for event data model, data I/O, event generation, detector simulation, event reconstruction, physics analysis, geometry service, event display, and database service.

In SNiPER, we use a buffer[1] to manage the event data in the memory. Then, one will be able to analyze the correlations between different events. The buffer in the memory corresponds to the path of the event data in the root file. The buffer at least contains a current event, and may also contains some other time-relative events to the current event.

[1] **Buffer means a sequence of events in a time window.**.

There are two kinds of buffers, the read-only buffer and the read-write one. General user just need to use the read-only one.

The detector control system (DCS) aims at establishing long-term monitoring of the parameters that might affect the performance of the experiment equipment. The parameters include temperature, humidity, liquid level of the LS, gas pressure and the pressure in the experimental hall. Some subsystems need to provide device control such as calibration system, gas system, water cycle system and power system. The real time operation status of the devices will be monitored and recorded into the database. After the completion of civil construction, all subsystems will be installed to form the complete JUNO detector. The guidelines for integration, assembly, installation and commissioning need to be established and proper regulations will be introduced to control the onsite progress. The standardized review process will be implemented to ensure the experimental equipment meets the requirements for both performance and safety.

3.4 The Systematics and the Backgrounds

The JUNO systematic uncertainties and backgrounds originate from four main sources: the reactor related uncertainties, the detector related uncertainties, the background related uncertainties and the energy related uncertainties.

3.4.1 The reactor related uncertainties

As reported in [1], the absolute normalization uncertainty from the reactor flux at the current level has negligible impact on the MH determination. Because of the bump between $4-6\,\mathrm{MeV}$, the model predictions for the reactor antineutrino spectrum are inconsistent with the measurement from ongoing reactor experiments. A recent theoretical calculation trying to understand the above inconsistency observes additional high-frequency fine structures in the reactor antineutrino spectrum. Both of the mentioned spectral structures may induce additional systematics of the shape uncertainty. The MC studies of the MH sensitivity on the effects of these spectral structures indicate some changes of the test statistics (see later chapters). To conclude this point, it is mandatory to control the reactor spectral structures to reduce systematics of the shape uncertainty.

3.4.2 The detector related uncertainties

There are two sources for detector response: first the statistical fluctuations (in this particular case, the so-called photo-statistics in the liquid scintillor), second the systematic uncertainty associated to the correction of the linearity in energy of the detector response (for example from non-uniformity in the liquid scintillor, photomultiplier manufacturing and the electronics) [1]. The calibration of the detector energy non-linearity response is a critical factor to obtain reliable sensitivity of the MHD. The uncertainty from the detector non-linearity response can distort the $\overline{\nu}$ spectrum and is crucial for JUNO, since a precise energy spectrum of reactor $\overline{\nu}$ is required to resolve the MH. Assuming the energy non-linearity correction is imperfect, we study the impact on the sensitivity by including

in our simulation a residual non-linearity between the measured and expected neutrino spectra. In principle, one may find the worst case of non-linearity such that the wrong MH may perfectly mimic the true one. Thanks to the current measurements of the neutrino oscillation parameters, we can illustrate the specific non-linearity curves for the normal MH and inverted MH in Fig. 3.4.

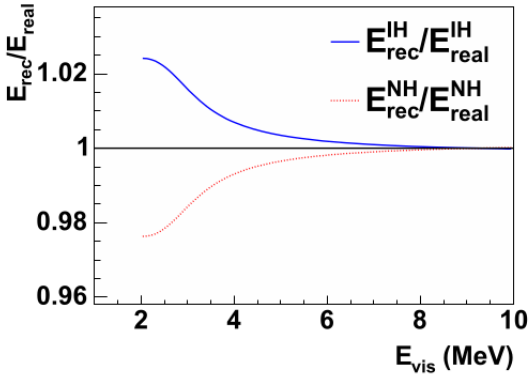

Figure 3.4: *The non-linearity models with the largest effects could mimic the normal and inverted hierarchys [1]. A possible non-linearity model is assumed to check its effect in MHD. In the plot the effect is parameterized for the Y-axis reconstructed energy over real energy.*

To conclude this point, the uncertainty in the detection absolute efficiency has negligible impact on the MHD. Therefore it is highly desirable to study the energy related uncertainties and it's impact on the MHD.

3.4.3 The background related uncertainties

There are two types of backgrounds, the major backgrounds and the accidental backgrounds. The major backgrounds are $^{8}He/^{9}Li$, Fast Neutron (FN), Geo-neutrinos and $^{13}C(\alpha, n)^{16}O$ as indicated below.

1. The cosmic ray generated backgrounds are:

   (a) $^{8}He/^{9}Li$ background from muon spallation and muon shower particles.

   (b) Fast neutron (FN) background in the detector from muon induced high energy neutrons.

   The cosmic ray muon induced backgrounds are the main backgrounds and they are hard to remove. The cosmic ray induced backgrounds also affect the study of the diffuse supernova neutrino flux. In order to reduce the experimental backgrounds, the neutrino detector must be placed in deep underground and a veto system is used to tag muons. The muons should be detected with high efficiency for the purpose of background reduction. Due to the strict requirements on background suppression, larger overburden of rocks on top of the detector is needed to reduce the cosmic ray muon flux. Therefore, there is about $700\,\mathrm{m}$ rock on top of the experimental hall. Muon rate is estimated at about $0.003\ \mathrm{Hz/m^2}$ and the average muon energy is about $214\,\mathrm{GeV}$ from simulation. The cosmic ray muon flux

is reduced by 60000 times compared to that at the ground surface. The remaining energetic cosmic ray muons can still produce a large number of neutrons in the rocks and other detector materials surrounding the central detector. These neutrons can produce fast neutron background in the central detector which mimics the inverse beta decay signal. This kind of background cannot be ignored. In order to shield the neutrons and the natural radioactivities from the surrounding rocks, at least $2\,\mathrm{meters}$ of water surrounding the central detector is needed. The water is effective for shielding against neutrons and gamma. And when being instrumented with photomultiplier tubes (PMTs), the water pool can serve as a water Cherenkov detector to tag muons. From simulation, muons with relatively long track in the detector can be detected with very high efficiency, while the undetected muons are mainly with a short track length that would induce less background since they are relatively away from central detector. Based on the Daya Bay experimental results (when the fast neutron background was about 0.2%), if the water shield thickness is at least $2.5\,\mathrm{meters}$ in JUNO, fast neutron background to signal ratio will be 0.3%, after taking into consideration the large detector volume and geometry effects.

2. $^{13}C(\alpha,n)^{16}O$: the α particles from Uranium (U) and Thorium (Th) radioactivities can react with the ^{13}C in LS. The $^{13}C(\alpha,n)^{16}O$ reaction could lead to a correlated background if the neutron is fast enough or there is a gamma from the de-excitation of the ^{16}O excited states.

3. Geo$-\nu$: constitute an intrinsic background, at the level of 1.1 events per day after the selection cuts. However their rate will be measured with very good precision by JUNO itself, reducing the current 30% rate uncertainty to a few percent. Anyhow, geo- $\nu's$ are detected up to about $3\,\mathrm{MeV}$ and they correspond to a negligible background for the present analysis, as shown later.

The accidental background mainly consists of three types of random coincidence: (radioactivity, radioactivity), (radioactivity, cosmogenic isotope) and (radioactivity, spallation neutrons). The rate of accidental backgrounds (R_{acc}) can be calculated as a multiplication of the rate of prompt signal R_p and the rate of delayed signal (R_d), the time coincidence window (DT),

$$R_{acc} = R_p \cdot R_d \cdot DT \tag{3.1}$$

The background can be reduced with a set of selection cuts that, in JUNO, decreases the efficiency to about 70%. The final yield corresponds to 60 signal events per day against a background of about 4 events, including geo-neutrinos. The efficiencies of anti-neutrino selection cuts, signal and backgrounds rates are listed in Tab. 3.2.

Table 3.2: *The efficiencies of anti-neutrino selection cuts, signal and backgrounds rates [1]*

Selection	IBD efficiency	IBD	Geo-νs	Accidental	^{9}Li/^{8}He	Fast n	(α, n)
—	—	83	1.5	$\sim 5.7 \times 10^4$	84	—	—
Fiducial volume	91.8%	76	1.4		77	0.1	0.05
Energy cut	97.8%			410			
Time cut	99.1%	73	1.3		71		
Vertex cut	98.7%			1.1			
Muon veto	83%	60	1.1	0.9	1.6		
Combined	73%	60			3.8		

To conclude this point, the rate uncertainties of backgrounds are negligible for the MHD since they are nicely constrained in the precision spectral measurements. The background summary table for the analysis of reactor anti-neutrinos is Tab. 3.3 and the expected energy spectra for the five kinds of main backgrounds is Fig. 3.5.

Table 3.3: *The background summary table for the analysis of reactor anti-neutrinos [1].*

Event type	Rate (per day)	Rate uncertainty (relative)	Shape uncertainty
IBD candidates	60	—	—
Geo-νs	1.1	30%	5%
Accidental signals	0.9	1%	negligible
Fast-n	0.1	100%	20%
^{9}Li–^{8}He	1.6	20%	10%
^{13}C (α, n)^{16}O	0.05	50%	50%

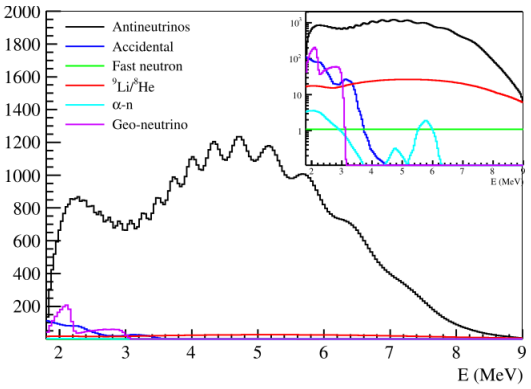

Figure 3.5: *Spectra for the anti-neutrino signal and five kinds of main backgrounds, including the accidental, $^{8}He/^{9}Li$, fast neutron, $^{13}C(\alpha, n)^{16}O$ and geo-neutrinos [1].*

3.5 The JUNO Simulation

JUNO simulation mainly consists of physics generators and detector simulation. Actually the full chain are physics generator, detector simulation, electronics simulation, waveform reconstruction and vertex/energy/track reconstruction. When running a detector simulation job, one or more primary particles will be generated in for each event. Then, these particles and their secondaries in the detector will transported. The event samples are all composed of $\sim 10^5$ events, which is a realistic assumption considering that the

expected event rate calculated with the JUNO experimental setup is about $60\,\mathrm{events/day}$, for a total running time of $6\,\mathrm{years}$. Throughout the thesis we will use a benchmark referring to $6\,\mathrm{years}$ to get 108357 events at a distance of $52.5\,\mathrm{km}$ with a total power $36\,\mathrm{GW}$ and relative energy resolution $\frac{3\%}{\sqrt{E}}$.

To perform analysis, one has to take into account the finite detector resolution. An alternative generation method has been chosen. On the generated single event one can add any of the expected systematic errors via a Gaussian[2] distribution centered at the expected mean and with the standard deviation of the estimated uncertainty. In our simulations, we used a $10\,\mathrm{keV}$ bin energy width. The oscillation parameters have been taken from the recent global fits. Note that we did not use the Asimov data set[3].

[2]The simple hypothesis of Gaussian approximation is used for the analysis.
[3]The one data set in which all observed quantities are set equal to their expected values.

CHAPTER 4

THE STATISTICAL ANALYSIS

This chapter is crucial to get better understanding for the reported sensitivity results in the dissertation. We present a brief summary of the MH statistics and relation to the sensitivity. Generally speaking, we want to compare between models and data. Thus, we are typically doing one of the two things: parameter estimation or hypothesis testing. The basic and the most important methods of parameter estimation are the maximal likelihood method, the least squares (LS) method and the generalized moments method. These methods are very well known and widely used in experimental physics.

4.1 The Frequentist Statistics

For the neutrino MH, the hypothesis testing is composite i.e. the two hypotheses depend on parameters that are the neutrino oscillation parameters. We can reject the null hypothesis at a certain confidence level, $CL(1-\alpha)$, only if we reject all parameters corresponding to the null hypothesis at the same confidence level, $CL(1-\alpha)$. Given a null hypothesis H_0 and the alternative hypothesis H_1, we can choose a test statistics T in order to test whether data can reject the null hypothesis. The $CL(1-\alpha)$ to reject H_0 is related to the type-I error rate α, where,

$$\int_{T_c^\alpha(\theta)}^{\infty} p(T|\theta\epsilon H_0)dT = \alpha, \tag{4.1}$$

$p(T|\theta\epsilon H_0)$ being the probability distribution of test statistics T define θ for the null hypothesis. The $[T_c^\alpha(\theta) \div \infty]$ is chosen such to minimize the probability. The probability α is usually converted into the number of the Gaussian standard deviations n σ. For two-sided Gaussian (each side from the mean) that correspondents to: $1\,\sigma$, $2\,\sigma$, $3\,\sigma$ with a $CL(1-\alpha)$ of 68.27%, 95.45%, 99.73%, respectively.

$$n_{2-side} = \sqrt{2} \quad \mathrm{erfc}^{-1}(\alpha) \tag{4.2}$$

Instead, for a one-sided Gaussian one gets $1\,\sigma$, $2\,\sigma$, $3\,\sigma$ with a $CL(1-\alpha)$ of 84.14%, 97.73%, 99.87%, respectively.

$$n_{1-side} = \sqrt{2} \quad \mathrm{erfc}^{-1}(2\alpha) \tag{4.3}$$

We keep in our minds that the frequentist approach does not provide an answer to the question how much the MH hypothesis is favored than the other hypothesis given the experimental data. Actually, one may choose NH to be the null hypothesis and IH to be the alternative one. The result of the testing will tell you if you are able to reject the null hypothesis or not. Similarly, you repeat the hypothesis testing assuming the IH is the null hypothesis and NH is the alternative one. The result of the second test will tell us whether the IH would be rejected or not.

4.2 The Parameter Estimation

Assume that we want to estimate the unknown value of a parameter a. An estimator $\hat{a}$ is a function of the data that aims to estimate the value of the parameter a as closely as possible to its true value. From the fundamental properties of estimators, we can characterize $\hat{a}$ as a good or a bad estimator.

The general estimator properties:

1. Consistency: the value of the estimator $\hat{a}$ and the true value a are close i.e. when the data is very large the estimator $\hat{a}$ goes to his true value.

$$\lim_{n \longrightarrow \infty} \hat{a} = a \tag{4.4}$$

2. Unbias: the expectation value $\langle \hat{a} \rangle$ corresponds to true value.

$$\langle \hat{a} \rangle = a \tag{4.5}$$

3. Efficiency: the estimated value of the estimator depends on the given data sample and the fluctuations of the sample influence the estimator value. An efficient estimator exhibits a small fluctuation, or spread, which is measured in terms of the variance of the estimator distribution. Formally, an estimator is more efficient when its distribution variance is small. There is a lower bound on the variance of an unbiased estimator that is given by the Cramer Rao-Frechet (CRF) inequality[1]. According to Cramer-Rao theorem, the efficiency of an estimator $\hat{a}$ is the inverse of the ratio of its variance to the minimum possible value,

$$\left(\frac{\sigma^2_{[\hat{a}]}}{\sigma^2_{CRF}} \right)^{-1} . \tag{4.6}$$

   The variance of the estimator $\hat{a}$ distribution (the second central moment of the estimator $\hat{a}$ distribution) is defined as the inverse of the Fisher information matrix $I(a)$.

$$\sigma^2_{[\hat{a}]} = [I(a)]^{-1} \tag{4.7}$$

[1] Sometimes is called Cramer-Rao inequality, Frechet-Darmois-Cramer-Rao inequality, or information inequality. It provides the minimum possible values of the variance of unbiased estimators.

The Fisher information matrix is a way of measuring the amount of information that an observable random variable carries about an unknown parameter of a distribution that models the variable. Formally, it is the expected value of the observed information. The Fisher information matrix is used to calculate the covariance matrices associated with maximum-likelihood estimates. The information matrix can be used in the formulation of test statistics, such as the Wald test. Different estimators of the same parameter can also be compared by looking at the ratios of the efficiencies. One then talks about relative efficiencies.

4. Robustness: is the (qualitative) degree of insensitivity of the estimator to deviations in the assumed pdf of the data.

4.2.1 The Likelihood Method

Assuming a parameter θ and the measurements x_i with Probability Density Function (PDF) $f(x_i, \theta)$, the likelihood function $\mathcal{L}(\theta \mid x_i)$ of θ and x_i is defined as the following

$$\mathcal{L}(\theta \mid x_i) = \prod_i f(x_i, \theta) \tag{4.8}$$

The LogLikelihood function $\ell(\theta \mid x_i)$ of parameter θ and measurements x_i is then defined

$$\ell(\theta \mid x_i) = \log \mathcal{L}(\theta \mid x_i) = \sum_i \log f(x_i, \theta) \tag{4.9}$$

The maximum likelihood estimation (MLE) is a method of estimating the parameters of a statistical model, given the observations x_i, by maximizing the likelihood function. The resulting estimate is called a maximum likelihood estimate. The Fisher's method of maximum likelihood yields estimators that are the most efficient and are more often unbiased.

The Likelihood Ratio Test (LR test) is a statistical test used for comparing the goodness of fit of two statistical models; a null or simple model H_0 against an alternative model H_1. The test is based on the likelihood ratio $\Lambda(x)$, which expresses how many times more likely the data are under one model than the other.

$$\Lambda(x) := \frac{\mathcal{L}(\theta_0 \mid x_i)}{\mathcal{L}(\theta_1 \mid x_i)} \tag{4.10}$$

The LR test is any test with critical region (or rejection region) of the form $\Lambda(x) \leq c$ where c is any number satisfying $0 \leq c \leq 1$. Many common test statistics such as the Z-test, the F-test, Pearson's chi-squared test and the G-test are tests for nested models and can be phrased as log-likelihood ratios or approximations thereof. This likelihood ratio, or equivalently its logarithm, can then be used to compute a p-value, or compared to a critical value to decide whether to reject the null model. When the logarithm of the likelihood ratio, Log-Likelihood Ratio (LLR), is used, the probability distribution of this test statistic, assuming that the null model is true, can be approximated using Wilks'

theorem. The Wilks' theorem offers an asymptotic distribution of the LLR statistic, which can be used as a test statistic for performing the Likelihood-ratio test. Assuming the PDF follows Gaussian distribution

$$f(x_i, \theta) = \frac{1}{\sqrt{2\pi\sigma^2}} \exp^{\frac{-(x_i-\theta)^2}{2\sigma^2}}, \tag{4.11}$$

then the relation between χ^2 and $\ell(\theta \mid x_i)$ is:

$$\begin{aligned} \ell(\theta \mid x_i) =& \sum_i \log f(x_i, \theta) \\ =& \sum_i \log \frac{1}{\sqrt{2\pi\sigma^2}} - \frac{1}{2} \sum_i \frac{(x_i - \theta)^2}{\sigma^2} \\ =& const - \frac{1}{2}\chi^2(\theta) \end{aligned} \tag{4.12}$$

i.e. the parameter values that maximize $\mathcal{L}$ are the same as those which minimize χ^2. Then the relation between χ^2 and LLR becomes:

$$\begin{aligned} LLR = \log \Lambda(x) =& \log \left(\frac{\mathcal{L}(\theta_0 \mid x_i)}{\mathcal{L}(\theta_1 \mid x_i)} \right) \\ =& \log \mathcal{L}(\theta_0 \mid x_i) - \log \mathcal{L}(\theta_1 \mid x_i) \\ =& \ell(\theta_0 \mid x_i) - \ell(\theta_1 \mid x_i) \\ =& \sum_i \log f(x_i, \theta_0) - \sum_i \log f(x_i, \theta_1) \\ =& \sum_i \log \sqrt{\frac{\sigma^2_{\theta_0}}{\sigma^2_{\theta_1}}} - \frac{1}{2} \sum_i \frac{(x_i - \theta_0)^2}{\sigma^2_{\theta_0}} + \frac{1}{2} \sum_i \frac{(x_i - \theta_1)^2}{\sigma^2_{\theta_1}} \\ =& \frac{1}{2} \log(\frac{\sigma_{\theta_0}}{\sigma_{\theta_1}}) - \frac{1}{2}\chi^2(\theta_0) + \frac{1}{2}\chi^2(\theta_1) \\ =& -\frac{1}{2} \left(\chi^2(\theta_0) - \chi^2(\theta_1) + \log(\frac{\sigma_{\theta_0}}{\sigma_{\theta_1}}) \right) \end{aligned} \tag{4.13}$$

The Wilks' theorem [1939] states that as the sample size n approaches ∞, the test statistic $-2log(\Lambda)$ for a nested model will be asymptotically[2] χ^2 distributed.

$$-2\log(\Lambda) = \chi^2(\theta_0) - \chi^2(\theta_1) + const \tag{4.14}$$

That means that for a great variety of hypotheses, a practitioner can compute the likelihood ratio Λ for the data and compare $-2\log(\Lambda)$ to the χ^2 value corresponding to a desired statistical significance as an approximate statistical test. The Neyman-Pearson lemma[3] states that $\Lambda(x)$ is a powerful test at a predefined significance level α.

The Pearson's χ^2 test, as short for χ^2 test, is usually used to assess goodness of fit. A test of goodness of fit establishes whether an observed frequency distribution differs from

[2] An asymptotic distribution is a probability distribution that corresponds to the "limiting" distribution of a sequence of distributions. One of the main uses of the idea of an asymptotic distribution stays in providing approximations to the cumulative distribution functions of statistical estimators.

[3] The Neyman-Pearson Lemma was introduced by Jerzy Neyman and Egon Pearson in a paper in 1933 [53].

a theoretical distribution. The computational procedure includes the following steps: first calculate the χ^2 test statistic as the normalized sum of squared deviations between observed and theoretical frequencies. Then, it determines the degrees of freedom of that statistic. For a test of goodness of fit, this is essentially the number of categories reduced by the number of parameters of the fitted distribution. Second, select a desired level of confidence (significance level, p-value or α level) for the result of the test. After that, compare χ^2 to the critical value from the chi-squared distribution, a special case of the gamma distribution, with degrees of freedom and the selected confidence level (one-sided since the test is only in one direction [4]), which in many cases gives a good approximation of the distribution of χ^2. Finally, accept or reject the null hypothesis whether the test statistic exceeds the critical value of χ^2. If the test statistic exceeds the critical value of χ^2, the null hypothesis can be rejected, and the alternative hypothesis can be accepted, both with the selected level of confidence.

4.2.2 The Method of Moments (MM)

In 1894, Pearson introduced the Method of Moments (MM) as an estimation method for population parameters. The moment conception will play a crucial role in the dissertation so it is worth going back to the basis to understand the mechanics of MM. One starts with deriving equations that relate the population moments to the parameters of interest. When a sample is available the population moments are estimated from the sample. The equations are then solved for the parameters of interest, using the sample moments in place of the (unknown) population moments. This results in estimates of those parameters.

Estimates by MM may be used as the first approximation to the solutions of the likelihood equations, and successive improved approximations may then be found by the Newton-Raphson method. In this way the method of moments can assist in finding maximum likelihood estimates.

The Method of Moments only works when the number of moment conditions equals the number of parameters to estimate. MM is fairly simple and yields consistent estimators, although these estimators are often biased.

In 1982, Peter Hansenas developed the Generalized Method of Moments[5][54]. GMM is a framework for deriving estimators. Its estimators use assumptions about the moments of the variables to derive an objective function. The GMM estimates make the sample moment conditions as true as possible by minimizing an objective function. The assumed moments of the random variables provide population moment conditions. We use the data to compute the analogous sample moment conditions. It is usually used when the full shape of the data distribution function may not be known, and therefore maximum likelihood estimation is not applicable.

Assume that there is a set of measurements (y_i) and the generalized moment ($\hat{\mu}^{GMM}$),

[4] is the test value greater than the critical value?

[5] Hansen shared the 2013 Nobel Prize in Economics in part for this work.

the sample moment condition for total measurements (N) is

$$\frac{1}{N}\sum_{i}^{N} y_i - \langle \hat{\mu}^{GMM} \rangle_{th} = 0, \tag{4.15}$$

and $\hat{\mu}^{GMM}$ is obtained by solving the sample moment condition

$$\langle \hat{\mu}^{GMM} \rangle_{th} = \frac{1}{N}\sum_{i}^{N} y_i. \tag{4.16}$$

The standard method of the generalized moments consists in choosing a generalized moment $\hat{\mu}^{GMM}(N)$ defined as a function on events and then finding θ by drawing its theoretical average value, $\langle \hat{\mu}^{GMM} \rangle_{th}$, against the corresponding experimental value, $\langle \hat{\mu}^{GMM} \rangle_{exp}$.

The optimal Moments

Assume a set of events N_i binned in bin number i with their probability $\pi^i(N_i)$. The probability distribution depends on a parameter θ whose exact value θ^* is unknown. The theoretical value of the mean of an arbitrary generalized moment/weight $\phi^i(N_i)$ is

$$\langle \phi^i(N_i) \rangle_{th} = \int \phi^i(N_i)\pi^i(N_i)dN. \tag{4.17}$$

One estimates θ^*, the exact value of θ, by choosing a weight $\phi^i(N_i)$ and equating the theoretical mean,

$$\langle \phi^i(N_i) \rangle_{th} \equiv h(\theta), \tag{4.18}$$

assumed to be a calculable function of θ called $h(\theta)$, to the corresponding experimental value,

$$\langle \phi^i(N_i) \rangle_{exp} = \frac{1}{N}\sum_{i} \phi^i(N_i). \tag{4.19}$$

Then, one solves the resulting equation

$$h(\theta) = \langle \phi^i(N_i) \rangle_{exp} \tag{4.20}$$

to obtain an estimate θ_{exp} for the unknown value θ^*:

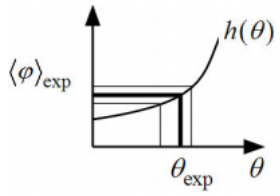

Requiring that $\langle \phi^i(N_i(\theta)) \rangle_{th} \equiv \langle \phi^i(N_i) \rangle_{exp} = h(\theta)$, we obtain an equation for θ. By taking a number of different weights $\phi^i(N_i)$, one can obtain a set of equations, whose solution will yield an estimate for θ.

The optimal wight minimizes the variance of the parameter, σ^2_θ. The problem is to minimized σ^2_θ by a suitable choice of ϕ. A necessary condition for a minimum can be written in terms of functional derivatives:

$$\frac{\delta\sigma^2_{\theta[\phi]}}{\delta\phi} = 0. \tag{4.21}$$

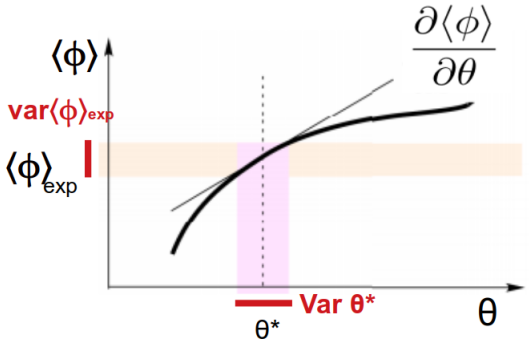

Now, our target is to get the functional $\sigma^2_{\theta[\phi]}$ then minimize it using Eq. 4.21 and obtain the optimal weight.

In the contest of the precision measurements one can assume the magnitude of errors to be small. One has a simple and explicit expression for the error estimation. Then, fluctuations in the values of θ are related to fluctuations in the values of $\langle\phi\rangle_{th}$ as

$$\frac{\delta\theta}{\delta\langle\phi\rangle_{th}} = \left(\frac{\partial\langle\phi\rangle_{th}}{\partial\theta}\right)^{-1}. \tag{4.22}$$

The derivative ($\frac{\partial\langle\phi\rangle_{th}}{\partial\theta}$) is applied only to the probability distribution:

$$\frac{\partial\langle\phi\rangle_{th}}{\partial\theta} = \frac{\partial}{\partial\theta}\left[\int \phi\pi dN\right] = \int \phi\frac{\partial\pi}{\partial\theta}dN. \tag{4.23}$$

For small fluctuations $\delta\langle\phi\rangle = N^{-1/2}\sqrt{\sigma^2_{\langle\phi\rangle}}$, where

$$\sigma^2_{\langle\phi\rangle_{exp}} = \left\langle\left[\phi - \langle\phi\rangle_{exp}\right]^2\right\rangle_{exp}, \quad \sigma^2_{\langle\phi\rangle} = \left\langle\left[\phi - \langle\phi\rangle\right]^2\right\rangle, \quad \sigma^2_{\langle\phi\rangle} \equiv \langle\phi^2\rangle - \langle\phi\rangle^2. \tag{4.24}$$

The variance of the generalized weight, σ^2_ϕ, is a function of the variance of experimental value of the parameter $\sigma^2_{\theta_{exp}}$.

$$\frac{\sigma^2_{\theta_{exp}}}{\sigma^2_\phi} = N^{-1}\left(\frac{\partial h(\theta_{exp})}{\partial\theta}\right)^{-2} \tag{4.25}$$

In terms of variations, Eq. 4.22 becomes:

$$\frac{\sigma^2_{\theta[\phi]}}{\sigma^2_\phi} = \left(\frac{\partial\langle\phi\rangle_{th}}{\partial\theta}\right)^{-2}, \tag{4.26}$$

resulting

$$\sigma^2_{\theta[\phi]} = \left(\frac{\partial\langle\phi\rangle_{th}}{\partial\theta}\right)^{-2}\sigma^2_{\phi}. \tag{4.27}$$

Substitute Eq. 4.27 into Eq. 4.21

$$0 = \frac{\delta\left[\left(\frac{\partial\langle\phi\rangle}{\partial\theta}\right)^{-2}\sigma^2_{\phi}\right]}{\delta\phi} \tag{4.28}$$

$$= \frac{\delta\left[\left(\frac{\partial\langle\phi\rangle}{\partial\theta}\right)^{-2}\left\langle[\phi-\langle\phi\rangle]^2\right\rangle\right]}{\delta\phi} \tag{4.29}$$

and use the following relation:

$$\frac{\delta\langle\phi\rangle}{\delta\phi} = \pi, \quad \frac{\delta\langle\phi^2\rangle}{\delta\phi} = 2\pi\phi, \quad \frac{\delta\left(\frac{\delta\langle\phi\rangle}{\delta\theta}\right)}{\delta\phi} = \frac{\partial\pi}{\partial\theta}, \tag{4.30}$$

to obtain this family of solutions:

$$\phi = \langle\phi\rangle + const\frac{\partial\ln\pi}{\partial\theta}, \tag{4.31}$$

where the constants are independent of N but may depend on θ. The constant plays no role since ϕ is defined by this reasoning only up to a constant factor. We arrive at the following general solution:

$$\phi_{opt} = \frac{\partial\ln\pi}{\partial\theta} \tag{4.32}$$

Notice that

$$\langle\phi_{opt}\rangle = \left\langle\frac{\partial\ln\pi}{\partial\theta}\right\rangle = \int\frac{\partial\ln\pi}{\partial\theta}\pi dN = \int\frac{\partial\pi}{\partial\theta}dN = \frac{\partial}{\partial\theta}\int\pi dN \equiv \frac{\partial}{\partial\theta}1 = 0. \tag{4.33}$$

The method yields the optimal weight (ϕ_{opt}) for the parameter θ whose variance $\sigma^2_{\phi_{opt}}$ is optimal because it is asymptotically equal to the minimal value established by the fundamental Cramer-Rao inequality:

$$\sigma^2_{\phi_{opt}} \approx \sigma^2_{CRF} = N^{-1}[Fisher\ Information]^{-1} \approx N^{-1}\left\langle\left[\frac{\partial\ln\pi}{\partial\theta}\right]^2\right\rangle^{-1} \tag{4.34}$$

The minimum of $\sigma^2_{\theta_{exp}}$ is located in the space of the generalized momentum ϕ at $\phi_{opt} = \frac{\partial\ln\pi}{\partial\theta}$ [55]. This is because θ is unknown, so even though the solution ϕ_{opt} will depend on θ, any such dependance is coincidental and therefore "frozen" in this calculation.

It turns out that there exists a simple formula for the optimum weight that yields a minimum variation of the estimate of θ (it corresponds to the Cramer-Rao bound); this

formula expresses the weight in terms of the respective probability distribution; that is, the optimum weight depends on the unknown θ. However, the deviations of the variation from the minimum are quadratic in the deviations of the weight from the optimum one. This means that, in practice, the unknown exact optimum weight can be replaced without a great loss of quality by an approximate expression (in particular, an optimum weight for a θ value obtained by means of rougher estimate can be employed). It is noticeable that, if the weight is chosen inappropriately, the estimate for θ remains correct, but it ceases to be optimal [56].

The Multi-distribution Case

First consider the independent N_i in the sample $\{N_i\}_i$ be governed by $\pi(\{N_i\}_i)$. With independent N_i, one can regard the sample $\{N_i\}_i$ as a cumulative event whose probability density is $\pi(\{N_i\}_i) = \prod_i \pi^i(N_i)$. Then the optimal weight is immediately obtained as follows:

$$N\phi_{opt}(\{N_i\}_i) = \frac{\partial \ln \pi(\{N_i\}_i)}{\partial\theta} = \sum_i \frac{\partial \ln \pi^i(N_i)}{\partial\theta} = \sum_i \phi^i_{opt}(N_i). \tag{4.35}$$

The weight (Eq. 4.35) is already enough for a direct generalization of the previously described method with all its nice properties preserved: one estimates θ^* by solving the equation

$$Nh(\theta) \equiv \sum_i h_i(\theta) \equiv \sum_i \int dN\pi_i\phi_i = \sum_i \phi_i(N_i), \tag{4.36}$$

with ϕ_i taken from Eq. 4.35 with some initial θ_0, etc.

Let is recap the method; first, one arbitrarily chooses weight functions ($\phi^i(N_i)$) for experimentally measured quantities (N_i). After that, one can calculate the weighted mean for a specific set of measurements and the respective theoretical mean, which is a calculable function of estimated parameters θ (since the probability distribution is assumed to be known apart from θ). The formulas for the variation of the quantity $\langle\phi\rangle_{exp}$ generalize the elementary formulas for the case of a homogeneous sample; from them, one obtains formulas for the errors in the estimates of θ. The main target is to find the generalized momentum ϕ which would allow one to extract θ with the highest precision from the event sample [55].

Connection with Maxiumum Likelihood

The two basic methods of parameter estimation, the method of maximal likelihood and the method of generalized moments are connected [57]. The connection views the method of maximal likelihood as corresponding to a special point in the space of generalized moments, and considers small deviations from that point. The method of maximal likelihood prescribes to choose θ which maximizes the likelihood function

$$\mathcal{L} = \prod_i \pi^i(N_i). \tag{4.37}$$

The maximum likelihood method prescribes to estimate θ by the value which maximizes the likelihood function,

$$\ln \mathcal{L} = \sum_i \ln \pi^i(N_i), \tag{4.38}$$

where summation runs over all events from the sample. The necessary condition for the maximum of Eq. 4.38 is

$$\frac{\partial \ln \mathcal{L}}{\partial \theta} = \frac{\partial}{\partial \theta}\left[\sum_i \ln \pi^i(N_i)\right] = \sum_i \frac{\partial \ln \pi^i(N_i)}{\partial \theta} \propto \langle \phi_{opt} \rangle = 0. \tag{4.39}$$

This agrees with Eq. 4.32 thanks to Eq. 4.33. The method yields the optimal weight (ϕ_{opt}) for the parameter θ whose variance $\sigma^2_{\phi_{opt}}$ is optimal because it is asymptotically equal to the minimal value established by the fundamental Cramer-Rao inequality, Eq. 4.34. That is why Eq. 4.32 can be regarded as a translation of the method of maximum likelihood (which is known to yield the theoretically best estimate for θ using the Cramar-Rao inequality) into the language of generalized moments. This approach offers what appears to be a new and useful algorithmic scheme which combines the theoretical advantage of the method of maximal likelihood (i.e. the fact that it yields the absolute minimum for the variance of the parameter being estimated with a given data sample) with the algorithmic simplicity of the method of moments. The point corresponds to the minimum of Cramer-Rao inequality, and small deviations from it introduces non-optimalities (compared with the maximal likelihood method) that are only quadratic in the deviations. Although theoretically ideal, what if $\pi(N_i)$ that represents the probability distribution is unknown as a formula? This is often the case in high energy physics where only a Monte Carlo event generator may be available but not an explicit expression for the probability distribution (this is due to a very high dimensionality of the event space) [58]. The χ^2 method makes a fit with a number of non-optimal moments (bins of a histogram). The histogramming implies a loss of information but the method is universal, verifies the probability distribution as a whole, and is implemented in standard software routines.

CHAPTER 5

THE DRAW-BACKS OF THE STANDARD ALGORITHM

The analysis of the ν MH significance usually proceeds from the standard method, the single dimensional estimator $\Delta\chi^2$, and its evaluation is based on the two separated hypotheses, NH and IH. This method shows some draw-backs and concerns. The issues on the ν MHD from the reactor experiments using the standard method are illustrated in details. I will explain the draw-backs and considerations of the standard method through the following three main issues.

First issue is the limited power of the standard method. The $\Delta\chi^2$ estimator provides us with different results when different simulation procedures were used. When the simulation is performed on a semi-analytical basis and not on a event-by-event basis, the significance drastically drops. The semi-analytical based simulation does not take into account the correlation between the bins due to systematic uncertainties. The systematic uncertainty due to the $\frac{3\%}{\sqrt{E}}$ energy resolution causes unbalanced migration between bins that manifests itself in the event-by-event simulations. That consequently creates side-bin correlations leading to a reduction in the experiment sensitivity. The simulations with infinite energy resolution are provided to confirm that the usual assumption used to evaluate the experiment sensitivity is valid ONLY when the side-bin correlations are neglected i.e. when the systematic uncertainties due to the energy resolution are neglected. Therefore, the power of the $\Delta\chi^2$ appears fully dependent of the statistical assumptions, as explained in Sec. 5.2.

Second issue, when $\chi^2_{min(NH)}$ and $\chi^2_{min(IH)}$ are drawn in a $2D$ map, their strong positive correlation manifests χ^2 as a bi-dimensional estimator. The overlapping between the χ^2 distributions of the two hypotheses leads to the experiment sensitivity reduction. The full details of the bi-dimensional statistics is explained in Sec. 5.3.

Third issue is the robustness of the standard method. When the JUNO sensitivity is obtained using different procedures, $\Delta\chi^2$ as one dimensional and χ^2 as two dimensional estimator, we have to study how the experimental sensitivity varies with the different values of the atmospheric mass, the input parameter. We computed the oscillation of $|\overline{\Delta\chi^2}|$ with the input parameter values, $|\Delta m^2|_{inj}$. The MH significance using the standard method, $\Delta\chi^2$, strongly depends on the values of the parameter $|\Delta m^2|_{inj}$. Consequently,

the experiment sensitivity depends on the precision of the atmospheric mass. This point is explained in details in Sec. 5.4.

5.1 The Standard Method

The neutrino mass hierarchy is encoded inside the $\overline{\nu}_e$ energy spectrum. That is why JUNO will need 3% at $1MeV$ energy resolution to detect electron neutrino coming from the Nuclear Power Plant (NPP's). The JUNO strategy is based on the study of the $\overline{\nu}_e$ vacuum oscillations in a medium baseline reactor experiment. The discrimination power of JUNO is maximized when the Δm^2_{21} oscillation is maximal and the baseline has been chosen in such a way to realize this condition [1]. In fact, there are two important requirements essential to reach the desired discrimination: first, a big sensitive mass of the detector, second, a very good energy resolution $\frac{3\%}{\sqrt{E}}$. As described in Ch. 3, the toy simulations are based on a single event basis. In event-by-event simulations, energy resolution smearing per each single event causes unbalance migration for events i.e. the number of events in each bin becomes correlated with the number of events in the side bins.

From the statistics point of view, MHD is a test to distinguish between two discrete hypotheses, normal hierarchy (NH) and inverted hierarchy (IH). The two discrete hypotheses are not nested[1] and they correspond to a discrete choice. Then, the conditions for Wilks theorem are violated.

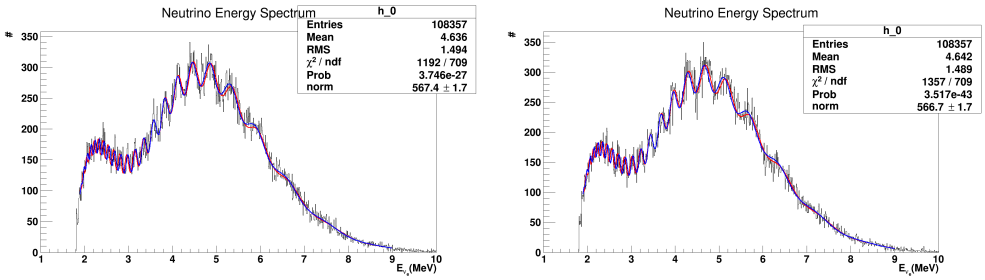

Figure 5.1: *Reactor $\overline{\nu}_e$ energy spectrum for JUNO toy-like simulated at $\Delta m^2 = 2.500 \times 10^{-3}\mathrm{eV}^2$ for NH hypothesis (left panel) and at $\Delta m^2 = -2.460 \times 10^{-3}\mathrm{eV}^2$ for IH hypothesis (right panel) with six years of exposure and the ten near reactor cores. An infinite energy resolution is assumed.*

After obtaining the energy distribution of reactor $\overline{\nu}_e$, a further step will be the estimation of the JUNO sensitivity in determining MH using either a χ^2 estimator (this chapter) or the new F-estimator (next chapter). According to [1], the standard statistical analysis method for JUNO data sets is based on a χ^2 constructed as

$$\chi^2_{rea} = \sum_i^{N_{bin}} \frac{\left[M_i - T_i\left(1 + \sum_k \alpha_{ik}\epsilon_k\right)\right]^2}{M_i} + \sum_k \frac{\epsilon^2}{\sigma_k^2}, \tag{5.1}$$

where M_i is the measured neutrino events in the "i" energy bin, T_i is the predicted neutrino events with oscillations, σ_k^2 is the k-systematic uncertainty, ϵ_k is the corresponding pull

[1] Hypothesis (A) states that x is a real a number. Hypothesis (B) states that $x = x_0$, for a particular real number x_0. Clearly hypothesis (B) is a special case of hypothesis (A). These hypotheses are said to be nested.

parameter, and α_{ik} is the fraction of neutrino event contribution of the k^{th} pull parameter to the i^{th} energy bin.

A different definition with of the χ^2 function based on the Poisson distribution yields a consistent MH sensitivity [1]. χ^2 is divided into three parts as indicated in

$$\chi^2 = \chi^2_{para} + \chi^2_{sys} + \chi^2_{stat}. \tag{5.2}$$

χ^2_{para} summarizes the prior knowledge on oscillation parameters. In JUNO these parameters are $\sin^2 2\theta_{12}, \sin^2 2\theta_{13}, \Delta m^2_{12}$ and Δm^2_{13}. Then χ^2_{para} becomes:

$$\begin{aligned}
\chi^2_{para} = & \left(\frac{(\sin^2 2\theta_{12})^{fit} - (\sin^2 2\theta_{12})^{input}}{\sigma_{\sin^2 2\theta_{12}}} \right)^2 \\
+ & \left(\frac{(\sin^2 2\theta_{13})^{fit} - (\sin^2 2\theta_{13})^{input}}{\sigma_{\sin^2 2\theta_{13}}} \right)^2 \\
+ & \left(\frac{(|\Delta m^2_{31}|)^{fit} - (|\Delta m^2_{31}|)^{input}}{\sigma_{|\Delta m^2_{31}|}} \right)^2 \\
+ & \left(\frac{(\Delta m^2_{21})^{fit} - (\Delta m^2_{21})^{input}}{\sigma_{\Delta m^2_{21}}} \right)^2 .
\end{aligned} \tag{5.3}$$

The reactor anti-neutrino flux, the IBD cross section, the fiducial volume and the weight fraction of free proton can all be combined into a single overall factor. Consequently, their contributions to the χ^2 function can be represented by a single term as,

$$\chi^2_{sys} = \left(\frac{f^{fit}_{sys} - f^{input}_{sys}}{\sigma_{f_{sys}}} \right)^2 , \tag{5.4}$$

where $f^{input}_{sys} = 1$, and $\sigma_{f_{sys}} = 0.03$.

The last term of Eq. 5.2, χ^2_{stat}, represents the statistical fluctuation. When we introduce binning with respect to E^{obs}_{vis}, it looks like

$$\chi^2_{stat} = \sum_i \left(\frac{N^{fit}_i - N^{NH(IH)}_i}{\sqrt{N^{NH(IH)}_i}} \right)^2 \tag{5.5}$$

with the summation running over all the bins. Here, $N^{NH(IH)}_i$ is the event number for the i_{th} bin when the hierarchy is NH(IH). N^{fit}_i is the fitted number of events, calculated as a function of the four model parameters and the normalization factor f_{sys}. All parameters are varied under the NH(IH) constraints of Eq. 5.3 and Eq. 5.4.

In the minimization procedure all the parameters were initially set to their global best values that are indicated in Tab. 1.1. The fitting procedures and the minimization of χ^2 are done with the TMinuit algorithm (ROOT libraries). The χ^2 distributions are obtained for four parameters ($sin^2\theta_{12}$, $sin^2\theta_{13}$, δm^2_{sol} and Δm^2), based on a total of 108357 signal events (Fig. 5.2 and Fig. 5.3).

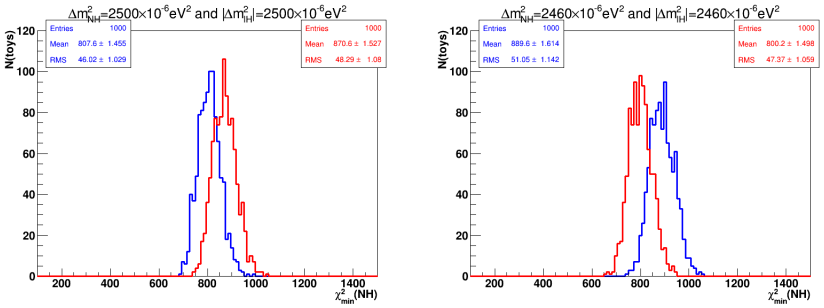

Figure 5.2: *Two χ^2 distributions for 1000 (NH) + 1000 (IH) toy JUNO-like simulations generated at $\Delta m^2 = 2.500 \times 10^{-3}\text{eV}^2$ for NH hypothesis (left panel) and $\Delta m^2 = -2.460 \times 10^{-3}\text{eV}^2$ for IH hypothesis (right panel), with six years of exposure and the ten near reactor cores with infinite energy resolution. The intrinsic strong positive correlation between the two components $\chi^2_{min(NH)}$ and $\chi^2_{min(IH)}$ leads to the overlapping between the two χ^2 distributions.*

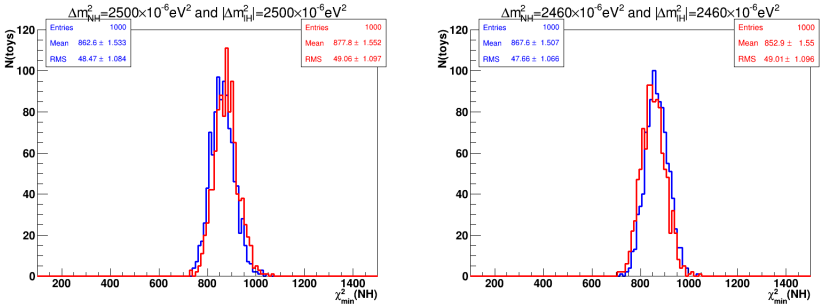

Figure 5.3: *Two χ^2 distributions for 1000 (NH) + 1000 (IH) toy JUNO-like simulations generated at $\Delta m^2 = 2.500 \times 10^{-3}\text{eV}^2$ for NH hypothesis (left plot) and $\Delta m^2 = -2.460 \times 10^{-3}\text{eV}^2$ for IH hypothesis (right panel) with six years of exposure and the ten near reactor cores, with 3% relative energy resolution. The intrinsic strong positive correlation between the two components $\chi^2_{min(NH)}$ and $\chi^2_{min(IH)}$ leads to an overlapping between the two χ^2 distributions.*

5.2 The Limited Power of $\Delta\chi^2$ as a Single Dimensional Estimator

The two discrete hypotheses are not nested, thus the Wilks theorem is not applicable in this problem when it is based on the $\Delta\chi^2$ defined in Eq. 5.6. As a consequence, $\Delta\chi^2$ does not follow a χ^2 distribution [59]. The MO significance is usually obtained in terms of the single dimensional estimator $\Delta\chi^2$ and its evaluation is based on two distinct hypotheses, NH and IH. For each MO the best solution is found: the χ^2_{min} comes from two different best-fit values for NH model to be $\chi^2_{min(NH)}$ and IH model to be $\chi^2_{min(IH)}$. The $\Delta\chi^2$ is the result of the internal adjustments of the two separate fits:

$$\Delta\chi^2 = \chi^2_{min(NH)} - \chi^2_{min(IH)}, \tag{5.6}$$

where the two minima are evaluated spanning the uncertainties on the three-neutrino oscillation parameters. The experimental sensitivity to the neutrino mass hierarchy arises

from the small phase shift in the oscillation terms depending on the two large mass-squared differences Δm^2_{32} and Δm^2_{31}. JUNO sensitivity can be calculated using the single dimensional test statistics $\Delta\chi^2$. The median sensitivity can be obtained using the Z-test, where $z^{(NH)}_{score}$ is the number of σ_{NH} assuming NH be the true model and $z^{(IH)}_{score}$ is the number of σ_{IH} assuming IH be the true model,

$$z^{(NH)}_{score} = \frac{\overline{\Delta\chi^2}^{(IH)} - \overline{\Delta\chi^2}^{(NH)}}{\sigma_{NH}} \qquad z^{(IH)}_{score} = \frac{\overline{\Delta\chi^2}^{(NH)} - \overline{\Delta\chi^2}^{(IH)}}{\sigma_{IH}}. \tag{5.7}$$

The $\overline{\Delta\chi^2}^{(NH)}$, σ_{NH}, $\overline{\Delta\chi^2}^{(IH)}$ and σ_{IH} are the mean value and standard deviation of the $\Delta\chi^2$ distribution assuming NH and IH be the true model, respectively. There an approximation is usually used [1, 47, 60, 61]:

$$\sigma_{\Delta\chi^2} = 2\sqrt{\overline{\Delta\chi^2}}, \tag{5.8}$$

therefore Eq. 5.7 becomes:

$$z^{(NH)}_{score} = \sqrt{\overline{\Delta\chi^2}^{(NH)}} \qquad z^{(IH)}_{score} = \sqrt{\overline{\Delta\chi^2}^{(IH)}}. \tag{5.9}$$

When the analysis is performed on a event-by-event basis and not a semi-analytical simulations as in [1], the dispersions of the distributions cannot be described by Eq. 5.8 anymore. That significantly affect the statistical significance that drops to less than $2\,\sigma$ as indicated in Tab. 5.2. The reason stays in the convolution of the energy resolution. To chick it: the analysis is done also at an infinite energy resolution to find out whether it works (Fig. 5.4).

The investigation of the origin of the approximation have been pursued by looking whether it is still valid in event-by-event simulations as it is in semi-analytical simulations. In fact, we found that the dispersion of the two distributions becomes wider than in semi-analytical simulations when an finite energy resolution is taken into account. The energy error introduces strong correlations between bins and it corresponds to a further systematic error.

The limited power of the $\Delta\chi^2$ manifests itself being controlled by the statistical assumption i.e. Eq. 5.8. The experimental sensitivity is reduced when the energy systematic error is taken into account, and Eq. 5.8 is no more valid. So that specific cases are reported in the following figures and tables and the rest are reported in SubSec. 7.1.1.

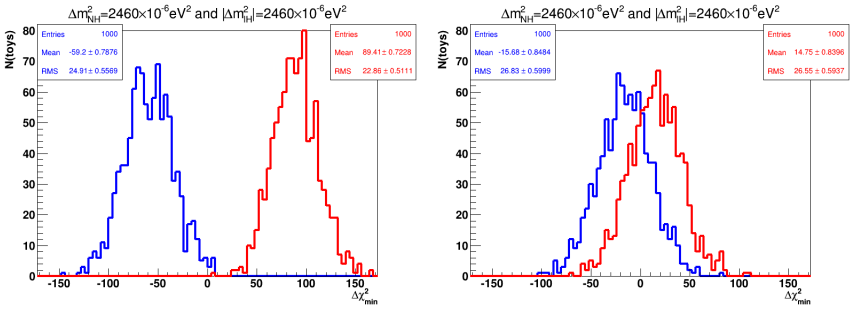

Figure 5.4: *$\Delta\chi^2$ estimator for 1000 (NH) + 1000 (IH) toy JUNO-like simulations generated at $|\Delta m^2| = 2.460 \times 10^{-3}\text{eV}^2$ for NH and IH hypotheses with six years of exposure and the ten near reactor cores. An infinite energy resolution is assumed for the left plot and 3% relative energy resolution for the right plot. The experimental sensitivities under these terms are reported in Tab. 5.2 and Tab. 5.1.*

Table 5.1: *The comparison of the MH sensitivity at infinite energy resolution for NH sample and IH sample at $|\Delta m^2| = 2.460 \times 10^{-3}\text{eV}^2$ in two cases. The first case uses Eq. 5.7 and the second one uses Eq. 5.9.*

Infinite Energy Resolution		
μ_{NH}	-59.20 ± 0.79	
σ_{NH}	24.91 ± 0.56	
μ_{IH}	89.41 ± 0.72	
σ_{IH}	22.86 ± 0.51	
$z_{score}^{(NH)}$	5.966	7.694(app.)
$z_{score}^{(IH)}$	6.501	9.456(app.)

Table 5.2: *The comparison of the MH sensitivity at energy resolution $3\%/\sqrt{E}$ for NH sample and IH sample at $|\Delta m^2| = 2.460 \times 10^{-3}\text{eV}^2$ in two cases. The first case uses Eq. 5.7 and the second one uses Eq. 5.9.*

energy resolution $3\%/\sqrt{E}$		
μ_{NH}	-15.68 ± 0.85	
σ_{NH}	26.83 ± 0.60	
μ_{IH}	14.75 ± 0.84	
σ_{IH}	26.55 ± 0.60	
$z_{score}^{(NH)}$	1.134	3.960(app.)
$z_{score}^{(IH)}$	1.146	3.841(app.)

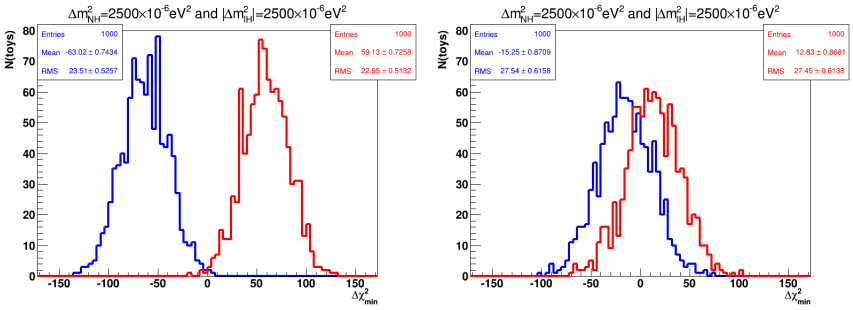

Figure 5.5: *$\Delta\chi^2$ estimator for 1000 (NH) + 1000 (IH) toy JUNO-like simulations generated at $|\Delta m^2| = 2.500 \times 10^{-3}\text{eV}^2$ for NH hypothesis (left panel) and IH hypothesis (right panel) with six years of exposure and the ten near reactor cores. An infinite energy resolution is assumed for the left plot and 3% relative energy resolution for the right plot. The experimental sensitivities under these terms are reported in Tab. 5.3 and Tab. 5.4, respectively.*

Table 5.3: *The comparison of the MH sensitivity for ideal distributions for NH sample and IH sample at $|\Delta m^2| = 2.500 \times 10^{-3}\text{eV}^2$ in two cases. The first case uses Eq. 5.7 and the second one uses Eq. 5.9.*

Infinite Energy Resolution		
μ_{NH}	-63.02 ± 0.74	
σ_{NH}	23.51 ± 0.53	
μ_{IH}	59.13 ± 0.73	
σ_{IH}	22.95 ± 0.51	
$z^{(NH)}_{score}$	5.203	7.950(app.)
$z^{(IH)}_{score}$	5.330	7.690(app.)

Table 5.4: *The comparison of the MH sensitivity for actual distributions for NH sample and IH sample at $|\Delta m^2| = 2.500 \times 10^{-3}\text{eV}^2$ in two cases. The first case uses Eq. 5.7 and the second one uses Eq. 5.9.*

$3\%/\sqrt{E}$ Energy Resolution		
μ_{NH}	-15.25 ± 0.87	
σ_{NH}	27.54 ± 0.62	
μ_{IH}	12.83 ± 0.87	
σ_{IH}	27.45 ± 0.61	
$z^{(NH)}_{score}$	1.020	3.901(app.)
$z^{(IH)}_{score}$	1.023	3.582(app.)

As reported in [1], the sensitivity can reach $|\overline{\Delta\chi^2}| > 16$ in the ideal case of single reactor and single detector, and $|\overline{\Delta\chi^2}| > 9$ considering the spread of reactor cores and uncertainties of the detector response. All these results has been reached using semi-analytical simulations i.e. simulations as used in [1] and [62]. Semi-Analytical simulations are generated by fluctuating the bin-content according to Poisson or Gaussian distributions that represent the number of events. In addition, a second fluctuation is added by applying $3\%/\sqrt{E}$ energy smearing in each single bin not in each single event. If the energy resolution smearing per each single event is replaced by smearing for the whole bin, an

event balance migration occurs and the number of events per each single bin becomes uncorrelated with side bins leading to the results reported in the [1].

We provided the simulation performed on a event-by-event basis and computed the experimental sensitivity for the JUNO by changing the atmospheric neutrino mass. Fig. 5.6 for NH sample at $\Delta m^2 = 2.500 \times 10^{-3}\text{eV}^2$ and IH sample for $\Delta m^2 = -2.460 \times 10^{-3}\text{eV}^2$, shows the $\Delta\chi^2$ distributions for a relative 3% and an infinite energy resolution. The JUNO sensitivity is clearly different from that reported in [1].

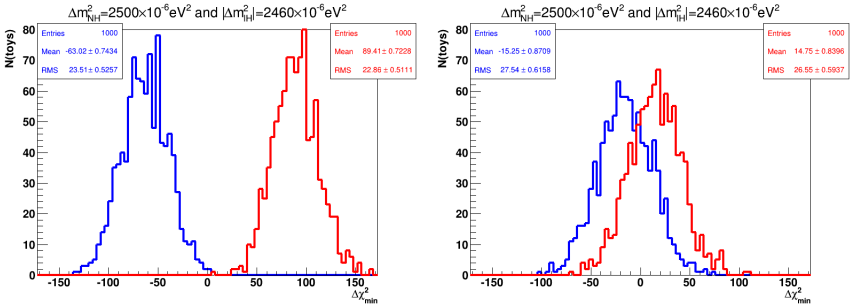

Figure 5.6: *$\Delta\chi^2$ estimator for 1000 (NH) + 1000 (IH) toy JUNO-like simulations generated at $\Delta m^2 = 2.500 \times 10^{-3}\text{eV}^2$ for NH hypothesis (blue) and $\Delta m^2 = -2.460 \times 10^{-3}\text{eV}^2$ for IH hypothesis (red) with six years of exposure and the ten near reactor cores. The left plot is for infinite energy resolution and the blue plot is for 3% relative energy resolution. The experimental sensitivities under these terms are reported in Tab. 5.5 and Tab. 5.6.*

Table 5.5: *The comparison of the MH sensitivity for ideal distributions for NH sample at $\Delta m^2 = 2.500 \times 10^{-3}\text{eV}^2$ and IH sample for $\Delta m^2 = -2.460 \times 10^{-3}\text{eV}^2$ in two cases. The first case uses Eq. 5.7 and the second one uses Eq. 5.9.*

Infinite Energy Resolution		
μ_{NH}	-63.02 ± 0.74	
σ_{NH}	23.51 ± 0.53	
μ_{IH}	89.41 ± 0.72	
σ_{IH}	22.86 ± 0.51	
$z_{score}^{(NH)}$	6.484	7.950(app.)
$z_{score}^{(IH)}$	6.668	9.456(app.)

When only statistical fluctuations are included, the MH sensitivities using Z-test ($z_{score}^{(NH)}$ and $z_{score}^{(IH)}$) do not exact equal to the MH sensitivities obtained in the approximated Eq. 5.8($z_{score}^{(NH)}(app.)$ and $z_{score}^{(IH)}(app.)$) as reported in Tab. 5.3. This observation is consistent with what obtained at the atmospheric mass, $|\Delta m^2| = 2.460 \times 10^{-3}\text{eV}^2$ as reported in Tab. 5.5. This conclusion will be confirmed for other 18 different values for the atmospheric mass at infinite energy resolution in SubSec. 7.1.1.

Table 5.6: *The comparison of the MH sensitivity for actual distributions for NH sample at* $\Delta m^2 = 2.500 \times 10^{-3}\text{eV}^2$ *and IH sample for* $\Delta m^2 = -2.460 \times 10^{-3}\text{eV}^2$ *in two cases. The first case uses Eq. 5.7 and the second one uses Eq. 5.9.*

$3\%/\sqrt{E}$ energy resolution		
μ_{NH}	-15.25 ± 0.87	
σ_{NH}	27.54 ± 0.62	
μ_{IH}	14.75 ± 0.84	
σ_{IH}	26.55 ± 0.60	
$z_{score}^{(NH)}$	1.089	3.960(app.)
$z_{score}^{(IH)}$	1.130	3.841(app.)

5.3 Non-bright Results Using χ^2 as a Bi-Dimensional Estimator

When $\chi^2_{min(IH)}$ and $\chi^2_{min(NH)}$ are drawn in $2D$ dimensional map, their strong positive correlation manifests χ^2 as a bi-dimensional estimator. This strong positive correlation leads to overlap between the χ^2 distributions of the two hypotheses, thus reducing the experiment sensitivity. When we look at χ^2 as a bi-dimensional estimator, the experiment sensitivity can be calculated with a Z-test for two dimensional test statistic providing the results indicated in Tab. 5.7 and Tab. 5.8.

Using Z-test for $2D$, the MH sensitivity can be calculated as

$$
\begin{aligned}
z_{score}^{(NH)} &= \frac{\sqrt{(\overline{\chi^2}_{IH}^{(NH)} - \overline{\chi^2}_{IH}^{(IH)})^2 + (\overline{\chi^2}_{NH}^{(NH)} - \overline{\chi^2}_{NH}^{(IH)})^2}}{\sqrt{(\sigma^2_{IH})^{NH} + (\sigma^2_{NH})^{NH}}} \\
z_{score}^{(IH)} &= \frac{\sqrt{(\overline{\chi^2}_{IH}^{(IH)} - \overline{\chi^2}_{IH}^{(NH)})^2 + (\overline{\chi^2}_{NH}^{(IH)} - \overline{\chi^2}_{NH}^{(NH)})^2}}{\sqrt{(\sigma^2_{IH})^{IH} + (\sigma^2_{NH})^{IH}}}
\end{aligned}
\tag{5.10}
$$

where $\overline{\chi^2}_{IH}^{(NH)}$ and $(\sigma^2_{IH})^{NH}$ are the mean and the standard derivation of χ^2 distribution of the NH sample assuming IH hypothesis is the true hypothesis. $\overline{\chi^2}_{NH}^{(NH)}$ and $(\sigma^2_{NH})^{NH}$ are the mean and the standard derivation of χ^2 distribution of the NH sample assuming NH hypothesis is the true hypothesis. $\overline{\chi^2}_{IH}^{(IH)}$ and $(\sigma^2_{IH})^{IH}$ are the mean and the standard deviation of χ^2 distribution of the IH sample assuming IH hypothesis is the true hypothesis. $\overline{\chi^2}_{NH}^{(IH)}$ and $(\sigma^2_{NH})^{IH}$ are the mean and the standard deviation of χ^2 distribution of the IH sample assuming NH hypothesis is the true hypothesis.

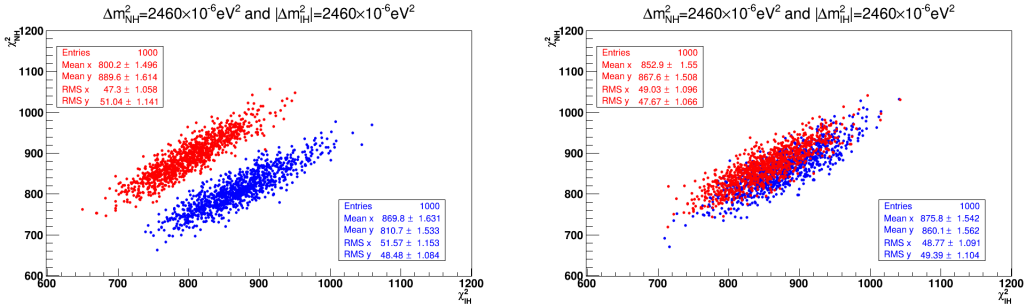

Figure 5.7: *Two islands of χ^2 for 1000 (NH) + 1000 (IH) toy JUNO-like simulations generated at $|\Delta m^2| = 2.460 \times 10^{-3}\text{eV}^2$ for NH hypothesis (blue color) and IH hypothesis (red color) with six years of exposure and the ten near reactor cores. An infinite energy resolution is assumed for left plot and $3\%/\sqrt{E}$ energy resolution for right plot. The experimental sensitivities under these terms are reported in Tab. 5.7.*

Table 5.7: *Two χ^2 distributions for 1000 (NH) + 1000 (IH) toy JUNO-like simulations generated at $|\Delta m^2| = 2.460 \times 10^{-3}\text{eV}^2$ for NH and IH hypotheses with six years of exposure and the ten near reactor cores. The sensitivity is calculated using Eq. 5.10.*

Energy resolution	infinite		3%	
	NH	**IH**	**NH**	**IH**
μ_{NH}	810.7 ± 1.53	889.6 ± 1.61	860.10 ± 1.56	867.60 ± 1.51
σ_{NH}	48.48 ± 1.08	51.05 ± 1.14	49.39 ± 1.10	47.67 ± 1.06
μ_{IH}	869.8 ± 1.63	800.2 ± 1.50	875.80 ± 1.54	852.9 ± 1.55
σ_{IH}	51.57 ± 1.15	47.30 ± 1.06	48.77 ± 1.09	49.03 ± 1.10
$z_{score}^{(NH)}$	$1.072\,\sigma$		$0.219\,\sigma$	
$z_{score}^{(IH)}$	$1.089\,\sigma$		$0.223\,\sigma$	

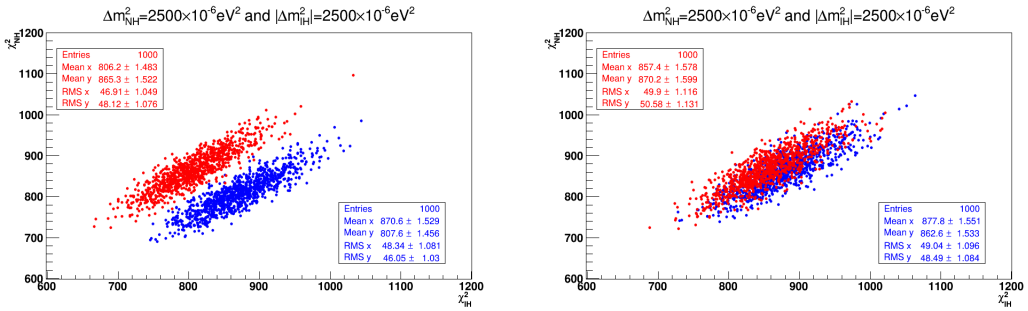

Figure 5.8: *Two islands of χ^2 for 1000 (NH) + 1000 (IH) toy JUNO-like simulations generated at $|\Delta m^2| = 2.500 \times 10^{-3}\text{eV}^2$ for NH hypothesis (blue island) and IH hypothesis (red island) with six years of exposure and the ten near reactor cores. An infinite energy resolution is assumed for left plot and 3% relative energy resolution for right plot. The experimental sensitivities under these terms are reported in Tab. 5.8.*

Table 5.8: *Two χ^2 distributions for 1000 (NH) + 1000 (IH) toy JUNO-like simulations generated at $|\Delta m^2| = 2.500 \times 10^{-3}\text{eV}^2$ for NH and IH hypotheses with six years of exposure and ten near reactor cores. The sensitivity is calculated using Eq. 5.10.*

	infinite		3%	
	NH	**IH**	**NH**	**IH**
μ_{NH}	807.6 ± 1.46	865.30 ± 1.52	862.60 ± 1.53	870.20 ± 1.60
σ_{NH}	46.05 ± 1.03	48.12 ± 1.08	48.49 ± 1.08	50.58 ± 1.13
μ_{IH}	870.60 ± 1.53	806.20 ± 1.48	877.80 ± 1.55	857.4 ± 1.58
σ_{IH}	48.34 ± 1.08	46.91 ± 1.05	49.04 ± 1.10	49.90 ± 1.12
$z_{score}^{(NH)}$	$0.916\,\sigma$		$0.204\,\sigma$	
$z_{score}^{(IH)}$	$0.910\,\sigma$		$0.200\,\sigma$	

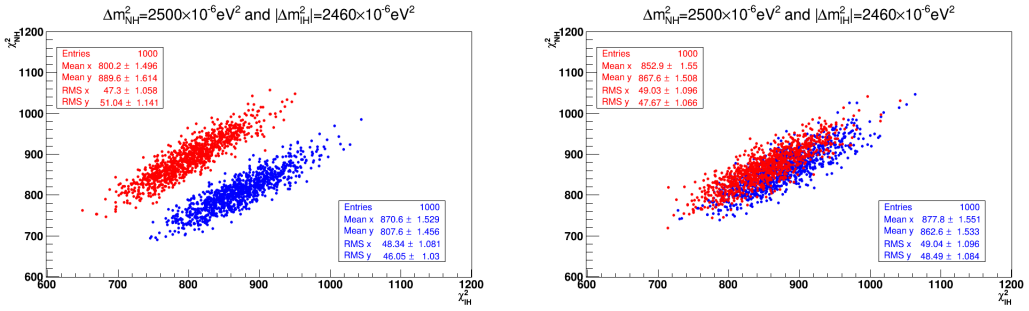

Figure 5.9: *Two islands of χ^2 for 1000 (NH) + 1000 (IH) toy JUNO-like simulations generated at $\Delta m^2 = 2.500 \times 10^{-3}\text{eV}^2$ for NH hypothesis (blue island) and $\Delta m^2 = -2.460 \times 10^{-3}\text{eV}^2$ for IH hypothesis (red island) with six years of exposure and the ten near reactor cores. An infinite energy resolution is assumed for left plot and 3% relative energy resolution for right plot. The experimental sensitivities under these terms are reported in Tab. 5.9.*

Table 5.9: *Two χ^2 distributions for 1000 (NH) + 1000 (IH) toy JUNO-like simulations generated at $\Delta m^2 = 2.500 \times 10^{-3}\text{eV}^2$ for NH hypothesis and $\Delta m^2 = -2.460 \times 10^{-3}\text{eV}^2$ for IH hypothesis with six years of exposure and ten near reactor cores. The sensitivity is calculated using Eq. 5.10.*

	infinite		3%	
	NH	**IH**	**NH**	**IH**
μ_{NH}	807.6 ± 1.46	889.6 ± 1.61	862.60 ± 1.53	867.6 ± 1.51
σ_{NH}	46.05 ± 1.03	51.05 ± 1.14	48.49 ± 1.08	47.67 ± 1.07
μ_{IH}	870.60 ± 1.53	800.2 ± 1.50	877.80 ± 1.55	852.90 ± 1.55
σ_{IH}	48.34 ± 1.08	47.30 ± 1.06	49.04 ± 1.08	49.03 ± 1.07
$z_{score}^{(NH)}$	$1.159\,\sigma$		$0.217\,\sigma$	
$z_{score}^{(IH)}$	$1.113\,\sigma$		$0.219\,\sigma$	

5.4 Robustness of the Standard Method

In statistics, the term robustness refers to the strength of a statistical model, tests, and procedures according to the specific conditions of the applied statistical analysis. Given

these conditions being met, the models can be verified to be true through the use of mathematical proofs.

However, many models are based upon ideal situations that do not exist when working with real-world data. As a result, the model may provide correct results even if the conditions are not met exactly.

Robust statistics, therefore, are any statistics that yield good performance when data is drawn from a wide range of probability distributions that are largely unaffected by outliers or small departures from model assumptions in a given data set. In other words, a robust statistic is resistant to "errors" in the results.

The main focus of the statistical analysis using the $\Delta\chi^2$ standard method is to calculate neutrino mass hierarchy determination sensitivity and none pay attention that the method may not establish its robustness. SubSec. 5.4.1 will discuss how the standard method using $\Delta\chi^2$ is not able to maintain the robustness while SubSec. 5.4.2 will discuss inability of the χ^2 to establish the robustness as a bi-dimensional estimator. This study is done for 20 different data values of the injection atmospheric neutrino mass in the range, $2.450 \times 10^{-3}\text{eV}^2 \leq |\Delta m^2|_{inj} \leq 2.580 \times 10^{-3}\text{eV}^2$.

5.4.1 The $|\overline{\Delta\chi^2}|$ oscillations with Δm^2_{inj}

There are trends in our data to confirm that the $|\overline{\Delta\chi^2}|$ varies with the atmospheric neutrino mass injected $|\Delta m^2|_{inj}$. We studied the relation between the $|\overline{\Delta\chi^2}|$ values and the value of the input parameter for 20 different values, $|\Delta m^2|_{inj}$ in the range, $2.450 \times 10^{-3}\text{eV}^2 \leq |\Delta m^2|_{inj} \leq 2.580 \times 10^{-3}\text{eV}^2$ and we computed the corresponding experimental sensitivity for the two cases with/without including the systematic uncertainties. Fig. 5.10 illustrates the variation of $|\overline{\Delta\chi^2}|$ as a function of the injected atmospheric neutrino mass $|\Delta m^2|_{inj}$, in the range of $2.450\times10^{-3}\text{eV}^2 \leq |\Delta m^2|_{inj} \leq 2.580\times10^{-3}\text{eV}^2$, assuming infinite energy resolution. Fig. 5.11 illustrates the variation of $\Delta\chi^2$ with the injected atmospheric neutrino mass $|\Delta m^2|_{inj}$, in the range of $2.450 \times 10^{-3}\text{eV}^2 \leq |\Delta m^2|_{inj} \leq 2.580 \times 10^{-3}\text{eV}^2$ when the 3% relative energy resolution is included. We performed additional data collection ignoring the systematic uncertainties in order to provide a strong evidence for the result. How the $|\overline{\Delta\chi^2}|$ oscillations with Δm^2_{inj} reflects on the neutrino mass hierarchy determination sensitivity depends on how the significance will be calculated, for example using Eq. 5.7 or Eq. 5.9.

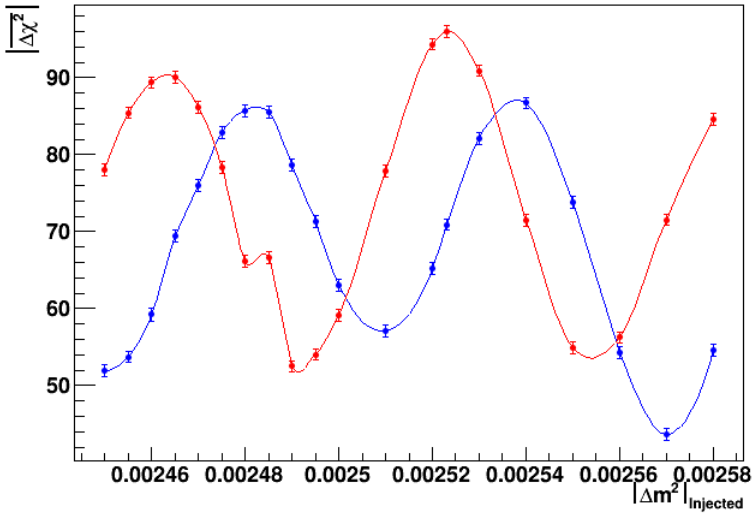

Figure 5.10: *$|\overline{\Delta\chi^2}|$ variation with $|\Delta m^2|_{inj}$ in the range of $2.450 \times 10^{-3}\text{eV}^2 \leq |\Delta m^2|_{inj} \leq 2.580 \times 10^{-3}\text{eV}^2$ for 1000 (NH) + 1000 (IH) toy JUNO-like simulations for each point of $|\Delta m^2|_{inj}$ with six years of exposure and the ten near reactor cores assuming an infinite energy resolution. The error bars correspond to the standard error of the $|\overline{\Delta\chi^2}|$ that is calculated as the standard deviation of the $\Delta\chi^2$ distribution divided by the square root of the sample size.*

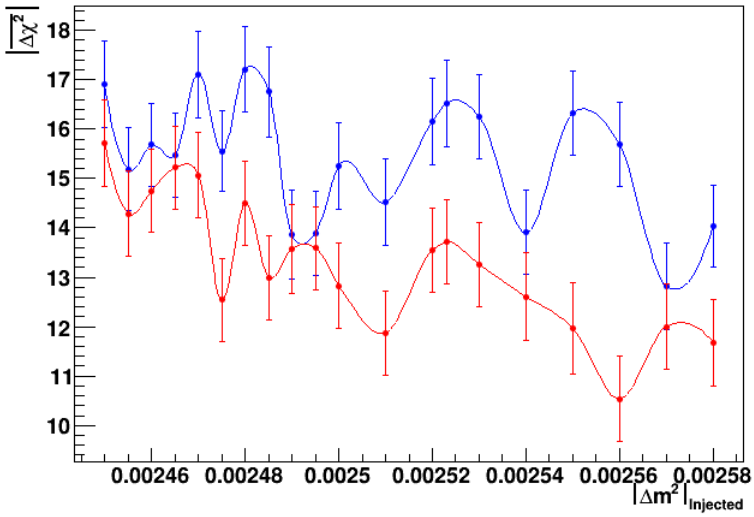

Figure 5.11: *$|\overline{\Delta\chi^2}|$ varies with $|\Delta m^2|_{inj}$ in the range of $2.450 \times 10^{-3}\text{eV}^2 \leq |\Delta m^2| \leq 2.580 \times 10^{-3}\text{eV}^2$ for 1000 (NH) + 1000 (IH) toy JUNO like simulations for each point of $|\Delta m^2|_{inj}$ with six years of exposure and the ten near reactor cores assuming 3% relative energy resolution. The error bars correspond to the standard error of the $|\overline{\Delta\chi^2}|$ that is calculated as the standard deviation of the $\Delta\chi^2$ distribution divided by the square root of the sample size.*

We can test the precision of the fit assuming infinite energy resolution drawing the relation of $|\overline{\Delta\chi^2}|$ and Δm^2_{rec} as indicated in Fig. 5.12. If the fit is able to find the true value of the reconstructed Δm^2_{rec}, the fit is accurate and we rely on it. The same test can be done assuming 3% relative energy resolution as done on Fig. 5.13.

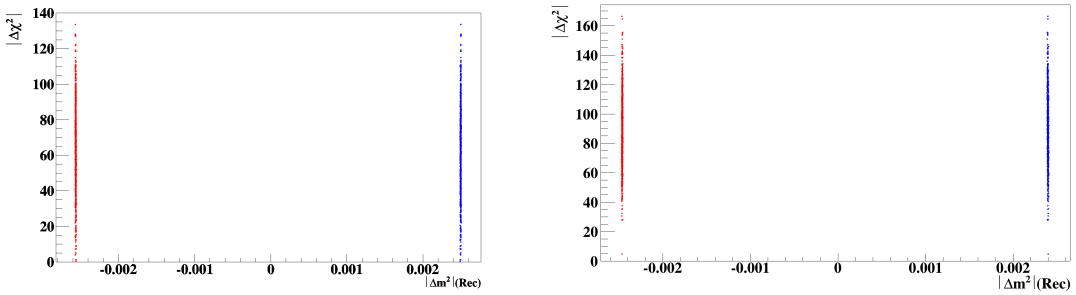

Figure 5.12: $|\overline{\Delta\chi^2}|$ *variation with* $|\Delta m^2|(rec)$ *in the range of* $2.450\times10^{-3}\mathrm{eV}^2 \leq |\Delta m^2|_{inj} \leq 2.580\times 10^{-3}\mathrm{eV}^2$ *for 1000 (NH) + 1000 (IH) toy JUNO-like simulations generated at* $\Delta m^2 = 2.500\times10^{-3}\mathrm{eV}^2$ *for NH hypothesis (left panel) and* $\Delta m^2 = -2.460\times10^{-3}\mathrm{eV}^2$ *for IH hypothesis (right panel) with six years of exposure and the ten near reactor cores assuming infinite energy resolution.*

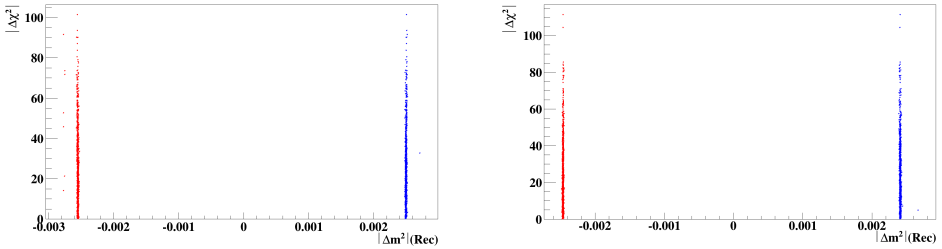

Figure 5.13: $|\Delta\chi^2|$ *variation with* $|\Delta m^2|(Rec)$ *in the range of* $2.450\times10^{-3}\mathrm{eV}^2 \leq |\Delta m^2| \leq 2.580\times 10^{-3}\mathrm{eV}^2$ *for 1000 (NH) + 1000 (IH) toy JUNO simulations generated at* $\Delta m^2 = 2.500\times10^{-3}\mathrm{eV}^2$ *for NH hypothesis (left panel) and* $\Delta m^2 = -2.460\times10^{-3}\mathrm{eV}^2$ *for IH hypothesis (right panel) with six years of exposure and the ten near reactor cores assuming* 3% *relative energy resolution.*

In case the approximation is not valid, the Z-test for 1D, Eq. 5.7, can be used to calculate the neutrino MH sensitivity. As was expected the variation of the estimator $|\overline{\Delta\chi^2}|$ will influence neutrino MH sensitivity. Fig. 5.14 confirms the influence on neutrino MH sensitivity in case that only the statistical uncertainties are included and the sensitivity varies from about $4.5\,\sigma$ to $7.5\,\sigma$. Fig. 5.15 confirms this influence in case that the systematic and statistical uncertainties are included and the sensitivity oscillates from about $0.9\,\sigma$ to $1.5\,\sigma$.

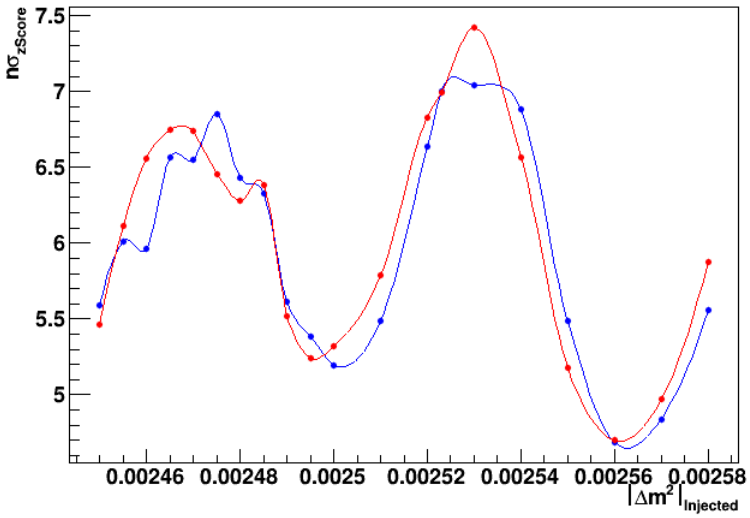

Figure 5.14: *The oscillation of significance with* $|\Delta m^2|_{inj}$ *in the range of* $2.450 \times 10^{-3}\text{eV}^2 \leq |\Delta m^2| \leq 2.580 \times 10^{-3}\text{eV}^2$ *for* 1000 *(NH) +* 1000 *(IH) JUNO-toy like simulations for one banchmark assuming an infinite energy resolution where blue line is for NH sample and red line is for IH sample. The sensitivity using the Eq. 5.7 varies from about* $4.5\,\sigma$ *to* $7.5\,\sigma$.

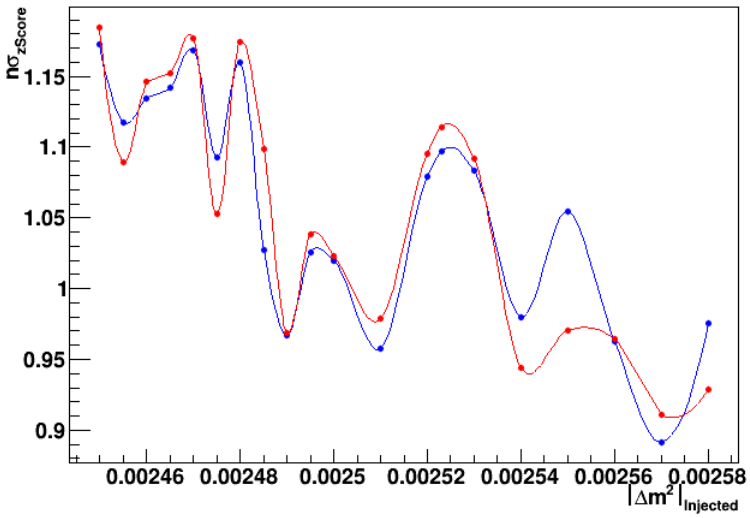

Figure 5.15: *The variation of significance with* $|\Delta m^2|_{inj}$ *in the range of* $2.450 \times 10^{-3}\text{eV}^2 \leq |\Delta m^2| \leq 2.580 \times 10^{-3}\text{eV}^2$ *for* 1000 *(NH) +* 1000 *(IH) JUNO-toy like simulations for one banchmark assuming* $3\%/\sqrt{E}$ *energy resolution where blue line is for NH sample and red line is for IH sample. The sensitivity using the Eq. 5.7 oscillates from about* $0.9\,\sigma$ *to* $1.5\,\sigma$.

Assuming the approximation of Eq. 5.8 is valid at infinite energy resolution, the neutrino mass hierarchy determination sensitivity is expected to have high variation with the input parameter as confirmed in Fig. 5.17. The sensitivity may vary from about $9.5\,\sigma$ to $7.5\,\sigma$.

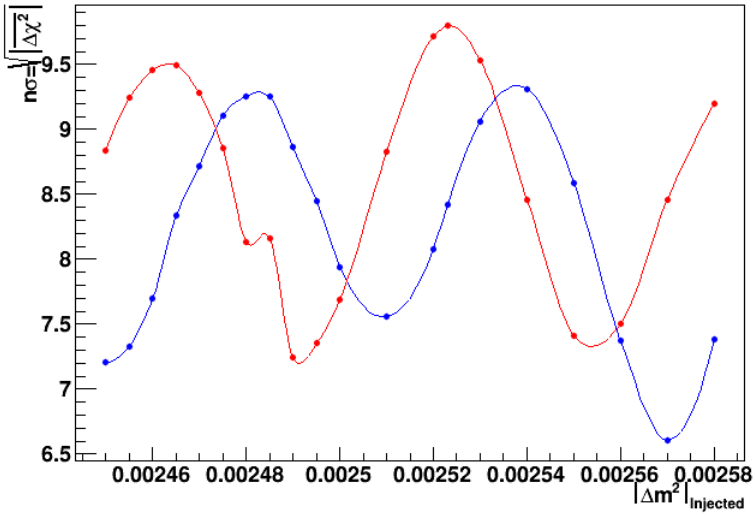

Figure 5.16: *The oscillation of significance with* $|\Delta m^2|_{inj}$ *in the range of* $2.450 \times 10^{-3}\text{eV}^2 \leq |\Delta m^2| \leq 2.580 \times 10^{-3}\text{eV}^2$ *for* 1000 *(NH) +* 1000 *(IH) JUNO-toy like simulations for one banchmark assuming an infinite energy resolution where blue line is for NH sample and red line is for IH sample. The sensitivity using the Eq. 5.9 varies from about* $6.5\,\sigma$ *to* $9.5\,\sigma$.

Assuming that the approximation Eq. 5.8 is still valid at 3% relative energy resolution, the neutrino mass hierarchy determination sensitivity is not robust as confirmed in Fig. 5.17. The sensitivity using the Eq. 5.9 varies from a maximum of $4.1\,\sigma$ to about $3.2\,\sigma$.

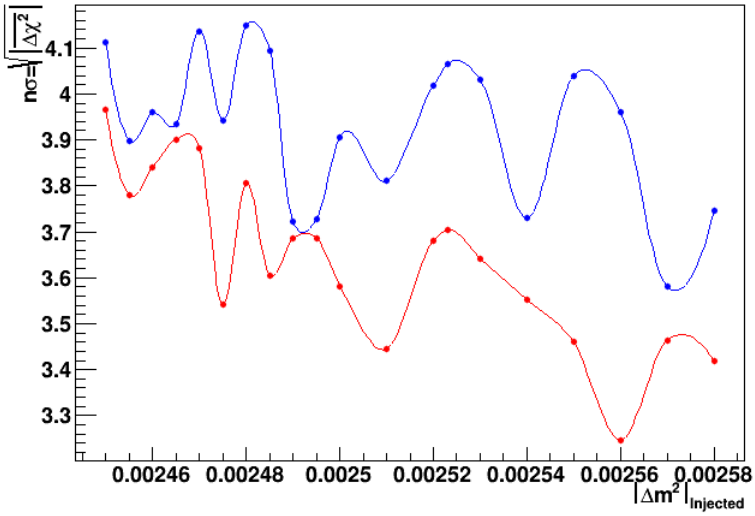

Figure 5.17: *The variation of significance with* $|\Delta m^2|_{inj}$ *in the range of* $2.450 \times 10^{-3}\text{eV}^2 \leq |\Delta m^2| \leq 2.580 \times 10^{-3}\text{eV}^2$ *for* 1000 *(NH) +* 1000 *(IH) JUNO-toy like simulations for one benchmark assuming* $3\%/\sqrt{E}$ *energy resolution where blue line is for NH sample and red line is for IH sample. The sensitivity using the Eq. 5.9 varies from about* $3.2\,\sigma$ *to* $4.1\,\sigma$.

5.4.2 The χ^2 Robustness

The significance using χ^2 as bi-dimensional distribution through Eq. 5.10 varies from $1.3\,\sigma$ to $0.9\,\sigma$ assuming an infinite energy resolution as shown in Fig. 5.18 and from $0.24\,\sigma$ to $0.18\,\sigma$ assuming 3% relative energy resolution, as shown in Fig. 5.19.

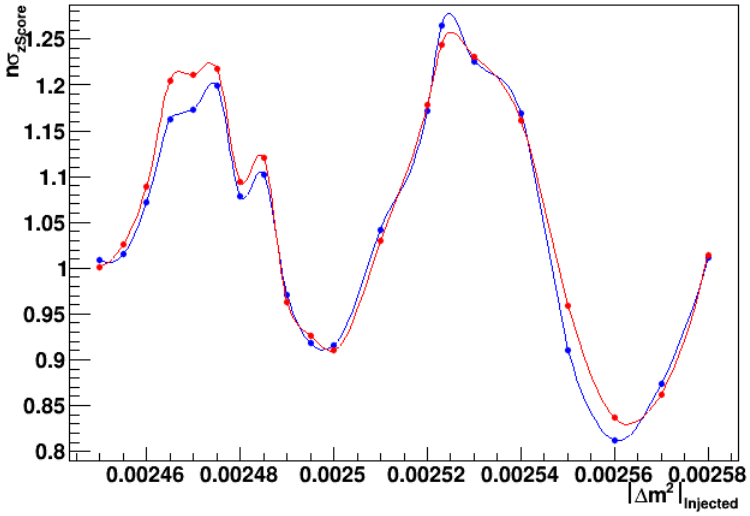

Figure 5.18: *The oscillation of significance using χ^2 as bi-dimensional distribution through Eq. 5.10 with $|\Delta m^2|_{inj}$ in the range of $2.450 \times 10^{-3}\mathrm{eV}^2 \leq |\Delta m^2|_{inj} \leq 2.580 \times 10^{-3}\mathrm{eV}^2$ for 1000 (NH) + 1000 (IH) JUNO-toy like simulations for one banchmark assuming an infinite energy resolution where blue line is for NH sample and red line is for IH sample. The significance varies from about $0.8\,\sigma$ to $1.3\,\sigma$.*

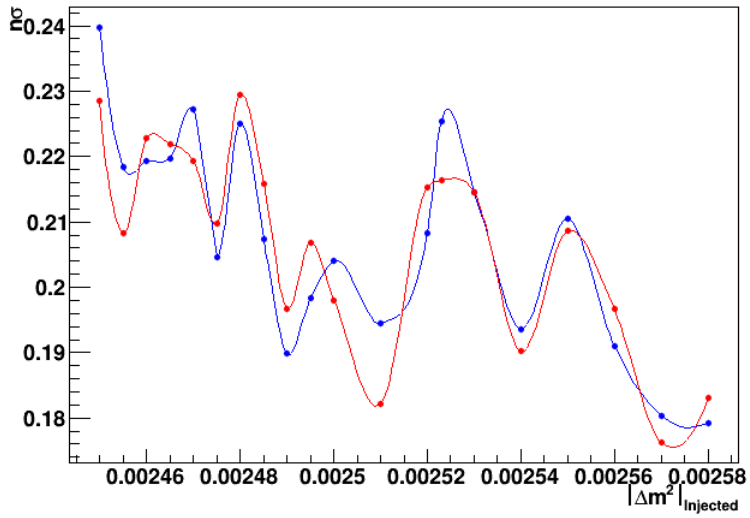

Figure 5.19: *The oscillation of the experimental significance using χ^2 as bi-dimensional distribution with $|\Delta m^2|_{inj}$ in the range of $2.450 \times 10^{-3}\mathrm{eV}^2 \leq |\Delta m^2|_{inj} \leq 2.580 \times 10^{-3}\mathrm{eV}^2$ for 1000 (NH) + 1000 (IH) JUNO-toy like simulations for one banchmark assuming an 3% relative energy resolution where blue line is for NH sample and red line is for IH sample. The significance using Eq. 5.10 varies from about $0.175\,\sigma$ to $0.24\,\sigma$.*

The oscillation of the experimental sensitivity with the value of the input parameter, the neutrino atmospheric mass difference ($|\Delta m^2|_{inj}$), implies that the standard method results have strong dependency on the input parameter value. Whatever the approximation is not valid or not, systematic uncertainties included or not, this dependence still hold.

CHAPTER 6

THE ALTERNATIVE METHOD $\vec{F}_{MO}$

The maximum separation between the heaviest mass eignstate of the neutrino and the lightest one is called Δm^2_{atm}. In this chapter, it is equivalent for the both orderings to

$$(\Delta m^2_{31})_{NH} \equiv |\Delta m^2_{32}|_{(IH)} = |\Delta m^2_{atm}|. \tag{6.1}$$

We recall the definition of the neutrino survival probability, Eq. 1.5,

$$\begin{aligned} p_{(\bar{\nu}_e \to \bar{\nu}_e)} = 1 \quad &- \quad \frac{1}{2}\sin^2 2\theta_{13}(1 - cos\frac{\Delta m^2_{atm} L}{2E}) \\ &- \quad \frac{1}{2}\cos^4\theta_{13}\sin^2 2\theta_{12}(1 - cos\frac{\delta m^2_{sol} L}{2E}) \\ &+ \quad \frac{1}{2}\sin^2 2\theta_{13}\left[\cos^2\left(\theta_{12} + \frac{\lambda\pi}{2}\right)\right](cos\frac{L}{2E}(\Delta m^2_{atm} - \delta m^2_{sol}) - cos\frac{L\Delta m^2_{atm}}{2E}). \end{aligned}$$

The neutrino survival probability distribution depends on a parameter λ, the parameter of interest. For λ equals to 0, the probability distribution follows IH model. For λ equals to 1, the probability distribution follows NH model.

Let develop the number of events N_i from the beginning. First, consider the independent events N_{obs} in the bin number i, $\{N_{obs}\}_i$, be governed by the probability density function $\pi(\{N_{obs}\}_i)$. With independent N_{obs}, one can regard the sample $\{N_{obs}\}_i$ as a cumulative sample with probability density

$$\pi(\{N_{obs}\}_i) = \prod_i \pi^i(N_{obs}).$$

The assumed probability $\pi^i(N_{obs})$ follows Poisson distribution,

$$\pi^i(N_{obs}) = \frac{\mu_i^{N_{obs}}}{N_{obs}!}e^{-\mu_i},$$

where μ_i is the expected number of events per energy bin i.

$$\mu_i(E) \sim \sigma_E \times \phi_E \times p_{\bar{\nu}_e \longrightarrow \bar{\nu}_e} \tag{6.2}$$

Then, the optimal weight is obtained using Eq. 4.35 as follows:

$$N\phi_{opt}(\{N_{obs}\}_i) = \frac{\partial \ln \pi(\{N_{obs}\}_i)}{\partial \lambda} = \sum_i \frac{\partial \ln \pi^i(N_{obs})}{\partial \lambda} = \sum_i \phi^i_{opt}(N_{obs}). \tag{6.3}$$

The $\phi^i_{opt}(N_{obs})$ as defined in Eq. 4.32 is given by:

$$\phi^i_{opt}(N_{obs}) = \frac{\partial ln\pi^i(N_{obs})}{\partial \lambda} = \frac{\partial}{\partial \lambda}\left(\ln \mu_i - \mu_i\right) = \left(\frac{\partial \ln \mu_i}{\partial \lambda}\right)\left(N_{obs} - \mu_i\right). \tag{6.4}$$

From the definition of the survival probability (Eq. 1.5) we obtain:

$$\frac{\partial \mu_i}{\partial \lambda} = \sigma_E \times \phi_E \times \frac{1}{2}\sin^2 2\theta_{13} \times \left(cos\frac{L}{2E}(\Delta m^2_{atm} - \delta m^2_{sol}) - cos\frac{L\Delta m^2_{atm}}{2E}\right) \times \frac{\pi}{2}\left[\cos^2\left(2\theta_{12} + \pi\lambda\right)\right]. \tag{6.5}$$

From Eq. 6.3 and Eq. 6.4, we define a new variable F_λ as

$$\begin{aligned}
F_\lambda &= \langle \phi(N_{obs}) \rangle_{exp} \\
&= N\phi_{opt}(\{N_{obs}\}_i) \\
&= \sum_i \phi^i_{opt}(N_{obs}) \\
&= \sum_i \left(\frac{\partial \ln \mu^\lambda_i}{\partial \lambda}\right)\left(N_{obs} - \mu^\lambda_i\right) \\
&= \sum_i \left[\begin{cases} +1, & in \quad I^+ \quad intervals \quad when \quad \mu^{NH}_i > \mu^{IH}_i \\ -1, & in \quad I^- \quad intervals \quad when \quad \mu^{NH}_i < \mu^{IH}_i \end{cases}\right]\left(N_{obs} - \mu^\lambda_i\right) \\
&= \sum_{i\epsilon I^+}\left(N_{obs} - \mu^\lambda_i\right) + \sum_{i\epsilon I^-}\left(\mu^\lambda_i - N_{obs}\right) \\
&= \sum_{i\epsilon I^+}\Delta^+_i + \sum_{i\epsilon I^-}\Delta^-_i
\end{aligned} \tag{6.6}$$

where

$$\begin{aligned}
\Delta^+_i &= (N_{obs} - \mu^\lambda_i) \quad in \quad I^+ \quad intervals \quad when \quad \mu^{NH}_i > \mu^{IH}_i \\
\Delta^-_i &= (\mu^\lambda_i - N_{obs}) \quad in \quad I^- \quad intervals \quad when \quad \mu^{IH}_i < \mu^{NH}_i
\end{aligned}$$

Simply speaking, Δ_i represents the difference between the observed number of events and the expected number of events in each single bin. For example, Δ^+_i is the difference between the observed number of events and the expected number of events in each single bin of type I^+. While Δ^-_i is the difference between the observed number of events and the expected number of events in each single bin of type I^-. Clearly, F_λ is based on the expectation that one of the two mass hierarchies produces more/less events than the opposite one in a definite energy interval. That is the source of the internal power of the F_λ according to Fig. 6.1 that manifests the variation of the difference between the expected number of events produced by IH model and the expected number of events produced by NH model, ΔN, for six years of JUNO-like data taking, within the energy intervals. The overall normalization is given by the supposed signal event rate of $60\,\mathrm{events/day}$, foreseen by JUNO with its predefined acceptance analysis procedure [1]. A total of 108357 signal events have been used in our simulation, corresponding to the ten reactor cores, each weighted by its baseline. The used global best fit values for the oscillation parameters are indicated in Tab. 6.1.

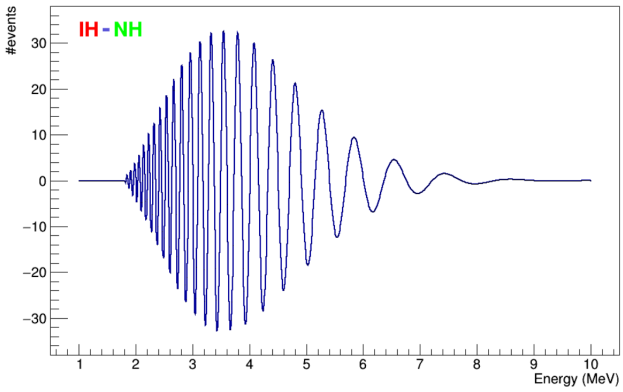

Figure 6.1: *Differential distribution of ΔN for six years of JUNO-like data taking, normalized as described in the text as a function of the $\overline{\nu}_e$ energy. The modulation is essentially due to Δm^2_{atm}.*

To conclude this section, the optimal weight proposed to solve the neutrino mass ordering using reactor spectrum is the difference in number of events per each single energy bin between the observed spectrum and the model. Since the neutrino mass ordering has two possible models, normal ordering model and inverted ordering model, the optimal weight has two dimensions as well. The component along X axis is F_{IH} and the component along Y axis is F_{NH}. Then, the bi-dimensional $F_{MO} = (F_{IH}, F_{NH})$ is mathematically represented as

$$\vec{F}_{MO} = F_{IH}\,\hat{e}_x + F_{NH}\,\hat{e}_y. \tag{6.7}$$

To confirm the bi-dimensional of the optimal weight of the neutrino mass ordering problem using reactor spectrum, the energy intervals are classified into two groups I^+ and I^-. For every group of energy intervals, Δ_i should be calculated for the two components of $\vec{F}_{MO}$.

Table 6.1: *The used best-fit values for the oscillation parameters, as indicated in [63].*

	best-fit	1σ region
$Sin^2\theta_{12}$	0.2970	± 0.017
$Sin^2\theta_{13}$	0.02150	± 0.0007
δm^2_{sol}	7.37e-5	0.16×10^{-5}
$\Delta m^2_{31}(NH)$	2.562e-3	$(-3.0 + 4.3) \times 10^{-5}$
$\Delta m^2_{32}(IH)$	2.545e-3	$(-3.2 + 3.4) \times 10^{-5}$

6.1 The $\vec{F}_{MO}$ Computation

As described in Ch. 1, the survival probability, assuming normal model, is

$$\begin{aligned} P_{NH} = 1 &- \frac{1}{2}\sin^2 2\theta_{13}(1 - cos\frac{\Delta m^2_{atm} L}{2E}) \\ &- \frac{1}{2}\cos^4\theta_{13}\sin^2 2\theta_{12}(1 - cos\frac{\delta m^2_{sol} L}{2E}) \\ &+ \frac{1}{2}\sin^2 2\theta_{13}\left[\cos^2\left(\theta_{12} + \frac{\pi}{2}\right)\right](cos\frac{L}{2E}(\Delta m^2_{atm} - \delta m^2_{sol}) - cos\frac{L\Delta m^2_{atm}}{2E}) \end{aligned} \tag{6.8}$$

and the survival probability assuming inverted model is

$$\begin{aligned} P_{IH} &= 1 - \frac{1}{2}\sin^2 2\theta_{13}(1 - cos\frac{\Delta m^2_{atm}L}{2E}) \\ &- \frac{1}{2}\cos^4\theta_{13}\sin^2 2\theta_{12}(1 - cos\frac{\delta m^2_{sol}L}{2E}) \\ &+ \frac{1}{2}\sin^2 2\theta_{13}\left[\cos^2(\theta_{12})\right](cos\frac{L}{2E}(\Delta m^2_{atm} - \delta m^2_{sol}) - cos\frac{L\Delta m^2_{atm}}{2E}). \end{aligned} \tag{6.9}$$

The only difference between P_{NH} and P_{IH} is a coefficient of the last terms, being either $\sin^2\theta_{12}$ or $\cos^2\theta_{12}$ for NH and IH, respectively. Then:

$$\Delta p_{IH-NH} = \sin^2 2\theta_{13} \times \cos(2\theta_{12}) \times \sin(\frac{\delta m^2 L}{4E}) \times \sin(\frac{(\Delta m^2_{atm} - \delta m^2_{sol}/2)L}{2E}). \tag{6.10}$$

And:

$$\begin{aligned} \Delta N(E) &= (\frac{dN}{dE})_{IH} - (\frac{dN}{dE})_{NH} \\ &= T \times \sigma_{IBD} \times \phi \times \Delta p_{IH-NH} \\ &= T \times \sigma_{IBD} \times \phi \times \sin^2 2\theta_{13} \times \cos(2\theta_{12}) \times \sin(\frac{\delta m^2 L}{4E}) \times \sin(\frac{(\Delta m^2_{atm} - \delta m^2_{sol}/2)L}{2E}) \end{aligned} \tag{6.11}$$

The first component F_{IH} is at $\lambda \to 0$, and the second F_{NH} is at $\lambda \to 1$. In our data sets, $\vec{F}_{MO}$ is computed for energy intervals with $10\,\mathrm{KeV}$ energy width. As the intervals are continuous, the summation turns to integration, and Eq. 6.6 becomes:

$$F_\lambda = \int_{1.8}^{8.0} |\Delta N(E)| dE, \tag{6.12}$$

$$\begin{aligned} F_\lambda = &\int_{1.8}^{8.0} \Delta^+(E)dE \quad in \quad I^+ \quad when \quad \mu^{NH}(E) > \mu^{IH}(E) \\ + &\int_{1.8}^{8.0} \Delta^-(E)dE \quad in \quad I^- \quad when \quad \mu^{NH}(E) < \mu^{IH}(E) \end{aligned} \tag{6.13}$$

To help in the understanding the $\vec{F}_{MO}$ computation, we provided the carton (Fig. 6.2). As indicated in Eq. 6.7, $\vec{F}_{MO}$ has two components (F_{IH}, F_{NH}) for each hierarchy of the two neutrino mass hierarchies and they are computed as;

$$\begin{aligned} F_{IH} = &\int_{1.8}^{8.0} |N_{obs}(E) - \mu^{IH}(E)| dE \quad in \quad I^+ \quad when \quad N^{NH}(E) > \mu^{IH}(E) \\ + &\int_{1.8}^{8.0} |\mu^{IH}(E) - N_{obs}(E)| dE \quad in \quad I^- \quad when \quad N^{NH}(E) < \mu^{IH}(E) \end{aligned} \tag{6.14}$$

$$\begin{aligned} F_{NH} = &\int_{1.8}^{8.0} |N_{obs}(E) - \mu^{NH}(E)| dE \quad in \quad I^- \quad when \quad N^{IH}(E) > \mu^{NH}(E) \\ + &\int_{1.8}^{8.0} |\mu^{NH}(E) - N_{obs}(E)| dE \quad in \quad I^+ \quad when \quad N^{IH}(E) < \mu^{NH}(E) \end{aligned} \tag{6.15}$$

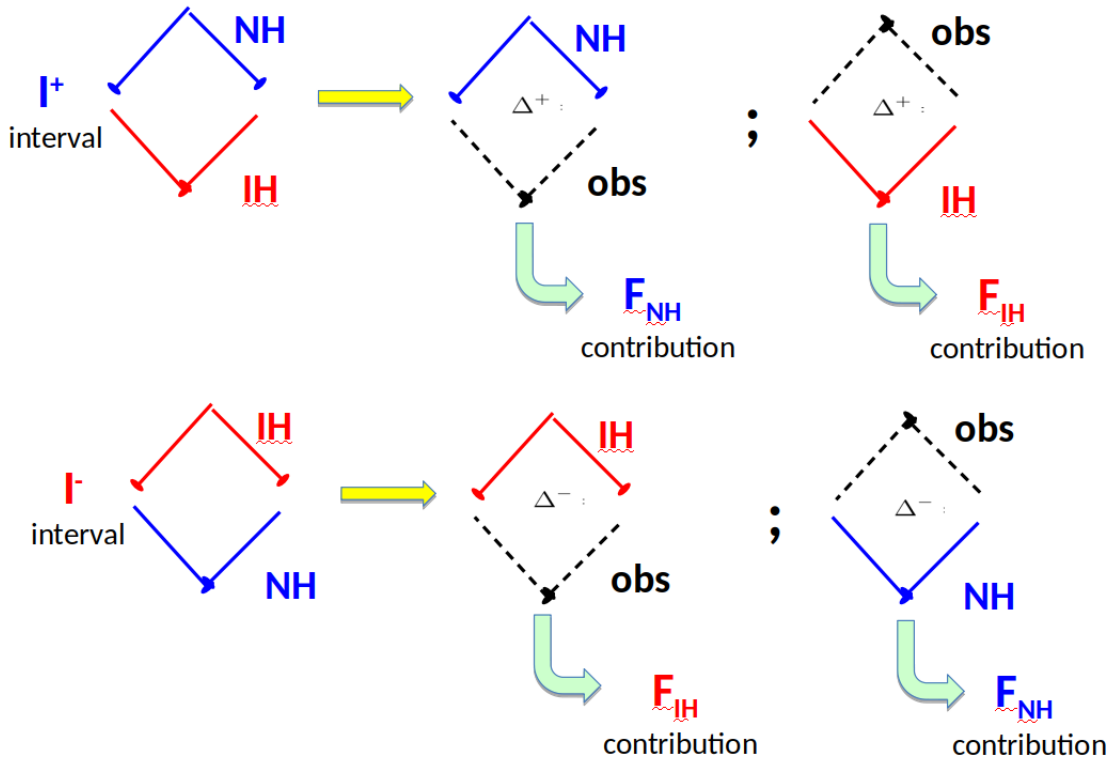

Figure 6.2: *The carton describes the $\vec{F}_{MO}$ computation.*

When the statistical fluctuations and systematic uncertainties are not included, $F_{\lambda}^{true} \approx 0$, as theoretically confirmed in Eq. 4.33, and $F_{\lambda}^{wrong} \sim 6500$ for for six years of JUNO-like data taking, normalized to 108357 signal events corresponding to the ten reactor cores, each weighted by its baseline (Fig. 6.3). The used best-fit values for the oscillation parameters are indicated in Tab. 6.1.

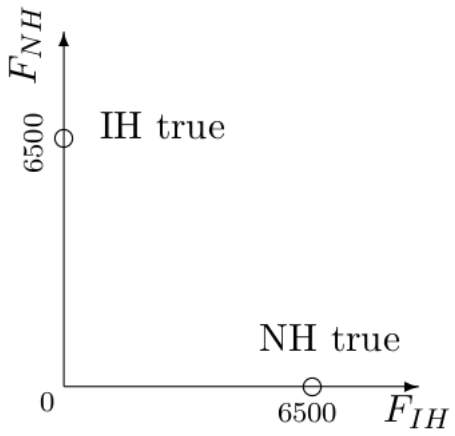

Figure 6.3: *The carton describes $2D$ $\vec{F}_{MO}$ (not to scale) for six years of data taking in a JUNO-like experiment. Oscillation parameters, reactor power, baseline and normalization to JUNO-like event selection have been chosen as described in the text [63].*

When the statistical fluctuations are included, Fig. 6.3 turns to Fig. 6.4: the single values of F_{λ}^{true} and F_{λ}^{wrong} get distributed. Given the $\vec{F}_{MO}$ definition (Eq. 6.7), the distributions are expected to be centered at larger values than the ideal one[1]. Even the true hierarchy choice (ideally, $F_{\lambda}^{true} = 0$) gets a certain positive amount when fluctuations are taken into account. On average, the F_{λ}^{true} is around 3300 counts for the true case and around 8000 counts for F_{λ}^{wrong} one (Fig. 6.4).

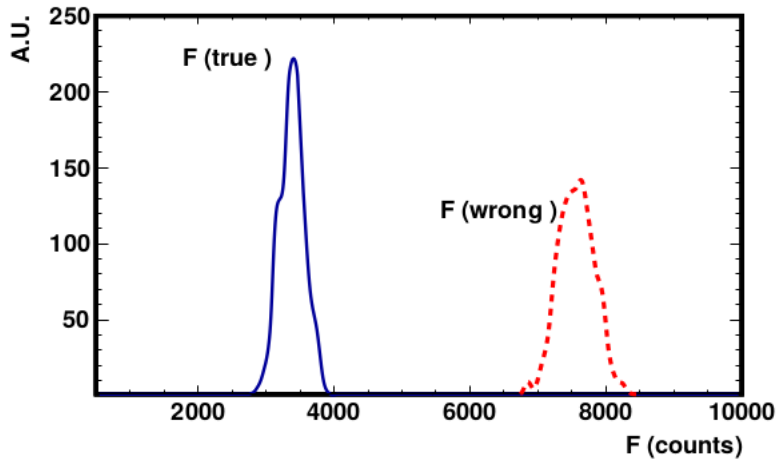

Figure 6.4: *(color online) F_{NH}^{true} (left) and F_{IH}^{wrong} (right) for 1000 JUNO-like toy experiments, assuming NH and an infinite energy resolution. The two distributions show the effect due to the statistical fluctuations in the collected number of events. Oscillation parameters and the other variables are chosen as described in the text, for a JUNO-like experiment six years long. The ten reactor cores of the Yangjiang and Taishan sites have been taking into account.*

Fig. 6.5 reports the bi-dimensional estimator $\vec{F}_{MO}$ for both hierarchies including the statistical fluctuations only. The blue 2D distribution (blue island) represents $\vec{F}_{MO}$ in case the true hierarchy is the normal hierarchy and the red 2D distribution (red island) represents $\vec{F}_{MO}$ in case the true hierarchy is the inverted one. The distributions correspond to the statistical fluctuations of 1000 toys JUNO-like experiment, with six years of exposure and the ten near reactor cores, each with its own baseline.

[1]We did not discard the fast modulation region of ΔN between $1.8 - 3.0$ because that may reduce the significance [63].

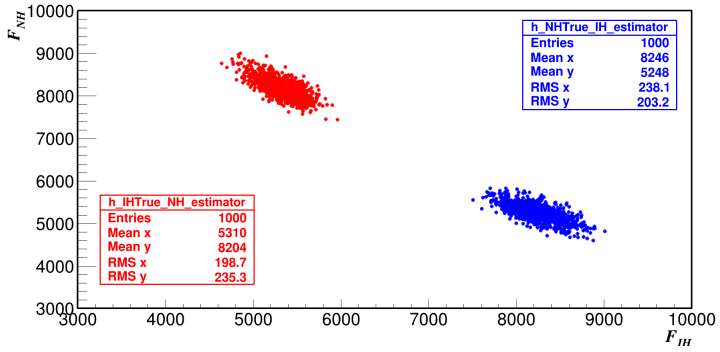

Figure 6.5: *(color online) F_{NH} vs F_{IH} distributions for 1000 (NH) + 1000 (IH) toys JUNO-like experiment, with six years of exposure and the ten near reactor cores, each with its own baseline. The "island" top-left (blue) corresponds to the IH simulation, while the one on the bottom-right (red) corresponds to the NH simulation. An infinite energy resolution is assumed. Note the asymmetric position of NH and IH domains, due to the non symmetric behavior of NH and IH in the oscillation model.*

When the statistical fluctuations and systematic uncertainties are included, the bi-Gaussian fits of $\vec{F}_{MO}$ for JUNO-like for different energy resolutions are drawn in Fig. 6.6, for six years of JUNO-like data taking, normalized to 108357 signal events corresponding to the ten reactor cores, each weighted by its baseline. The used best-fit values for the oscillation parameters are indicated in Tab. 6.1.

If one assumes that the inverted hierarchy is the null hypothesis H_0 and the normal hierarchy is the alternative hypothesis H_1, the *p*-value computation provides the sensitivity of how much the two hypotheses can be distinguished assuming the the null hypothesis be true. For example, $p_{val}(IH)$ corresponds to how much two the hypotheses can be distinguished assuming IH hypothesis be the true hierarchy[2]. The experimental sensitivity can be calculated using *p*-value method for bi-dimensional estimator as described in Appendix B.

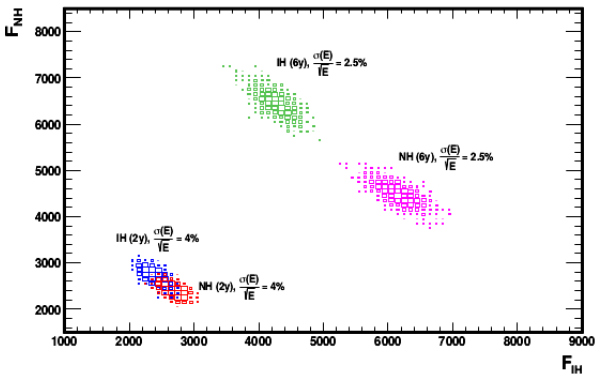

Figure 6.6: *(color online) F_{NH} vs F_{IH} distributions for 1000 (NH) + 1000 (IH) toys JUNO-like experiment, in two different configurations: the most favorable, six years of exposure with a $2.5\%/E$ energy resolution, against a short one for two years of exposure and $4\%/E$.*

[2] $p_{val}(NH)$ corresponds to how much the two hypotheses can be distinguished assuming NH hypothesis be the true hierarchy.

6.2 The $\vec{F}_{MO}$ Coupling

$\vec{F}_{MO}$, that couples NH/IH, gets a fast modulation in energy due to the last factor in Eq. 6.11, all the other factors showing a slow variation in energy. The thermal power, the flux and the cross-section are factorized out. Actually, $\vec{F}_{MO}$ is affected by the baseline L, the atmospheric and the solar masses. For δm^2_{sol}, the modulation is very smooth because the first minimum for a generic baseline of $50\,\mathrm{km}$ and the current value of δm^2_{sol} occurs around $1\,\mathrm{MeV}$, its fast modulation being below the $1.8\,\mathrm{MeV}$ cutoff. Mainly, the intervals are constrains by two variables; the atmospheric mass Δm^2_{atm} as indicated in SubSec. 6.2.1 and baseline L as indicated in SubSec. 6.2.3 while the other parameters act like scaling factors or with a smooth dependence. The current uncertainty on Δm^2_{atm} corresponds to about half δm^2_{sol}. All that is responsible for a variable discrimination level of NH/IH. These modulations are essentially driven by Δm^2_{atm}.

6.2.1 The Atmospheric Mass Δm^2_{atm}

When a scan is performed, both components of $\vec{F}_{MO}$ are indicating the same value of Δm^2_{atm}, contrary to χ^2 that provides us with two different values of Δm^2_{atm} for their two components. Since a fitting process is performed in the standard method, the best fit values (χ^2_{min}) are selected for each of the two hypotheses. $\vec{F}_{MO}$ dependence on Δm^2_{atm}enters in the definition of $I^{\pm}$ intervals. Suppose that we used a wrong $\Delta m^2_{atm}$for energy interval construction, $\vec{F}_{MO}$ would be easily affected. Any difference between the true value of $\Delta m^2_{atm}$and any wrong value of Δm^2_{atm}decreases (increases) the $\vec{F}_{MO}$ value of the wrong (true) hypothesis. As indicated in Fig. 6.7, the two components of the bi-dimensional estimator that are $F^{wrong}_{\lambda} \sim 6500$ and $F^{true}_{\lambda} \sim 0$ neglecting the statistical fluctuations and systematic uncertainties for six years of JUNO-like data taking, normalized to 108357 signal events corresponding to a baseline $= 52.5\,\mathrm{km}$ and a true $\Delta m^2_{atm} = 0.002\,56\,\mathrm{eV}^2$, will vary as a function of Δm^2_{atm}. At the true value of the Δm^2_{atm}, F^{wrong}_{λ} has the maximum value and F^{true}_{λ} has the minimum value. Contrary to the standard algorithm that collects two minimum values for its two components ($\chi^2_{min(IH)}, \chi^2_{min(NH)}$), the $\vec{F}_{MO}$ manifests its ability to collect the minimum counts when it picks up the true value of Δm^2_{atm} through its component $F^{true}_{\lambda} = F^{minimum}_{\lambda}$ and to collect the maximum counts through its other component $F^{wrong}_{\lambda} = F^{maximum}_{\lambda}$. Fig. 6.8 confirms the high performance of the $\vec{F}_{MO}$ in case the 3% relative energy resolution and the statistical fluctuations are included.

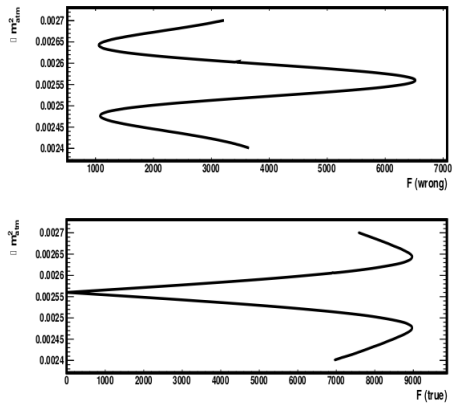

Figure 6.7: *(color online) Variation of the two components of $\vec{F}_{MO}$ for the wrong (true) hypothesis on the top (bottom) plot as function of the chosen Δm^2_{atm}, for a specific true Δm^2_{atm} and MO. A baseline of L= $52.5\,\mathrm{km}$ and a true Δm^2_{atm}= $0.002\,56\,\mathrm{eV}^2$ for the NH case have been selected, all the other parameters being fixed as described in the text to match six years of JUNO-like data taking. Note that going from F_{max} to F_{min} or vice-versa corresponds to changing Δm^2_{atm} of a δm^2_{sol} amount. The non-symmetric behavior of $\vec{F}_{MO}(true)$ and $F_{MO}(wrong)$ is due to the initial choice of the model that constraints the $I^{\pm}$ intervals.*

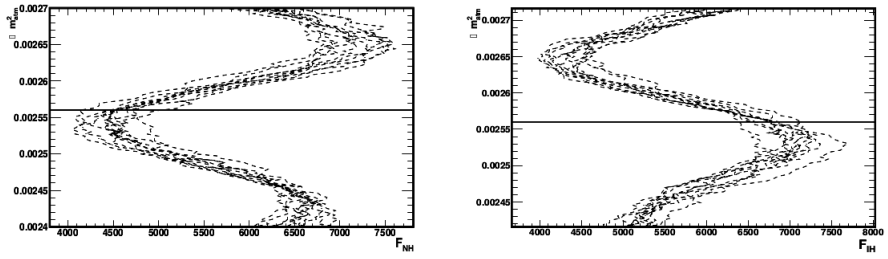

Figure 6.8: *(color online) $\vec{F}_{MO}$ modulations due to the differences between the "true" Δm^2_{atm} (NH) and the assumed one for ten JUNO-like toy experiments, including a $3\%/\sqrt{E}$ energy resolution and the real distribution of the baselines ($\pm 5\,\mathrm{m}$) of the ten reactor cores in Yangjiang and Taishan sites. On the left plot the dashed lines correspond to F_{NH}, whereas F_{IH} modulations are shown in the right plot. The horizontal lines correspond to the "true" Δm^2_{atm}. The observed bias is due to the finite energy resolution, as explained in the text.*

Fig. 6.9 reports $F(wrong)$ for a wide range of Δm^2_{31} vs Δm^2_{23}. The ciclic behaviour corresponds to the degeneracy $\Delta m^2_{31}(NH) = \Delta m^2_{23}(IH) \pm \delta^2 m_{sol}$. $F(wrong)$ is quite stable for different choices of the assumed Δm^2_{atm} (i.e. along the bisector on Fig. 4), with a dispersion of about 0.02%.

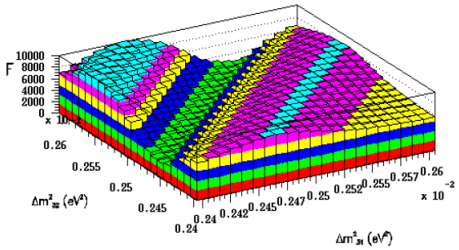

Figure 6.9: *(color online) Variation of $F(wrong)$ for $\Delta m^2_{31}(NH)$ vs $\Delta m^2_{23}(IH)$. Oscillation parameters and the other variables are chosen as described in the text, for a JUNO-like experiment and a six years exposure.*

6.2.2 The Degeneracy Effect

For each neutrino mass ordering case two full cycles are observed with maximum amplitude. Noticeably, there is an absolute minimum for each hypothesis. The two ordering can be discriminated when Δm^2_{atm} varies less than 12×10^{-5} eV^2. That corresponds to the distance between a peak and the valley, or, equivalently, the distance between the two absolute minima of NH and IH. The dispersions of the single minimum is less than 10^{-5} eV^2. Fig. 6.10 illuminates the separation of Δm^2_{atm}(true) with the degenerated one. $\vec{F}_{MO}$ holds a Δm^2_{atm}degeneracy at the level of 12×10^{-5} eV^2, which is much larger than the current global fits uncertainty. However, we argued that the new technique here outlined bears in itself a mean to resolve such ambiguity, allowing to measure Δm^2_{atm} with an unprecedented precision at reactors, less than 1%. That is due to the strong correlation of $\vec{F}_{MO}$ to Δm^2_{atm}, which will deserve more refined analyses and promise even more interesting results.

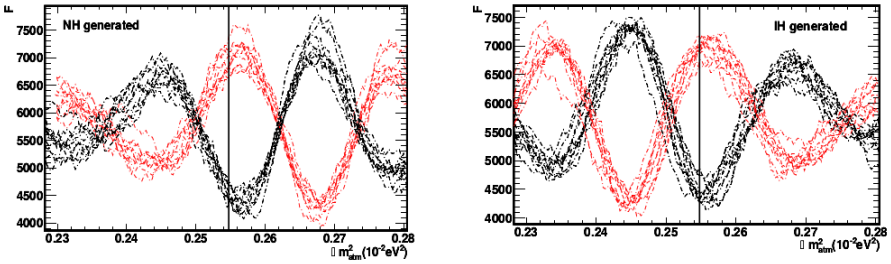

Figure 6.10: *(color online) $\vec{F}_{MO}$ vs $\Delta m^2_{atm}$for ten generated JUNO-like toy experiments, in the NH (right) and the IH (left) hypotheses. The black (red) curves correspond to the analysis when the true (false) hypothesis is taken. The vertical lines indicate the selected Δm^2_{atm}. The experimental conditions are the same as in text.*

There is a degeneracy between Δm^2_{atm} and $\vec{F}_{MO}$ i.e. for the correct Δm^2_{atm}we should have one minima but actually we have two: that creates the degeneracy. For a single reconstructed Δm^2_{atm} two solutions can be identified. For example, when $\vec{F}_{MO}$ identifies $\Delta m^2_{atm}(recons) = 2.50 \times 10^{-3}$eV^2 there are two solutions: $\Delta m^2_{atm} = 2.50 \times 10^{-3} \pm 0.1 \times 10^{-4}$eV^2 for NH and $\Delta m^2_{atm} = 2.62 \times 10^{-3} \pm 0.1 \times 10^{-4}$eV^2 for IH. Due to this intrinsic degeneracy it is not possible to have a single solution if only one experiment is taken into account. Information about Δm^2_{atm} should be injected from external, like e.g. a global fit

analysis, to definitively select between the two solutions. The final result depends on the knowledge about Δm^2_{atm} from other neutrino oscillation experiments, although it is not so stringent because the two solutions are $12 \times 10^{-5}\text{eV}^2$ far away.

The bottom line is that if one is just interested in the discrimination between the two degenerate solutions, by taking into account the external Δm^2_{atm} uncertainty a standard sensitivity around $4\,\sigma$ is roughly obtained. For example a 1% uncertainty on Δm^2_{atm} corresponds to a $\sim 4.5\,\sigma$ significance, computed from the difference of the two $\vec{F}_{MO}$ solutions, which are far away 12×10^{-5} eV^2. This applies to any kind of Δm^2_{atm}, either input or reconstructed.

This conclusion applies either to the parameterization used in this chapter or to the Δm^2_{ee} one. Suppose that $\Delta m^2_{atm} = 2.50 \times 10^{-3}\text{eV}^2$ and NH be the true values. If the external measurement $\Delta m^2_{atm} = 2.50 \times 10^{-3}\text{eV}^2 \pm 2.5 \times 10^{-5}\text{eV}^2$ is available, in the $\vec{F}_{MO}$ framework one obtains $\chi^2_{NH}(min) = 0$ with $\Delta m^2_{atm}(NH) = 2.50 \times 10^{-3}\text{eV}^2$ and $\chi^2_{IH}(min) \sim 16$ with $\Delta m^2_{atm}(IH) \sim 2.62 \times 10^{-3}\text{eV}^2$. The $\Delta\chi^2$ would give the usual sensitivity. That is almost equivalent to compute the χ^2 of the two ordering cases at the same $\Delta m^2_{atm}(recons)$ including its uncertainty. In other words, $\Delta\chi^2$ is equivalent to the $\chi^2_{MO-false}(min)$ of the wrong hypothesis at $\Delta m^2_{atm}(true)$. We argue that is the asymptotic trend of the χ^2 procedure at a JUNO-like experiment.

Only a procedure that internally estimates Δm^2_{atm} would be able to achieve much higher sensitivities on the NH/IH discrimination. Repeating the same computation, if 10^{-5}eV^2 is taken for Δm^2_{atm} uncertainty, $\sim 8.5\,\sigma$ are reachable. However, this procedure is very rough since it does not include treatments of systematic error and backgrounds. That is the reason the $2D$ approach has been used in the main text. It is surely more robust and complete, even though more conservative.

6.2.3 The baseline L

$\vec{F}_{MO}$ is in principle very sensitive to the baseline L. F_{NH} shows a degeneracy with F_{IH} when it is computed using an L different from the right one ($\pm 1.5\,\text{km}$). In the JUNO experiment there are several reactors with a baseline difference up to $0.64\,\text{km}$ Tab. 3.1. Therefore, it is mandatory to properly handle the baseline composition of the event sample. The most straightforward way is to weight the sub-samples with the thermal power of each single reactor core. The procedure is acceptable as far as $\vec{F}_{MO}$ is stable under different choices of L, as demonstrated in Fig. 6.11. When the exact baseline of each core is taken into account and properly weighted to its power, F^{wrong}_{λ} drops from 6503 to 5918, due to the slight negative interference between the different reactor-baselines. Taking into account the whole set of the ten reactor cores a global 0.3% variation is obtained on F^{wrong}_{λ}. A uniform $\pm 5\,\text{m}$ dispersion has also been added to the baseline of each core. The net result is totally negligible corresponding to about a factor 10 smaller effect (0.03%).

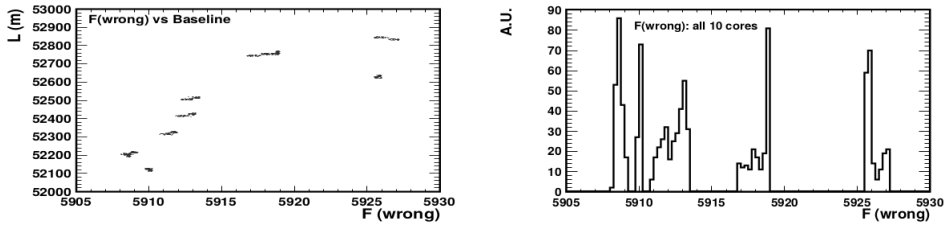

Figure 6.11: *(color online) Variation of F_{MO}(wrong) due to different baselines' cores. The 10 baselines correspond to the 10 reactor cores of the Yangjiang and Taishan sites. A uniform ± 5 m dispersion for the baseline of each core have been included in the computation. Oscillation parameters and the other variables are chosen as described in the text, for a JUNO-like experiment six years long.*

The performances of $\vec{F}_{MO}$ have been evaluated for baselines from $10\,\mathrm{km}$ to $90\,\mathrm{km}$ for a JUNO-like experiment with $3\%/\sqrt{E}$ energy resolution. Results are shown in Fig. 6.12. At baselines smaller than $50\,\mathrm{km}$ the dispersion of the minima are very large. Therefore, the bands of Fig. 6.15 become four times wider, forbidding the use of $\vec{F}_{MO}$ due to the unbroken degeneracy with Δm^2_{atm}. At baselines larger than $60\,\mathrm{km}$ the NH/IH patterns loose accuracy and tend to overlap each other (the interference effect between Δm^2_{31} and Δm^2_{32} is vanishing). In the latter case the sensitivity decreases, up to disappear at $80 - 90\,\mathrm{km}$.

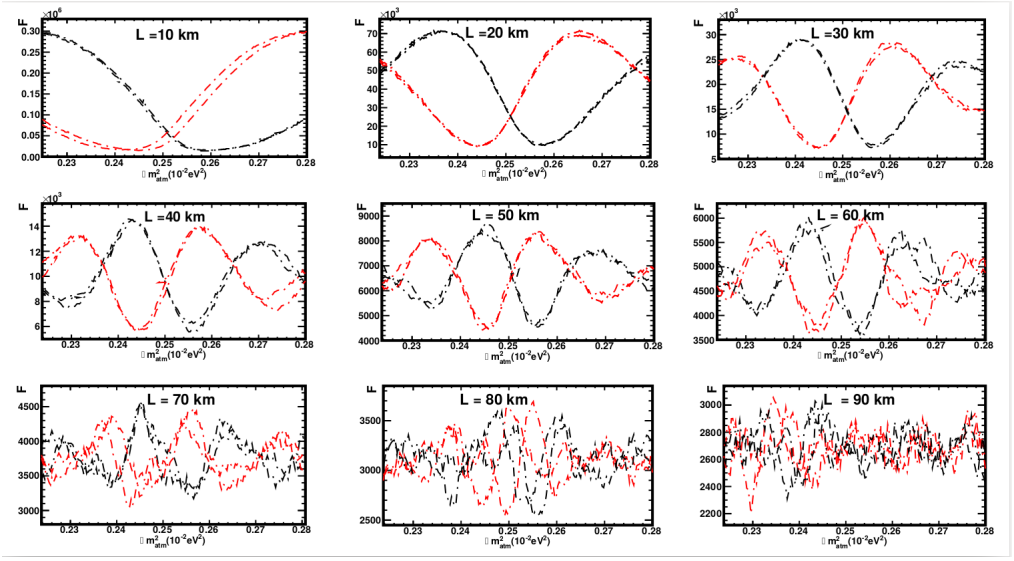

Figure 6.12: *(color online) F_{MO} vs Δm^2_{atm} for a couple of generated JUNO-like toy experiments, in the IH hypothesis. The black (red) curves correspond to the analysis when the true (false) hypothesis is taken. The experimental configuration is the same as in Fig. 6.8. Different baselines have been considered, as indicated in each plot.*

Even if the analysis is only sketched out, we would any how conclude that only the combined effect of a small uncertainty on Δm^2_{atm} as extracted by the $\vec{F}_{MO}$ procedure and the observed patterns for a specific experiment configuration, would allow us to obtain the quoted sensitivities larger than $5\,\sigma$. Such combination is only possible for a medium baseline reactor experiment with a baseline around $50\,\mathrm{km}$.

6.3 The Robustness of $\vec{F}_{MO}$

The $\vec{F}_{MO}$ shows a direct dependence behavior with the neutrino atmospheric mass manifesting in Fig. 6.13 that shows the separation distance between the two components is maintained along the range. As can be inferred from Fig. 6.13 computing that sensitivity is technically equivalent to use the same Δm^2_{atm} value for both hypotheses. In Fig. 6.13 the 68% and 95% C.L. contours of the current Δm^2_{atm} uncertainty are drawn. It seems reasonable to assume that only one solution be selected by F_{MO}, at 95% C.L. and for the current Δm^2_{atm} uncertainty. The sensitivity computed in this chapter corresponds to the probability to discriminate between NH/IH when only one solution is admitted. The quoted sensitivity owns a slightly different meaning from the standard one, which instead gives the probability to distinguish NH/IH in the whole parameter space. Since the $\vec{F}_{MO}$ technique identifies two solutions, one for NH and one for IH, each one at a different Δm^2_{atm}, with less than a 0.5% uncertainty, our sensitivity corresponds to the probability to misidentify the two solutions at their own Δm^2_{atm}. The patterns are consistently reproduced across the whole range of Δm^2_{atm}: defining $\Delta m^2_{atm}(recons)$ as the Δm^2_{atm} at the absolute minimum $\vec{F}_{MO}$, the central values and their $\pm\sigma$ bands are drawn in Fig. 6.13 for a large $\Delta m^2_{atm}(true)$ range.

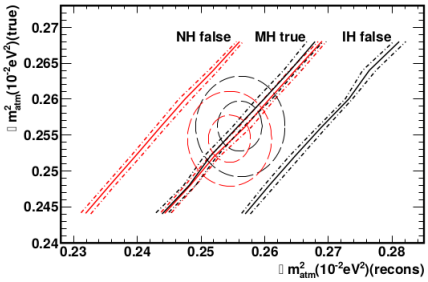

Figure 6.13: *(color online)* $\Delta m^2_{atm}(true)$ *vs* $\Delta m^2_{atm}(recons)$ *is drawn,* $\Delta m^2_{atm}(recons)$ *being obtained by the minimum* $\vec{F}_{MO}$*. The continuous lines correspond to the central values, the dashed ones to the* $\pm\sigma$ *bands. Black (red) curves corresponds to the NH (IH) generation. The central circles correspond to the* 68% *and* 95% *C.L. contours of the current* Δm^2_{atm} *uncertainties for NH and IH, from Tab. 6.1.*

When the input parameter $|\Delta m^2_{atm}|$ is drawn vs $\Delta m^2_{atm}(recons)$, the separation distance between the two components is maintained along the range. That naturally leads to the robustness of $\vec{F}_{MO}$ against Δm^2_{atm} because the MH sensitivity mainly depends on how much the two hypotheses can be discriminated and the separation between the two hypotheses is almost constant as it is described in Fig. 6.14.

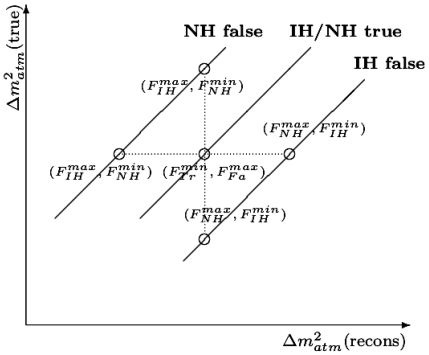

Figure 6.14: *The couplings of $\Delta m^2_{atm}(true)$ and $\Delta m^2_{atm}(recons)$ are pointed out. The quoted sensitivities corresponds to the probability to mis-identify $(F^{min}_{IH}, F^{max}_{NH})$ with $(F^{max}_{IH}, F^{min}_{NH})$, either at the same $\Delta m^2_{atm}(true)$ or the same $\Delta m^2_{atm}(recons)$. An equivalent probability applies to $(F^{min}_{NH}, F^{max}_{IH})$.*

One should not confuse the experimental conditions with the physical context: there is obviously only one set of true parameters, regardless of the MO established in nature. If χ^2 is able to single out such deconvolution, the result would be extremely efficient. Unfortunately, the χ^2 performs a best fit over the multidimensional space of the parameters' uncertainties. Therefore, one usually obtains two different sets of best fit values, one for NH and one for IH. The $\vec{F}_{MO}$ procedure operates distinctively being based on expressions with a factorized dependence on all the parameters except the atmospheric mass. To be more precise, the factorization of the other parameters is only true at the leading order and approximately for the solar mass. For example, if the mass terms dependencies are included in the survival probabilities, the factorization of Eq. 6.11 does not hold. Nevertheless, the latter are minor effects that do not spoil the performances of $\vec{F}_{MO}$. To confirm the $\vec{F}_{MO}$ properties with respect to the quantities, including reactor flux and reaction cross-section, other than Δm^2_{atm}, a large Monte Carlo simulation has been done. The parameters that are allowed to float freely in the simulation are reported in Tab. 6.2. 500 different sets of parameters have been randomly selected. For each set of parameters 20 JUNO-like experiments, 6 years of exposure, have been simulated including a $3\%/\sqrt{E}$ energy resolution. A uniform uncertainty of $\pm 5\,\mathrm{m}$ for the baseline of each of the ten reactors at $52.5\,\mathrm{km}$ away has been considered. We have not included the two remote reactors as well as any background contribution. The aim of the simulation is to demonstrate the independence of the evaluated sensitivity from the parameters except Δm^2_{atm}, as argued from Eq. 6.11. Specifically, the relative position of NH and IH in the (F_{NH}, F_{IH}) plane should not change. It is clear that 500 sets are not reproducing the full multiparameter space. However, the generation can be considered sufficient if no correlation is shown. The result is reported in Fig. 6.15: all the quantities except Δm^2_{atm} are let fluctuate within their uncertainty. No correlation between F_{NH} and F_{IH} is evident, the net result being the linear increase of both components values of $\vec{F}_{MO}$. There is no observed change on the dispersion nor in the relative distance. That confirms the expectation, the separation between two F_{IH} and F_{NH} remains constant.

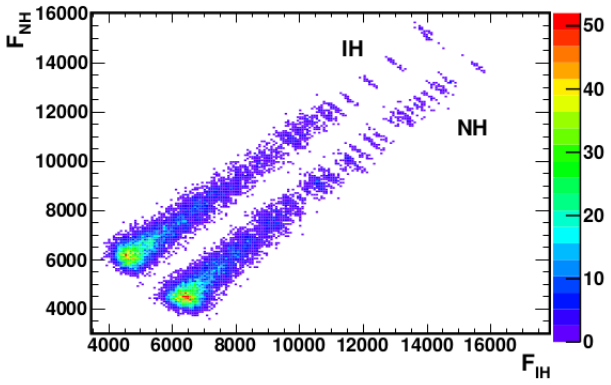

Figure 6.15: *(color online) F_{NH} vs F_{IH} distributions when all the parameters but Δm^2_{atm} are letting free within their uncertainties, as in Tab. 6.1. The two populations correspond to the NH (bottom region) and the IH (top region) generations. There is no observed change on the dispersions nor in the relative distance. Then, the result is that the separation between two F_{IH} and F_{NH} remains constant.*

6.4 Other $\vec{F}_{MO}$ dependences

To complete our study about the alternative method $\vec{F}_{MO}$, we have to study how the $\vec{F}_{MO}$ behaviors depend on the different systematic sources and backgrounds, uncertainties in the reactor flux, and the bump effect.

6.4.1 The Background and systematic studies

This subsection will answer how the different systematic sources and backgrounds affect the distribution of $\vec{F}_{MO}$. In JUNO-like experiments at reactors several sources of background and systematic errors are present, more details being available in Sec. 3.4. As already discussed, the major backgrounds for the reactor neutrino oscillation analysis are the accidentals, the $^8He/^9Li$ cosmogenic, the fast neutron and (α, n) interactions. In principle, all these background sources produce events uncorrelated in energy with the signal. The background conservatively included in the $\vec{F}_{MO}$ analysis, due to its slow variation in energy, does not change the $\vec{F}_{MO}$ dispersions and consequentiality does not affect MH sensitivity. Fig. 6.16 represents the sum of the background sources in shape of ^9Li.

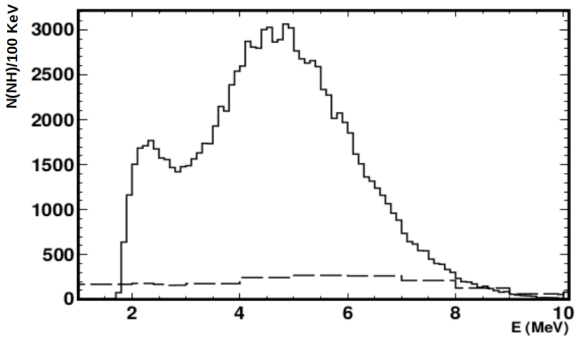

Figure 6.16: *(color online) The cosmogenic background distribution due to ^9Li for a six year long JUNO-like experiment. This is the distribution, conservatively scaled to the total amount of expected incoherent background, used to extract the sensitivity on NH/IH with this kind of background.*

As mentioned in Sec. 3.4, there are two sources for detector response: first the statistical fluctuations (in this particular case, the so-called photo-statistics in the liquid scintillor), second the systematic uncertainty associated to the correction of the linearity in energy of the detector response (for example from non-uniformity in the liquid scintillor, photomultiplier manufacturing and the electronics) [1]. About the systematic uncertainties, $\vec{F}_{MO}$ is expected to act differently from them especially due to the bump effect at $4 \sim 6$ MeV energy region [63]. The other sources of incoherent systematic errors, related to the energy reconstruction, will enter in quadrature with the energy resolution itself [63]. The coherent systematic error due to a residual non-linear energy scaling is a detector dependent effect. We verified that a parametric form as in [64], eq. (13), would produce a linear dependence on both F_{NH} and F_{IH}. That linearity could be used to self-calibrate the energy spectrum.

6.4.2 The Flux Effect

The reactor flux uncertainties include several components, concerning both the overall normalization and the shape as a function of the anti-neutrino energy. Regarding the integrated flux normalization, we add in quadrature the relative uncertainties associated with the power, the energy produced per fission, the spent fuel, the non-equilibrium and the fission fraction at a given time. All but the last one can be assumed as correlated across all cores, because they derive from the same physical modeling uncertainty, intrinsic to a typical fission core. The latter is instead uncorrelated across cores, because the relative fractions of the four leading burning elements will likely be different for the cores considered at a given time (switching on/off and re-fueling at independent times). By taking the sum in quadrature of the maximum uncertainty coherently for all the considered cores the "envelope" total uncertainty is therefore used. Conservatively, we vary the overall flux by $\pm 3\%$ with respect to the expected nominal flux at JUNO.

With regard to the energy dependence on the flux modeling uncertainty, from [65] this is estimated to be less than 10% up to $E_{(\overline{\nu}_e)} = 10$ MeV. However, a systematic uncertainty on the reactor flux is already considered by introducing the "bump" between 4 and 6 MeV in the simulation (SubSec. 6.4.3). That is, the deformation of the spectrum due to the bump is taken and studied as a source of systematic uncertainty, as an example of

how a stretching of the energy spectrum would affect the $\vec{F}_{MO}$. The deformation is bin-dependent and lies between 5% and 20% of the original energy spectrum. Since the bump contribution is neglected in the analytical calculation and in the $\vec{F}_{MO}$ definitions it can be considered a genuine systematic effect of the energy shape. Therefore, it is deemed safe to discard any further uncertainties on the reactor flux shape. The parameters that are allowed to float freely in the simulation are reported in Tab. 6.2.

Table 6.2: *The quantities used in the large simulation are listed. For each of them the chosen central values and their uncertainties are quoted. They are allowed freely varying at the same time, each following a Gaussian distribution. The baselines uncertainties follows a $\pm 5\,\mathrm{m}$ uniform distribution. The chosen value for Δm^2_{atm} has been added to the list. Central values for flux and cross-sections are taken from the computations described in the text. The cross-section uncertainty has been included just to show its possible correlation with the $\vec{F}_{MO}$ estimator.*

	best-fit	1σ region
$Sin^2\theta_{12}$	0.2970	± 0.017
$Sin^2\theta_{13}$	0.02150	± 0.0007
δm^2_{sol}	7.37e-5	0.16×10^{-5}
flux	$\pm 3\%$	
cross-section	$\pm 1\%$	
baselines	$\pm 5\,\mathrm{m}$	
Δm^2_{atm}	2.56×10^{-3}	

The experimental sensitivities of JUNO including $\pm 3\%$ variations of the flux are reported in Tab. 6.3.

Table 6.3: *The bi-gaussian fits of the $\vec{F}_{MO}$ distributions are reported, for the JUNO-like configuration of six years of data taking and a $3\%/\sqrt{E}$ energy resolutions, μ_{MH}, σ_{MH} and r_{MH} being the means, the standard deviations and the correlation coefficients, respectively, of the fitted $2D$ Gaussians. The ten near reactor cores have been considered with a $\pm 5\,\mathrm{m}$ uniform dispersion on their relative baseline, as well as the two remote reactor plants with a $\pm 0.5\,\mathrm{km}$ uniform dispersion on their relative baseline. The two data sets correspond to a -3% and $+3\%$ on the reactor flux. The sensitivity has been computed from the p-values estimation as described in the text in terms of number of σ's in the two-sided option. $n\,\sigma$ (IH) stays for the IH rejection significance, and equivalently for NH. As expected the results are not so sensitive to $\pm 3\%$ variations of the flux, although the $\vec{F}_{MO}$ islands are shifted. The slight increase (decrease) of the sensitivity corresponding to -3% $(+3\%)$ is due to the two remote reactor cores contribution. The counter-intuitive effect is explained by the greater (smaller) influence of the destructive oscillation pattern of the two remote cores than the increase (decrease) of the flux.*

10 reactor cores plus the 2 remote cores, 6 years			
		with -3% on flux	with +3% on flux
NH true	μ_{NH}	5553.1 ± 5.9	7652.8 ± 6.2
	σ_{NH}	212.5 ± 4.5	197.3 ± 3.6
	μ_{IH}	6823.3 ± 7.0	8915.8 ± 6.6
	σ_{IH}	240.2 ± 5.1	211.2 ± 3.9
	r_{NH}	-0.607 ± 0.019	-0.825 ± 0.006
IH true	μ_{NH}	6994.8 ± 4.9	8991.2 ± 7.1
	σ_{NH}	247.6 ± 5.2	214.8 ± 4.2
	μ_{IH}	5426.0 ± 4.7	7603.9 ± 6.4
	σ_{IH}	213.8 ± 4.1	196.3 ± 3.7
	r_{IH}	-0.603 ± 0.012	-0.815 ± 0.005
	$p-$value (IH)	7.53×10^{-8}	1.48×10^{-7}
	$n\,\sigma$ (IH)	5.38	5.25
	$p-$value (NH)	9.68×10^{-8}	1.59×10^{-7}
	$n\,\sigma$ (NH)	5.34	5.24

6.4.3 The Bump Effect

According to [65] and references inside, there is a observed bump in neutrino flux at energy $4 \sim 6\,\mathrm{MeV}$. The bump around $4 \sim 6\,\mathrm{MeV}$ has been modeled and included in the flux for one configuration. Contrary to intuitive expectations it will slightly increase the significance by about $0.2\,\sigma$. The bump contribution and the reactor flux uncertainties are coherent in energy with the expected signal as shown in Fig. 6.18. Therefore, they give a corresponding percentage of increase/decrease to the $\vec{F}_{MO}$ test-statistic sensitivity. In other words, they simply act as an increase/decrease of exposure. Instead, the remote reactor contribution is incoherent due to the large baselines.

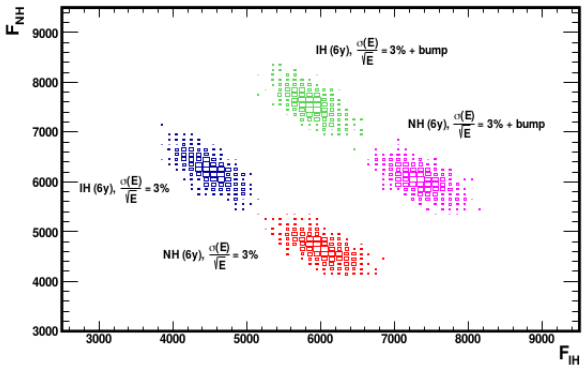

Figure 6.17: *(color online) F_{NH} vs F_{NH} distributions for 1000 (NH) + 1000 (IH) toys JUNO-like experiment, in two different configurations. The benchmark of six years exposure is compared to the same exposure result when the $4 \sim 6\,\mathrm{MeV}$ bump is added. The sensitivity is calculated and reported in Tab. 6.4.*

Table 6.4: *The bi-Gaussian fits of the $\vec{F}_{MO}$ distributions are reported, for the JUNO-like configuration of six years of data taking and a $3\%/\sqrt{E}$ energy resolutions, μ_{MH}, σ_{MH} and r_{MH} being the means, the standard deviations and the correlation coefficients, respectively, of the fitted $2D$ Gaussians. The ten near reactor cores have been considered with a $\pm 5\,\mathrm{m}$ uniform dispersion on their relative baseline. In the first set of data the uncorrelated background has been included from the ^9Li, scaled to the total amount. In the second set the correlated bump around $4 \sim 6\,\mathrm{MeV}$ has been considered. The sensitivity has been computed from the p-values estimation as described in the text in terms of number of σ's in the two-sided option. $n\,\sigma$ (IH) stays for the IH rejection significance, and equivalently for NH.*

10 reactor cores, 6 years			
		with uncorrelated background	with correlated bump around $4 \sim 6$ MeV
NH true	μ_{NH}	8908.2 $\pm$ 6.1	6039.3 $\pm$ 7.4
	σ_{NH}	187.0 $\pm$ 3.4	226.9 $\pm$ 4.4
	μ_{IH}	10315.2 $\pm$ 6.5	7346.8 $\pm$ 7.7
	σ_{IH}	201.9 $\pm$ 3.6	238.9 $\pm$ 4.9
	r_{NH}	-0.841 $\pm$ 0.005	-0.573 $\pm$ 0.015
IH true	μ_{NH}	10230.0 $\pm$ 6.3	7573.7 $\pm$ 4.9
	σ_{NH}	196.5 $\pm$ 3.4	243.6 $\pm$ 4.7
	μ_{IH}	8998.8 $\pm$ 5.9	5861.0 $\pm$ 5.5
	σ_{IH}	181.5 $\pm$ 3.2	219.1 $\pm$ 3.1
	r_{IH}	-0.835 $\pm$ 0.007	-0.617 $\pm$ 0.010
	$p-$value (IH)	2.88×10^{-8}	1.57×10^{-8}
	$n\,\sigma$ (IH)	5.55	5.65
	$p-$value (NH)	1.90×10^{-8}	1.75×10^{-8}
	$n\,\sigma$ (NH)	5.62	5.63

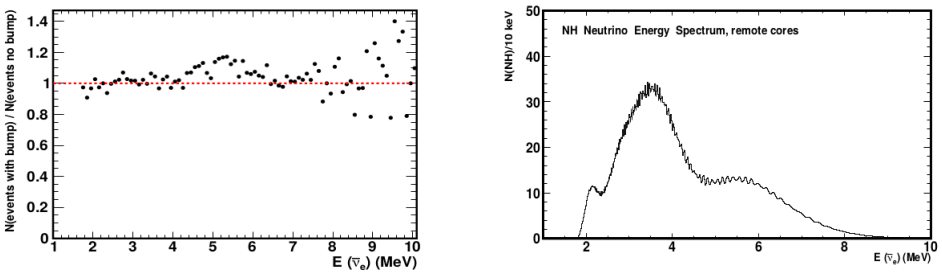

Figure 6.18: *(color online) The antineutrino event distribution when a modeled bump around* $4 \sim 6$ MeV *is added to the ten reactor production (left plot), is drawn. A single JUNO-like, six years exposure, toy Monte Carlo is shown in terms of the relative percentage with/without the addition. In the right plot the distribution due to the two remote reactor production is shown (NH case).*

CHAPTER 7

RESULTS

In order to present the findings of the thesis as clear as possible, it is imperative to divide the chapter in two parts. The first part explains the statistical problem representing the standard method issues. The second part is the new alternative method representing the solution to this problem.

7.1 The problem: Standard Method Issues

In this section we report the experimental sensitivities for the determination of the neutrino mass ordering using the standard method. After the investigation reported in Ch. 5, we had to study the experimental sensitivity at each single value of the atmospheric neutrino mass proposed in that chapter. The three reported issues of the standard algorithm were studied in the range of the atmospheric mass between $2.450 \times 10^{-3}\text{eV}^2$ and $2.580 \times 10^{-3}\text{eV}^2$. Theses issues are categorized into two types depending on which estimator being used. The first sensitivity category using $\Delta\chi^2$ estimator is reported in SubSec. 7.1.1. The second sensitivity category using χ^2 is reported in SubSec. 7.1.2. For each category, a detailed study is provided for 20 different values of the atmospheric mass in the range of $2.450 \times 10^{-3}\text{eV}^2 \leq |\Delta m^2| \leq 2.580 \times 10^{-3}\text{eV}^2$, with and without systematic errors. The final results now provide solid evidences about the problematic use of the standard algorithm. That is explicitly explained in Ch. 5 and it will be confirmed in this chapter.

7.1.1 The Issues of $\Delta\chi^2$

Here we report two results. First, our result on the limited power of $\Delta\chi^2$ (issue one) confirming that, when systematic uncertainties are included, the approximated Eq. 5.8 is not acceptable in the range of neutrino atmospheric mass, $2.450 \times 10^{-3}\text{eV}^2 \leq |\Delta m^2| \leq 2.580 \times 10^{-3}\text{eV}^2$. We provide the results of 20 different values of the $|\Delta m^2|$ in that range showing the limit of the approximation when including the systematic uncertainties

(as confirmed in Fig. 7.2). Although Eq. 5.8 is widely accepted, it suffers from some limitations due to its limitation when systematic uncertainties are included (Fig. 7.2). The limitation manifests itself decreasing the power of the $\Delta\chi^2$ estimator to determine the correct neutrino MH. The reasons behind this limitation are explained in details in Sec. 5.2. As a result the power of this estimator for the MH discrimination is not promising as reported in Tab. 7.2. On the contrary, without including the systematic uncertainties Eq. 5.8 is valid and the $\Delta\chi^2$ results are very good as reported in Fig. 7.1 and Tab. 7.1.

Second, the studies about the $\Delta\chi^2$ robustness in the range $2.450 \times 10^{-3}\text{eV}^2 \leq |\Delta m^2| \leq 2.580 \times 10^{-3}\text{eV}^2$ shows its dependence. This result is directly in line with previous result in Sec. 5.4. From these sensitivity tables (Tab. 7.1 and Tab. 7.2), it is clear that the experimental sensitivity using $\Delta\chi^2$ has strongly dependence on the injected neutrino atmospheric mass. If the value of the input parameter, the injected neutrino atmospheric mass, is modified, the experimental sensitivity will change according to it. This change is not affected by the systematic uncertainties. It is an intrinsic property of the $\Delta\chi^2$ itself. Tab. 7.1 shows the sensitivities using $\Delta\chi^2$ with infinite energy resolution. As can be seen in the table, the experimental sensitivities vary a lot with different values of the atmospheric neutrino mass proving that the robustness of $\Delta\chi^2$ is not well established even at infinite energy resolution. Tab. 7.2 provides the sensitivities including the systematic uncertainties: the neutrino mass ordering discrimination varies a lot. The implications of this issue is fully discussed in Sec. 5.4.

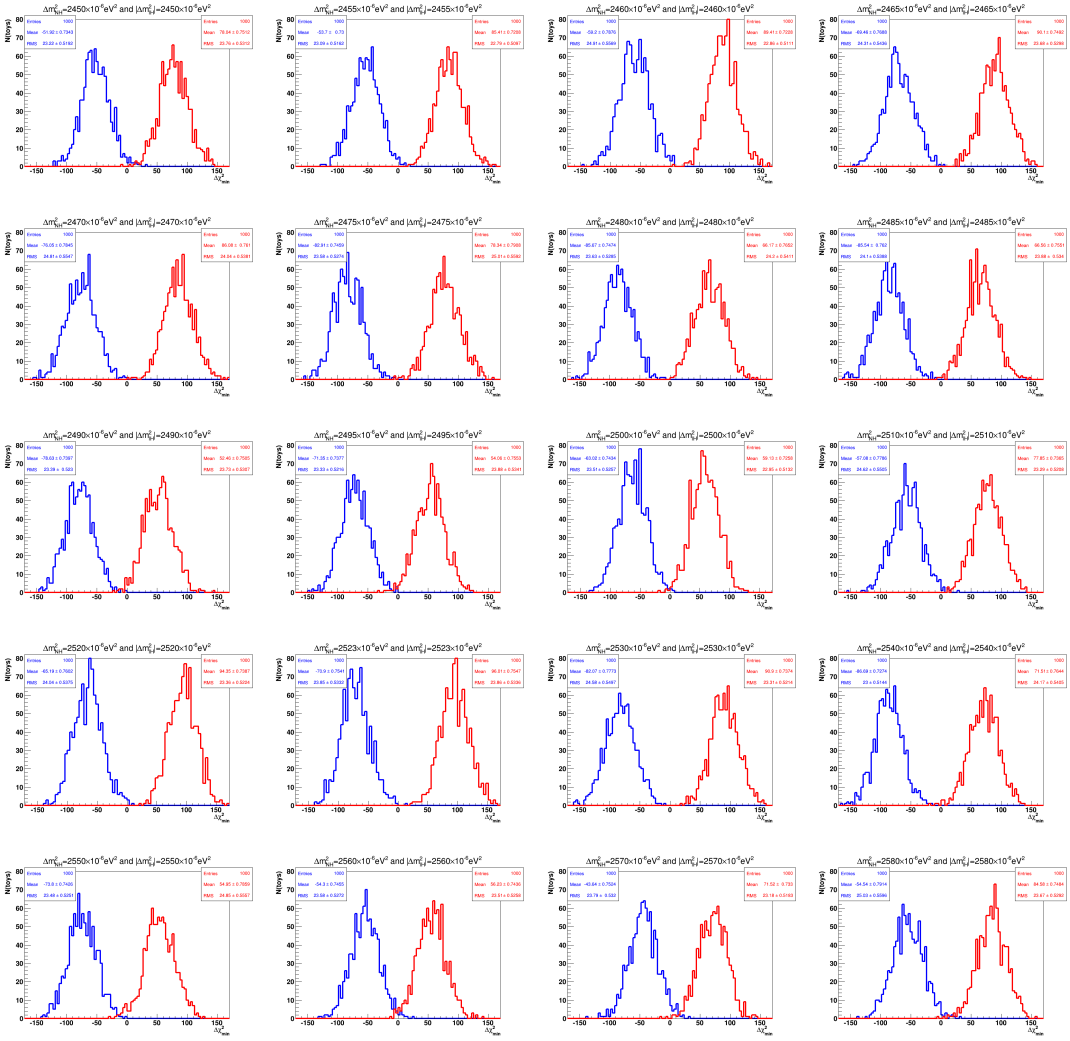

Figure 7.1: $\Delta\chi^2$ *estimator for 1000 (NH) + 1000 (IH) toy JUNO-like simulations generated at* 20 *different values of the atmospheric mass in the range of* $2.450\times10^{-3}\text{eV}^2 \leq |\Delta m^2| \leq 2.580\times10^{-3}\text{eV}^2$ *for NH hypothesis (blue distribution in each plot) and IH hypothesis (red distribution in each plot) with six years of exposure and the ten near reactor cores. An infinite energy resolution is assumed. The sensitivities due to these conditions are reported in Tab. 7.1.*

Table 7.1: *The comparison of the MH sensitivity using $\Delta\chi^2$ assuming infinite energy resolution for NH sample and IH sample, for 20 different values of the atmospheric mass in the range of $2.450 \times 10^{-3}\text{eV}^2 \leq |\Delta m^2| \leq 2.580 \times 10^{-3}\text{eV}^2$. The table indicates the sensitivity calculations using the Z-test for $1D$ test in two cases. The first case is without the approximation of Eq. 5.8 and the second one is obtained using the approximation of Eq. 5.8.*

Infinite Energy Resolution								
$\lvert\Delta m^2\rvert_{NH/IH} \times 10^{-3}$	2.450		2.455		2.460		2.465	
μ_{NH}	-51.90 ± 0.735		-53.72 ± 0.732		-59.20 ± 0.788		-69.43 ± 0.7681	
σ_{NH}	23.24 ± 0.520		23.14 ± 0.518		24.91 ± 0.557		24.29 ± 0.5431	
μ_{IH}	78.03 ± 0.752		85.41 ± 0.720		89.41 ± 0.723		90.09 ± 0.7482	
σ_{IH}	23.77 ± 0.532		22.76 ± 0.520		22.86 ± 0.511		23.65 ± 0.5291	
$z_{score}^{(NH)}$	5.590	7.204(app.)	6.013	7.329(app.)	5.966	7.694(app.)	6.567	8.332(app.)
$z_{score}^{(IH)}$	5.466	8.833(app.)	6.113	9.242(app.)	6.501	9.456(app.)	6.745	9.456(app.)
$\lvert\Delta m^2\rvert_{NH/IH} \times 10^{-3}$	2.470		2.475		2.480		2.485	
μ_{NH}	-76.04 ± 0.7834		-82.90 ± 0.7452		-55.70 ± 0.7471		-85.54 ± 0.7595	
σ_{NH}	24.77 ± 0.554		23.55 ± 0.5269		23.62 ± 0.5283		24.29 ± 0.5431	
μ_{IH}	86.13 ± 0.762		78.36 ± 0.7904		66.17 ± 0.7649		90.09 ± 0.7482	
σ_{IH}	24.07 ± 0.5388		24.99 ± 0.5589		24.19 ± 0.5409		23.65 ± 0.5291	
$z_{score}^{(NH)}$	6.547	8.720(app.)	6.848	9.105(app.)	5.160	7.463(app.)	7.231	9.249(app.)
$z_{score}^{(IH)}$	6.737	9.281(app.)	6.453	8.852(app.)	5.038	8.134(app.)	7.426	9.492(app.)
$\lvert\Delta m^2\rvert_{NH/IH} \times 10^{-3}$	2.490		2.495		2.500		2.510	
μ_{NH}	-76.63 ± 0.7387		-71.32 ± 0.7365		-63.02 ± 0.743		57.12 ± 0.778	
σ_{NH}	23.36 ± 0.5223		23.29 ± 0.5208		23.51 ± 0.526		24.60 ± 0.550	
μ_{IH}	52.48 ± 0.7507		54.03 ± 0.7557		59.13 ± 0.726		77.89 ± 0.738	
σ_{IH}	23.74 ± 0.5308		23.90 ± 0.5344		22.95 ± 0.513		23.33 ± 0.522	
$z_{score}^{(NH)}$	5.527	8.445(app.)	5.382	8.445(app.)	5.196	7.939(app.)	5.488	7.556(app.)
$z_{score}^{(IH)}$	5.439	7.244(app.)	5.280	7.351(app.)	5.322	7.690(app.)	5.787	8.826(app.)
$\lvert\Delta m^2\rvert_{NH/IH} \times 10^{-3}$	2.520		2.523		2.530		2.540	
μ_{NH}	-65.19 ± 0.760		-70.90 ± 0.754		-82.07 ± 0.777		-86.72 ± 0.727	
σ_{NH}	24.04 ± 0.538		23.85 ± 0.533		24.58 ± 0.550		23.00 ± 0.514	
μ_{IH}	94.35 ± 0.739		96.01 ± 0.755		90.90 ± 0.737		71.51 ± 0.762	
σ_{IH}	23.36 ± 0.523		23.89 ± 0.534		23.31 ± 0.521		24.10 ± 0.539	
$z_{score}^{(NH)}$	6.636	8.074(app.)	6.998	8.420(app.)	7.037	9.059(app.)	6.880	9.312(app.)
$z_{score}^{(IH)}$	6.830	9.713(app.)	6.987	9.798(app.)	7.420	9.534(app.)	6.566	8.456(app.)
$\lvert\Delta m^2\rvert_{NH/IH} \times 10^{-3}$	2.550		2.560		2.570		2.580	
μ_{NH}	-73.80 ± 0.743		-54.30 ± 0.746		-43.64 ± 0.752		-54.54 ± 0.791	
σ_{NH}	23.48 ± 0.525		23.58 ± 0.527		23.79 ± 0.532		25.03 ± 0.560	
μ_{IH}	54.95 ± 0.786		56.23 ± 0.744		71.52 ± 0.733		84.58 ± 0.748	
σ_{IH}	24.85 ± 0.556		23.51 ± 0.526		23.18 ± 0.518		23.67 ± 0.529	
$z_{score}^{(NH)}$	5.483	8.591(app.)	4.687	7.369(app.)	4.841	6.606(app.)	5.848	7.385(app.)
$z_{score}^{(IH)}$	5.181	7.413(app.)	4.701	7.50(app.)	5.0	8.457(app.)	5.877	9.197(app.)

As mentioned in Sec. 5.2, the MH sensitivities using Z-test, $z_{score}^{(NH)}$ and $z_{score}^{(IH)}$, do not exact equal to the MH sensitivities obtained in the approximated Eq. 5.8, $z_{score}^{(NH)}(app.)$ and $z_{score}^{(IH)}(app.)$. Tab. 7.2 reports this observation for 20 different values for the atmospheric mass at infinite energy resolution providing a solid experimental evidence for over-estimation behavior for this approximation.

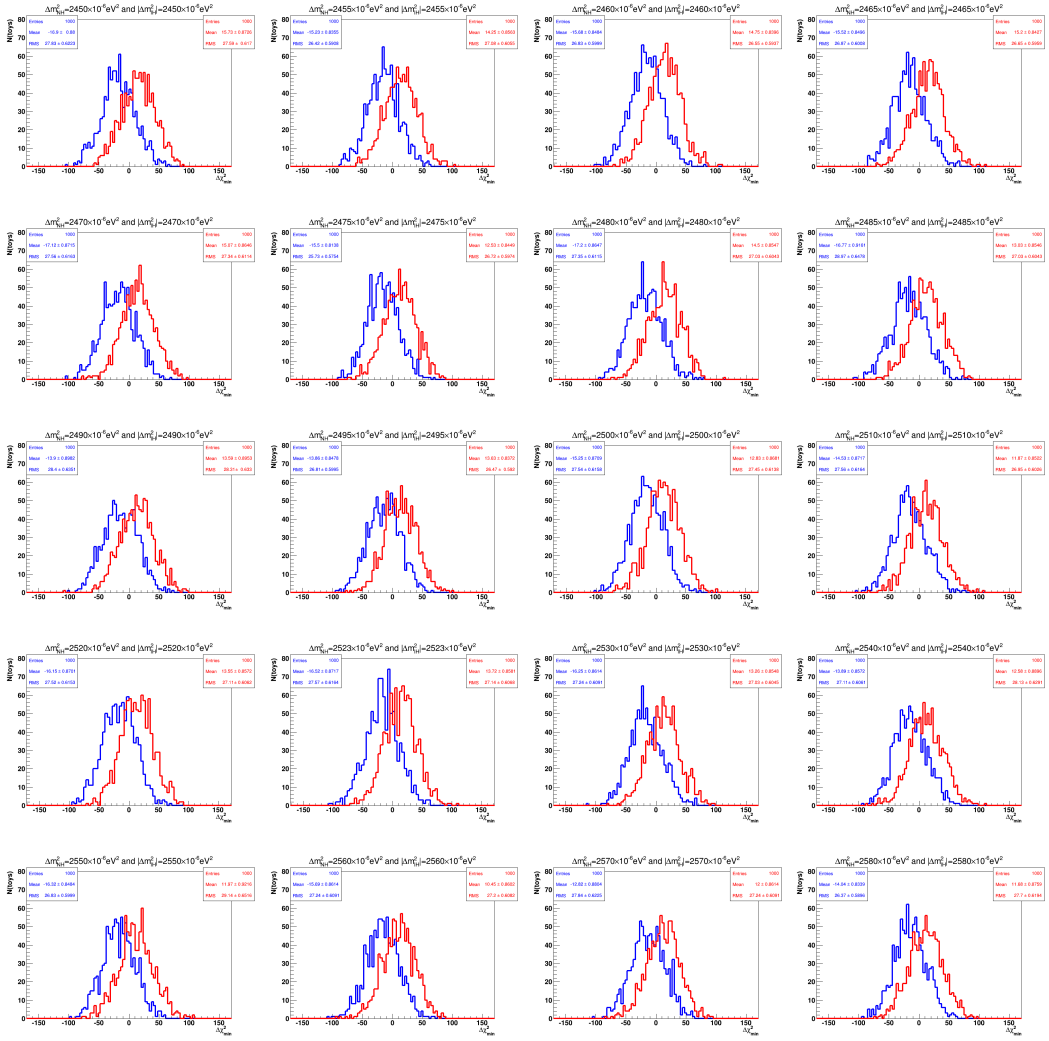

Figure 7.2: *$\Delta\chi^2$ estimator for 1000 (NH) + 1000 (IH) toy JUNO-like simulations generated at 20 different values of the atmospheric mass in the range of $2.450\times10^{-3}\text{eV}^2 \leq |\Delta m^2| \leq 2.580\times10^{-3}\text{eV}^2$ for NH hypothesis (blue distribution in each plot) and IH hypothesis (red distribution in each plot) with six years of exposure and the ten near reactor cores, with energy resolution $3\%/\sqrt{E}$. The sensitivities due to these conditions are reported in Tab. 7.2.*

Table 7.2: *The comparison of the MH sensitivity using $\Delta\chi^2$ for actual distributions for NH sample and IH sample, for for 20 different values of the atmospheric mass in the range of $2.450 \times 10^{-3}\text{eV}^2 \leq |\Delta m^2| \leq 2.580 \times 10^{-3}\text{eV}^2$. The table indicates the sensitivity calculations using the Z-test for $1D$ test in two cases. The first case is without the approximation of Eq. 5.8 and the second one is using the approximation of Eq. 5.8.*

Relative Energy Resolution $3\%/\sqrt{E}$								
$\lvert\Delta m^2\rvert_{NH/IH} \times 10^{-3}$	2.450		2.455		2.460		2.465	
μ_{NH}	-16.91 ± 0.880		-15.19 ± 0.834		-15.68 ± 0.8484		-15.48 ± 0.85	
σ_{NH}	27.82 ± 0.622		26.38 ± 0.590		26.83 ± 0.5999		26.88 ± 0.601	
μ_{IH}	15.72 ± 0.871		14.29 ± 0.856		14.75 ± 0.8396		15.22 ± 0.8427	
σ_{IH}	27.55 ± 0.616		27.06 ± 0.605		26.55 ± 0.5937		26.65 ± 0.5959	
$z_{score}^{(NH)}$	1.173	4.112(app.)	1.118	3.897(app.)	1.134	3.960(app.)	1.142	3.934(app.)
$z_{score}^{(IH)}$	1.184	3.965(app.)	1.089	3.780(app.)	1.146	3.841(app.)	1.152	3.901(app.)
$\lvert\Delta m^2\rvert_{NH/IH} \times 10^{-3}$	2.470		2.475		2.480		2.485	
μ_{NH}	-17.10 ± 0.8709		-15.55 ± 0.8126		-17.21 ± 0.8646		-16.76 ± 0.9159	
σ_{NH}	27.54 ± 0.6158		25.70 ± 0.5746		27.34 ± 0.6114		28.96 ± 0.6477	
μ_{IH}	15.07 ± 0.8645		12.54 ± 0.8437		14.49 ± 0.8539		12.99 ± 0.856	
σ_{IH}	27.34 ± 0.6113		26.68 ± 0.5966		27.00 ± 0.6038		27.07 ± 0.6053	
$z_{score}^{(NH)}$	1.168	4.135(app.)	1.093	3.943(app.)	1.159	4.148(app.)	1.027	4.094(app.)
$z_{score}^{(IH)}$	1.177	3.882(app.)	1.053	3.541(app.)	1.174	3.807(app.)	1.099	3.604(app.)
$\lvert\Delta m^2\rvert_{NH/IH} \times 10^{-3}$	2.490		2.495		2.500		2.510	
μ_{NH}	-13.86 ± 0.8974		-13.89 ± 0.8476		-15.25 ± 0.8709		14.52 ± 0.871	
σ_{NH}	28.38 ± 0.6345		26.80 ± 0.5994		27.54 ± 0.6158		27.55 ± 0.616	
μ_{IH}	13.58 ± 0.8955		13.59 ± 0.8372		12.83 ± 0.8681		11.87 ± 0.853	
σ_{IH}	28.32 ± 0.6332		26.47 ± 0.5920		27.45 ± 0.6138		26.97 ± 0.603	
$z_{score}^{(NH)}$	0.967	3.723(app.)	1.025	3.727(app.)	1.020	3.905(app.)	0.958	3.811(app.)
$z_{score}^{(IH)}$	0.969	3.685(app.)	1.038	3.686(app.)	1.023	3.582(app.)	0.978	3.445(app.)
$\lvert\Delta m^2\rvert_{NH/IH} \times 10^{-3}$	2.520		2.523		2.530		2.540	
μ_{NH}	-16.15 ± 0.870		-16.52 ± 0.872		-16.25 ± 0.861		-13.91 ± 0.856	
σ_{NH}	27.52 ± 0.615		27.57 ± 0.616		27.24 ± 0.609		27.07 ± 0.605	
μ_{IH}	13.55 ± 0.857		13.72 ± 0.858		13.26 ± 0.855		12.61 ± 0.888	
σ_{IH}	27.11 ± 0.606		27.14 ± 0.607		27.03 ± 0.605		28.08 ± 0.628	
$z_{score}^{(NH)}$	1.079	4.019(app.)	1.097	4.064(app.)	1.083	4.031(app.)	0.9797	3.30(app.)
$z_{score}^{(IH)}$	1.096	3.681(app.)	1.114	3.704(app.)	1.092	3.641(app.)	0.944	3.551(app.)
$\lvert\Delta m^2\rvert_{NH/IH} \times 10^{-3}$	2.550		2.560		2.570		2.580	
μ_{NH}	-16.32 ± 0.848		-15.69 ± 0.861		-12.82 ± 0.880		-14.04 ± 0.834	
σ_{NH}	26.83 ± 0.600		27.24 ± 0.609		27.84 ± 0.623		26.37 ± 0.590	
μ_{IH}	11.97 ± 0.922		10.54 ± 0.860		12.00 ± 0.861		11.68 ± 0.876	
σ_{IH}	29.14 ± 0.652		27.20 ± 0.608		27.24 ± 0.609		27.70 ± 0.619	
$z_{score}^{(NH)}$	1.054	4.040(app.)	0.963	3.961(app.)	0.892	3.581(app.)	0.975	3.747(app.)
$z_{score}^{(IH)}$	0.971	3.460(app.)	0.964	3.247(app.)	0.911	3.464(app.)	0.944	3.418(app.)

7.1.2 The Issues of χ^2

Each plot of Fig. 7.3 and Fig. 7.4 proves that χ^2 has not enough ability to produce high sensitivity to distinguish between the right and wrong ordering of the neutrino using the medium baseline reactor spectrum.

From the sensitivity tables (Tab. 7.3 and Tab. 7.4), it is clear that the experimental sensitivity using the χ^2 estimator has strongly dependence on the injected neutrino atmospheric mass. If the injected neutrino atmospheric mass value is modified, the experimental sensitivity will change according to it, even when the systematic uncertainties are not included.

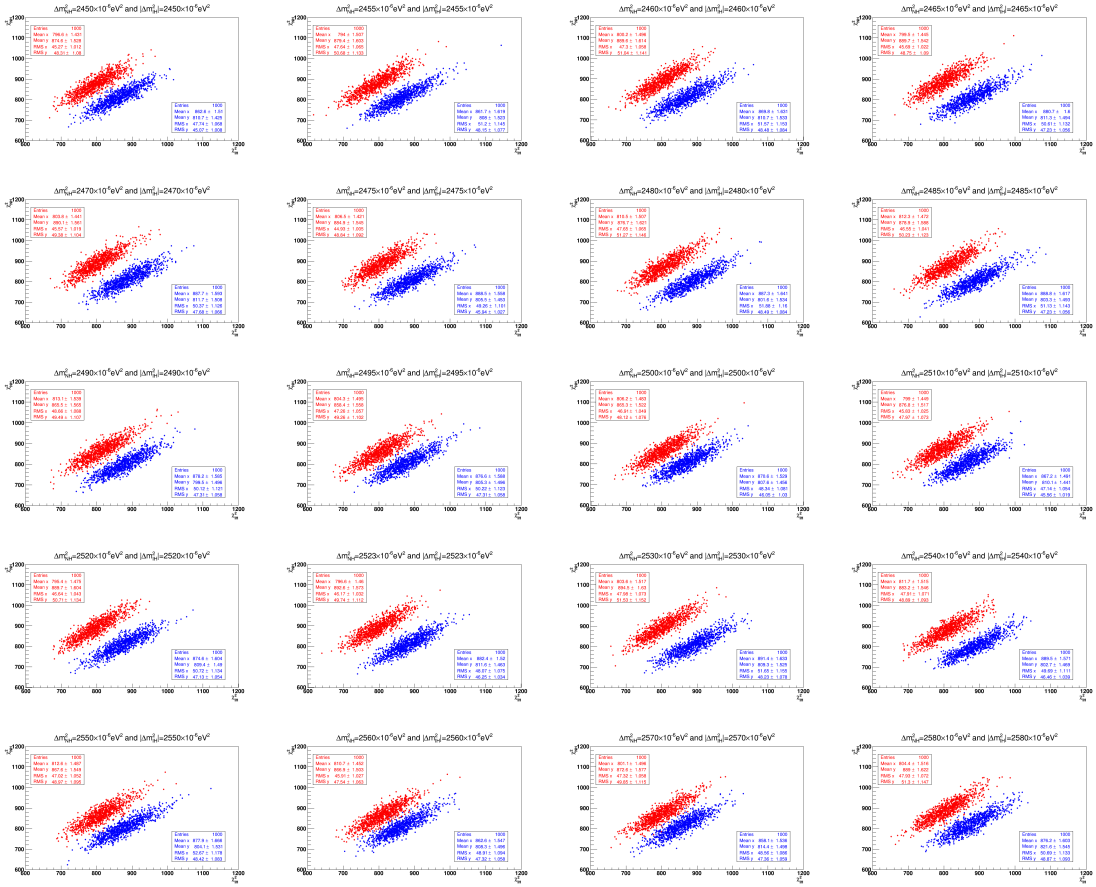

Figure 7.3: *Two χ^2 distributions for 1000 (NH) + 1000 (IH) toy JUNO-like simulations that generated at 20 different values of the atmospheric mass in the range of $2.450 \times 10^{-3}\mathrm{eV}^2 \leq |\Delta m^2| \leq 2.580 \times 10^{-3}\mathrm{eV}^2$ for NH hypothesis (blue distribution in each plot) and IH hypothesis (blue distribution in each plot) with six years of exposure and the ten near reactor cores with infinite energy resolution. The sensitivities due to these conditions are reported in Tab. 7.3*

Table 7.3: *The comparison of the MH sensitivity using χ^2 as a bi-dimensional estimator assuming infinite energy resolution for, NH sample and IH sample, for 20 different values of the atmospheric mass in the range of $2.450 \times 10^{-3}\text{eV}^2 \leq |\Delta m^2| \leq 2.580 \times 10^{-3}\text{eV}^2$. The table indicates the sensitivity calculations using the Z-test for $2D$.*

Infinite Energy Resolution										
$\|\Delta m^2\|_{NH/IH} \times 10^{-3}$	2.450		2.455		2.460		2.465		2.470	
	NH	**IH**	**NH**	**IH**	**NH**	**IH**	**NH**	**IH**	**NH**	**IH**
μ_{NH}	810.7 ± 1.425	874.6 ± 1.528	808 ± 1.523	879.4 ± 1.602	810.7 ± 1.533	889.6 ± 1.614	811.3 ± 1.494	889.7 ± 1.542	811.7 ± 1.593	890.1 ± 1.441
σ_{NH}	45.07 ± 1.008	48.31 ± 1.080	48.17 ± 1.077	50.67 ± 1.133	48.48 ± 1.084	51.04 ± 1.141	47.23 ± 1.056	48.76 ± 1.090	47.7 ± 1.067	49.39 ± 1.104
μ_{IH}	862.6 ± 1.510	796.6 ± 1.432	861.7 ± 1.619	794 ± 1.507	869.8 ± 1.631	800.2 ± 1.496	880.7 ± 1.601	799.5 ± 1.445	887.7 ± 1.593	803.8 ± 1.441
σ_{IH}	47.75 ± 1.068	45.27 ± 1.012	51.2 ± 1.145	47.67 ± 1.066	51.57 ± 1.153	47.3 ± 1.058	50.62 ± 1.132	45.69 ± 1.022	50.39 ± 1.127	45.57 ± 1.019
$z_{score}^{(NH)}$	1.0095		1.0154		1.0717		1.163		1.1728	
$z_{score}^{(IH)}$	1.0013		1.0261		1.0891		1.2050		1.2113	
$\|\Delta m^2\|_{NH/IH} \times 10^{-3}$	2.475		2.480		2.485		2.490		2.495	
	NH	**IH**	**NH**	**IH**	**NH**	**IH**	**NH**	**IH**	**NH**	**IH**
μ_{NH}	811.7 ± 1.508	890.1 ± 1.562	805.5 ± 1.453	884.9 ± 1.545	801.3 ± 1.641	876.7 ± 1.622	799.6 ± 1.496	865.5 ± 1.565	805.3 ± 1.495	858.4 ± 1.558
σ_{NH}	47.7 ± 1.067	49.39 ± 1.104	45.94 ± 1.027	48.85 ± 1.092	48.48 ± 1.084	51.28 ± 1.147	47.32 ± 1.058	49.50 ± 1.107	47.28 ± 1.057	49.28 ± 1.102
μ_{IH}	887.7 ± 1.593	803.8 ± 1.441	888.5 ± 1.558	806.5 ± 1.420	887.3 ± 1.641	810.5 ± 1.507	878.2 ± 1.585	813.10 ± 1.539	876.6 ± 1.588	804.3 ± 1.495
σ_{IH}	50.39 ± 1.127	45.57 ± 1.019	49.26 ± 1.102	44.92	51.9 ± 1.084	47.64 ± 1.065	50.11 ± 1.121	48.66 ± 1.088	47.28 ± 1.057	47.27 ± 1.057
$z_{score}^{(NH)}$	1.1990		1.0786		1.102		0.9703		0.9177	
$z_{score}^{(IH)}$	1.2172		1.0944		1.1201		0.9632		0.9268	
$\|\Delta m^2\|_{NH/IH} \times 10^{-3}$	2.500		2.510		2.520		2.523		2.530	
	NH	**IH**	**NH**	**IH**	**NH**	**IH**	**NH**	**IH**	**NH**	**IH**
μ_{NH}	807.6 ± 1.456	865.3 ± 1.522	810.10 ± 1.491	876.90 ± 1.516	809.4 ± 1.49	889.7 ± 1.604	811.6 ± 1.463	892.6 ± 1.573	809.3 ± 1.525	894.5 ± 1.630
σ_{NH}	46.05 ± 1.03	48.12 ± 1.076	45.57 ± 1.019	47.95 ± 1.072	47.13 ± 1.054	50.71 ± 1.134	46.25 ± 1.034	49.74 ± 1.112	48.23 ± 1.078	51.53 ± 1.152
μ_{IH}	870.6 ± 1.529	806.2 ± 1.483	867.2 ± 1.491	799 ± 1.449	874.6 ± 1.604	795.4 ± 1.475	882.4 ± 1.52	796.6 ± 1.460	891.4 ± 1.633	803.6 ± 1.517
σ_{IH}	48.34 ± 1.081	46.91 ± 1.049	47.14 ± 1.054	45.83 ± 1.516	50.72 ± 1.134	46.64 ± 1.043	48.07 ± 1.075	46.17 ± 1.032	51.65 ± 1.155	51.53 ± 1.152
$z_{score}^{(NH)}$	0.9159		1.0418		1.1720		1.2647		1.226	
$z_{score}^{(IH)}$	0.9099		1.0200		1.1781		1.2442		1.231	
$\|\Delta m^2\|_{NH/IH} \times 10^{-3}$	2.540		2.550		2.560		2.570		2.580	
	NH	**IH**	**NH**	**IH**	**NH**	**IH**	**NH**	**IH**	**NH**	**IH**
μ_{NH}	802.7 ± 1.469	883.2 ± 1.546	804.1 ± 1.531	867.6 ± 1.549	862.6 ± 1.547	866.9 ± 1.503	814.4 ± 1.498	872.6 ± 1.577	821.6 ± 1.545	889 ± 1.622
σ_{NH}	46.47 ± 1.039	48.89 ± 1.093	48.42 ± 1.083	48.97 ± 1.095	47.32 ± 1.058	47.54 ± 1.063	47.36 ± 1.059	49.85 ± 1.115	48.87 ± 1.093	51.3 ± 1.147
μ_{IH}	889.5 ± 1.571	811.7 ± 1.515	877.90 ± 1.666	812.6 ± 1.487	808.3 ± 1.496	810.7 ± 1.452	858.1 ± 1.536	801.1 ± 1.496	876.2 ± 1.603	804.4 ± 1.516
σ_{IH}	49.68 ± 1.111	47.91 ± 1.071	48.42 ± 1.083	47.02 ± 1.052	48.91 ± 1.058	45.91 ± 1.027	48.56 ± 1.086	47.32 ± 1.058	50.69 ± 1.133	47.93 ± 1.072
$z_{score}^{(NH)}$	1.1690		0.9103		0.8122		0.8734		1.0111	
$z_{score}^{(IH)}$	1.1613		0.9586		0.8364		0.8622		1.0144	

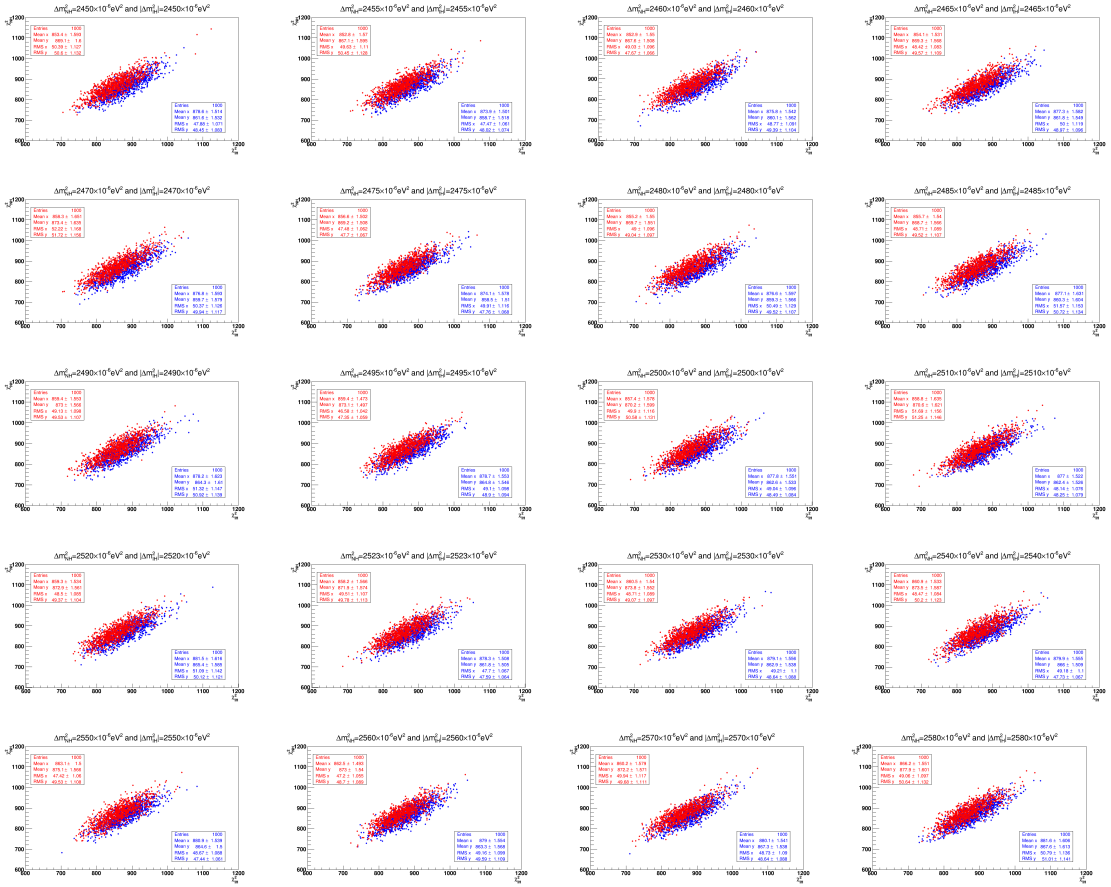

Figure 7.4: *Two χ^2 distributions for 1000 (NH) + 1000 (IH) toy JUNO-like simulations generated at 20 different values of the atmospheric mass in the range of $2.450\times10^{-3}\text{eV}^2 \leq |\Delta m^2| \leq 2.580\times10^{-3}\text{eV}^2$ for NH hypothesis (blue distribution in each plot) and IH hypothesis (blue distribution in each plot) with six years of exposure and the ten near reactor cores, with energy resolution $3\%/\sqrt{E}$. The sensitivities due to these conditions are reported in Tab. 7.4.*

The results about the standard algorithm confirmed the three statistical issues in the range $2.450 \times 10^{-3}\text{eV}^2 \leq |\Delta m^2| \leq 2.580 \times 10^{-3}\text{eV}^2$. The results are directly in line with previous results of Ch. 5.

7.2 The Solution: the Alternative Method Results

The alternative method results are better than the results currently accepted by the standard method and published in [1, 47, 60, 61]. Generally the achieved results using the $\vec{F}_{MO}$ algorithm are better than any results one could get from the standard algorithm. If JUNO will start to take data and not all the reactor cores will be ready to feed the detector, the alternative method will still provide good results, as reported in SubSec. 7.2.1 and SubSec. 7.2.2. The obtained results using $\vec{F}_{MO}$ for 6 years data taking as reported in SubSec. 7.2.3 are much better compared to the results obtained by the standard method, for the same configuration. These results demonstrate three things. First, the new alternative method overcomes the issues of the standard method. Second, $\vec{F}_{MO}$ is able

Table 7.4: *The comparison of the MH sensitivity using χ^2 as a bi-dimensional estimator for actual distributions for NH sample and IH sample, for 20 different values of the atmospheric mass in the range of $2.450 \times 10^{-3}\text{eV}^2 \leq |\Delta m^2| \leq 2.580 \times 10^{-3}\text{eV}^2$. The table indicates the sensitivity calculations using the Z-test for $2D$ test.*

relative energy resolution $3\%/\sqrt{E}$										
$\lvert\Delta m^2\rvert_{NH/IH} \times 10^{-3}$	2.450		2.455		2.460		2.465		2.470	
	NH	**IH**	**NH**	**IH**	**NH**	**IH**	**NH**	**IH**	**NH**	**IH**
μ_{NH}	861.7 ± 1.532	869.1 ± 1.601	858.7 ± 1.519	867.1 ± 1.596	860.1 ± 1.542	867.6 ± 1.508	861.8 ± 1.549	869.4 ± 1.567	864.4 ± 1.61	873 ± 1.566
σ_{NH}	48.45 ± 1.083	50.61 ± 1.127	48.03 ± 1.074	50.46 ± 1.128	49.39 ± 1.104	47.67 ± 1.066	48.97 ± 1.096	49.57 ± 1.108	50.90 ± 1.138	49.54 ± 1.108
μ_{IH}	878.6 ± 1.514	853.4 ± 1.594	873.8 ± 1.501	852.8 ± 1.570	875.8 ± 1.542	852.9 ± 1.55	877.3 ± 1.582	854.1 ± 1.531	878.2 ± 1.623	859.4 ± 1.554
σ_{IH}	48.45 ± 1.083	50.41 ± 1.132	47.48 ± 1.062	49.64 ± 1.110	48.77 ± 1.091	49.03 ± 1.096	50 ± 1.119	49.57 ± 1.108	51.31 ± 1.147	49.14 ± 1.099
$z_{score}^{(NH)}$	0.2397		0.2184		0.2194		0.2198		0.2273	
$z_{score}^{(IH)}$	0.2286		0.2084		0.2227		0.2220		0.2193	
$\lvert\Delta m^2\rvert_{NH/IH} \times 10^{-3}$	2.475		2.480		2.485		2.490		2.495	
	NH	**IH**	**NH**	**IH**	**NH**	**IH**	**NH**	**IH**	**NH**	**IH**
μ_{NH}	858.5 ± 1.511	869.2 ± 1.509	859.4 ± 1.566	869.7 ± 1.551	860.3 ± 1.604	868.7 ± 1.565	864.4 ± 1.61	873 ± 1.566	864.8 ± 1.546	873 ± 1.497
σ_{NH}	47.77 ± 1.068	47.73 ± 1.067	49.51 ± 1.107	49.05 ± 1.097	50.71 ± 1.134	49.50 ± 1.107	50.9 ± 1.138	49.54 ± 1.108	48.89 ± 1.093	47.35 ± 1.059
μ_{IH}	874.1 ± 1.578	856.7 ± 1.502	876.6 ± 1.596	855.2 ± 1.55	877.1 ± 1.631	855.7 ± 1.54	878.2 ± 1.623	859.4 ± 1554	878.7 ± 1.553	859.4 ± 1.473
σ_{IH}	49.89 ± 1.116	47.49 ± 1.062	50.46 ± 1.128	49.05 ± 1.097	51.57 ± 1.153	48.71 ± 1.089	51.31 ± 1.147	49.14 ± 1.099	49.10 ± 1.098	46.6 ± 1.059
$z_{score}^{(NH)}$	0.2045		0.2250		0.2073		0.1898		0.1983	
$z_{score}^{(IH)}$	0.2098		0.2294		0.2159		0.1967		0.2068	
$\lvert\Delta m^2\rvert_{NH/IH} \times 10^{-3}$	2.500		2.510		2.520		2.523		2.530	
	NH	**IH**	**NH**	**IH**	**NH**	**IH**	**NH**	**IH**	**NH**	**IH**
μ_{NH}	862.6 ± 1.533	870.2 ± 1.599	862.4 ± 1.526	870.6 ± 1.621	865.4 ± 1.585	872.9 ± 1.561	861.8 ± 1.505	871.9 ± 1.574	862.9 ± 1.538	873.8 ± 1.552
σ_{NH}	48.49 ± 1.084	50.58 ± 1.131	48.24 ± 1.079	51.68 ± 1.156	50.12 ± 1.121	49.37 ± 1.104	47.59 ± 1.064	49.78 ± 1.113	48.64 ± 1.088	49.07 ± 1.097
μ_{IH}	877.8 ± 1.551	857.4 ± 1.578	877 ± 152	858.8 ± 1.634	881.5 ± 1.616	859.3 ± 1.534	878.3 ± 1.508	858.2 ± 1.566	879.1 ± 1.556	860.5 ± 1.54
σ_{IH}	49.04 ± 1.096	49.90 ± 1.116	48.14 ± 1.08	51.25 ± 1.146	51.09 ± 1.142	48.50 ± 1.065	47.7 ± 1.067	49.51 ± 1.107	49.21 ± 1.10	860.5 ± 1.54
$z_{score}^{(NH)}$	0.2040		0.1945		0.2083		0.2253		0.2145	
$z_{score}^{(IH)}$	0.1980		0.1822		0.2153		0.2164		0.2146	
$\lvert\Delta m^2\rvert_{NH/IH} \times 10^{-3}$	2.540		2.550		2.560		2.570		2.580	
	NH	**IH**	**NH**	**IH**	**NH**	**IH**	**NH**	**IH**	**NH**	**IH**
μ_{NH}	866.0 ± 1.509	873.5 ± 1.587	864.6 ± 1.50	875.1 ± 1.566	863.3 ± 1.568	873.0 ± 1.540	867.3 ± 1.538	872.2 ± 1.571	867.6 ± 1.613	877.9 ± 1.601
σ_{NH}	47.73 ± 1.067	50.19 ± 1.122	47.44 ± 1.061	49.53 ± 1.108	49.59 ± 1.109	48.70 ± 1.089	48.64 ± 1.088	49.68 ± 1.111	51.01 ± 1.141	50.64 ± 1.132
μ_{IH}	879.9 ± 1.555	860.9 ± 1.533	880.9 ± 1539	863.1 ± 1.5	879.0 ± 1.554	862.5 ± 1.493	880.1 ± 1.541	860.2 ± 1.579	881.6 ± 1.606	866.20 ± 1.551
σ_{IH}	49.17 ± 1.067	48.47 ± 1.084	48.67 ± 1.061	47.42 ± 1.06	49.16 ± 1.099	47.2 ± 1.055	48.73 ± 1.09	$49.941.117$	50.79 ± 1.136	49.06 ± 1.097
$z_{score}^{(NH)}$	0.1936		0.2104		0.1909		0.1803		0.1793	
$z_{score}^{(IH)}$	0.1902		0.2086		0.1966		0.1763		0.1831	

to distinguish the correct ordering even if it shows a degeneracy. Third, the alternative method is the one with the most robust results.

We reported the details of the fits on the $\vec{F}_{MO}$ distributions for several configurations of JUNO-like data taking, adding background and several systematic errors (Ch. 6). Results on MH sensitivity are not affected by this kind of background due to its slow variation in energy: it does not change the $\vec{F}_{MO}$ dispersions. The only net effect is a coherent shift of the $\vec{F}_{MO}$ peak distributions of NH and IH. The effects of systematic uncertainties on the MH measurement in reactor anti-neutrino oscillations are not relevant as discussed in SubSec. 6.4.1. The systematic uncertainties related to the reactor flux contribute to $\vec{F}_{MO}$ as simple scaling factors without changing the sensitivity on NH/IH.

The remote reactors systematic uncertainty constitutes a coherent contribution. Due to their large power they give a sizable contribution (about 12%) to the total flux. That 12% contribution may also be a relevant source of uncertainty. Tab. 7.5, Tab. 7.9 and Tab. 7.12 show the effect of adding the two remote reactors to the sensitivities results. The remote reactor contribution slightly decreases the sensitivity. Specifically, the results for $\vec{F}_{MO}$ are given by adding the remote reactors in the simulation, as well as for two and four years of exposure, 8 cores instead of 10. Ten reactors in two different sites are considered, Yangjiang and Taishan, at about $52.5\,\mathrm{km}$. In some of the tables the two remote reactor plants at Daya-Bay and Huizhou are also included.

To check the reliability of the bi-Gaussian fits for $\vec{F}_{MO}$ a large Monte Carlo simulation has been performed, $50000 + 50000$ toys, in the NH and IH hypothesis, respectively, for several random configurations. Each toy corresponds to a JUNO-like experiment, six year long in data taking. More than 10 billions of single anti-neutrino detected events were simulated. The results of this large simulation turned out to be very stable in terms of the fitted values of the Gaussian parameters. The *p*-values undergo a variation of $0.01 - 0.02\ \sigma$ in terms of sensitivity. That confirms the reliability of the assumed Gaussian approximation[1] for the used $1000 + 1000$ toy distributions [63]. Under these large Monte Carlo simulations, the variation of the two components of bi-dimensional estimator, $\vec{F}_{MO}$, remains constant confirming the robustness of the estimator (Fig. 6.15).

7.2.1 After 2 years of data taking

JUNO will not probably start the data taking with the planned 10 reactors, corresponding to less thermal power. We underwent the exercise of estimating the sensitivity in such realistic case. The $\vec{F}_{MO}$ estimator provides interesting perspectives already after two years of JUNO-like exposure, with a significance of about $3\,\sigma$ when full power will be provided. The bi-Gaussian fits of $\vec{F}_{MO}$ for JUNO-like for two years data taking for different energy resolutions for 10 near reactor cores plus the 2 remote reactor plants and no background has been obtained (Fig. 7.5) and reported (Tab. 7.5). If the two remote reactor cores are not included, the significance is still good about: $3.26\,\sigma$ for $\frac{3\%}{E}$ energy resolutions for 10 near reactor cores and no background has been considered as reported in Tab. 7.6. For a $\frac{3\%}{E}$ energy resolution a $2.7\,\sigma$ significance is obtained for 2 years data taking and 8 reactor cores plus the two far cores included as reported in Tab. 7.7. In case of 8 reactor cores without the two remote reactor cores, the significance slightly increases to $2.88\,\sigma$ as

[1] The islands of $\vec{F}_{MO}$ have been fitted to a 2D- Gaussian function.

reported in Tab. 7.8.

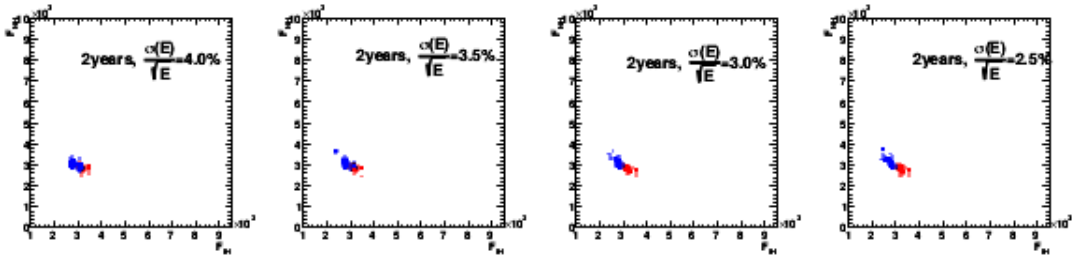

Figure 7.5: *(color online)* F_{NH} *vs* F_{IH} *distributions for* 1000 *(NH) +* 1000 *(IH) toys JUNO-like experiment, for different configurations in energy resolution. The two remote reactor cores have been added. The island top-left (blue) corresponds to the IH simulation, while the one on the bottom-right (red) corresponds to the NH simulation. The corresponding fitted values to the* $2D$ *Gaussians are those reported in Tab. 7.5.*

Table 7.5: *The bi-Gaussian fits of the* $\vec{F}_{MO}$ *distributions are reported, for the JUNO-like configuration of two years of data taking and different energy resolutions* μ_{MH}, σ_{MH} *and* r_{MH} *being the means, the standard deviations and the correlation coefficients, respectively, of the fitted* $2D$ *Gaussians. The* 10 *near reactor cores have been considered with a* $\pm 5\,\mathrm{m}$ *uniform dispersion on their relative baseline, as well as the two remote reactor plants with a* $\pm 0.5\,\mathrm{km}$ *uniform dispersion on their baseline. The sensitivity has been computed from the p-values estimation as described in the text in terms of number of* σ*'s in the two-sided option.* $n\,\sigma(\mathrm{IH})$ *stays for the IH rejection significance, and equivalently for NH.*

10 reactor cores plus the 2 remote cores					
		2 years			
		4%	3.5%	3%	2.5%
NH true	μ_{NH}	2834.2 ± 3.9	2807.4 ± 3.8	2770.5 ± 3.9	2726.6 ± 3.7
	σ_{NH}	115.6 ± 1.5	117.2 ± 2.4	121.1 ± 2.5	115.5 ± 1.5
	μ_{IH}	3125.2 ± 3.9	3145.5 ± 4.1	3179.8 ± 4.0	3220.9 ± 4.1
	σ_{IH}	123.5 ± 1.6	126.8 ± 2.7	125.7 ± 2.5	125.6 ± 1.6
	r_{NH}	-0.585 ± 0.018	-0.606 ± 0.013	-0.620 ± 0.014	-0.644 ± 0.012
IH true	μ_{NH}	3138.9 ± 4.2	3177.9 ± 4.3	3225.0 ± 4.1	3264.5 ± 3.9
	σ_{NH}	131.7 ± 2.6	132.3 ± 1.8	126.0 ± 2.6	130.2 ± 2.8
	μ_{IH}	2831.9 ± 4.0	2785.5 ± 4.1	2732.2 ± 3.8	2691.4 ± 3.8
	σ_{IH}	124.6 ± 2.5	125.4 ± 1.5	118.9 ± 0.8	118.1 ± 2.3
	r_{IH}	-0.632 ± 0.016	-0.628 ± 0.010	-0.610 ± 0.016	-0.618 ± 0.018
	$p-$value (IH)	3.21×10^{-2}	1.14×10^{-2}	1.92×10^{-3}	2.20×10^{-4}
	$n\,\sigma$ (IH)	2.14	2.53	3.10	3.69
	$p-$value (NH)	4.23×10^{-2}	1.46×10^{-2}	1.85×10^{-3}	2.59×10^{-4}
	$n\,\sigma$ (NH)	2.03	2.44	3.11	3.65

Table 7.6: *The bi-Gaussian fits of the $\vec{F}_{MO}$ distributions are reported, for the JUNO-like configuration of two years of data taking and different energy resolutions μ_{MH}, σ_{MH} and r_{MH} being the means, the standard deviations and the correlation coefficients, respectively, of the fitted $2D$ Gaussians. The ten near reactor cores have been considered with a $\pm 5\,\mathrm{m}$ uniform dispersion on their relative baseline. No background source has been included. The sensitivity has been computed from the p-values estimation as described in the text in terms of number of σ's in the two-sided option. n $\sigma(\mathrm{IH})$ stays for the IH rejection significance, and equivalently for NH.*

ten reactor cores, no background					
		2 years			
		4%	3.5%	3%	2.5%
NH true	μ_{NH}	2413.7 ± 3.8	2382.1 ± 3.7	2339.4 ± 3.8	2290.3 ± 3.8
	σ_{NH}	117.4 ± 1.6	116.9 ± 2.4	120.2 ± 2.5	117.3 ± 1.6
	μ_{IH}	2680.9 ± 4.0	2705.4 ± 4.1	2742.3 ± 4.1	2784.7 ± 4.2
	σ_{IH}	123.8 ± 1.7	127.8 ± 2.6	128.1 ± 1.6	130.0 ± 1.7
	r_{NH}	-0.557 ± 0.014	-0.581 ± 0.0.18	-0.585 ± 0.018	-0.621 ± 0.012
IH true	μ_{NH}	2730.0 ± 4.3	2771.6 ± 4.3	2819.5 ± 4.2	2864.8 ± 4.2
	σ_{NH}	135.6 ± 2.7	133.3 ± 2.7	130.5 ± 1.8	132.4 ± 2.4
	μ_{IH}	2377.4 ± 3.9	2327.5 ± 4.0	2268.3 ± 3.9	2226.2 ± 3.7
	σ_{IH}	123.7 ± 2.5	125.6 ± 2.6	120.3 ± 1.6	117.4 ± 1.7
	r_{IH}	-0.618 ± 0.017	-0.591 ± 0.017	-0.585 ± 0.013	-0.594 ± 0.012
	$p-$value (IH)	2.73×10^{-2}	7.66×10^{-3}	1.07×10^{-3}	1.07×10^{-4}
	$n\,\sigma$ (IH)	2.21	2.67	3.27	3.87
	$p-$value (NH)	3.64×10^{-2}	1.00×10^{-2}	1.12×10^{-3}	1.11×10^{-4}
	$n\,\sigma$ (NH)	2.09	2.58	3.26	3.86

Table 7.7: *The bi-Gaussian fits of the $\vec{F}_{MO}$ distributions are reported, for the JUNO-like configuration of two years of data taking and different energy resolutions μ_{MH}, σ_{MH} and r_{MH} being the means, the standard deviations and the correlation coefficients, respectively, of the fitted $2D$ Gaussians. The eight near reactor cores have been considered with a $\pm 5\,\mathrm{m}$ uniform dispersion on their relative baseline as well as the two remote reactor plants with a $\pm 0.5\,\mathrm{km}$ uniform dispersion on their relative baseline. No background source has been included. The sensitivity has been computed from the p-values estimation as described in the text in terms of number of σ's in the two-sided option. n $\sigma(IH)$ stays for the IH rejection significance, and equivalently for NH.*

8 near reactor cores plus the 2 remote cores					
		2 years			
		4%	3.5%	3%	2.5%
NH true	μ_{NH}	4192.6 ± 6.9	4149.4 ± 6.8	4083.4 ± 6.9	4016.1 ± 6.6
	σ_{NH}	212.4 ± 5.0	214.6 ± 4.4	215.2 ± 4.5	209.2 ± 4.5
	μ_{IH}	4606.3 ± 7.2	4639.1 ± 7.4	4699.3 ± 7.2	4747.1 ± 7.2
	σ_{IH}	225.2 ± 4.7	232.1 ± 4.8	226.6 ± 4.7	228.1 ± 4.7
	r_{NH}	-0.570 ± 0.012	-0.555 ± 0.019	-0.545 ± 0.020	-0.566 ± 0.013
IH true	μ_{NH}	4637.6 ± 6.7	4711.0 ± 7.6	4775.1 ± 7.0	4841.5 ± 7.5
	σ_{NH}	239.8 ± 3.7	236.9 ± 4.8	219.9 ± 4.5	232.2 ± 4.9
	μ_{IH}	4167.6 ± 5.2	4095.3 ± 7.2	4018.7 ± 6.8	3951.7 ± 6.8
	σ_{IH}	224.3 ± 3.7	225.1 ± 4.6	212.6 ± 4.4	211.5 ± 4.4
	r_{IH}	-0.588 ±0.019	-0.597 ± 0.017	-0.552± 0.019	-0.601 ± 0.013
	$p-$value (IH)	7.60×10^{-2}	3.14×10^{-2}	6.71×10^{-3}	1.57×10^{-3}
	$n\,\sigma$ (IH)	1.77	2.15	2.71	3.16
	$p-$value (NH)	9.44×10^{-2}	3.59×10^{-2}	6.08×10^{-3}	1.72×10^{-3}
	$n\,\sigma$ (NH)	1.67	2.10	2.74	3.13

Table 7.8: *The bi-Gaussian fits of the $\vec{F}_{MO}$ distributions are reported, for the JUNO-like configuration of two years of data taking and different energy resolutions, μ_{MH} , σ_{MH} and r_{MH} being the means, the standard deviations and the correlation coefficients, respectively, of the fitted $2D$ Gaussians. The eight near reactor cores have been considered with a $\pm 5\,\mathrm{m}$ uniform dispersion on their relative baseline. No background source has been included. The sensitivity has been computed from the p-values estimation as described in the text in terms of number of σ's in the two-sided option. $n\,\sigma(IH)$ stays for the IH rejection significance, and equivalently for NH.*

8 reactor cores without the two remote cores					
		2 years			
		4%	3.5%	3%	2.5%
NH true	μ_{NH}	4026.9 ± 6.5	3979.9 ± 4.1	3912.9 ± 6.6	3845.6 ± 5.5
	σ_{NH}	203.9 ± 4.2	204.7 ± 3.2	203.6 ± 3.2	198.4 ± 2.9
	μ_{IH}	4438.1 ± 6.9	4474.3 ± 3.6	4537.4 ± 7.1	4590.8 ± 4.7
	σ_{IH}	215.8 ± 4.4	221.9 ± 3.2	219.3 ± 2.7	220.9 ± 4.8
	r_{NH}	-0.575 ± 0.018	-0.564 ± 0.015	-0.553 ± 0.014	-0.575 ± 0.013
IH true	μ_{NH}	4474.2 ± 7.3	4546.0 ± 7.1	4614.9 ± 6.8	4680.5 ± 7.2
	σ_{NH}	225.7 ± 4.8	223.7 ± 4.6	212.9 ± 4.4	224.5 ± 3.9
	μ_{IH}	3998.8 ± 6.8	3928.5 ± 6.9	3849.7 ± 6.4	3782.6 ± 5.6
	σ_{IH}	210.1 ± 4.5	215.4 ± 4.4	200.9 ± 4.1	202.1 ± 4.1
	r_{IH}	-0.597 ±0.012	-0.572 ± 0.018	-0.571± 0.018	-0.580 ± 0.018
	$p-$value (IH)	6.48×10^{-2}	2.33×10^{-2}	4.33×10^{-3}	8.34×10^{-4}
	$n\,\sigma$ (IH)	1.85	2.27	2.85	3.34
	$p-$value (NH)	7.41×10^{-2}	2.65×10^{-2}	3.93×10^{-3}	9.26×10^{-4}
	$n\,\sigma$ (NH)	1.79	2.22	2.88	3.31

7.2.2 After 4 years of data taking

A further integrating result is that after only 4 years of data taking, $\vec{F}_{MO}$ will be able to distinguish the correct mass ordering with a sensitivity of $4.21\,\sigma$ using the 10 near reactor cores plus the 2 remote ones, or higher than $4.48\,\sigma$ using the 10 near reactor cores and no background has been included. The detailed sensitivities calculations for different configurations are reported in Tab. 7.9 and Tab. 7.10. The $\vec{F}_{MO}$ distributions using anti-neutrino spectrum coming from JUNO-like experiment for 4 different energy resolutions, $2.5\%, 3.0\%, 3.5\%$ and 4.0% and the 10 near reactor cores plus the 2 remote reactor plants are in Fig. 7.6.

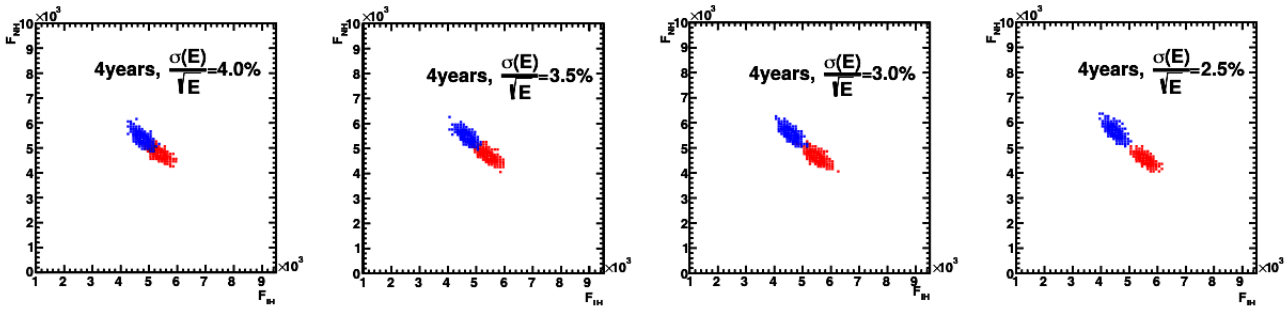

Figure 7.6: *(color online) F_{NH} vs F_{IH} distributions for 1000 (NH) + 1000 (IH) toys JUNO-like experiment, for different configurations in energy resolution. The two remote reactor cores have been added. The island top-left (blue) corresponds to the IH simulation, while the one on the bottom-right (red) corresponds to the NH simulation. The corresponding fitted values to the $2D$ Gaussian are those reported in Tab. 7.9.*

Table 7.9: *The bi-Gaussian fits of the $\vec{F}_{MO}$ distributions are reported, for the JUNO-like configuration of four years of data taking and different energy resolutions, μ_{MH}, σ_{MH} and r_{MH} being the means, the standard deviations and the correlation coefficients, respectively, of the fitted $2D$ Gaussian. The 10 near reactor cores have been considered with a $\pm 5\,\mathrm{m}$ uniform dispersion on their relative baseline, as well as the two remote reactor plants with a $\pm 0.5\,\mathrm{km}$ uniform dispersion on their relative baseline. The sensitivity has been computed from the p-values estimation as described in the text in terms of number of σ's in the two-sided option. n $\sigma(IH)$ stays for the IH rejection significance, and equivalently for NH.*

10 reactor cores plus the 2 remote cores					
		4 years			
		4%	3.5%	3%	2.5%
NH true	μ_{NH}	4784.8 ± 3.1	4712.3 ± 5.5	4638.2 ± 5.9	4545.7 ± 5.2
	σ_{NH}	170.2 ± 3.0	170.6 ± 2.3	174.4 ± 3.6	162.5 ± 2.0
	μ_{IH}	5357.8 ± 4.3	5411.3 ± 6.0	5483.2 ± 6.8	5560.4 ± 5.9
	σ_{IH}	178.8 ± 3.2	184.9 ± 2.1	190.9 ± 4.2	181.8 ± 2.3
	r_{NH}	-0.656 ± 0.009	-0.687 ± 0.010	-0.696 ± 0.014	-0.698 ±0.009
IH true	μ_{NH}	5399.6 ±6.0	5475.5 ± 5.2	5557.6 ± 6.1	5653.7 ± 6.1
	σ_{NH}	184.6 ± 3.8	181.4 ± 3.1	187.9 ±2.3	189.3 ± 2.3
	μ_{IH}	4754.5 ± 5.4	4668.3 ± 4.9	4576.9 ±5.4	4478.2 ± 5.4
	σ_{IH}	167.6 ± 3.5	170.4 ± 3.3	168.6 ± 2.0	167.0 ± 2.1
	r_{IH}	-0.650 ± 0.010	-0.670 ± 0.014	-0.707 ± 0.010	-0.687 ± 0.010
	$p-$value (IH)	3.50×10^{-3}	4.14×10^{-4}	3.06×10^{-5}	1.23×10^{-7}
	$n\,\sigma$ (IH)	2.92	3.53	4.17	5.29
	$p-$value (NH)	3.64×10^{-3}	3.92×10^{-4}	2.60×10^{-5}	1.85×10^{-7}
	$n\,\sigma$ (NH)	2.91	3.55	4.21	5.21

Table 7.10: *The bi-Gaussian fits of the $\vec{F}_{MO}$ distributions are reported, for the JUNO-like configuration of six years of data taking and different energy resolutions, μ_{MH}, σ_{MH} and r_{MH} being the means, the standard deviations and the correlation coefficients, respectively, of the fitted $2D$ Gaussian. The ten near reactor cores have been considered with a $\pm 5\,\mathrm{m}$ uniform dispersion on their relative baseline. No background source has been included. The sensitivity has been computed from the p-values estimation as described in the text in terms of number of σ's in the two-sided option. n $\sigma(IH)$ stays for the IH rejection significance, and equivalently for NH.*

ten reactor cores, no background					
		4 years			
		4%	3.5%	3%	2.5%
NH true	μ_{NH}	3763.2 ± 5.6	3674.5 ± 5.7	3586.8 ± 5.8	3470.8 ± 5.4
	σ_{NH}	176.8 ± 3.6	177.6 ± 3.8	180.7 ± 3.6	175.0 ± 2.9
	μ_{IH}	4313.9 ± 6.0	4367.7 ± 6.1	4449.0 ± 6.4	4538.6 ± 6.0
	σ_{IH}	186.5 ± 3.8	181.4 ± 3.9	201.5 ± 4.0	194.3 ± 2.6
	r_{NH}	-0.650 ± 0.016	-0.651 ± 0.010	-0.668 ± 0.015	-0.648 ± 0.010
IH true	μ_{NH}	4428.6 ± 6.2	4510.6 ± 6.1	4591.0 ± 6.2	4717.0 ± 6.3
	σ_{NH}	195.0 ± 4.0	191.4 ± 3.7	190.1 ± 2.5	173.5 ± 3.2
	μ_{IH}	3666.2 ± 5.8	3563.0 ± 5.7	3460.9 ± 5.9	3342.8 ± 5.3
	σ_{IH}	181.6 ± 3.6	177.4 ± 0.6	178.8 ± 2.4	173.5 ± 3.2
	r_{IH}	-0.629 ± 0.016	-0.644 ± 0.013	-0.663 ± 0.010	-0.633 ± 0.011
	$p-$value (IH)	2.58×10^{-3}	1.99×10^{-4}	9.69×10^{-6}	1.94×10^{-8}
	$n\,\sigma$ (IH)	3.01	3.73	4.42	5.21
	$p-$value (NH)	3.07×10^{-3}	1.95×10^{-4}	7.55×10^{-6}	2.49×10^{-8}
	$n\,\sigma$ (NH)	2.96	3.73	4.48	5.16

7.2.3 After 6 years of data taking

From the results showed above, the following key-points emerge: the results using the alternative method are much better than those using $\Delta\chi^2$ for the same conditions. Fig. 7.7 is the solid evidence of this results providing the distributions of $\vec{F}_{MO}$ for JUNO-like for 4 different energy resolutions, $2.5\%, 3.0\%, 3.5\%$ and 4.0%, for the 10 near reactor cores plus the 2 remote reactor plants. The corresponding fitted values are reported in Tab. 7.11. A similar pattern of results was reported in Tab. 7.12 but for 10 reactors only and no background being considered.

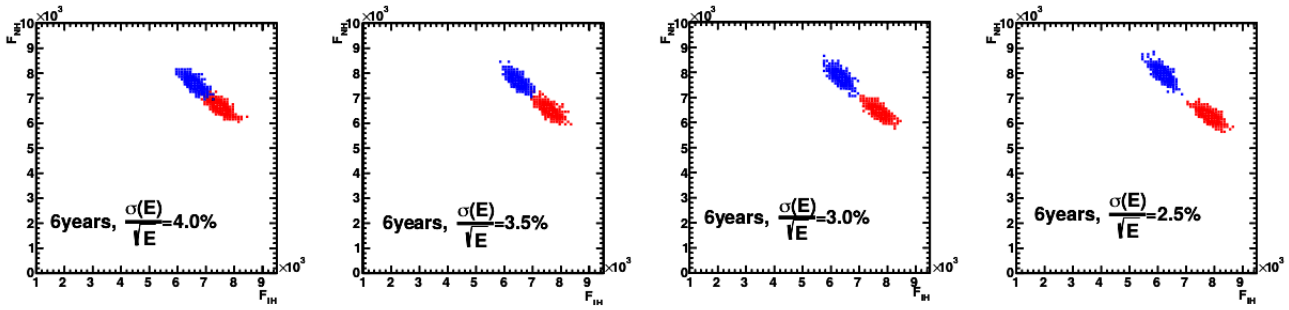

Figure 7.7: *(color online) F_{NH} vs F_{IH} distributions for 1000 (NH) + 1000 (IH) toys JUNO-like experiment for 4 different energy resolutions, $2.5\%, 3.0\%, 3.5\%$ and 4.0%. The two remote reactor cores have been added. The island top-left (blue) corresponds to the IH simulation, while the one on the bottom-right (red) corresponds to the NH simulation. The corresponding fitted values to the $2D$ Gaussians are those reported in Tab. 7.11.*

Table 7.11: *The bi-Gaussian fits of the $\vec{F}_{MO}$ distributions are reported, for the JUNO-like configuration of six years of data taking and different energy resolutions μ_{MH}, σ_{MH} and r_{MH} being the means, the standard deviations and the correlation coefficients, respectively, of the fitted $2D$ Gaussians. The 10 near reactor cores have been considered with a ± 5 m uniform dispersion on their relative baseline, as well as the two remote reactor plants with a ± 0.5 km uniform dispersion on their relative baseline. The sensitivity has been computed from the p-values estimation as described in the text in terms of number of σ's in the two-sided option. n $\sigma(IH)$ stays for the IH rejection significance, and equivalently for NH.*

10 reactor cores plus the 2 remote cores					
		6 years			
		4%	3.5%	3%	2.5%
NH true	μ_{NH}	6650.4 ± 6.8	6538.2 ± 6.8	6427.2 ± 6.6	6292.0 ± 6.5
	σ_{NH}	213.1 ± 4.1	212.1 ± 2.2	203.8 ± 4.0	201.1 ± 2.5
	μ_{IH}	7504.1 ± 7.2	7600.8 ±7.1	7693.3 ± 7.3	7817.2 ± 7.5
	σ_{IH}	224.7 ± 4.3	220.4 ± 2.8	226.4 ± 4.4	232.1 ± 2.9
	r_{NH}	-0.709 ± 0.013	-0.726 ±0.010	-0.736 ± 0.009	-0.719 ± 0.009
IH true	μ_{NH}	7583.7 ± 7.1	7685.1 ±7.3	7801.1 ± 7.3	7964.8 ± 7.2
	σ_{NH}	222.0 ± 2.7	226.7 ± 2.7	227.3 ± 4.6	222.5 ± 4.3
	μ_{IH}	6585.6 ± 6.7	6472.1 ± 6.5	6349.9 ± 6.4	6179.9 ± 6.2
	σ_{IH}	208.9 ± 2.5	202.8 ± 2.4	198.6 ± 4.0	193.5 ± 3.8
	r_{IH}	-0.704 ± 0.009	-0.731 ± 0.008	-0.713 ± 0.010	-0.708 ± 0.013
	$p-$value (IH)	4.67×10^{-4}	1.46×10^{-5}	1.36×10^{-7}	4.13×10^{-11}
	$n\,\sigma$ (IH)	3.50	4.34	5.27	6.50
	$p-$value (NH)	4.27×10^{-4}	1.35×10^{-5}	1.13×10^{-7}	1.96×10^{-11}
	$n\,\sigma$ (NH)	3.52	4.35	5.30	6.71

Table 7.12: *The bi-Gaussian fits of the $\vec{F}_{MO}$ distributions are reported, for the JUNO-like configuration of six years of data taking and different energy resolutions μ_{MH}, σ_{MH} and r_{MH} being the means, the standard deviations and the correlation coefficients, respectively, of the fitted $2D$ Gaussians. The ten near reactor cores have been considered with a $\pm 5\,\mathrm{m}$ uniform dispersion on their relative baseline. No background source has been included. The sensitivity has been computed from the p-values estimation as described in the text in terms of number of σ's in the two-sided option. n $\sigma(IH)$ stays for the IH rejection significance, and equivalently for NH.*

ten reactor cores, no background					
		6 years			
		4%	3.5%	3%	2.5%
NH true	μ_{NH}	4956.5 ± 7.3	4815.3 ± 7.1	4667.2 ± 7.0	4486.2 ± 7.1
	σ_{NH}	230.6 ± 4.3	222.3 ± 4.4	227.9 ± 4.3	219.9 ± 3.1
	μ_{IH}	5802.5 ± 7.9	5906.1 ± 7.7	6006.1 ± 7.4	6163.2 ± 8.3
	σ_{IH}	248.8 ± 0.9	239.7 ± 4.8	252.0 ± 4.6	255.9 ± 3.1
	r_{NH}	-0.674 ± 0.012	-0.684 ± 0.010	-0.682 ± 0.015	-0.706 ± 0.009
IH true	μ_{NH}	6001.9 ± 7.9	6110.2 ± 7.8	6242.9 ± 7.9	6440.7 ± 7.4
	σ_{NH}	246.4 ± 4.8	241.9 ± 5.0	248.4 ± 4.9	233.5 ± 2.9
	μ_{IH}	4791.1 ± 7.2	4644.1 ± 7.0	4491.3 ± 7.0	4280.0 ± 6.5
	σ_{IH}	226.8 ± 4.4	216.6 ± 4.5	219.2 ± 4.3	205.9 ± 2.7
	r_{IH}	-0.692 ± 0.014	-0.673 ± 0.011	-0.686 ± 0.14	-0.664 ± 0.010
	$p-$value (IH)	3.48×10^{-4}	3.51×10^{-6}	3.98×10^{-8}	7.96×10^{-11}
	$n\,\sigma$ (IH)	3.58	4.64	5.49	6.50
	$p-$value (NH)	3.30×10^{-4}	3.21×10^{-6}	3.12×10^{-8}	1.08×10^{-11}
	$n\,\sigma$ (NH)	3.59	4.66	5.53	6.79

7.2.4 Sensitivity using $\vec{F}_{MO}$ as a function of energy resolution

The experimental sensitivity using $\vec{F}_{MO}$ has direct connection with the energy resolution as confirmed in Fig. 7.8.

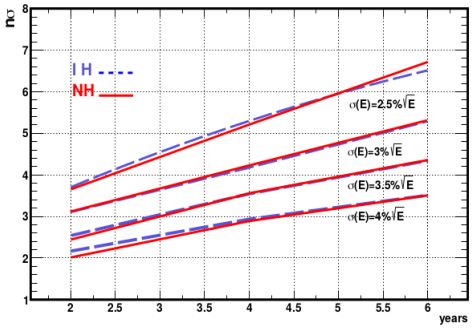

Figure 7.8: *(color online) Evolution of the NH/IH sensitivity as function of the data taking in JUNO-like experiment. The different curves correspond to different energy resolution (continuous/dashed are for NH/IH hypothesis, respectively). The background has been conservatively assumed to be described by the ^9Li component. Ten near reactor cores plus two remote cores have been used, each with a $\pm 5\,\mathrm{m}$ and $\pm 5\,\mathrm{km}$ uniform dispersions for the relative baseline, respectively.*

The result is very significant: at the foreseen six years of exposure JUNO will be able to set the mass hierarchy at more than $5\,\sigma$ significance when $\vec{F_{MO}}$. The relevance of the energy resolution is confirmed. The sensitivity curves are quite dependent on the resolution. A $4\%\sqrt{E}$ energy resolution will be critical to get a definite answer on the mass hierarchy in the JUNO context. Instead, already after two years of exposure (at a full

reactor power) JUNO would be able to provide first indications about the mass hierarchy, at a level slightly above $3\,\sigma$, for an overall $3\%\sqrt{E}$ energy resolution.

CHAPTER 8

CONCLUSIONS

It is often said that the language of science is mathematics. It could well be said that the language of experimental science is statistics. It is through statistical concepts that we quantify the correspondence between theoretical predictions and experimental observations. While the statistical analysis of the data is often treated as a final subsidiary step to an experimental physics result, a more direct approach would be quite the opposite. In fact, thinking through the requirements for a robust statistical statement is an excellent way to organize an analysis strategy.

The Neutrino Mass Hierarchy Determination (ν MHD) is one of the main goals of the major current and future neutrino experiments. The analysis usually proceeds from the standard method, the $\Delta\chi^2$ estimator. In the thesis I devoted significant attention to the standard strategy used in neutrino mass ordering determination providing a comparison between two different statistical methods; construction, implementation and results outcomes from medium baseline neutrino reactor experiments. The two main achieved targets of the thesis are; the draw-backs of the standard algorithm and the very positive results of the new alternative method.

Advances in statistical methods may play a decisive role in the discovery reached at neutrino physics experiments. So that evaluating the used statistical methods and updating them is a necessary step in building a robust statistical analysis for answering the open questions in neutrino physics. The evaluation of the standard method shows several draw-backs and concerns, together with a debatable strategy. The statistical issues on the ν MHD from the reactor experiments have been illustrated, starting from the limited power of the $\Delta\chi^2$. The $\Delta\chi^2$ estimator provides us with different results due to different simulation procedures. When the simulation is performed on a event-by-event basis and not on a semi-analytical one, the significance drastically drops. In fact, the systematic uncertainties due to the 3% relatively energy resolution causes unbalanced migration effect between events that do not show up except the simulations are done on a event-by-event basis. To confirm the effect, the simulations at infinite energy resolution are done supporting the validation of the assumption of Eq. 5.8 in case of exclusion of the systematic uncertainties. $\Delta\chi^2$ is fully controlled by the statistical assumptions as explained in Sec. 5.2. That is the major limit to the approximation, reducing the

experimental standard sensitivity that is officially reported. Second, the strong positive correlations between the $\chi^2_{min(NH)}$ and $\chi^2_{min(IH)}$ when they are drawn in a 2 dimensional map confirms the $\chi^2 = (\chi^2_{min(IH)}, \chi^2_{min(NH)})$ being a bi-dimensional estimator. JUNO sensitivity using χ^2 as bi-dimensional estimator is not promising as well. Third, the $\Delta\chi^2$ is dominated by the $|\Delta m^2|$ value as described in Sec. 5.4. Then, the MH significance using $|\overline{\Delta\chi^2}|$ depends on the values of the input parameter $|\Delta m^2|$. That is the reason we were interested in study the MHD problem using the standard method at 20 different values of $|\Delta m^2|$ in the range between $2.450 \times 10^{-3}\text{eV}^2$ and $2.580 \times 10^{-3}\text{eV}^2$.

The new alternative method, $\vec{F}_{MO}$, is based on the technique of the generalized moments to solve the standard method issues. The $\vec{F}_{MO}$ is analytically constructed using the optimal weight method [66]. As explained in Ch. 4, this method provides a recipe to derive statistical criteria for testing various hypotheses (in our case the two MH hypotheses)[1]. From the analysis of MHD, it is valuable to try to identify an estimator that couples NH/IH and decouples the Δm^2_{atm} dependence. We give insight about the strong correlation between Δm^2_{atm} and the mass hierarchy discrimination at neutrino reactor experiments. Coupling of the NH/IH hypotheses is performed by constructing an estimator that includes information from both of them. Therefore, it is no longer needed at the final stage to compare the two NH/IH hypotheses, which would incur into errors of type I and II. The sensitivity is instead evaluated as rejection of the wrong hypothesis. The F-estimator follows from that suggested in [13], and its successful application to the NOνA results [68].

The new bi-dimensional estimator, $\vec{F}_{MO}$, is representing a new alternative method to solve the neutrino mass hierarchy problem in the medium base-line neutrino reactor experiments. $\vec{F}_{MO}$ has been introduced to determine the correct ν mass hierarchy with reactor anti-neutrinos in a JUNO-like experiment. We demonstrated that $\vec{F}_{MO}$ owns several properties. First, it allows coupling the two hypotheses, NH and IH, so granting the use of the simple approach suggested in [13]. Under the assumption of the 3-neutrino oscillation paradigm only one of the two hypotheses is possible. If data analysis will be compatible with e.g. NH, then IH can be rejected via a simple *p*-value computation. We introduced a conservative procedure to define the sensitivity in terms of *p*-values[2]. The results are very promising: the two mass hierarchies can be largely discriminated ($> 5\,\sigma$) in JUNO after six years of exposure, keeping the total energy resolution at 3%. After two years of running and the foreseen initially-reduced available reactor power a little less than $3\,\sigma$ will still be possible. The price to pay is to admit a Δm^2_{atm} degeneracy at the level of $12 \times 10^{-5}\text{eV}^2$, which is much larger than the current global fits uncertainty. Our study confirms the very positive perspectives for JUNO to determine the mass ordering using the new alternative method. Second, the $\vec{F}_{MO}$ successfully avoids the standard method issues. $\vec{F}_{MO}$ is stable under different choices of the baseline L. Third, the background conservatively included in the $\vec{F}_{MO}$ analysis due to its slow variation in energy that does not change the $\vec{F}_{MO}$ dispersions and consequentiality does not affect MH sensitivity. Furthermore, $\vec{F}_{MO}$ is so defined to factorize out all the incoherent background sources and their systematics. The background components produce insensitive shifts of the two NH/IH regions in $\vec{F}_{MO}$. Systematic components, smoothly varying with the neutrino energy, are responsible of a coherent depletion of $\vec{F}_{MO}$, which can be overcome with a

[1] The same method was successfully used in data analysis of Troitsk neutrino mass experiment that resulted in the best neutrino mass limit [3]. In addition, it has been used to construct specific statistical tests for searches of anomalies in tritium $\beta-$spectrum [67].

[2] In Appendix B, we explained the procedures used for p-value calculations for $2D$ test statistics.

corresponding (small) increase in exposure. Only the coherent background due to the two remote reactor plants, at 215 and $265\,\mathrm{km}$ away, gives a decrease of about $0.2\,\sigma$ on the sensitivity.

As a side result the new technique provides the evaluation of Δm^2_{atm} with an unprecedented precision at reactors, less than 1%. That is due to the strong correlation of $\vec{F}_{MO}$ to Δm^2_{atm}, which will deserve more refined analyses and promise even more interesting results. The study here presented contributes to clarify the impact of Δm^2_{atm} on the mass hierarchy determination at reactor experiments, and the corresponding limited sensitivity that can be obtained with a $\Delta\chi^2$ procedure. The new alternative $2D$ test statistics, $\vec{F}_{MO}$, provides much better results than those from the standard algorithm, $\Delta\chi^2$.

SUMMARY

The thesis describes an statistical analysis project for the ν mass hierarchy determination (MHD). The aim was to achieve a complete statistical analysis based on a full comparison between a new bi-dimensional estimator and the standard algorithm (Δchi^2). From statistical point of view, this problem is a test to distinguish between two hypothesis; normal hierarchy (NH) and inverted hierarchy (IH). 20 different samples have been produced, each sample being 1000 JUNO-toys simulations for each hypothesis (IH & NH) and two energy resolution (3% and infinite). Then, the statistical analysis was preformed to determine the correct neutrino mass hierarchy using the standard algorithm. The evaluation of the standard method showed several draw-backs and concerns, together with a debatable strategy. The three main draw-backs of the standard method are: first, when the side-bins correlations are taking into account the statistical assumptions are no more valid and the limited power of the $\Delta\chi^2$ manifests itself; second, the experimental sensitivity strongly depends on the value of the neutrino atmospheric mass difference; third, the overlapping between the χ^2 distributions of the two hypotheses leads to a reduction of the experimental sensitivity.

We identified an estimator that couples NH/IH and decouples the Δm^2_{atm} dependence. The $\vec{F}_{MO}$ is representing a new alternative method to solve the neutrino mass hierarchy problem in the neutrino medium baseline reactor experiments. The $\vec{F}_{MO}$, provides much better results than those from $\Delta\chi^2$. The $\vec{F}_{MO}$ successfully avoids the standard method issues. Possible results after two, four and six years of running and the foreseen initially-reduced available reactor power have been studied as well. $\vec{F}_{MO}$ estimator gives confidence to reject the false mass hierarchy at more than $5\,\sigma$ at the price of a degenerate two values of the Δm^2_{atm}. However, this degeneracy can be properly handled. These results confirm the very positive perspectives for JUNO to determine the mass ordering in a vacuum-oscillation dominated regime if the proper statistical analysis is used.

APPENDIX A

THE PARAMETERIZATION

The $\vec{F}_{MO}$ is constructed using the parameterization used in [27], which is different than the parametrization used for χ^2 [1]. Therefore, we checked that the neutrino MH significance does not depend on the used parameterization. In the other words, the two different parameterizations of the reactor ν_e survival probability that are used in the two estimator constructions are equivalent to each other. The neutrino survival probability in terms of $(\Delta m^2_{ee}, \phi)$ that is used for χ^2 in [1], is

$$P_{(\nu_e \to \nu_e)} = 1 - \frac{1}{2} sin^2 2\theta_{13} [1 - \sqrt{1 - sin^2 2\theta_{12} sin^2 \triangle_{21}} \times \cos(2|\triangle_{ee}| \pm \phi)] - cos^4 \theta_{13} sin^2 2\theta_{12} sin 2\triangle_{21}, \tag{A.1}$$

where θ_{13} and θ_{12} are the ν mixing angles. Then, the survival probability assuming normal and inverted hierarchy are P_{NH} and P_{IH} respectively. The difference between the two survival probability (ΔP) is:

$$\Delta P = P_{NH} - P_{IH} = (\frac{1}{2} sin^2 2\theta_{13})(\sqrt{1 - sin^2 2\theta_{12} sin^2 \triangle_{21}}) \left[\cos(2|\triangle_{ee}| + \phi) - \cos(2|\triangle_{ee}| - \phi)\right] \tag{A.2}$$

$$\Delta_{21} = \Delta m^2_{21} L/4E, \quad \Delta_{ee} = \Delta m^2_{ee} L/4E, \quad \Delta m^2_{ee} = \Delta m^2 + \frac{\alpha}{2}(C^2_{12} - S^2_{12})\delta m^2. \tag{A.3}$$

where $\alpha = \pm 1$ for NH/IH, respectively. ΔP can be expressed as:

$$\Delta P = (\frac{1}{2} sin^2 2\theta_{13})(\sqrt{1 - sin^2 2\theta_{12} sin^2 \triangle_{21}}) \times \left[cos(\frac{2\Delta m^2 L + (c^2_{12} - s^2_{12})\delta m^2 L}{4E} + \phi) - cos(\frac{2\Delta m^2 L - (c^2_{12} - s^2_{12})\delta m^2 L}{4E} - \phi)\right] \tag{A.4}$$

Defining

$$\beta = \frac{(c^2_{12} - s^2_{12})\delta m^2 L}{4E} \qquad q = \frac{2\Delta m^2 L}{4E}, \tag{A.5}$$

then

$$\cos(\frac{2\Delta m^2 L + (c^2_{12} - s^2_{12})\delta m^2 L}{4E} + \phi) - \cos(\frac{2\Delta m^2 L - (c^2_{12} - s^2_{12})\delta m^2 L}{4E} - \phi) = \cos(q + \beta + \phi) - \cos(q - \beta - \phi). \tag{A.6}$$

Using trigonometric identities we rewrite it as:

$$\cos(q+\beta+\phi)-\cos(q-\beta-\phi)=-2\sin(q)[\sin(\beta+\phi)]=-2\sin(q)[sin\beta cos\phi+cos\beta sin\phi] \tag{A.7}$$

Recalling the definitions;

$$sin\phi=\frac{c_{12}^2 sin(2s_{12}^2\triangle_{21})-s_{12}^2 sin(2c_{12}^2\triangle_{21})}{\sqrt{1-sin^2 2\theta_{12} sin^2\triangle_{21}}},\quad cos\phi=\frac{c_{12}^2 cos(2s_{12}^2\triangle_{21})+s_{12}^2 cos(2c_{12}^2\triangle_{21})}{\sqrt{1-sin^2 2\theta_{12} sin^2\triangle_{21}}} \tag{A.8}$$

Then,

$$sin\beta cos\phi+cos\beta sin\phi=\frac{sin(\frac{L\delta m^2}{4E})(c_{12}^2-s_{12}^2)}{\sqrt{1-sin^2 2\theta_{12} sin^2\triangle_{21}}} \tag{A.9}$$

Eq. A.4 becomes:

$$\Delta P=(\frac{1}{2}sin^2 2\theta_{13})(\sqrt{1-sin^2 2\theta_{12} sin^2\triangle_{21}})\times(-2\sin(\frac{2\Delta m^2 L}{4E}))\frac{sin(\frac{L\delta m^2}{4E})(c_{12}^2-s_{12}^2)}{\sqrt{1-sin^2 2\theta_{12} sin^2\triangle_{21}}}. \tag{A.10}$$

After arrangement becomes

$$\Delta P=(\frac{1}{2}sin^2 2\theta_{13})\times(-2\sin(\frac{2\Delta m^2 L}{4E}))\times sin(\frac{L\delta m^2}{4E})(c_{12}^2-s_{12}^2). \tag{A.11}$$

Knowing that

$$\Delta P_{IH-NH}=-\Delta P_{NH-IH},\qquad c_{12}^2-s_{12}^2=\cos(2\theta_{12}), \tag{A.12}$$

Eq. A.4 becomes

$$\Delta P_{IH-NH}=\sin^2 2\theta_{13}\times\cos(2\theta_{12})\times\sin(\frac{\delta m^2 L}{4E})\times\sin(\frac{\Delta m^2 L}{2E}) \tag{A.13}$$

Since $\Delta m^2=\Delta m^2=\Delta m^2_{atm}-\delta m^2/2$, Eq. A.4 becomes

$$\Delta P_{IH-NH}=\sin^2 2\theta_{13}\times\cos(2\theta_{12})\times\sin(\frac{\delta m^2 L}{4E})\times\sin(\frac{L}{2E}(\Delta m^2_{atm}-\delta m^2/2)) \tag{A.14}$$

that is the exact expression used for the $\vec{F}_{MO}$ parameterization (Eq. 6.10).

APPENDIX B

METHODOLOGY FOR *P*-VALUE CALCULATIONS FOR BI-DIMENSIONAL TEST STATISTICS

Since the JUNO real data are not available yet, we used an estimated *p*-value corresponding to the weighted *p*-value over the domain of the alternative hypothesis at a certain $C.L.$ In this appendix, we explain the mathematical procedures used for *p*-value calculations for a generic $2D$ test statistics (T). Assuming the null hypothesis is true within a certain confidence level, an average *p*-value for the alternative hypothesis is evaluated weighted by the true hypothesis probability. An error ellipse is define at certain $C.L.$ on the alternative hypothesis. Then, for each point inside this error ellipse, the weighted *p*-value is calculated for the null hypothesis, as indicated in the equation below assuming that the IH is the null hypothesis and NH is the alternative one:

$$P_{val}(IH)_{weighted} = P_{val}(IH) \otimes Weight \tag{B.1}$$

$$= \int_{\Omega_{NH}} d\bar{x} \left[\int_{\Omega_{NH}(\bar{x})} d\bar{x} \left(G(T|IH)_{\bar{x}} \bullet G(T|NH)_{\bar{x}} \right] \right. \tag{B.2}$$

$$\Omega_{NH} \perp \int_{\Omega_{NH}} d\bar{x} G(T|NH)_{\bar{x}} = C.L.$$

$$\Omega_{NH}(\bar{x}) \ni T(\bar{x'}|IH) \leqslant T(\bar{x}|IH);\ \bar{x'} \epsilon\, \Omega_{NH} \tag{B.3}$$

$G(T|IH)$ is the density distribution of the test statistics T assuming the null hypothesis and $G(T|NH)$ is the density distribution the test statistics T assuming the alternative hypothesis. The $C.L.$ is the chosen confidence level for the alternative hypothesis. For the visual explanation, Fig. B.1 is provided.

Assuming a $C.L.$ of 95% then the computed *p*-value has to be read as: the value corresponds to the significance to reject the wrong hierarchy at the 95% C.L. for the true one. We preferred to be very conservative and a $99.7\% C.L.$, was chosen to define the domain where the true hypothesis is expected to be observed. This procedure is

more conservative than the evaluation of the standard *p*-value on the median of the true hypothesis $(50\% C.L.)$. For larger $C.L.$, e.g. at $95\% C.L.$ of the true hypothesis, our method is more conservative when the two hypotheses are distant from each others by at least $3-4\ \sigma$. When the two hypothesis probabilities are closer than $3\,\sigma$, with a $C.L. = 99.7\%$, our method gives slightly less conservative *p*-values than the standard ones. That is explained by the depletion due to the low probability of the true hypothesis in the far domain.

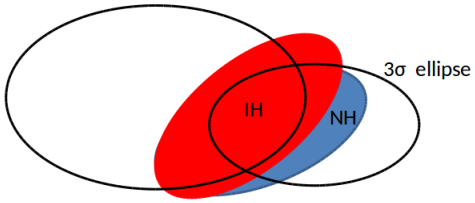

Figure B.1: *The carton represents how p-value for bi-dimensional test statistics can be calculated.*

APPENDIX C

FITTING WITH TMINUIT CLASS

The fitting procedures and the minimization of χ^2 are done via the ROOT minimization libraries (the TMinuit algorithm). In the minimization procedure all the oscillation parameters were fixed to the best-fitting values of [1]. A total of 108357 signal events are processed for each toy-simulations. The official version of JUNO Software "J17v1r1" is used. $\Delta\chi^2$ will be often scaled with the number of degrees of freedom, which is clearly equal to the number of fitted data minus the constraints: $bin - 6$. Fig. C.1 and Fig. C.2 indicate χ^2 distributions for 1000 toy JUNO-like simulations generated for NH and IH samples respectively. The simulations are generated at 20 different values of the atmospheric mass in the range of $2.450 \times 10^{-3}\text{eV}^2 \leq |\Delta m^2| \leq 2.580 \times 10^{-3}\text{eV}^2$ for NH hypothesis (blue graphs) and for IH hypothesis (red graphs) with six years of exposure and the ten near reactor cores with an infinite energy resolution. Fig. C.3 and Fig. C.4 indicate the χ^2 distributions for 1000 toy JUNO-like simulations generated for NH and IH samples respectively. The simulations are generated at 20 different values of the atmospheric mass in the range of $2.450 \times 10^{-3}\text{eV}^2 \leq |\Delta m^2| \leq 2.580 \times 10^{-3}\text{eV}^2$ for NH hypothesis (blue graphs) and for IH hypothesis (red graphs) with six years of exposure and the ten near reactor cores with an $3\%/\sqrt{E}$ energy resolution.

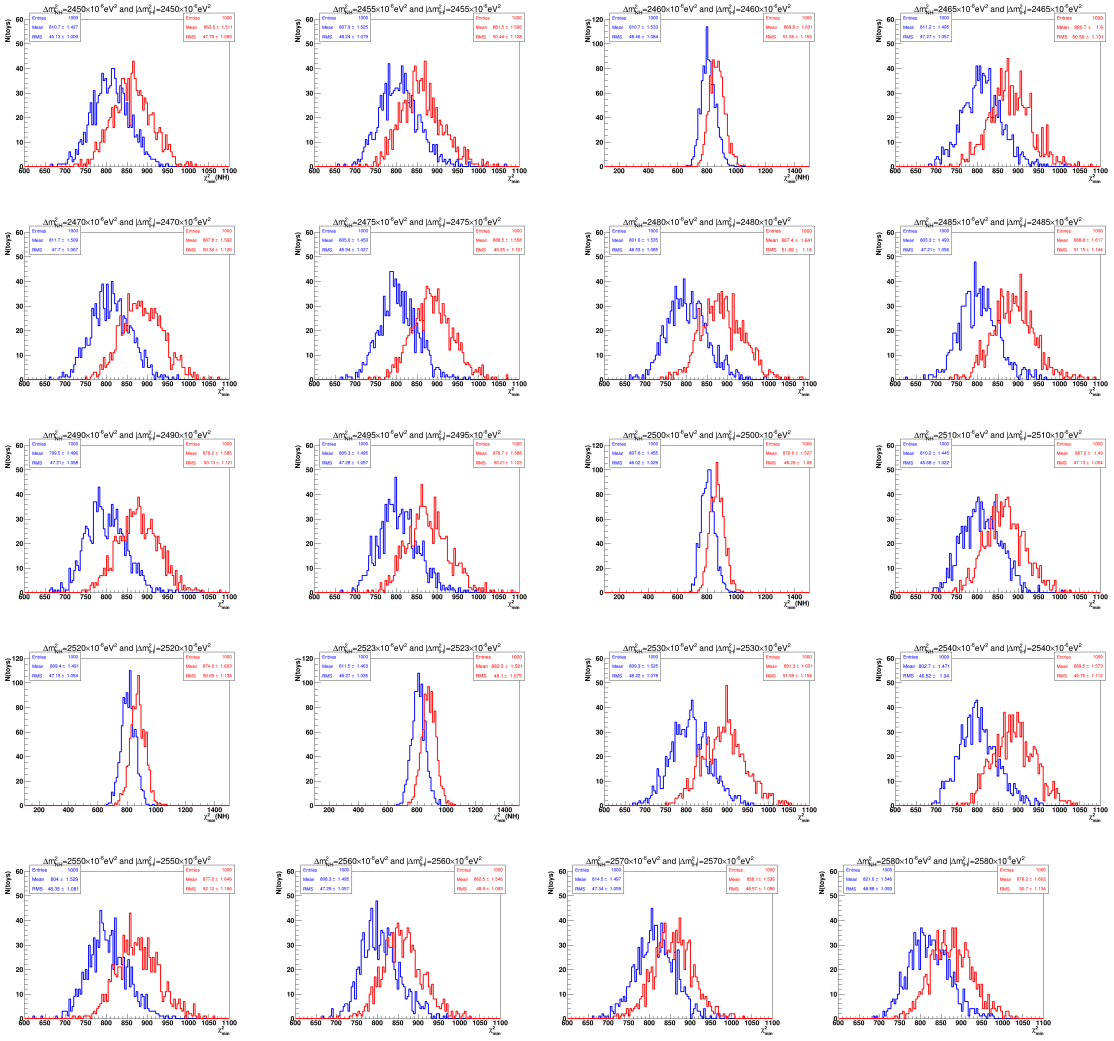

Figure C.1: *χ^2 distributions for 1000 toy JUNO-like simulations generated for NH samples at 20 different values of the atmospheric mass in the range of $2.450\times10^{-3}\text{eV}^2 \leq |\Delta m^2| \leq 2.580\times10^{-3}\text{eV}^2$ for NH hypothesis (blue graphs) and for IH hypothesis (red graphs) with six years of exposure and the ten near reactor cores with an infinite energy resolution.*

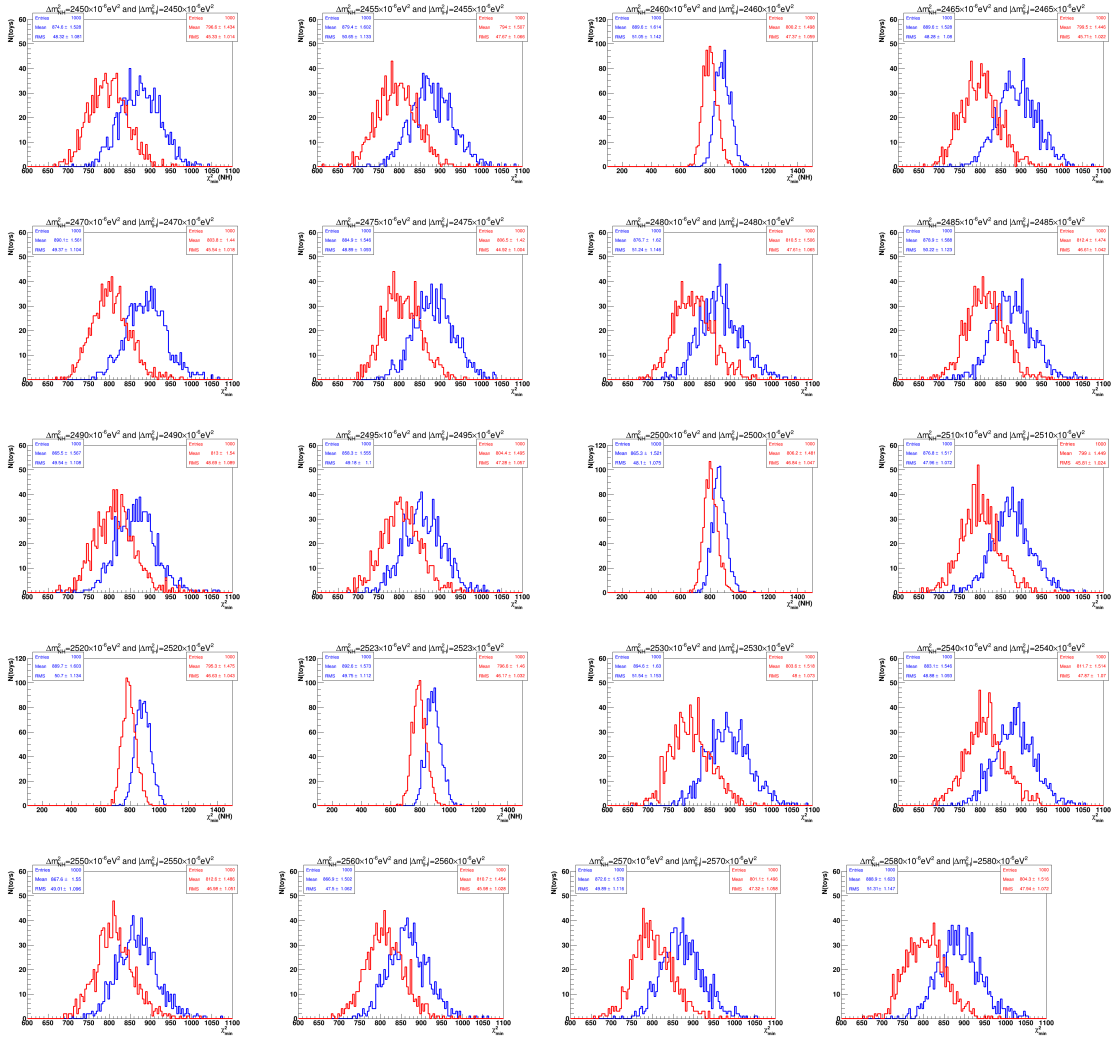

Figure C.2: *χ^2 distributions for 1000 toy JUNO-like simulations generated for IH samples at 20 different values of the atmospheric mass in the range of $2.450\times10^{-3}\text{eV}^2 \leq |\Delta m^2| \leq 2.580\times10^{-3}\text{eV}^2$ for NH hypothesis (blue graphs) and for IH hypothesis (red graphs) with six years of exposure and the ten near reactor cores with an infinite energy resolution.*

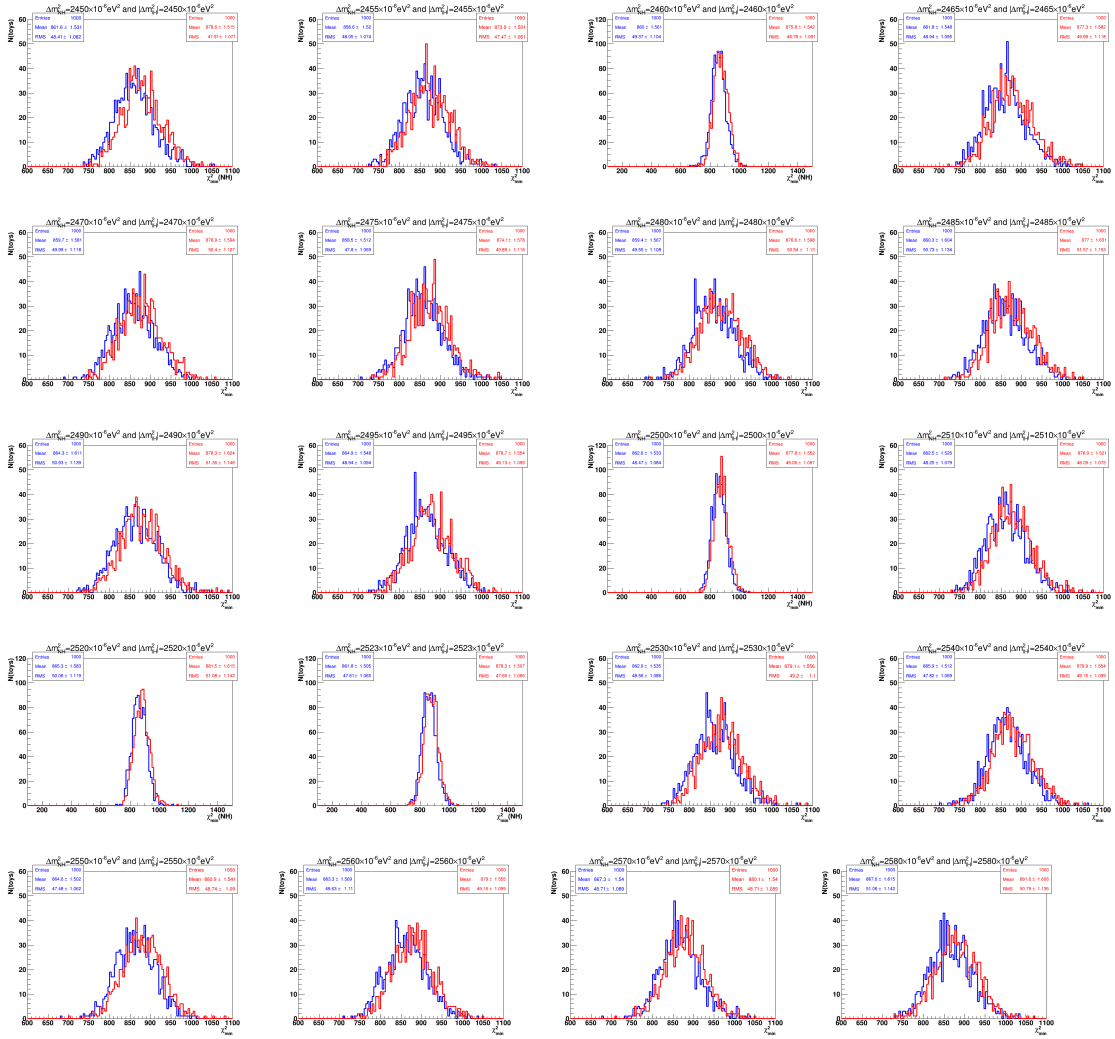

Figure C.3: χ^2 *distributions for 1000 toy JUNO-like simulations generated for NH samples at* 20 *different values of the atmospheric mass in the range of* $2.450\times10^{-3}\text{eV}^2 \leq |\Delta m^2| \leq 2.580\times10^{-3}\text{eV}^2$ *for NH hypothesis (blue graphs) and for IH hypothesis (red graphs) with six years of exposure and the ten near reactor cores with an* $3\%/\sqrt{E}$ *energy resolution.*

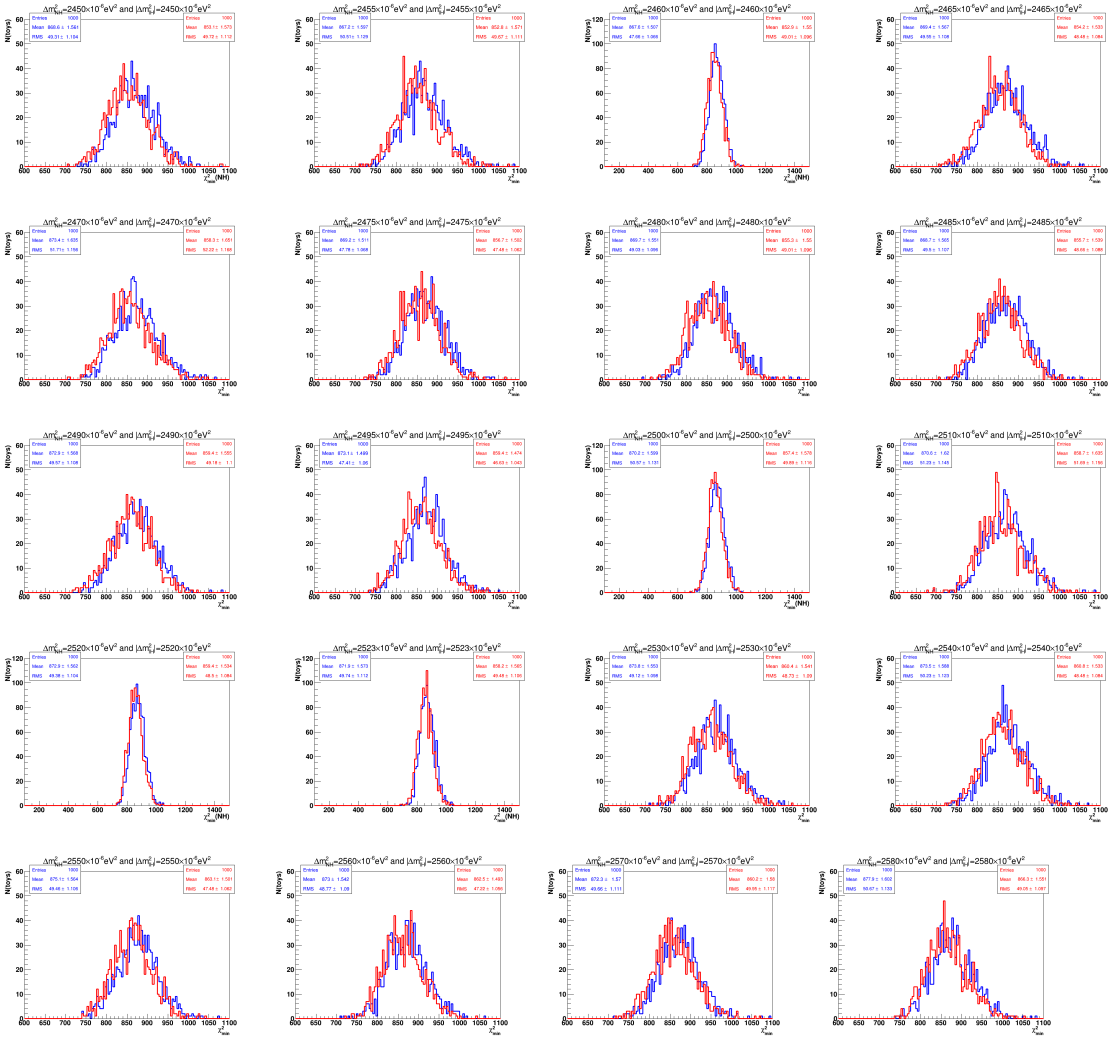

Figure C.4: *χ^2 distributions for 1000 toy JUNO-like simulations generated for IH samples at 20 different values of the atmospheric mass in the range of $2.450\times10^{-3}\text{eV}^2 \leq |\Delta m^2| \leq 2.580\times10^{-3}\text{eV}^2$ for NH hypothesis (blue graphs) and for IH hypothesis (red graphs) with six years of exposure and the ten near reactor cores with an $3\%/\sqrt{E}$ energy resolution.*

BIBLIOGRAPHY

[1] Fengpeng An and Guangpeng et al An. “Neutrino physics with JUNO”. In: *Journal of Physics G: Nuclear and Particle Physics* 43.3 (2016), p. 030401.

[2] VM Lobashev. “The search for the neutrino mass by direct method in the tritium beta-decay and perspectives of study it in the project KATRIN”. In: *Nuclear Physics A* 719 (2003), pp. C153–C160.

[3] VN Aseev et al. “Upper limit on the electron antineutrino mass from the Troitsk experiment”. In: *Physical Review D* 84.11 (2011), p. 112003.

[4] http://www-numi.fnal.gov/public/story.html.

[5] Fumihiko Suekane. *Neutrino oscillations: a practical guide to basics and applications*. Vol. 898. Springer, 2015.

[6] Zhizhong Xing and Shun Zhou. *Neutrinos in particle physics, astronomy and cosmology*. Springer Science & Business Media, 2011.

[7] Frederick Reines and C Cowan. “The Reines-Cowan experiments: detecting the poltergeist”. In: *Los Alamos Sci.* 25 (1997), pp. 4–27.

[8] Bruno Pontecorvo. “Neutrino experiments and the problem of conservation of leptonic charge”. In: *Sov. Phys. JETP* 26.984-988 (1968), p. 165.

[9] Bruce T. Cleveland and Timothy et al Daily. “Measurement of the solar electron neutrino flux with the Homestake chlorine detector”. In: *The Astrophysical Journal* 496.1 (1998), p. 505.

[10] Carlo Giunti and Chung W Kim. *Fundamentals of neutrino physics and astrophysics*. Oxford university press, 2007.

[11] http://www.hyper-k.org/en/overview.html.

[12] N Agafonova et al. “Observation of a first ν_τ candidate event in the OPERA experiment in the CNGS beam”. In: *Physics Letters B* 691.3 (2010), pp. 138–145.

[13] Luca Stanco. “A view of neutrino studies with the next generation facilities”. In: *Reviews in Physics* 1 (2016), pp. 90–100.

[14] Sandhya Choubey, ST Petcov, and M Piai. “Precision neutrino oscillation physics with an intermediate baseline reactor neutrino experiment”. In: *Physical Review D* 68.11 (2003), p. 113006.

[15] Francesco Iachello. “Open problems in neutrino physics”. In: *Journal of Physics: Conference Series*. Vol. 1056. 1. IOP Publishing. 2018, p. 012027.

[16] JJ Gomez-Cadenas and Justo Martin-Albo. “Phenomenology of neutrinoless double beta decay”. In: *arXiv preprint arXiv:1502.00581* (2015).

[17] SM Bilenky and Carlo Giunti. “Neutrinoless double-beta decay: A brief review”. In: *Modern Physics Letters A* 27.13 (2012), p. 1230015.

[18] Peter AR Ade et al. “Planck 2013 results. XVI. Cosmological parameters”. In: *Astronomy & Astrophysics* 571 (2014), A16.

[19] M Fukugita and Tsutomu Yanagida. “Barygenesis without grand unification”. In: *Physics Letters B* 174.1 (1986), pp. 45–47.

[20] A Aguilar-Arevalo and W et al Metcalf. “Evidence for neutrino oscillations from the observation of anti-neutrino (electron) appearance in a anti-neutrino (muon) beam”. In: *Physical Review D* 64.hep-ex/0104049 (2001), p. 112007.

[21] AA Aguilar-Arevalo et al. “Event excess in the MiniBooNE search for $\nu_\mu \to \nu_e$ oscillations”. In: *Physical review letters* 105.18 (2010), p. 181801.

[22] G Mention et al. “Reactor antineutrino anomaly”. In: *Physical Review D* 83.7 (2011), p. 073006.

[23] Joachim Kopp et al. “Sterile neutrino oscillations: the global picture”. In: *Journal of High Energy Physics* 2013.5 (2013), p. 50.

[24] C Giunti et al. “Pragmatic view of short-baseline neutrino oscillations”. In: *Physical Review D* 88.7 (2013), p. 073008.

[25] AA Aguilar-Arevalo et al. “Unexplained excess of electronlike events from a 1-GeV neutrino beam”. In: *Physical Review Letters* 102.10 (2009), p. 101802.

[26] Zhi-zhong Xing, Zhen-hua Zhao, and Ye-Ling Zhou. “How to interpret a discovery or null result of the $0\nu2\beta$ decay”. In: *The European Physical Journal C* 75.9 (2015), p. 423.

[27] SM Bilenky, F Capozzi, and ST Petcov. “An alternative method of determining the neutrino mass ordering in reactor neutrino experiments”. In: *Physics Letters B* 772 (2017), pp. 179–183.

[28] Francesco Capozzi et al. “Global constraints on absolute neutrino masses and their ordering”. In: *Physical Review D* 95.9 (2017), p. 096014.

[29] X Qian et al. “Mass hierarchy resolution in reactor anti-neutrino experiments: parameter degeneracies and detector energy response”. In: *Physical Review D* 87.3 (2013), p. 033005.

[30] JL Hewett and H et al Weerts. “Planning the future of US particle physics (Snowmass 2013): Chapter 2: Intensity frontier”. In: *arXiv preprint arXiv:1401.6077* (2014).

[31] http://t2k-experiment.org/.

[32] Y Suzuki. “Talk at XVIII International Conferance on Neutrino Physics and Astrophysics”. In: *Physical Review Letters* 81 (1998), p. 1158.

[33] KamLAND Eguchi and S et al Enomoto. “First results from KamLAND: evidence for reactor antineutrino disappearance”. In: *Physical Review Letters* 90.2 (2003), p. 021802.

[34] Kazuto Hirata and Takaaki et al Kajita. “Observation of a neutrino burst from the supernova SN1987A”. In: *Physical Review Letters* 58.14 (1987), p. 1490.

[35] F Suekane et al. “An overview of the KamLAND 1-kiloton liquid scintillator”. In: *arXiv preprint physics/0404071* (2004).

[36] Yasaman Farzan and Mariam Tortola. “Neutrino Oscillations and Non-standard Interactions”. In: *Frontiers in Physics* 6 (2018), p. 10. ISSN: 2296-424X. DOI: 10.3389/fphy.2018.00010. URL: https://www.frontiersin.org/article/10.3389/fphy.2018.00010.

[37] FP An et al. “A side-by-side comparison of Daya Bay antineutrino detectors”. In: *Nuclear Instruments and Methods in Physics Research Section A: Accelerators, Spectrometers, Detectors and Associated Equipment* 685 (2012), pp. 78–97.

[38] http://dayabay.ihep.ac.cn/docs/experiment.html.

[39] Soo-Bong Kim, Thierry Lasserre, and Yifang Wang. “Reactor neutrinos”. In: *Advances in High Energy Physics* 2013 (2013).

[40] Feng Peng An et al. “Measurement of electron antineutrino oscillation based on 1230 days of operation of the Daya Bay experiment”. In: *Physical Review D* 95.7 (2017), p. 072006.

[41] A Minotti et al. “Latest results from Double CHOOZ”. In: *Physics of Particles and Nuclei* 48.1 (2017), pp. 47–54.

[42] Carmen Palomares, Double CHOOZ Collaboration, et al. “Double-Chooz neutrino experiment”. In: *Journal of Physics: Conference Series*. Vol. 335. 1. IOP Publishing. 2011, p. 012055.

[43] JK Ahn and Reno Collaboration. “RENO: An Experiment for Neutrino Oscillation Parameter θ_{13} Using Reactor Neutrinos at Yonggwang”. In: *preprint arXiv:1003.1391* (2010).

[44] Soo-Bong Kim. “Observation of Reactor electron antinetrino disapperance at RENO”. In: *Nuclear Physics B-Proceedings Supplements* 235 (2013), pp. 24–29.

[45] Seon-Hee Seo. “New results from RENO”. In: *arXiv preprint arXiv:1312.4111* (2013).

[46] PF de Salas and DV et al Forero. “Status of neutrino oscillations 2018: 3σ hint for normal mass ordering and improved CP sensitivity”. In: *Physics Letters B* 782 (2018), pp. 633–640.

[47] Valencia-Globalfit. http://globalfit.astroparticles.es/. 2018.

[48] Feng Peng An et al. “Measurement of electron antineutrino oscillation based on 1230 days of operation of the Daya Bay experiment”. In: *Physical Review D* 95.7 (2017), p. 072006.

[49] Myoung Youl Pac. “Recent results from RENO”. In: *arXiv preprint arXiv:1801.04049* (2018).

[50] Y Abe and JC et al Dos Anjos. “Improved measurements of the neutrino mixing angle θ_13 with the Double Chooz detector”. In: *Journal of High Energy Physics* 2014.10 (2014), p. 86.

[51] http://juno.ihep.cas.cn/.

[52] T. Adam and F. et al An. “JUNO conceptual design report”. In: *arXiv preprint arXiv:1508.07166* (2015).

[53] Jerzy Neyman and Egon Sharpe Pearson. “IX. On the problem of the most efficient tests of statistical hypotheses”. In: *Philosophical Transactions of the Royal Society of London. Series A, Containing Papers of a Mathematical or Physical Character* 231.694-706 (1933), pp. 289–337.

[54] Lars Peter Hansen. “Large sample properties of generalized method of moments estimators”. In: *Econometrica: Journal of the Econometric Society* (1982), pp. 1029–1054.

[55] Fyodor V Tkachov. “Approaching the parameter estimation quality of maximum likelihood via generalized moments”. In: *arXiv preprint physics/0001019* (2000).

[56] VN Aseev et al. “Measurement of the electron antineutrino mass in tritium beta decay in the Troitsk nu-mass experiment”. In: *Physics of atomic nuclei* 75.4 (2012), pp. 464–478.

[57] Fyodor V Tkachov. “Quasi-optimal observables: Attaining the quality of maximal likelihood in parameter estimation when only a MC event generator is available”. In: *arXiv preprint physics/0108030* (2001).

[58] Fyodor Tkachov. “Quasi-optimal weights: a versatile tool of data analysis”. In: *Journal of Physics: Conference Series*. Vol. 523. 1. IOP Publishing. 2014, p. 012030.

[59] Emilio Ciuffoli, Jarah Evslin, and Xinmin Zhang. “Confidence in a neutrino mass hierarchy determination”. In: *Journal of High Energy Physics* 2014.1 (2014), p. 95.

[60] P. F. de Salas et al. “Neutrino Mass Ordering from Oscillations and Beyond: 2018 Status and Future Prospects”. In: (2018). DOI: 10.3389/fspas.2018.00036. arXiv: 1806.11051 [hep-ph].

[61] S. Gariazzo et al. “Neutrino masses and their ordering: Global Data, Priors and Models”. In: *JCAP* 1803.03 (2018), p. 011. DOI: 10.1088/1475-7516/2018/03/011. arXiv: 1801.04946 [hep-ph].

[62] Shao-Feng Ge et al. “Determination of mass hierarchy with medium baseline reactor neutrino experiments”. In: *Journal of High Energy Physics* 2013.5 (2013), p. 131.

[63] Luca Stanco et al. “A new way to determine the neutrino mass hierarchy at reactors”. In: *arXiv preprint arXiv:1707.07651* (2017).

[64] Yu-Feng Li et al. “Unambiguous determination of the neutrino mass hierarchy using reactor neutrinos”. In: *Physical Review D* 88.1 (2013), p. 013008.

[65] Feng Peng An et al. “Improved measurement of the reactor antineutrino flux and spectrum at Daya Bay”. In: *Chinese Physics C* 41.1 (2017), p. 013002.

[66] Fyodor V Tkachov. “Transcending the least squares”. In: *arXiv preprint physics 0604127* (2006).

[67] AV Lokhov, FV Tkachov, and PS Trukhanov. “Application of quasi-optimal weights to searches of anomalies. Statistical criteria for step-like anomalies in cumulative spectra”. In: *Nuclear Instruments and Methods in Physics Research Section A: Accelerators, Spectrometers, Detectors and Associated Equipment* 686 (2012), pp. 162–167.

[68] L Stanco, Stefano Dusini, and M Tenti. “Determination of the neutrino mass hierarchy with a new statistical method”. In: *Physical Review D* 95.5 (2017), p. 053002.

[69] Yu-Feng Li et al. “Unambiguous determination of the neutrino mass hierarchy using reactor neutrinos”. In: *Physical Review D* 88.1 (2013), p. 013008.

[70] X Qian et al. “Statistical evaluation of experimental determinations of neutrino mass hierarchy”. In: *Physical Review D* 86.11 (2012), p. 113011.

[71] Scott Dodelson, Alessandro Melchiorri, and Anvze Slosar. “Is cosmology compatible with sterile neutrinos?” In: *Physical review letters* 97.4 (2006), p. 041301.

[72] Ulrich F Katz and Ch Spiering. “High-energy neutrino astrophysics: Status and perspectives”. In: *Progress in Particle and Nuclear Physics* 67.3 (2012), pp. 651–704.

[73] Sheldon L Glashow. “Resonant scattering of antineutrinos”. In: *Physical Review* 118.1 (1960), p. 316.

[74] Brent Follin et al. “First detection of the acoustic oscillation phase shift expected from the cosmic neutrino background”. In: *Physical Review Letters* 115.9 (2015), p. 091301.

[75] Vladimir Nikolaevich Gavrin. “The Russian-American gallium experiment SAGE”. In: *Uspekhi Fizicheskikh Nauk* 181.9 (2011), pp. 975–984.

[76] A Caminata et al. “Short distance neutrino oscillations with Borexino”. In: *EPJ Web of Conferences*. Vol. 121. EDP Sciences. 2016, p. 01002.

[77] Q Retal Ahmad et al. “Measurement of the Rate of ν_e + d $\rightarrow$ p + p + e Interactions Produced by B^8 Solar Neutrinos at the Sudbury Neutrino Observatory”. In: *Physical Review Letters* 87.7 (2001), p. 071301.

[78] P Adamson and K et al Anderson. “The NuMI neutrino beam”. In: *Nuclear Instruments and Methods in Physics Research Section A: Accelerators, Spectrometers, Detectors and Associated Equipment* 806 (2016), pp. 279–306.

[79] Sowjanya et al Gollapinni. “Accelerator-based short-baseline neutrino oscillation experiments”. In: *arXiv preprint arXiv:1510.04412* (2015).

[80] http://www.globalneutrinonetwork.org/.

[81] https://sno.phy.queensu.ca/sno/.

[82] https://www.lngs.infn.it/en/borexino.

[83] http://www.dunescience.org.

[84] http://www-sk.icrr.u-tokyo.ac.jp/sk/sk/srn-e.html.

[85] https://www.lngs.infn.it/en/lngs-overview.

[86] https://ship.web.cern.ch/ship/.

[87] Y Kudenko and V Paolone. “Neutrino Physics: Status and Open questions”. In: *Nuclear and Particle Physics Proceedings* 260 (2015), pp. 167–171.

[88] Alastair R Hall. *Generalized method of moments*. Oxford university press, 2005.

[89] DN Abdurashitov and AI et al Belesev. “The current status of Troitsk nu-mass experiment in search for sterile neutrino”. In: *Journal of Instrumentation* 10.10 (2015), T10005.

[90] AA Borokov. “Mathematical statistics”. In: (2019).

[91] William Templeton Eadie, Daniel Drijard, and Frederick E James. “Statistical methods in experimental physics”. In: *Amsterdam: North-Holland, 1971* (1971).

The upper bound of $|\langle m\rangle_{ee}|$ has been set to be about $0.2\,\mathrm{eV}$ by the present $0\nu\beta\beta$ -decay experiments [1]. Another way is to detect the effective neutrino mass in the beta decays, such as

$$^3_1H \rightarrow {}^3_2He + e + \overline{\nu}_e. \tag{1.11}$$

The KATRIN experiment is the most promising next-generation direct mass search experiment, which may hopefully probe m_{ν_e} with a sensitivity of about $0.2\,\mathrm{eV}$.

$$\langle m\rangle_e \equiv \sqrt{m_1^2|U_{e1}|^2 + m_2^2|U_{e2}|^2 + m_3^2|U_{e3}|^2} \tag{1.12}$$

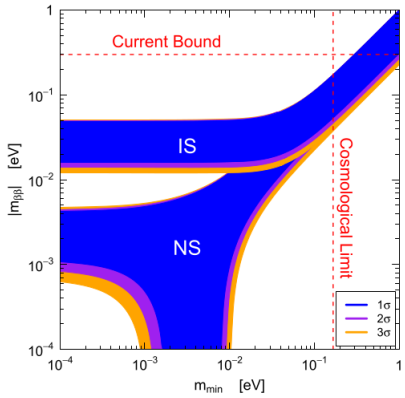

Figure 1.3: *Values of the effective Majorana mass $|m_{\beta\beta}|$ as a function of the lightest neutrino mass in the normal (NS, with $m_{min} = m_1$) and inverted (IS, with $m_{min} = m_3$) neutrino mass spectra after the measurement of non-zero θ_{13}. Republished with permission of World Scientific, from [17], copyright 1986; permission conveyed through Copyright Clearance Center Inc.*

Furthermore, one may get useful information on the mass scale of light neutrinos from cosmology and astrophysics. A global analysis of current cosmological data (especially those on the cosmic microwave background (CMB) and large-scale structures) has actually provided us with the most powerful sensitivity to the sum of light neutrino masses,

$$\sum_\nu \equiv \sum_i m_i. \tag{1.13}$$

For example, $\sum_\nu < 0.23\,\mathrm{eV}$ has recently been reported by the Planck Collaboration at the 95% confidence level [18]. Given the values of Δm^2_{21} and $|\Delta m^2_{31}|$ extracted from current neutrino oscillation data, the results of $|\langle m\rangle_{ee}|$, $\langle m\rangle_e$ and $\sum_\nu$ are all sensitive to the sign Δm^2_{31}.

1.3.2 Extra neutrino species and unitarity tests

From the definition of neutrino, it is an elementary particle and has a spin $\frac{1}{2}$, thus being a fermion. Neutrinos belong to the family of the leptons. It has a non vanishing mass. One of the fundamental questions in the neutrino physics and cosmology is whether there exist extra species of neutrinos that do not directly participate in the standard weak interactions. Such sterile (light or heavy) neutrinos are certainly hypothetical, but their possible existence is either theoretically motivated or experimentally implied. For

octant of the mixing angle θ_{23}(i.e., $\theta_{23} < \pi/4$ or $\theta_{23} > \pi/4$) and the value of δ_{cp} are both known. Large mixing and especially a large value of θ_{13} gives us an opportunity to search for CPV in neutrino oscillations i.e. CP violation in the lepton sector. In comparison, the CKM quark flavor mixing matrix $\bigvee$ is found to possess a clearly hierarchical structure, $\bigvee_{tb} > \bigvee_{ud} > \bigvee_{cs} \gg \bigvee_{us} > \bigvee_{cd} \gg \bigvee_{cb} > \bigvee_{ts} \gg \bigvee_{td} > \bigvee_{ub}$, since its three mixing angles satisfy $\theta_{12} \gg \theta_{23} \gg \theta_{13}$, which should have something to do with the strong quark mass hierarchies. Fig. 1.4 represents the schematic illustration of the "flavor hierarchy" and "flavor desert" in the fermion mass spectrum at the electroweak scale.

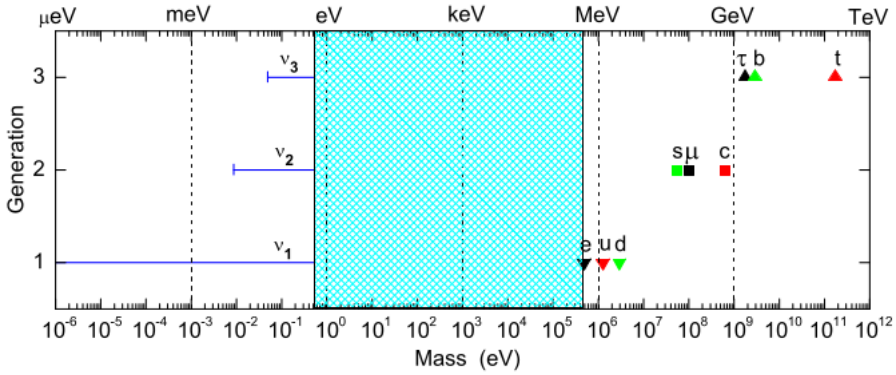

Figure 1.4: *A schematic illustration of the "flavor hierarchy" and "flavor desert" in the fermion mass spectrum at the electroweak scale. Here the neutrino masses are assumed to have a normal ordering. Reprinted from [1], Copyright 2011, with permission from Elsevier.*

1.3.4 The neutrino mass hierarchy problem

Determining the type of neutrino mass spectrum is one of the principal goals of the program on future research in neutrino physics because;

1. The neutrino mass hierarchy is one of the remaining undetermined fundamental features of the neutrino Standard Model.

2. Without the knowledge of what is the neutrino mass ordering, or the spectrum of neutrino masses, it is impossible to make progress in understanding the mechanism giving rise to non-zero neutrino masses and neutrino mixing [27]. Actually, determining this hierarchy is important for the neutrino Standard Model building.

3. Many basic neutrino physics observables that are planned to be measured in currently running and/or upcoming neutrino experiments, depend critically on the neutrino mass ordering. These include the CP violation asymmetry in long baseline neutrino oscillation experiments, the effective Majorana mass in neutrinoless double beta decay experiments, the sum of neutrino masses in the case of hierarchical neutrino mass spectrum etc. [27].

in terms of Δm^2, the neutrino atmospheric mass, and δm^2_{sol} the neutrino solar mass (Fig. 1.7).

$$\Delta m^2_{31} = \Delta m^2 + \frac{\delta m^2_{sol}}{2} \tag{1.17}$$

$$\Delta m^2_{32} = \Delta m^2 - \frac{\delta m^2_{sol}}{2} \tag{1.18}$$

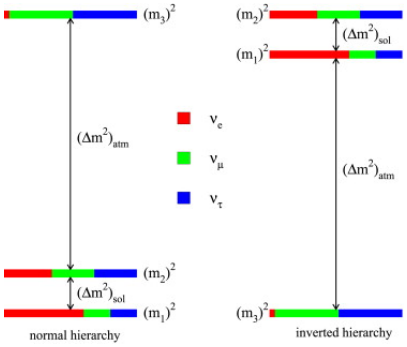

Figure 1.7: *Neutrino mass eigenstates for normal and inverted mass ordering.*

Determining the exact values of neutrino mass and mixing parameters is crucial to test neutrino models and flavor symmetries designed to predict these neutrino parameters. According to [29] and references within, the precise determination of mass hierarchy relies on the knowledge of Δm^2_{32}. They have shown that an incorrect Δm^2_{32} may bias the mass hierarchy determination to some extent. According to the global fit, the two values of neutrino atmospheric mass (the separation between the lightest and the heavier neutrino mass) in case of NH model and IH model are obviously not equal.

$$|\Delta m^2_{atm}|_{(NH)} \neq |\Delta m^2_{atm}|_{(IH)} \tag{1.19}$$

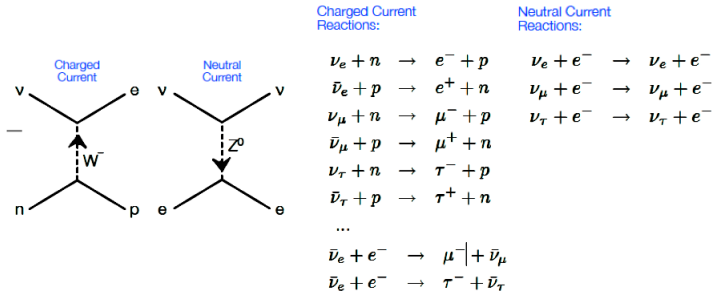

Figure 2.1: *Neutrino interactions via weak interaction.*

where N_{obs} is the observed number of neutrinos, M is the target mass, T is the exposure time, ϕ is the flux of neutrino in $\mathrm{events/cm^2/s}$, and σ is the reaction cross-section. Since the probability for interaction is very small ($\sim 10^{-38}\,\mathrm{cm}^2$), the chances of seeing a neutrino event are increased by using a detector of large mass (with high event efficiency) and high flux, i.e. sending a lot of neutrinos through it. There are various detection methods that have been used to detect neutrino. We will report about some of them.

This chapter is dedicated for the experimental neutrino physics and an overview of the status of the present knowledge of experimental neutrino physics.

Liquid Scintillators

Electron anti-neutrino $\overline{\nu}_e$ is usually detected in liquid scintillator experiments via inverse beta decay reaction (IBD), as shown in the following equation:

$$\overline{\nu}_e + p \rightarrow e^+ + n. \tag{2.2}$$

The $\overline{\nu}_e$ with an energy above the threshold of $1.8\,\mathrm{MeV}$ produces charged current interactions with the protons in the water, yielding positrons (e^+) and neutrons (n_0^1). This is very much like β^+ decay, where energy is used to convert a proton (p_1^1) into a neutron (n_0^1), a positron (e^+) and an electron neutrino ν_e, emitted through Eq. 2.2. The resulting positron annihilation with electrons in the detector material creates gamma rays $(\gamma - rays)$ with an energy of about $511\,\mathrm{KeV}$ that gives a prompt signal. The prompt signal corresponds to a pair of photons in coincidence that could be detected by the two scintillation detection around the target. The neutrons were captured by nuclei resulting in $\gamma - rays$ of about $2.2\,\mathrm{MeV}$ detected a $\sim 200\,\mu\mathrm{s}$ after the prompt signal from a (e^+) annihilation. It corresponds to a delayed signal, as indicated in Eq. 2.3.

$$n + p \rightarrow d + \gamma\,(2.2\,\mathrm{MeV}) \tag{2.3}$$

The coincidence of the prompt signal (positron signal) and delayed signal (neutron signal) in short time significantly reduced the background [1]. That is called "delayed coincidence". e^+ carries almost all energy of the $\overline{\nu}_e$ in this reaction. Therefore, generally the neutrino spectrum can be obtained just from the prompt signal with a $\sim 0.8\,\mathrm{MeV}$ shift. Since protons are at rest and neutrons are so heavy compared to electrons, the

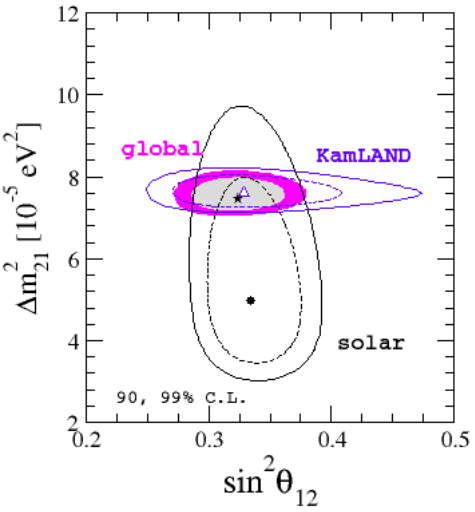

Figure 2.6: *The neutrino global fit result. Allowed regions at* 90 *and* 99% *C.L. from the analysis of solar data (black lines), KamLAND (blue lines) and the global fit (colored regions).* θ_{13} *has been marginalized according to the latest reactor measurements [39]. Triangle and circle respectively denote KamLAND and solar best fit. The global best fit is denoted by a star.*

Daya Bay

The Daya Bay is a Chinese Reactor Neutrino Experiment located roughly 50 km northeast of Hong Kong, in China. Daya Bay makes use of anti-neutrinos produced by the Daya Bay nuclear power plant to measure the neutrino mixing angle θ_{13}. The Daya Bay is designed to determine precisely θ_{13} with a sensitivity better than 0.01 for the parameter $sin^2 2\theta_{13}$, at the 90% confidence level [37].

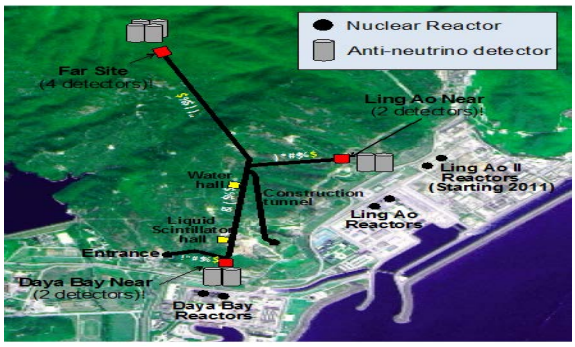

Figure 2.7: *Satellite photograph of the Daya Bay nuclear power plant complex showing the location of the reactors, a possible tunnel layout and possible locations for the near and far detectors [38].*

The experiment consists of eight anti-neutrino detectors, clustered in three locations within $1.9\,\mathrm{km}$ of six nuclear reactors. Each detector consists of $20\,\mathrm{tons}$ of liquid scintillator (linear alkylbenzene doped with gadolinium) surrounded by photomultiplier tubes and shielding [39]. The detectors are immersed in very large pools of water in order to shield them from ambient radioactivity and to be able to detect incoming cosmic-rays. Electron antineutrinos produced at six reactor cores with $2.9\,\mathrm{GW}$ thermal power are observed

angle θ_{13}, one of the main neutrino oscillation parameters responsible for ν_e oscillations into other neutrino flavors (ν_μ or ν_τ) [44]. RENO has two identical detectors, placed at distances of $294\,\mathrm{m}$ and $1383\,\mathrm{m}$ [44], that observe electron anti-neutrinos produced by six reactors at the Hanbit Nuclear Power Plant (the old name: the Yeonggwang Nuclear Power Plant) in Korea [43]. Each detector consists of $16.5\,\mathrm{tons}$ of gadolinium-doped liquid scintillator (LAB), surrounded by an additional $450\,\mathrm{tons}$ of buffer, veto, and shielding liquids. The detection methods and setup of the RENO experiment are discussed in detail elsewhere [43].

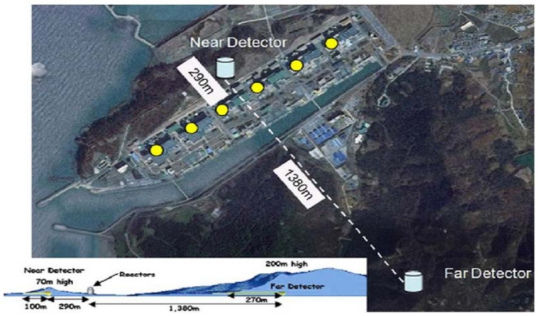

Figure 2.9: *A schematic setup of the RENO experiment.*

In 2012, RENO collaboration announced a $4.9\,\sigma$ observation of $\theta_{13} \neq 0$ [44], with

$$\sin^2 2\theta_{13} = 0.113 \pm 0.013(\mathrm{stat.}) \pm 0.019(\mathrm{syst.}) \tag{2.15}$$

In 2013, the RENO confirmed $\theta_{13} \neq 0$ with a significance of $6.3\,\sigma$ [45]:

$$\sin^2 2\theta_{13} = 0.100 \pm 0.010(\mathrm{stat.}) \pm 0.015(\mathrm{syst.}) \tag{2.16}$$

As indicated in Fig. 2.10, 90 and 99% C.L. (2 d.o.f.) allowed regions in the ($sin^2\theta_{13}$, Δm^2_{31}) plane from individual reactor neutrino experiments (dashed and solid lines) and from the combination of the three experiments (colored regions) [46].

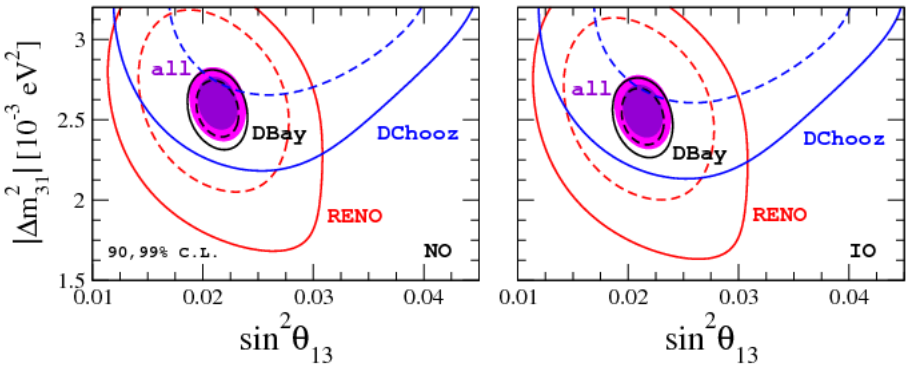

Figure 2.10: *The neutrino global fit result [47] of reactor neutrino experiments' simulations, Daya Bay [48], RENO [49] and Double Chooz [50]. The left (right) panels correspond to normal (inverted) mass ordering.*

After RENO, an underground detector of RENO-50 was planed to be constructed. RENO-50 would consist of $5000\,\mathrm{tons}$ of ultra low-radioactivity liquid scintillator and 3000

CHAPTER 3

THE JUNO EXPERIMENT

3.1 Introduction

The Institute of High Energy Physics proposed the second phase of the reactor neutrino experiment (JUNO) in 2008. In February 2013 JUNO was approved by the Chinese Academy of Sciences and supported through the Strategic Priority Research Programe [51]. The sensitivity analysis showed that the preferred range for the experimental stations must be $50 - 55\,\mathrm{km}$ from a nuclear reactor [1]. Jiangmen City was chosen for the JUNO detector site that is $\sim 53\,\mathrm{km}$ from both Yangjiang and Taishan Nuclear Power Plants (NPPs).

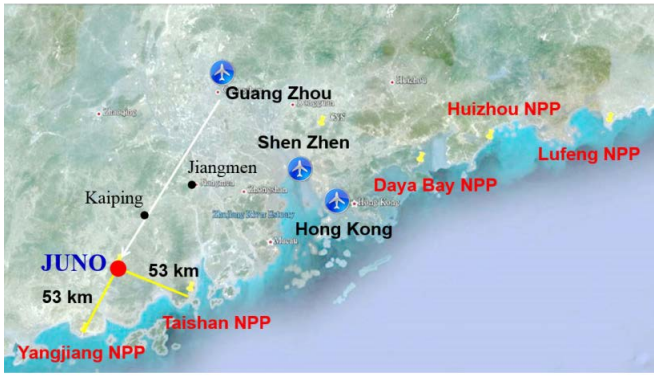

Figure 3.1: *Location of the JUNO site. The distances to the nearby Yangjiang NPP and Taishan NPP are both around* $53\,\mathrm{km}$. *Daya Bay NPP is* $215\,\mathrm{km}$ *away. Huizhou and Lufeng NPPs have not been approved yet [52].*

The JUNO detector will trap $\overline{\nu}_e$ generated from two NPPs located in Yangjiang and Taishan cities. The NNPs include six $2.9\,\mathrm{GW}$ reactors (second generation pressurized water reactor PWR) at Yangjiang NPP and four $4.6\,\mathrm{GW}$ reactors (third generation PWR) at Taishan NPP, giving a total thermal power of $35.8\,\mathrm{GW}$ [1]. A summary of the thermal power and baseline of each reactor to be used for JUNO is listed in Tab. 3.1.

Cores	YJ-C1	YJ-C2	YJ-C3	YJ-C4	YJ-C5	YJ-C6
Power (GW)	2.9	2.9	2.9	2.9	2.9	2.9
BaseLine (km)	52.75	52.84	52.42	52.51	52.12	52.21
Cores	TS-C1	TS-C2	TS-C3	TS-C4	DYB	HZ
Power (GW)	4.6	4.6	4.6	4.6	17.4	17.4
BaseLine (km)	52.76	52.63	52.32	52.20	215	265

Table 3.1: *The thermal power and baseline for JUNO detector of Yangjiang (YJ) and Taishan (TS) rector cores, in addition to the remote reactors Daya-Bay (DYB) and Huizhou (HZ) [1].*

The JUNO is designed to be a multipurpose experiment as reported in [1]. It can probe the neutrino oscillations to determine neutrino MH via measurement of reactor neutrino energy spectrum and to do precision measurements of neutrino oscillation mixing parameters. Moreover, the JUNO detector will provide an excellent opportunity for studying astro-neutrino physics being able to detect $\nu's$ from the astrophysical sources: supernova burst neutrinos, diffuse supernova neutrinos, Solar neutrinos and atmospheric neutrinos. In addition, JUNO will address the questions about other important current research topics like sterile neutrino and exotic searches. The data taking will possibly start in 2020.

3.2 The JUNO Detector

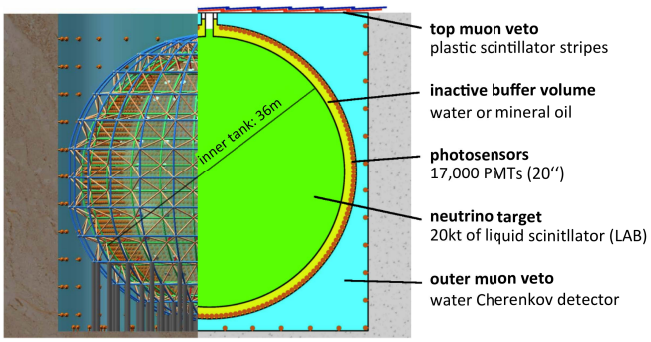

Figure 3.2: *Layout of the JUNO detector [1].*

The JUNO detector consists of:

1. The central detector (CD): it is a liquid scintillator detector of 20 kton target mass of Linear Alkyl-Benzene (LAB). The central detector is submerged in a water pool to be shielded from natural radioactivities from the surrounding rock and air. The central detector, which is the experiment's core component, will be the world's largest and highest precision liquid scintillator detector [1].

2. The veto system:

   (a) a water Cherenkov pool detector (WC). A pool filled with purified water and instrumented with PMTs. When energetic muons pass through the water, they can produce Cherenkov light. The Cherenkov photons can be detected by

in our simulation a residual non-linearity between the measured and expected neutrino spectra. In principle, one may find the worst case of non-linearity such that the wrong MH may perfectly mimic the true one. Thanks to the current measurements of the neutrino oscillation parameters, we can illustrate the specific non-linearity curves for the normal MH and inverted MH in Fig. 3.4.

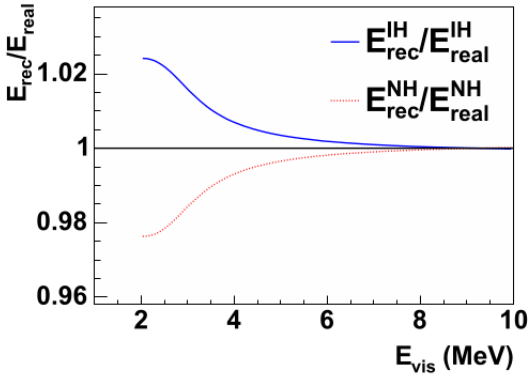

Figure 3.4: *The non-linearity models with the largest effects could mimic the normal and inverted hierarchys [1]. A possible non-linearity model is assumed to check its effect in MHD. In the plot the effect is parameterized for the Y-axis reconstructed energy over real energy.*

To conclude this point, the uncertainty in the detection absolute efficiency has negligible impact on the MHD. Therefore it is highly desirable to study the energy related uncertainties and it's impact on the MHD.

3.4.3 The background related uncertainties

There are two types of backgrounds, the major backgrounds and the accidental backgrounds. The major backgrounds are $^{8}He/^{9}Li$, Fast Neutron (FN), Geo-neutrinos and $^{13}C(\alpha,n)^{16}O$ as indicated below.

1. The cosmic ray generated backgrounds are:

   (a) $^{8}He/^{9}Li$ background from muon spallation and muon shower particles.

   (b) Fast neutron (FN) background in the detector from muon induced high energy neutrons.

   The cosmic ray muon induced backgrounds are the main backgrounds and they are hard to remove. The cosmic ray induced backgrounds also affect the study of the diffuse supernova neutrino flux. In order to reduce the experimental backgrounds, the neutrino detector must be placed in deep underground and a veto system is used to tag muons. The muons should be detected with high efficiency for the purpose of background reduction. Due to the strict requirements on background suppression, larger overburden of rocks on top of the detector is needed to reduce the cosmic ray muon flux. Therefore, there is about $700\,\mathrm{m}$ rock on top of the experimental hall. Muon rate is estimated at about $0.003\ \mathrm{Hz/m^2}$ and the average muon energy is about $214\,\mathrm{GeV}$ from simulation. The cosmic ray muon flux

Table 3.2: *The efficiencies of anti-neutrino selection cuts, signal and backgrounds rates [1]*

Selection	IBD efficiency	IBD	Geo-νs	Accidental	^{9}Li/^{8}He	Fast n	(α, n)
—	—	83	1.5	$\sim 5.7 \times 10^4$	84	—	—
Fiducial volume	91.8%	76	1.4		77	0.1	0.05
Energy cut	97.8%			410			
Time cut	99.1%	73	1.3		71		
Vertex cut	98.7%			1.1			
Muon veto	83%	60	1.1	0.9	1.6		
Combined	73%	60			3.8		

To conclude this point, the rate uncertainties of backgrounds are negligible for the MHD since they are nicely constrained in the precision spectral measurements. The background summary table for the analysis of reactor anti-neutrinos is Tab. 3.3 and the expected energy spectra for the five kinds of main backgrounds is Fig. 3.5.

Table 3.3: *The background summary table for the analysis of reactor anti-neutrinos [1].*

Event type	Rate (per day)	Rate uncertainty (relative)	Shape uncertainty
IBD candidates	60	—	—
Geo-νs	1.1	30%	5%
Accidental signals	0.9	1%	negligible
Fast-n	0.1	100%	20%
^{9}Li–^{8}He	1.6	20%	10%
^{13}C $(\alpha, n)^{16}$O	0.05	50%	50%

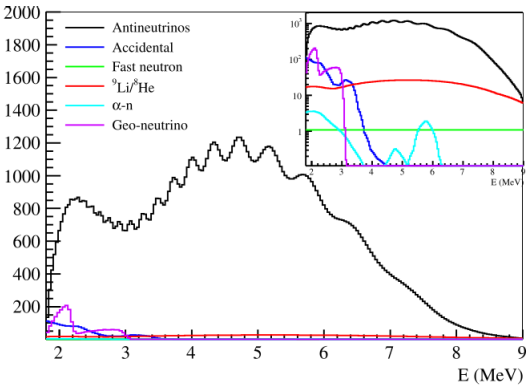

Figure 3.5: *Spectra for the anti-neutrino signal and five kinds of main backgrounds, including the accidental, $^8He/^9Li$, fast neutron, $^{13}C(\alpha, n)^{16}O$ and geo-neutrinos [1].*

3.5 The JUNO Simulation

JUNO simulation mainly consists of physics generators and detector simulation. Actually the full chain are physics generator, detector simulation, electronics simulation, waveform reconstruction and vertex/energy/track reconstruction. When running a detector simulation job, one or more primary particles will be generated in for each event. Then, these particles and their secondaries in the detector will transported. The event samples are all composed of $\sim 10^5$ events, which is a realistic assumption considering that the

the sample moment condition for total measurements (N) is

$$\frac{1}{N}\sum_{i}^{N} y_i - \langle \hat{\mu}^{GMM} \rangle_{th} = 0, \tag{4.15}$$

and $\hat{\mu}^{GMM}$ is obtained by solving the sample moment condition

$$\langle \hat{\mu}^{GMM} \rangle_{th} = \frac{1}{N}\sum_{i}^{N} y_i. \tag{4.16}$$

The standard method of the generalized moments consists in choosing a generalized moment $\hat{\mu}^{GMM}(N)$ defined as a function on events and then finding θ by drawing its theoretical average value, $\langle \hat{\mu}^{GMM} \rangle_{th}$, against the corresponding experimental value, $\langle \hat{\mu}^{GMM} \rangle_{exp}$.

The optimal Moments

Assume a set of events N_i binned in bin number i with their probability $\pi^i(N_i)$. The probability distribution depends on a parameter θ whose exact value θ^* is unknown. The theoretical value of the mean of an arbitrary generalized moment/weight $\phi^i(N_i)$ is

$$\langle \phi^i(N_i) \rangle_{th} = \int \phi^i(N_i)\pi^i(N_i)dN. \tag{4.17}$$

One estimates θ^*, the exact value of θ, by choosing a weight $\phi^i(N_i)$ and equating the theoretical mean,

$$\langle \phi^i(N_i) \rangle_{th} \equiv h(\theta), \tag{4.18}$$

assumed to be a calculable function of θ called $h(\theta)$, to the corresponding experimental value,

$$\langle \phi^i(N_i) \rangle_{exp} = \frac{1}{N}\sum_{i} \phi^i(N_i). \tag{4.19}$$

Then, one solves the resulting equation

$$h(\theta) = \langle \phi^i(N_i) \rangle_{exp} \tag{4.20}$$

to obtain an estimate θ_{exp} for the unknown value θ^*:

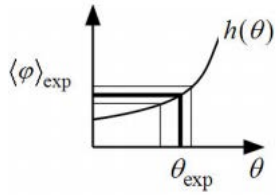

Requiring that $\langle \phi^i(N_i(\theta)) \rangle_{th} \equiv \langle \phi^i(N_i) \rangle_{exp} = h(\theta)$, we obtain an equation for θ. By taking a number of different weights $\phi^i(N_i)$, one can obtain a set of equations, whose solution will yield an estimate for θ.

The optimal wight minimizes the variance of the parameter, σ^2_θ. The problem is to minimized σ^2_θ by a suitable choice of ϕ. A necessary condition for a minimum can be written in terms of functional derivatives:

$$\frac{\delta\sigma^2_{\theta[\phi]}}{\delta\phi} = 0. \tag{4.21}$$

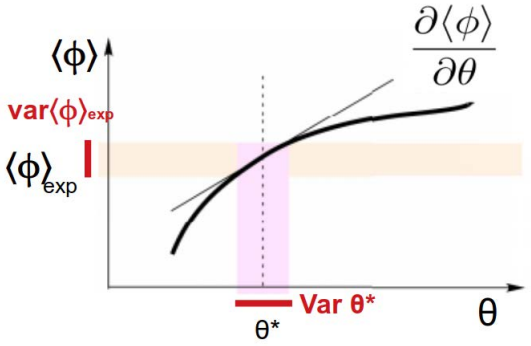

Now, our target is to get the functional $\sigma^2_{\theta[\phi]}$ then minimize it using Eq. 4.21 and obtain the optimal weight.

In the contest of the precision measurements one can assume the magnitude of errors to be small. One has a simple and explicit expression for the error estimation. Then, fluctuations in the values of θ are related to fluctuations in the values of $\langle\phi\rangle_{th}$ as

$$\frac{\delta\theta}{\delta\langle\phi\rangle_{th}} = \left(\frac{\partial\langle\phi\rangle_{th}}{\partial\theta}\right)^{-1}. \tag{4.22}$$

The derivative ($\frac{\partial\langle\phi\rangle_{th}}{\partial\theta}$) is applied only to the probability distribution:

$$\frac{\partial\langle\phi\rangle_{th}}{\partial\theta} = \frac{\partial}{\partial\theta}\left[\int \phi\pi dN\right] = \int \phi\frac{\partial\pi}{\partial\theta}dN. \tag{4.23}$$

For small fluctuations $\delta\langle\phi\rangle = N^{-1/2}\sqrt{\sigma^2_{\langle\phi\rangle}}$, where

$$\sigma^2_{\langle\phi\rangle_{exp}} = \left\langle\left[\phi - \langle\phi\rangle_{exp}\right]^2\right\rangle_{exp}, \quad \sigma^2_{\langle\phi\rangle} = \left\langle\left[\phi - \langle\phi\rangle\right]^2\right\rangle, \quad \sigma^2_{\langle\phi\rangle} \equiv \langle\phi^2\rangle - \langle\phi\rangle^2. \tag{4.24}$$

The variance of the generalized weight, σ^2_ϕ, is a function of the variance of experimental value of the parameter $\sigma^2_{\theta_{exp}}$.

$$\frac{\sigma^2_{\theta_{exp}}}{\sigma^2_\phi} = N^{-1}\left(\frac{\partial h(\theta_{exp})}{\partial\theta}\right)^{-2} \tag{4.25}$$

In terms of variations, Eq. 4.22 becomes:

$$\frac{\sigma^2_{\theta[\phi]}}{\sigma^2_\phi} = \left(\frac{\partial\langle\phi\rangle_{th}}{\partial\theta}\right)^{-2}, \tag{4.26}$$

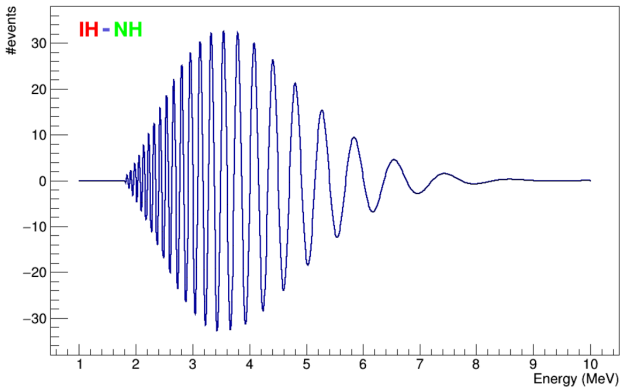

Figure 6.1: *Differential distribution of ΔN for six years of JUNO-like data taking, normalized as described in the text as a function of the $\overline{\nu}_e$ energy. The modulation is essentially due to Δm^2_{atm}.*

To conclude this section, the optimal weight proposed to solve the neutrino mass ordering using reactor spectrum is the difference in number of events per each single energy bin between the observed spectrum and the model. Since the neutrino mass ordering has two possible models, normal ordering model and inverted ordering model, the optimal weight has two dimensions as well. The component along X axis is F_{IH} and the component along Y axis is F_{NH}. Then, the bi-dimensional $F_{MO} = (F_{IH}, F_{NH})$ is mathematically represented as

$$\vec{F}_{MO} = F_{IH}\,\hat{e}_x + F_{NH}\,\hat{e}_y. \tag{6.7}$$

To confirm the bi-dimensional of the optimal weight of the neutrino mass ordering problem using reactor spectrum, the energy intervals are classified into two groups I^+ and I^-. For every group of energy intervals, Δ_i should be calculated for the two components of $\vec{F}_{MO}$.

Table 6.1: *The used best-fit values for the oscillation parameters, as indicated in [63].*

	best-fit	1σ region
$Sin^2\theta_{12}$	0.2970	± 0.017
$Sin^2\theta_{13}$	0.02150	± 0.0007
δm^2_{sol}	7.37e-5	0.16×10^{-5}
$\Delta m^2_{31}(NH)$	2.562e-3	$(-3.0 + 4.3) \times 10^{-5}$
$\Delta m^2_{32}(IH)$	2.545e-3	$(-3.2 + 3.4) \times 10^{-5}$

6.1 The $\vec{F}_{MO}$ Computation

As described in Ch. 1, the survival probability, assuming normal model, is

$$\begin{aligned} P_{NH} = 1 &- \frac{1}{2}\sin^2 2\theta_{13}(1 - cos\frac{\Delta m^2_{atm} L}{2E}) \\ &- \frac{1}{2}\cos^4\theta_{13}\sin^2 2\theta_{12}(1 - cos\frac{\delta m^2_{sol} L}{2E}) \\ &+ \frac{1}{2}\sin^2 2\theta_{13}\left[\cos^2\left(\theta_{12} + \frac{\pi}{2}\right)\right](cos\frac{L}{2E}(\Delta m^2_{atm} - \delta m^2_{sol}) - cos\frac{L\Delta m^2_{atm}}{2E}) \end{aligned} \tag{6.8}$$

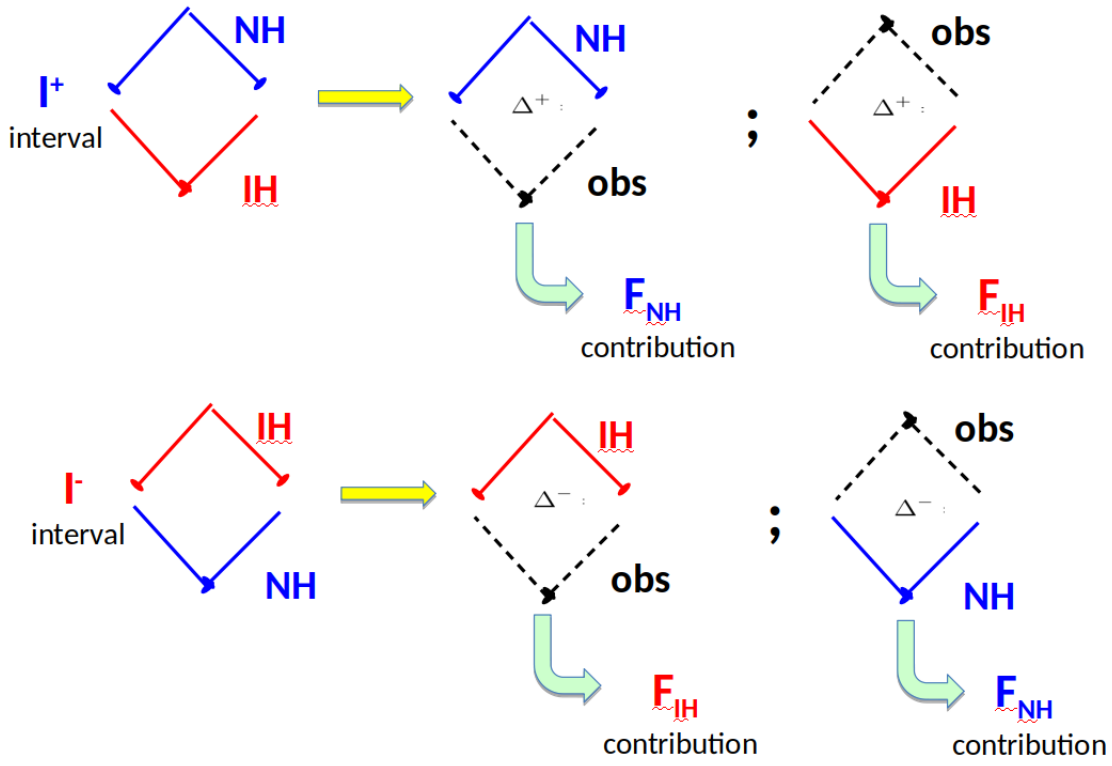

Figure 6.2: *The carton describes the $\vec{F}_{MO}$ computation.*

When the statistical fluctuations and systematic uncertainties are not included, $F_{\lambda}^{true} \approx 0$, as theoretically confirmed in Eq. 4.33, and $F_{\lambda}^{wrong} \sim 6500$ for for six years of JUNO-like data taking, normalized to 108357 signal events corresponding to the ten reactor cores, each weighted by its baseline (Fig. 6.3). The used best-fit values for the oscillation parameters are indicated in Tab. 6.1.

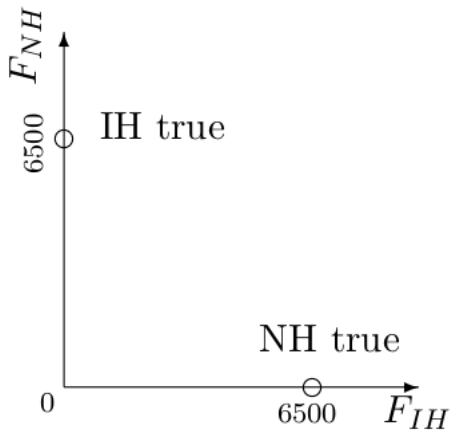

Figure 6.3: *The carton describes $2D$ $\vec{F}_{MO}$ (not to scale) for six years of data taking in a JUNO-like experiment. Oscillation parameters, reactor power, baseline and normalization to JUNO-like event selection have been chosen as described in the text [63].*

When the statistical fluctuations are included, Fig. 6.3 turns to Fig. 6.4: the single values of F_{λ}^{true} and F_{λ}^{wrong} get distributed. Given the $\vec{F}_{MO}$ definition (Eq. 6.7), the distributions are expected to be centered at larger values than the ideal one[1]. Even the true hierarchy choice (ideally, $F_{\lambda}^{true} = 0$) gets a certain positive amount when fluctuations are taken into account. On average, the F_{λ}^{true} is around 3300 counts for the true case and around 8000 counts for F_{λ}^{wrong} one (Fig. 6.4).

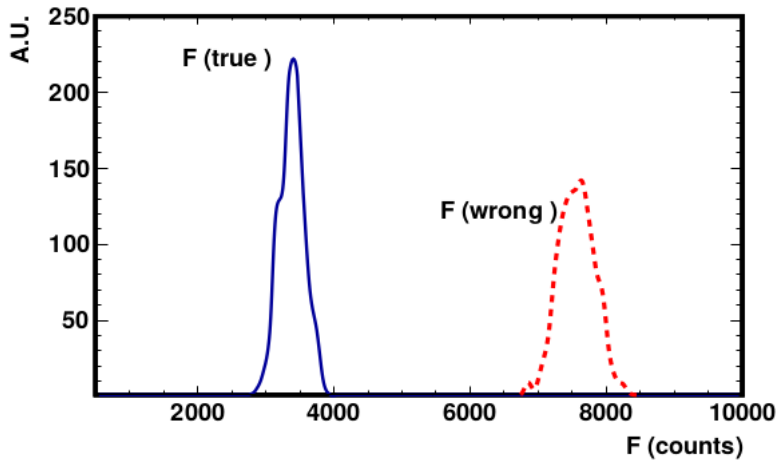

Figure 6.4: *(color online) F_{NH}^{true} (left) and F_{IH}^{wrong} (right) for 1000 JUNO-like toy experiments, assuming NH and an infinite energy resolution. The two distributions show the effect due to the statistical fluctuations in the collected number of events. Oscillation parameters and the other variables are chosen as described in the text, for a JUNO-like experiment six years long. The ten reactor cores of the Yangjiang and Taishan sites have been taking into account.*

Fig. 6.5 reports the bi-dimensional estimator $\vec{F}_{MO}$ for both hierarchies including the statistical fluctuations only. The blue 2D distribution (blue island) represents $\vec{F}_{MO}$ in case the true hierarchy is the normal hierarchy and the red 2D distribution (red island) represents $\vec{F}_{MO}$ in case the true hierarchy is the inverted one. The distributions correspond to the statistical fluctuations of 1000 toys JUNO-like experiment, with six years of exposure and the ten near reactor cores, each with its own baseline.

[1]We did not discard the fast modulation region of ΔN between $1.8 - 3.0$ because that may reduce the significance [63].

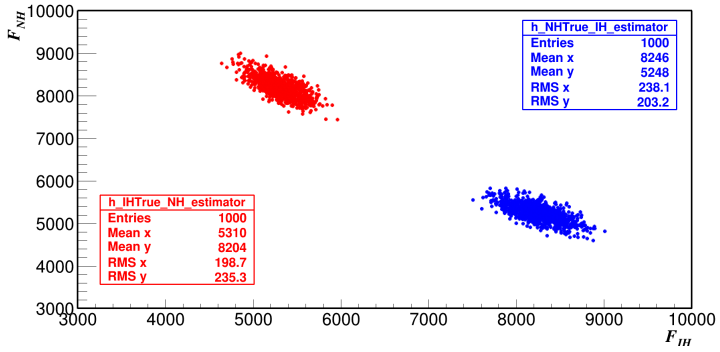

Figure 6.5: *(color online) F_{NH} vs F_{IH} distributions for 1000 (NH) + 1000 (IH) toys JUNO-like experiment, with six years of exposure and the ten near reactor cores, each with its own baseline. The "island" top-left (blue) corresponds to the IH simulation, while the one on the bottom-right (red) corresponds to the NH simulation. An infinite energy resolution is assumed. Note the asymmetric position of NH and IH domains, due to the non symmetric behavior of NH and IH in the oscillation model.*

When the statistical fluctuations and systematic uncertainties are included, the bi-Gaussian fits of $\vec{F}_{MO}$ for JUNO-like for different energy resolutions are drawn in Fig. 6.6, for six years of JUNO-like data taking, normalized to 108357 signal events corresponding to the ten reactor cores, each weighted by its baseline. The used best-fit values for the oscillation parameters are indicated in Tab. 6.1.

If one assumes that the inverted hierarchy is the null hypothesis H_0 and the normal hierarchy is the alternative hypothesis H_1, the *p*-value computation provides the sensitivity of how much the two hypotheses can be distinguished assuming the the null hypothesis be true. For example, $p_{val}(IH)$ corresponds to how much two the hypotheses can be distinguished assuming IH hypothesis be the true hierarchy[2]. The experimental sensitivity can be calculated using *p*-value method for bi-dimensional estimator as described in Appendix B.

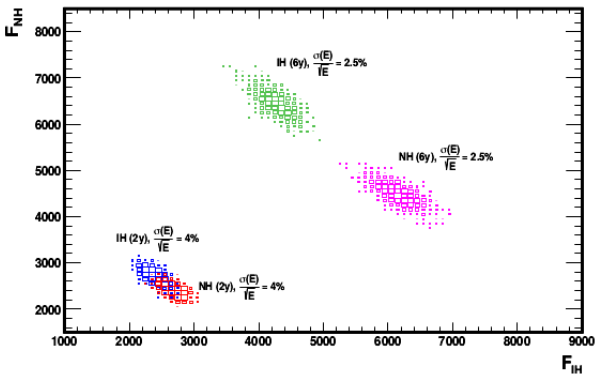

Figure 6.6: *(color online) F_{NH} vs F_{IH} distributions for 1000 (NH) + 1000 (IH) toys JUNO-like experiment, in two different configurations: the most favorable, six years of exposure with a $2.5\%/E$ energy resolution, against a short one for two years of exposure and $4\%/E$.*

[2] $p_{val}(NH)$ corresponds to how much the two hypotheses can be distinguished assuming NH hypothesis be the true hierarchy.

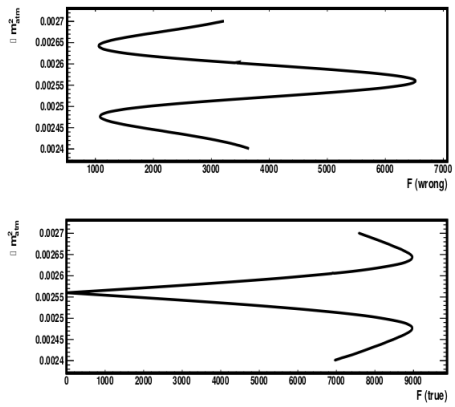

Figure 6.7: *(color online) Variation of the two components of $\vec{F}_{MO}$ for the wrong (true) hypothesis on the top (bottom) plot as function of the chosen Δm^2_{atm}, for a specific true Δm^2_{atm} and MO. A baseline of L= $52.5\,\mathrm{km}$ and a true Δm^2_{atm}= $0.002\,56\,\mathrm{eV}^2$ for the NH case have been selected, all the other parameters being fixed as described in the text to match six years of JUNO-like data taking. Note that going from F_{max} to F_{min} or vice-versa corresponds to changing Δm^2_{atm} of a δm^2_{sol} amount. The non-symmetric behavior of $\vec{F}_{MO}(true)$ and $F_{MO}(wrong)$ is due to the initial choice of the model that constraints the $I^{\pm}$ intervals.*

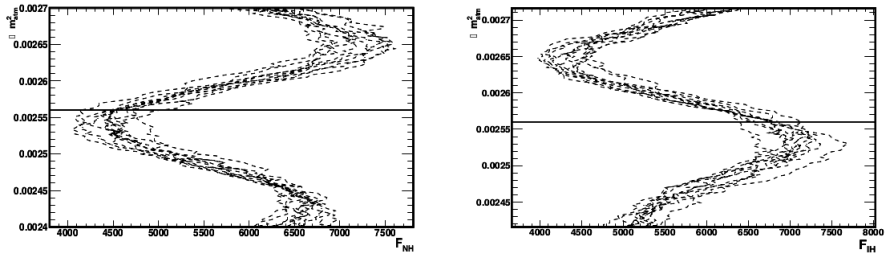

Figure 6.8: *(color online) $\vec{F}_{MO}$ modulations due to the differences between the "true" Δm^2_{atm} (NH) and the assumed one for ten JUNO-like toy experiments, including a $3\%/\sqrt{E}$ energy resolution and the real distribution of the baselines ($\pm 5\,\mathrm{m}$) of the ten reactor cores in Yangjiang and Taishan sites. On the left plot the dashed lines correspond to F_{NH}, whereas F_{IH} modulations are shown in the right plot. The horizontal lines correspond to the "true" Δm^2_{atm}. The observed bias is due to the finite energy resolution, as explained in the text.*

Fig. 6.9 reports $F(wrong)$ for a wide range of Δm^2_{31} vs Δm^2_{23}. The ciclic behaviour corresponds to the degeneracy $\Delta m^2_{31}(NH) = \Delta m^2_{23}(IH) \pm \delta^2 m_{sol}$. $F(wrong)$ is quite stable for different choices of the assumed Δm^2_{atm} (i.e. along the bisector on Fig. 4), with a dispersion of about 0.02%.

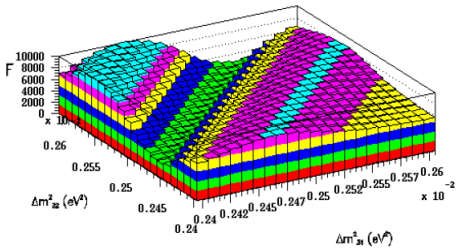

Figure 6.9: *(color online) Variation of $F(wrong)$ for $\Delta m^2_{31}(NH)$ vs $\Delta m^2_{23}(IH)$. Oscillation parameters and the other variables are chosen as described in the text, for a JUNO-like experiment and a six years exposure.*

6.2.2 The Degeneracy Effect

For each neutrino mass ordering case two full cycles are observed with maximum amplitude. Noticeably, there is an absolute minimum for each hypothesis. The two ordering can be discriminated when Δm^2_{atm} varies less than 12×10^{-5} eV^2. That corresponds to the distance between a peak and the valley, or, equivalently, the distance between the two absolute minima of NH and IH. The dispersions of the single minimum is less than 10^{-5} eV^2. Fig. 6.10 illuminates the separation of Δm^2_{atm}(true) with the degenerated one. $\vec{F}_{MO}$ holds a Δm^2_{atm}degeneracy at the level of 12×10^{-5} eV^2, which is much larger than the current global fits uncertainty. However, we argued that the new technique here outlined bears in itself a mean to resolve such ambiguity, allowing to measure Δm^2_{atm} with an unprecedented precision at reactors, less than 1%. That is due to the strong correlation of $\vec{F}_{MO}$ to Δm^2_{atm}, which will deserve more refined analyses and promise even more interesting results.

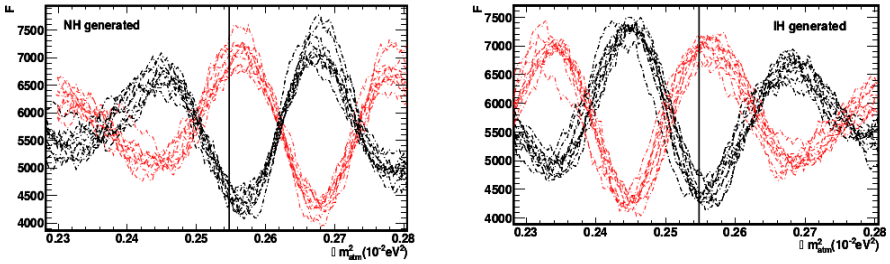

Figure 6.10: *(color online) $\vec{F}_{MO}$ vs $\Delta m^2_{atm}$for ten generated JUNO-like toy experiments, in the NH (right) and the IH (left) hypotheses. The black (red) curves correspond to the analysis when the true (false) hypothesis is taken. The vertical lines indicate the selected Δm^2_{atm}. The experimental conditions are the same as in text.*

There is a degeneracy between Δm^2_{atm} and $\vec{F}_{MO}$ i.e. for the correct Δm^2_{atm}we should have one minima but actually we have two: that creates the degeneracy. For a single reconstructed Δm^2_{atm} two solutions can be identified. For example, when $\vec{F}_{MO}$ identifies $\Delta m^2_{atm}(recons) = 2.50 \times 10^{-3}$eV^2 there are two solutions: $\Delta m^2_{atm} = 2.50 \times 10^{-3} \pm 0.1 \times 10^{-4}$eV^2 for NH and $\Delta m^2_{atm} = 2.62 \times 10^{-3} \pm 0.1 \times 10^{-4}$eV^2 for IH. Due to this intrinsic degeneracy it is not possible to have a single solution if only one experiment is taken into account. Information about Δm^2_{atm} should be injected from external, like e.g. a global fit

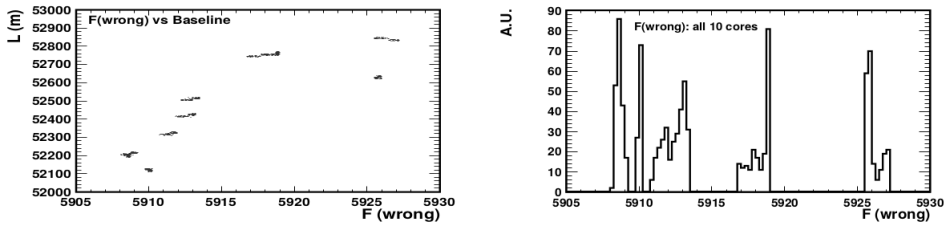

Figure 6.11: *(color online) Variation of F_{MO}(wrong) due to different baselines' cores. The 10 baselines correspond to the 10 reactor cores of the Yangjiang and Taishan sites. A uniform ± 5 m dispersion for the baseline of each core have been included in the computation. Oscillation parameters and the other variables are chosen as described in the text, for a JUNO-like experiment six years long.*

The performances of $\vec{F}_{MO}$ have been evaluated for baselines from $10\,\mathrm{km}$ to $90\,\mathrm{km}$ for a JUNO-like experiment with $3\%/\sqrt{E}$ energy resolution. Results are shown in Fig. 6.12. At baselines smaller than $50\,\mathrm{km}$ the dispersion of the minima are very large. Therefore, the bands of Fig. 6.15 become four times wider, forbidding the use of $\vec{F}_{MO}$ due to the unbroken degeneracy with Δm^2_{atm}. At baselines larger than $60\,\mathrm{km}$ the NH/IH patterns loose accuracy and tend to overlap each other (the interference effect between Δm^2_{31} and Δm^2_{32} is vanishing). In the latter case the sensitivity decreases, up to disappear at $80 - 90\,\mathrm{km}$.

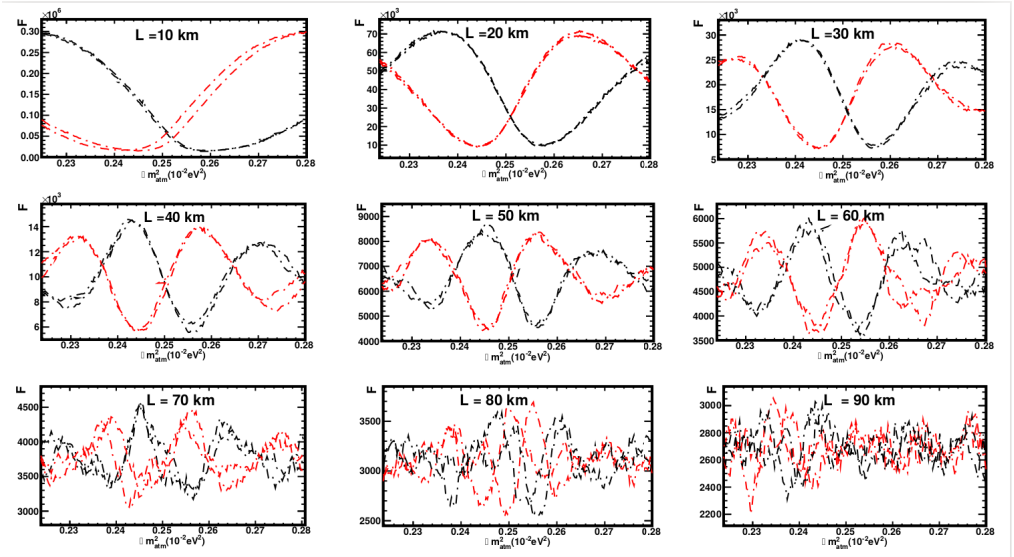

Figure 6.12: *(color online) F_{MO} vs Δm^2_{atm} for a couple of generated JUNO-like toy experiments, in the IH hypothesis. The black (red) curves correspond to the analysis when the true (false) hypothesis is taken. The experimental configuration is the same as in Fig. 6.8. Different baselines have been considered, as indicated in each plot.*

Even if the analysis is only sketched out, we would any how conclude that only the combined effect of a small uncertainty on Δm^2_{atm} as extracted by the $\vec{F}_{MO}$ procedure and the observed patterns for a specific experiment configuration, would allow us to obtain the quoted sensitivities larger than $5\,\sigma$. Such combination is only possible for a medium baseline reactor experiment with a baseline around $50\,\mathrm{km}$.

6.3 The Robustness of $\vec{F}_{MO}$

The $\vec{F}_{MO}$ shows a direct dependence behavior with the neutrino atmospheric mass manifesting in Fig. 6.13 that shows the separation distance between the two components is maintained along the range. As can be inferred from Fig. 6.13 computing that sensitivity is technically equivalent to use the same Δm^2_{atm} value for both hypotheses. In Fig. 6.13 the 68% and 95% C.L. contours of the current Δm^2_{atm} uncertainty are drawn. It seems reasonable to assume that only one solution be selected by F_{MO}, at 95% C.L. and for the current Δm^2_{atm} uncertainty. The sensitivity computed in this chapter corresponds to the probability to discriminate between NH/IH when only one solution is admitted. The quoted sensitivity owns a slightly different meaning from the standard one, which instead gives the probability to distinguish NH/IH in the whole parameter space. Since the $\vec{F}_{MO}$ technique identifies two solutions, one for NH and one for IH, each one at a different Δm^2_{atm}, with less than a 0.5% uncertainty, our sensitivity corresponds to the probability to misidentify the two solutions at their own Δm^2_{atm}. The patterns are consistently reproduced across the whole range of Δm^2_{atm}: defining $\Delta m^2_{atm}(recons)$ as the Δm^2_{atm} at the absolute minimum $\vec{F}_{MO}$, the central values and their $\pm\sigma$ bands are drawn in Fig. 6.13 for a large $\Delta m^2_{atm}(true)$ range.

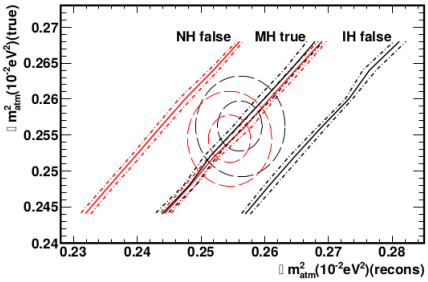

Figure 6.13: *(color online)* $\Delta m^2_{atm}(true)$ *vs* $\Delta m^2_{atm}(recons)$ *is drawn,* $\Delta m^2_{atm}(recons)$ *being obtained by the minimum* $\vec{F}_{MO}$*. The continuous lines correspond to the central values, the dashed ones to the* $\pm\sigma$ *bands. Black (red) curves corresponds to the NH (IH) generation. The central circles correspond to the* 68% *and* 95% *C.L. contours of the current* Δm^2_{atm} *uncertainties for NH and IH, from Tab. 6.1.*

When the input parameter $|\Delta m^2_{atm}|$ is drawn vs $\Delta m^2_{atm}(recons)$, the separation distance between the two components is maintained along the range. That naturally leads to the robustness of $\vec{F}_{MO}$ against Δm^2_{atm} because the MH sensitivity mainly depends on how much the two hypotheses can be discriminated and the separation between the two hypotheses is almost constant as it is described in Fig. 6.14.

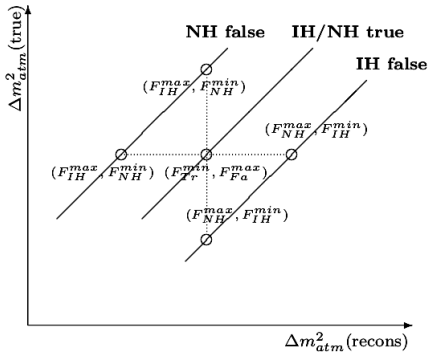

Figure 6.14: *The couplings of $\Delta m^2_{atm}(true)$ and $\Delta m^2_{atm}(recons)$ are pointed out. The quoted sensitivities corresponds to the probability to mis-identify $(F^{min}_{IH}, F^{max}_{NH})$ with $(F^{max}_{IH}, F^{min}_{NH})$, either at the same $\Delta m^2_{atm}(true)$ or the same $\Delta m^2_{atm}(recons)$. An equivalent probability applies to $(F^{min}_{NH}, F^{max}_{IH})$.*

One should not confuse the experimental conditions with the physical context: there is obviously only one set of true parameters, regardless of the MO established in nature. If χ^2 is able to single out such deconvolution, the result would be extremely efficient. Unfortunately, the χ^2 performs a best fit over the multidimensional space of the parameters' uncertainties. Therefore, one usually obtains two different sets of best fit values, one for NH and one for IH. The $\vec{F}_{MO}$ procedure operates distinctively being based on expressions with a factorized dependence on all the parameters except the atmospheric mass. To be more precise, the factorization of the other parameters is only true at the leading order and approximately for the solar mass. For example, if the mass terms dependencies are included in the survival probabilities, the factorization of Eq. 6.11 does not hold. Nevertheless, the latter are minor effects that do not spoil the performances of $\vec{F}_{MO}$. To confirm the $\vec{F}_{MO}$ properties with respect to the quantities, including reactor flux and reaction cross-section, other than Δm^2_{atm}, a large Monte Carlo simulation has been done. The parameters that are allowed to float freely in the simulation are reported in Tab. 6.2. 500 different sets of parameters have been randomly selected. For each set of parameters 20 JUNO-like experiments, 6 years of exposure, have been simulated including a $3\%/\sqrt{E}$ energy resolution. A uniform uncertainty of $\pm 5\,\mathrm{m}$ for the baseline of each of the ten reactors at $52.5\,\mathrm{km}$ away has been considered. We have not included the two remote reactors as well as any background contribution. The aim of the simulation is to demonstrate the independence of the evaluated sensitivity from the parameters except Δm^2_{atm}, as argued from Eq. 6.11. Specifically, the relative position of NH and IH in the (F_{NH}, F_{IH}) plane should not change. It is clear that 500 sets are not reproducing the full multiparameter space. However, the generation can be considered sufficient if no correlation is shown. The result is reported in Fig. 6.15: all the quantities except Δm^2_{atm} are let fluctuate within their uncertainty. No correlation between F_{NH} and F_{IH} is evident, the net result being the linear increase of both components values of $\vec{F}_{MO}$. There is no observed change on the dispersion nor in the relative distance. That confirms the expectation, the separation between two F_{IH} and F_{NH} remains constant.

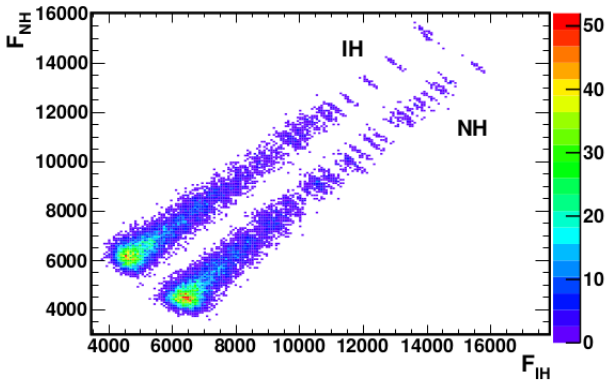

Figure 6.15: *(color online) F_{NH} vs F_{IH} distributions when all the parameters but Δm^2_{atm} are letting free within their uncertainties, as in Tab. 6.1. The two populations correspond to the NH (bottom region) and the IH (top region) generations. There is no observed change on the dispersions nor in the relative distance. Then, the result is that the separation between two F_{IH} and F_{NH} remains constant.*

6.4 Other $\vec{F}_{MO}$ dependences

To complete our study about the alternative method $\vec{F}_{MO}$, we have to study how the $\vec{F}_{MO}$ behaviors depend on the different systematic sources and backgrounds, uncertainties in the reactor flux, and the bump effect.

6.4.1 The Background and systematic studies

This subsection will answer how the different systematic sources and backgrounds affect the distribution of $\vec{F}_{MO}$. In JUNO-like experiments at reactors several sources of background and systematic errors are present, more details being available in Sec. 3.4. As already discussed, the major backgrounds for the reactor neutrino oscillation analysis are the accidentals, the $^8He/^9Li$ cosmogenic, the fast neutron and (α, n) interactions. In principle, all these background sources produce events uncorrelated in energy with the signal. The background conservatively included in the $\vec{F}_{MO}$ analysis, due to its slow variation in energy, does not change the $\vec{F}_{MO}$ dispersions and consequentiality does not affect MH sensitivity. Fig. 6.16 represents the sum of the background sources in shape of ^9Li.

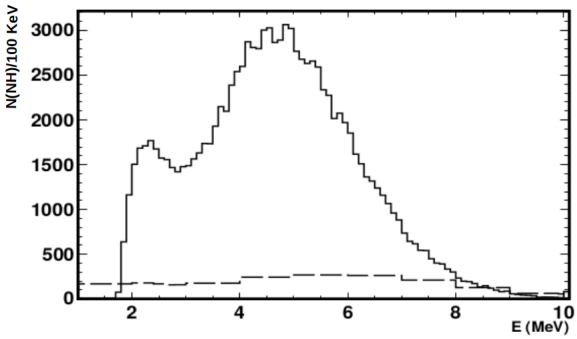

Figure 6.16: *(color online) The cosmogenic background distribution due to ^9Li for a six year long JUNO-like experiment. This is the distribution, conservatively scaled to the total amount of expected incoherent background, used to extract the sensitivity on NH/IH with this kind of background.*

As mentioned in Sec. 3.4, there are two sources for detector response: first the statistical fluctuations (in this particular case, the so-called photo-statistics in the liquid scintillor), second the systematic uncertainty associated to the correction of the linearity in energy of the detector response (for example from non-uniformity in the liquid scintillor, photomultiplier manufacturing and the electronics) [1]. About the systematic uncertainties, $\vec{F}_{MO}$ is expected to act differently from them especially due to the bump effect at $4 \sim 6$ MeV energy region [63]. The other sources of incoherent systematic errors, related to the energy reconstruction, will enter in quadrature with the energy resolution itself [63]. The coherent systematic error due to a residual non-linear energy scaling is a detector dependent effect. We verified that a parametric form as in [64], eq. (13), would produce a linear dependence on both F_{NH} and F_{IH}. That linearity could be used to self-calibrate the energy spectrum.

6.4.2 The Flux Effect

The reactor flux uncertainties include several components, concerning both the overall normalization and the shape as a function of the anti-neutrino energy. Regarding the integrated flux normalization, we add in quadrature the relative uncertainties associated with the power, the energy produced per fission, the spent fuel, the non-equilibrium and the fission fraction at a given time. All but the last one can be assumed as correlated across all cores, because they derive from the same physical modeling uncertainty, intrinsic to a typical fission core. The latter is instead uncorrelated across cores, because the relative fractions of the four leading burning elements will likely be different for the cores considered at a given time (switching on/off and re-fueling at independent times). By taking the sum in quadrature of the maximum uncertainty coherently for all the considered cores the "envelope" total uncertainty is therefore used. Conservatively, we vary the overall flux by $\pm 3\%$ with respect to the expected nominal flux at JUNO.

With regard to the energy dependence on the flux modeling uncertainty, from [65] this is estimated to be less than 10% up to $E_{(\overline{\nu}_e)} = 10$ MeV. However, a systematic uncertainty on the reactor flux is already considered by introducing the "bump" between 4 and 6 MeV in the simulation (SubSec. 6.4.3). That is, the deformation of the spectrum due to the bump is taken and studied as a source of systematic uncertainty, as an example of

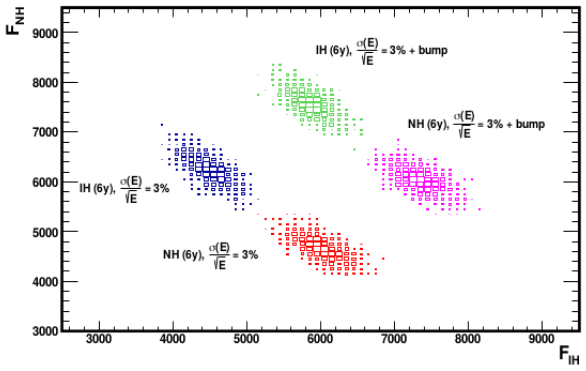

Figure 6.17: *(color online) F_{NH} vs F_{NH} distributions for 1000 (NH) + 1000 (IH) toys JUNO-like experiment, in two different configurations. The benchmark of six years exposure is compared to the same exposure result when the $4 \sim 6\,\mathrm{MeV}$ bump is added. The sensitivity is calculated and reported in Tab. 6.4.*

Table 6.4: *The bi-Gaussian fits of the $\vec{F}_{MO}$ distributions are reported, for the JUNO-like configuration of six years of data taking and a $3\%/\sqrt{E}$ energy resolutions, μ_{MH}, σ_{MH} and r_{MH} being the means, the standard deviations and the correlation coefficients, respectively, of the fitted $2D$ Gaussians. The ten near reactor cores have been considered with a $\pm 5\,\mathrm{m}$ uniform dispersion on their relative baseline. In the first set of data the uncorrelated background has been included from the ^9Li, scaled to the total amount. In the second set the correlated bump around $4 \sim 6\,\mathrm{MeV}$ has been considered. The sensitivity has been computed from the p-values estimation as described in the text in terms of number of σ's in the two-sided option. $n\,\sigma$ (IH) stays for the IH rejection significance, and equivalently for NH.*

10 reactor cores, 6 years			
		with uncorrelated background	with correlated bump around $4 \sim 6$ MeV
NH true	μ_{NH}	8908.2 $\pm$ 6.1	6039.3 $\pm$ 7.4
	σ_{NH}	187.0 $\pm$ 3.4	226.9 $\pm$ 4.4
	μ_{IH}	10315.2 $\pm$ 6.5	7346.8 $\pm$ 7.7
	σ_{IH}	201.9 $\pm$ 3.6	238.9 $\pm$ 4.9
	r_{NH}	-0.841 $\pm$ 0.005	-0.573 $\pm$ 0.015
IH true	μ_{NH}	10230.0 $\pm$ 6.3	7573.7 $\pm$ 4.9
	σ_{NH}	196.5 $\pm$ 3.4	243.6 $\pm$ 4.7
	μ_{IH}	8998.8 $\pm$ 5.9	5861.0 $\pm$ 5.5
	σ_{IH}	181.5 $\pm$ 3.2	219.1 $\pm$ 3.1
	r_{IH}	-0.835 $\pm$ 0.007	-0.617 $\pm$ 0.010
	$p-$value (IH)	2.88×10^{-8}	1.57×10^{-8}
	$n\,\sigma$ (IH)	5.55	5.65
	$p-$value (NH)	1.90×10^{-8}	1.75×10^{-8}
	$n\,\sigma$ (NH)	5.62	5.63

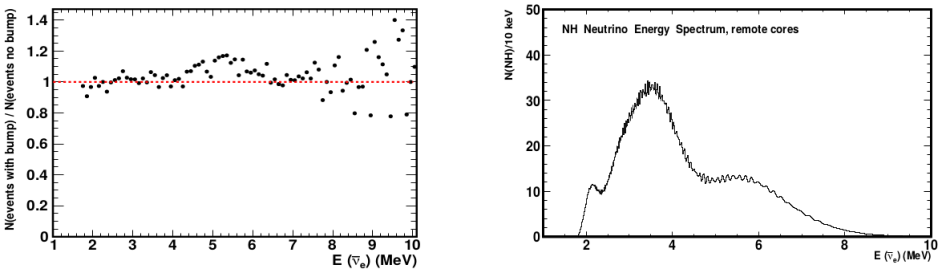

Figure 6.18: *(color online) The antineutrino event distribution when a modeled bump around* $4 \sim 6$ MeV *is added to the ten reactor production (left plot), is drawn. A single JUNO-like, six years exposure, toy Monte Carlo is shown in terms of the relative percentage with/without the addition. In the right plot the distribution due to the two remote reactor production is shown (NH case).*

reported in Tab. 7.8.

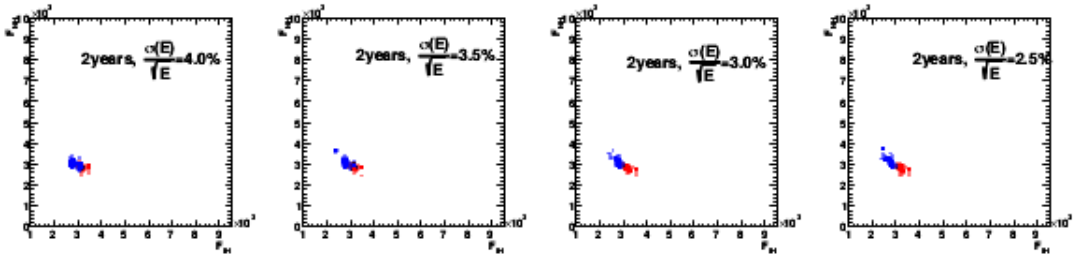

Figure 7.5: *(color online)* F_{NH} *vs* F_{IH} *distributions for* 1000 *(NH) +* 1000 *(IH) toys JUNO-like experiment, for different configurations in energy resolution. The two remote reactor cores have been added. The island top-left (blue) corresponds to the IH simulation, while the one on the bottom-right (red) corresponds to the NH simulation. The corresponding fitted values to the* $2D$ *Gaussians are those reported in Tab. 7.5.*

Table 7.5: *The bi-Gaussian fits of the* $\vec{F}_{MO}$ *distributions are reported, for the JUNO-like configuration of two years of data taking and different energy resolutions* μ_{MH}, σ_{MH} *and* r_{MH} *being the means, the standard deviations and the correlation coefficients, respectively, of the fitted* $2D$ *Gaussians. The* 10 *near reactor cores have been considered with a* $\pm 5\,\mathrm{m}$ *uniform dispersion on their relative baseline, as well as the two remote reactor plants with a* $\pm 0.5\,\mathrm{km}$ *uniform dispersion on their baseline. The sensitivity has been computed from the p-values estimation as described in the text in terms of number of* σ*'s in the two-sided option.* $n\,\sigma(\mathrm{IH})$ *stays for the IH rejection significance, and equivalently for NH.*

10 reactor cores plus the 2 remote cores					
		2 years			
		4%	3.5%	3%	2.5%
NH true	μ_{NH}	2834.2 ± 3.9	2807.4 ± 3.8	2770.5 ± 3.9	2726.6 ± 3.7
	σ_{NH}	115.6 ± 1.5	117.2 ± 2.4	121.1 ± 2.5	115.5 ± 1.5
	μ_{IH}	3125.2 ± 3.9	3145.5 ± 4.1	3179.8 ± 4.0	3220.9 ± 4.1
	σ_{IH}	123.5 ± 1.6	126.8 ± 2.7	125.7 ± 2.5	125.6 ± 1.6
	r_{NH}	-0.585 ± 0.018	-0.606 ± 0.013	-0.620 ± 0.014	-0.644 ± 0.012
IH true	μ_{NH}	3138.9 ± 4.2	3177.9 ± 4.3	3225.0 ± 4.1	3264.5 ± 3.9
	σ_{NH}	131.7 ± 2.6	132.3 ± 1.8	126.0 ± 2.6	130.2 ± 2.8
	μ_{IH}	2831.9 ± 4.0	2785.5 ± 4.1	2732.2 ± 3.8	2691.4 ± 3.8
	σ_{IH}	124.6 ± 2.5	125.4 ± 1.5	118.9 ± 0.8	118.1 ± 2.3
	r_{IH}	-0.632 ± 0.016	-0.628 ± 0.010	-0.610 ± 0.016	-0.618 ± 0.018
	$p-$value (IH)	3.21×10^{-2}	1.14×10^{-2}	1.92×10^{-3}	2.20×10^{-4}
	$n\,\sigma$ (IH)	2.14	2.53	3.10	3.69
	$p-$value (NH)	4.23×10^{-2}	1.46×10^{-2}	1.85×10^{-3}	2.59×10^{-4}
	$n\,\sigma$ (NH)	2.03	2.44	3.11	3.65

Table 7.8: *The bi-Gaussian fits of the $\vec{F}_{MO}$ distributions are reported, for the JUNO-like configuration of two years of data taking and different energy resolutions, μ_{MH} , σ_{MH} and r_{MH} being the means, the standard deviations and the correlation coefficients, respectively, of the fitted $2D$ Gaussians. The eight near reactor cores have been considered with a $\pm 5\,\mathrm{m}$ uniform dispersion on their relative baseline. No background source has been included. The sensitivity has been computed from the p-values estimation as described in the text in terms of number of σ's in the two-sided option. n $\sigma(IH)$ stays for the IH rejection significance, and equivalently for NH.*

8 reactor cores without the two remote cores					
		2 years			
		4%	3.5%	3%	2.5%
NH true	μ_{NH}	4026.9 ± 6.5	3979.9 ± 4.1	3912.9 ± 6.6	3845.6 ± 5.5
	σ_{NH}	203.9 ± 4.2	204.7 ± 3.2	203.6 ± 3.2	198.4 ± 2.9
	μ_{IH}	4438.1 ± 6.9	4474.3 ± 3.6	4537.4 ± 7.1	4590.8 ± 4.7
	σ_{IH}	215.8 ± 4.4	221.9 ± 3.2	219.3 ± 2.7	220.9 ± 4.8
	r_{NH}	-0.575 ± 0.018	-0.564 ± 0.015	-0.553 ± 0.014	-0.575 ± 0.013
IH true	μ_{NH}	4474.2 ± 7.3	4546.0 ± 7.1	4614.9 ± 6.8	4680.5 ± 7.2
	σ_{NH}	225.7 ± 4.8	223.7 ± 4.6	212.9 ± 4.4	224.5 ± 3.9
	μ_{IH}	3998.8 ± 6.8	3928.5 ± 6.9	3849.7 ± 6.4	3782.6 ± 5.6
	σ_{IH}	210.1 ± 4.5	215.4 ± 4.4	200.9 ± 4.1	202.1 ± 4.1
	r_{IH}	-0.597 ±0.012	-0.572 ± 0.018	-0.571± 0.018	-0.580 ± 0.018
	$p-$value (IH)	6.48×10^{-2}	2.33×10^{-2}	4.33×10^{-3}	8.34×10^{-4}
	$n\,\sigma$ (IH)	1.85	2.27	2.85	3.34
	$p-$value (NH)	7.41×10^{-2}	2.65×10^{-2}	3.93×10^{-3}	9.26×10^{-4}
	$n\,\sigma$ (NH)	1.79	2.22	2.88	3.31

7.2.2 After 4 years of data taking

A further integrating result is that after only 4 years of data taking, $\vec{F}_{MO}$ will be able to distinguish the correct mass ordering with a sensitivity of $4.21\,\sigma$ using the 10 near reactor cores plus the 2 remote ones, or higher than $4.48\,\sigma$ using the 10 near reactor cores and no background has been included. The detailed sensitivities calculations for different configurations are reported in Tab. 7.9 and Tab. 7.10. The $\vec{F}_{MO}$ distributions using anti-neutrino spectrum coming from JUNO-like experiment for 4 different energy resolutions, $2.5\%, 3.0\%, 3.5\%$ and 4.0% and the 10 near reactor cores plus the 2 remote reactor plants are in Fig. 7.6.

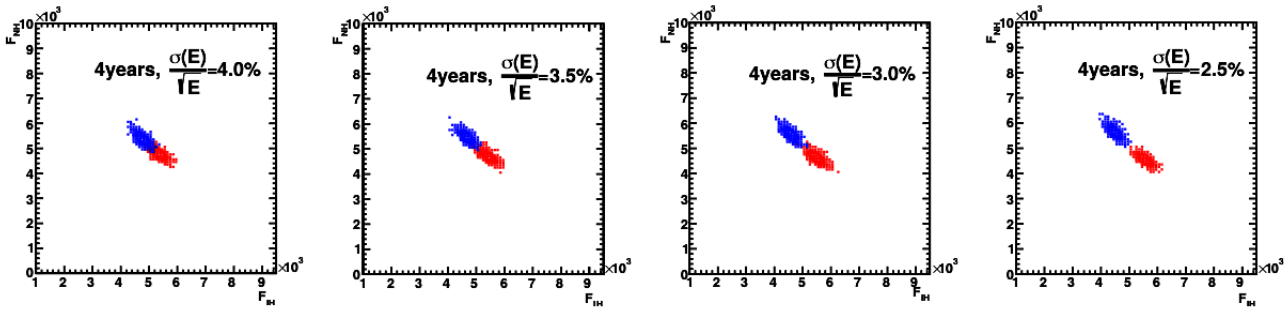

Figure 7.6: *(color online) F_{NH} vs F_{IH} distributions for 1000 (NH) + 1000 (IH) toys JUNO-like experiment, for different configurations in energy resolution. The two remote reactor cores have been added. The island top-left (blue) corresponds to the IH simulation, while the one on the bottom-right (red) corresponds to the NH simulation. The corresponding fitted values to the $2D$ Gaussian are those reported in Tab. 7.9.*

7.2.3 After 6 years of data taking

From the results showed above, the following key-points emerge: the results using the alternative method are much better than those using $\Delta\chi^2$ for the same conditions. Fig. 7.7 is the solid evidence of this results providing the distributions of $\vec{F}_{MO}$ for JUNO-like for 4 different energy resolutions, $2.5\%, 3.0\%, 3.5\%$ and 4.0%, for the 10 near reactor cores plus the 2 remote reactor plants. The corresponding fitted values are reported in Tab. 7.11. A similar pattern of results was reported in Tab. 7.12 but for 10 reactors only and no background being considered.

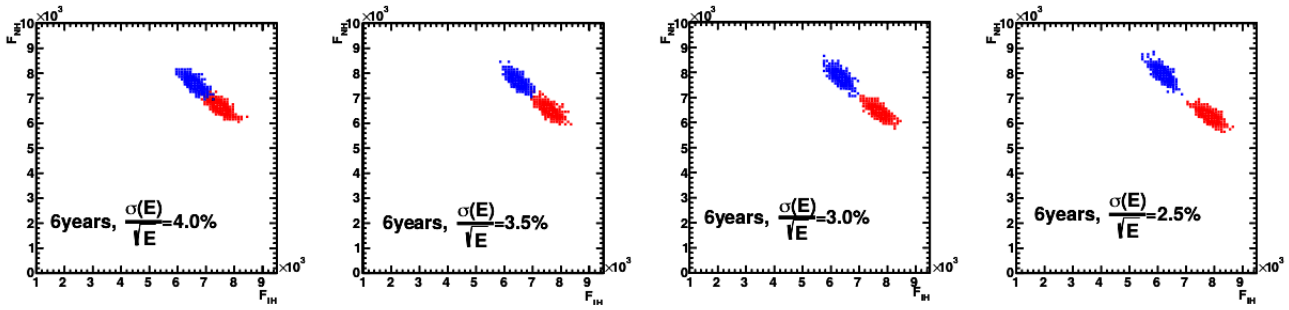

Figure 7.7: *(color online) F_{NH} vs F_{IH} distributions for 1000 (NH) + 1000 (IH) toys JUNO-like experiment for 4 different energy resolutions, $2.5\%, 3.0\%, 3.5\%$ and 4.0%. The two remote reactor cores have been added. The island top-left (blue) corresponds to the IH simulation, while the one on the bottom-right (red) corresponds to the NH simulation. The corresponding fitted values to the $2D$ Gaussians are those reported in Tab. 7.11.*

Table 7.11: *The bi-Gaussian fits of the $\vec{F}_{MO}$ distributions are reported, for the JUNO-like configuration of six years of data taking and different energy resolutions μ_{MH}, σ_{MH} and r_{MH} being the means, the standard deviations and the correlation coefficients, respectively, of the fitted $2D$ Gaussians. The 10 near reactor cores have been considered with a ± 5 m uniform dispersion on their relative baseline, as well as the two remote reactor plants with a ± 0.5 km uniform dispersion on their relative baseline. The sensitivity has been computed from the p-values estimation as described in the text in terms of number of σ's in the two-sided option. n $\sigma(IH)$ stays for the IH rejection significance, and equivalently for NH.*

10 reactor cores plus the 2 remote cores					
		6 years			
		4%	3.5%	3%	2.5%
NH true	μ_{NH}	6650.4 ± 6.8	6538.2 ± 6.8	6427.2 ± 6.6	6292.0 ± 6.5
	σ_{NH}	213.1 ± 4.1	212.1 ± 2.2	203.8 ± 4.0	201.1 ± 2.5
	μ_{IH}	7504.1 ± 7.2	7600.8 ±7.1	7693.3 ± 7.3	7817.2 ± 7.5
	σ_{IH}	224.7 ± 4.3	220.4 ± 2.8	226.4 ± 4.4	232.1 ± 2.9
	r_{NH}	-0.709 ± 0.013	-0.726 ±0.010	-0.736 ± 0.009	-0.719 ± 0.009
IH true	μ_{NH}	7583.7 ± 7.1	7685.1 ±7.3	7801.1 ± 7.3	7964.8 ± 7.2
	σ_{NH}	222.0 ± 2.7	226.7 ± 2.7	227.3 ± 4.6	222.5 ± 4.3
	μ_{IH}	6585.6 ± 6.7	6472.1 ± 6.5	6349.9 ± 6.4	6179.9 ± 6.2
	σ_{IH}	208.9 ± 2.5	202.8 ± 2.4	198.6 ± 4.0	193.5 ± 3.8
	r_{IH}	-0.704 ± 0.009	-0.731 ± 0.008	-0.713 ± 0.010	-0.708 ± 0.013
	$p-$value (IH)	4.67×10^{-4}	1.46×10^{-5}	1.36×10^{-7}	4.13×10^{-11}
	$n\,\sigma$ (IH)	3.50	4.34	5.27	6.50
	$p-$value (NH)	4.27×10^{-4}	1.35×10^{-5}	1.13×10^{-7}	1.96×10^{-11}
	$n\,\sigma$ (NH)	3.52	4.35	5.30	6.71

Table 7.12: *The bi-Gaussian fits of the $\vec{F}_{MO}$ distributions are reported, for the JUNO-like configuration of six years of data taking and different energy resolutions μ_{MH}, σ_{MH} and r_{MH} being the means, the standard deviations and the correlation coefficients, respectively, of the fitted $2D$ Gaussians. The ten near reactor cores have been considered with a $\pm 5\,\mathrm{m}$ uniform dispersion on their relative baseline. No background source has been included. The sensitivity has been computed from the p-values estimation as described in the text in terms of number of σ's in the two-sided option. n $\sigma(IH)$ stays for the IH rejection significance, and equivalently for NH.*

ten reactor cores, no background					
		6 years			
		4%	3.5%	3%	2.5%
NH true	μ_{NH}	4956.5 ± 7.3	4815.3 ± 7.1	4667.2 ± 7.0	4486.2 ± 7.1
	σ_{NH}	230.6 ± 4.3	222.3 ± 4.4	227.9 ± 4.3	219.9 ± 3.1
	μ_{IH}	5802.5 ± 7.9	5906.1 ± 7.7	6006.1 ± 7.4	6163.2 ± 8.3
	σ_{IH}	248.8 ± 0.9	239.7 ± 4.8	252.0 ± 4.6	255.9 ± 3.1
	r_{NH}	-0.674 ± 0.012	-0.684 ± 0.010	-0.682 ± 0.015	-0.706 ± 0.009
IH true	μ_{NH}	6001.9 ± 7.9	6110.2 ± 7.8	6242.9 ± 7.9	6440.7 ± 7.4
	σ_{NH}	246.4 ± 4.8	241.9 ± 5.0	248.4 ± 4.9	233.5 ± 2.9
	μ_{IH}	4791.1 ± 7.2	4644.1 ± 7.0	4491.3 ± 7.0	4280.0 ± 6.5
	σ_{IH}	226.8 ± 4.4	216.6 ± 4.5	219.2 ± 4.3	205.9 ± 2.7
	r_{IH}	-0.692 ± 0.014	-0.673 ± 0.011	-0.686 ± 0.14	-0.664 ± 0.010
	$p-$value (IH)	3.48×10^{-4}	3.51×10^{-6}	3.98×10^{-8}	7.96×10^{-11}
	$n\,\sigma$ (IH)	3.58	4.64	5.49	6.50
	$p-$value (NH)	3.30×10^{-4}	3.21×10^{-6}	3.12×10^{-8}	1.08×10^{-11}
	$n\,\sigma$ (NH)	3.59	4.66	5.53	6.79

7.2.4 Sensitivity using $\vec{F}_{MO}$ as a function of energy resolution

The experimental sensitivity using $\vec{F}_{MO}$ has direct connection with the energy resolution as confirmed in Fig. 7.8.

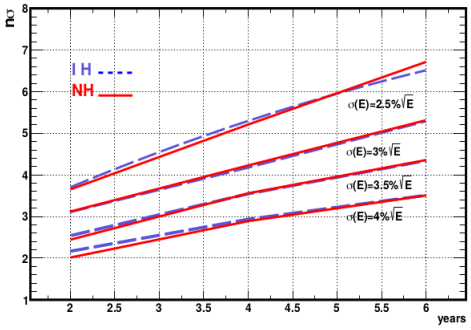

Figure 7.8: *(color online) Evolution of the NH/IH sensitivity as function of the data taking in JUNO-like experiment. The different curves correspond to different energy resolution (continuous/dashed are for NH/IH hypothesis, respectively). The background has been conservatively assumed to be described by the ^9Li component. Ten near reactor cores plus two remote cores have been used, each with a $\pm 5\,\mathrm{m}$ and $\pm 5\,\mathrm{km}$ uniform dispersions for the relative baseline, respectively.*

The result is very significant: at the foreseen six years of exposure JUNO will be able to set the mass hierarchy at more than $5\,\sigma$ significance when $\vec{F_{MO}}$. The relevance of the energy resolution is confirmed. The sensitivity curves are quite dependent on the resolution. A $4\%\sqrt{E}$ energy resolution will be critical to get a definite answer on the mass hierarchy in the JUNO context. Instead, already after two years of exposure (at a full